

ADDRESS OF PUBLISHER  
& EDITOR'S OFFICE:

GDANŃSK UNIVERSITY  
OF TECHNOLOGY

Faculty of Ocean Engineering  
& Ship Technology  
ul. Narutowicza 11/12  
80-233 Gdańsk, POLAND

tel.: +48 58 347 13 66  
fax: +48 58 341 13 66

EDITORIAL STAFF:

Jacek Rudnicki  
| Editor in Chief  
Przemysław Wierzchowski  
| Scientific Editor  
Jan Michalski  
| Editor for review matters  
Aleksander Kniat  
| Editor for international  
relations  
Kazimierz Kempa  
| Technical Editor  
Piotr Bzura  
| Managing Editor

Price:  
single issue: 25 zł

Prices for abroad  
single issue:  
- in Europe EURO 15  
- overseas USD 20

WEB:  
[www.bg.pg.gda.pl/pmr/pmr.php](http://www.bg.pg.gda.pl/pmr/pmr.php)

ISSN 1233-2585

## CONTENS

- 3 **JÓZEF LISOWSKI**  
*Comparison of dynamic games in application to safe ship control*
- 13 **MIROSLAW TOMERA**  
*Dynamic positioning system for a ship on harbour manoeuvring with different observers. Experimental results*
- 25 **IMANOL BASTERRETxea IRIBAR1, JESÚS ANGEL VILA MUÑOZ1, CARLOS ANGEL PÉREZ LABAJOS**  
*Latitude error in compass deviation*
- 32 **TOMASZ BUGALSKI, JAN A. SZANTYR**  
*Numerical Analysis of the Unsteady Propeller Performance in the Ship Wake Modified By Different Wake Improvement Devices*
- 40 **TADEUSZ CHRUSCIEL, EWELINA CIBA, JULITA DOPKE**  
*CFD and FEM model of an underwater vehicle propeller*
- 46 **B. MOUSAVI, A. RAHROVI, S. KHERADMAND**  
*Numerical simulation of tonal and broadband hydrodynamic noises of non-cavitating underwater propeller*
- 54 **CZESLAW DYMARSKI, PAWEŁ DYMARSKI**  
*Computational simulation of motion of a rescue module during its launching from ship at rough sea*
- 61 **TADEUSZ SZELANGIEWICZ, BERNARD WIŚNIEWSKI, KATARZYNA ŻELAZNY**  
*The influence of wind, wave and loading condition on total resistance and speed of the vessel*
- 68 **DONGSHENG QIAO, JUN YAN, JINPING OU**  
*Fatigue analysis of deepwater hybrid mooring line under corrosion effect*
- 77 **GRZEGORZ SZALA**  
*Comments on linear summation hypothesis of fatigue failures*
- 86 **ZDZISLAW STELMASIAK**  
*Application of alcohols to dual – fuel feeding the spark-ignition and self-ignition engines*

## Editorial

POLISH MARITIME RESEARCH is a scientific journal of worldwide circulation. The journal appears as a quarterly four times a year. The first issue of it was published in September 1994. Its main aim is to present original, innovative scientific ideas and Research & Development achievements in the field of :

### **Engineering, Computing & Technology, Mechanical Engineering,**

which could find applications in the broad domain of maritime economy. Hence there are published papers which concern methods of the designing, manufacturing and operating processes of such technical objects and devices as : ships, port equipment, ocean engineering units, underwater vehicles and equipment as well as harbour facilities, with accounting for marine environment protection.

The Editors of POLISH MARITIME RESEARCH make also efforts to present problems dealing with education of engineers and scientific and teaching personnel. As a rule, the basic papers are supplemented by information on conferences , important scientific events as well as cooperation in carrying out international scientific research projects.

### Scientific Board

**Chairman : Prof. JERZY GIRTLER - Gdańsk University of Technology, Poland**

**Vice-chairman : Prof. ANTONI JANKOWSKI - Institute of Aeronautics, Poland**

**Vice-chairman : Prof. MIROŚLAW L. WYSZYŃSKI - University of Birmingham, United Kingdom**

<b>Dr POUL ANDERSEN</b> Technical University of Denmark Denmark	<b>Prof. WOLFGANG FRICKE</b> Technical University Hamburg- Harburg Germany	<b>Prof. YASUHIKO OHTA</b> Nagoya Institute of Technology Japan
<b>Dr MEHMET ATLAR</b> University of Newcastle United Kingdom	<b>Prof. STANISŁAW GUCMA</b> Maritime University of Szczecin Poland	<b>Dr YOSHIO SATO</b> National Traffic Safety and Environment Laboratory Japan
<b>Prof. GÖRAN BARK</b> Chalmers University of Technology Sweden	<b>Prof. ANTONI ISKRA</b> Poznań University of Technology Poland	<b>Prof. KLAUS SCHIER</b> University of Applied Sciences Germany
<b>Prof. SERGEY BARSUKOV</b> Army Institute of Odessa Ukraine	<b>Prof. JAN KICIŃSKI</b> Institute of Fluid-Flow Machinery of PASci Poland	<b>Prof. FREDERICK STERN</b> University of Iowa, IA, USA
<b>Prof. MUSTAFA BAYHAN</b> Süleyman Demirel University Turkey	<b>Prof. ZYGMUNT KITOWSKI</b> Naval University Poland	<b>Prof. JÓZEF SZALA</b> Bydgoszcz University of Technology and Agriculture Poland
<b>Prof. VINCENZO CRUPI</b> University of Messina, Italy	<b>Prof. JAN KULCZYK</b> Wrocław University of Technology Poland	<b>Prof. TADEUSZ SZELANGIEWICZ</b> Technical University of Szczecin Poland
<b>Prof. MAREK DZIDA</b> Gdańsk University of Technology Poland	<b>Prof. NICOS LADOMMATOS</b> University College London United Kingdom	<b>Prof. WITALIJ SZCZAGIN</b> State Technical University of Kaliningrad Russia
<b>Prof. ODD M. FALTINSEN</b> Norwegian University of Science and Technology Norway	<b>Prof. JÓZEF LISOWSKI</b> Gdynia Maritime University Poland	<b>Prof. BORIS TIKHOMIROV</b> State Marine University of St. Petersburg Russia
<b>Prof. PATRICK V. FARRELL</b> University of Wisconsin Madison, WI USA	<b>Prof. JERZY MATUSIAK</b> Helsinki University of Technology Finland	<b>Prof. DRACOS VASSALOS</b> University of Glasgow and Strathclyde United Kingdom
	<b>Prof. EUGEN NEGRUS</b> University of Bucharest Romania	

# Comparison of dynamic games in application to safe ship control

Józef Lisowski, Prof.;  
Gdynia Maritime University, Poland

## ABSTRACT

The paper introduces methods of dynamic games for automation of ship control in the collision situation, the game control processes in marine navigation and the fundamental mathematical model of the game ship control. First, state equations, control and state constraints and then control goal function in the form of payments: the integral payment and the final one, have been defined. Multi-stage positional, and multi-step matrix, non-cooperative and cooperative, game and optimum control algorithms for a collision situation, have been presented. The considerations have been illustrated with an exemplary computer simulation of algorithms to determine a safe own ship's trajectory in the process of passing the ships encountered in Kattegat Strait.

**Keywords:** marine transport; safety at sea; safe ship control; optimum control; dynamic games positional game; matrix game; computer simulation

## INTRODUCTION

The control of the ship's movement may be treated as a multilevel problem ( Fig. 1) which results from the division of the entire control system of ship - within the frame of shipping the cargo by ship's operator - into clearly determined subsystems to which appropriate layers of control are ascribed.

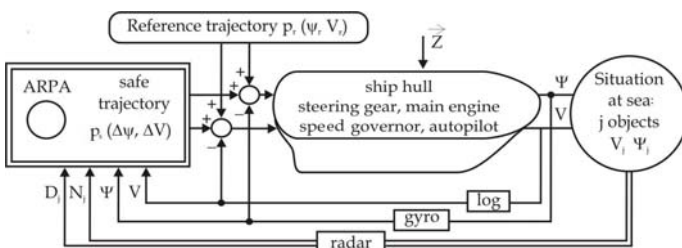


Fig. 1. Multilevel ship movement control system

This is connected both with a large number of dimensions of the control vector and status of the process, its random, fuzzy and decision-making characteristics - which are affected by strong interference resulting from sea current,

wind and wave motion on the one hand, and a complex nature of the equations describing the ship's dynamics with non-linear and non-stationary characteristics. The determination of the global control of the steering systems has in practice become too costly and ineffective.

The integral part of the entire system is the process of the ship's movement control, which may be described with appropriate differential equations of the kinematics and dynamics of a ship being an object of the control under a variety of the ship's operational conditions such as:

- stabilisation of ship course or trajectory,
- adjustment of ship's speed,
- precise steering at small speeds in port with the use of thrusters or adjustable-pitch propeller,
- stabilisation of ship's rolling,
- commanding the towing group,
- dynamic positioning of ship.

The functional diagram of the system corresponds to an actual arrangement of the equipment. The increasing demands with regard to the safety of navigation force the ship's operators to install integrated navigation systems on board their ships. By improving the ship's control, such systems rise the navigation safety of ship, a very expensive

object, whose value includes also the shipped cargo, and improve the effectiveness of cargo shipping by sea [3].

### SAFE SHIP CONTROL

The challenge in search for effective methods to prevent ship collisions has become crucial with the increasing of size, speed and number of ships participating in sea transport. An obvious contribution in increasing safety at sea has been first of all the application of radars and then the development of ARPA (Automatic Radar Plotting Aids) anti-collision system [4].

The ARPA system enables to track automatically at least 20 encountered  $j$ -objects, as shown in Fig. 2, in order to determine their movement parameters (speed  $V_j$ , course  $\psi_j$ ) and elements of approach to the own ship  $D_{\min}^j = \text{DCPA}_j$  - Distance at the Closest Point of Approach,  $T_{\min}^j = \text{TCPA}_j$  - Time to the Closest Point of Approach, and also to estimate the collision risk  $r_j$ .

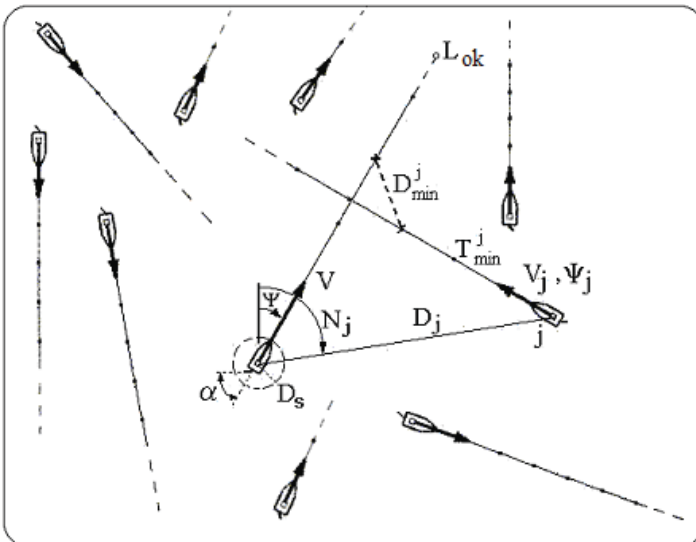


Fig. 2. Navigational situation representing the passing of the own ship with the  $j$ -th ship.

The risk value (1) is possible to be defined by referring the current situation of approach, described by parameters  $D_{\min}^j$  and  $T_{\min}^j$ , to the assumed evaluation of the situation as safe, determined by a safe distance of approach  $D_s$  and a safe time  $T_s$  - which are necessary to execute a collision avoiding manoeuvre with consideration of distance  $D_j$  to  $j$ -th met ship (Fig. 3).

$$r_j = \left[ \alpha_1 \left( \frac{D_{\min}^j}{D_s} \right)^2 + \alpha_2 \left( \frac{T_{\min}^j}{T_s} \right)^2 + \left( \frac{D_j}{D_s} \right)^2 \right]^{\frac{1}{2}} \quad (1)$$

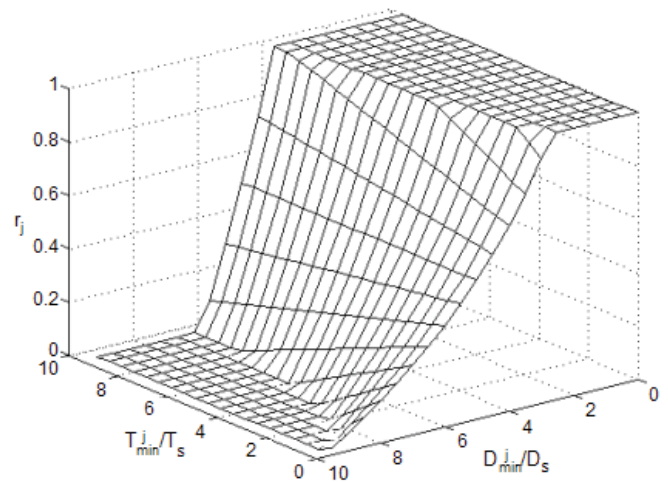


Fig. 3. The ship's collision risk space in function of relative distance and time of approaching  $j$ -th ship

The weight coefficients  $\alpha_1$  and  $\alpha_2$  are dependent on state of visibility at sea, the dynamic length  $L_d$  and dynamic beam  $B_d$  of the ship and a kind of water region. They are in practice equal to:

$$0 \leq [\alpha_1(L_d, B_d) \quad \alpha_2(L_d, B_d)] \leq 1 \quad (2)$$

$$L_d = 1.1 (1 + 0.345 V^{1.6}) \quad (3)$$

$$B_d = 1.1 (B + 0.767 V^{0.4}) \quad (4)$$

The functional scope of a standard ARPA system ends with the trial manoeuvre by altering the course  $\pm \Delta\psi$  or the ship's speed  $\pm \Delta V$  selected by the navigator, as shown in Fig. 4.

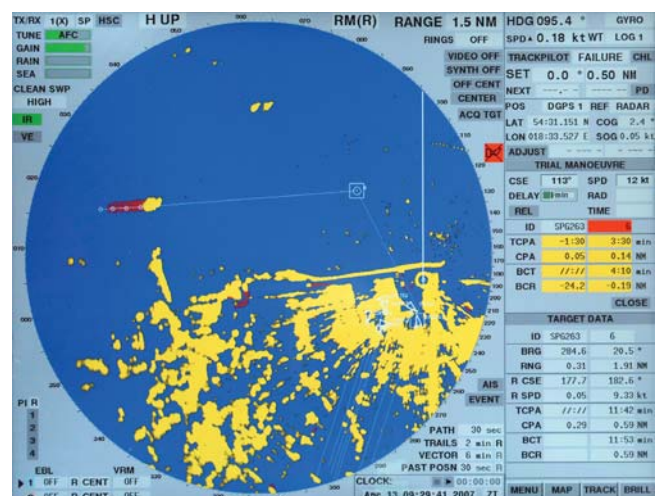


Fig. 4. The screen of SAM Electronics ARPA system installed on the research and training ship HORIZONT II

The problem of selecting such manoeuvre is very difficult as the control process is very complex due to its dynamic, non-linear, multi-dimensional, non-stationary and game making character.

In practice, methods of selecting a manoeuvre assume a form of appropriate steering algorithms supporting navigator decision in a collision situation. The algorithms are inserted into the memory of a Programmable Logic Controller PLC. This provides an option within the ARPA anti-collision system or a training simulator [11,13].

There are various methods to avoid ships collision. The simplest method is determination of the manoeuvre of a change in course or speed of own ship in relation to the most dangerous ship to be encountered. A more effective method is to determine safe trajectory of the ship. Most adequate to the real character of control process is determination of a game trajectory of the ship [5,8,16,19].

## GAME CONTROL

The classical issues of the theory of the decision process in marine navigation include the safe steering of a ship. The problem of non-collision strategies in the steering at sea appeared in the Isaacs' work [9] called "the father of the differential games" and was developed by many authors both within the context of the game theory and also in the steering under uncertainty conditions [1,2,10,14].

The definition of the problem of avoiding a collision seems to be obvious, however, apart from the issue of the uncertainty of information which may be a result of external factors (weather conditions, sea state), incomplete knowledge about other objects and imprecise nature of the recommendations concerning the right of way contained in International Regulations for Preventing Collision at Sea COLREG [6].

The problem of determining safe strategies is still an urgent issue as a result of an ever increasing traffic of vessels on particular water areas. It is also important due to the increasing requirements as to the safety of shipping and environmental protection, from one side, and to the improving opportunities to use computer supporting the navigator's duties. In order to ensure safe navigation, the ships are obliged to observe legal requirements contained in the COLREG Rules.

However, the Rules refer exclusively to two ships under good visibility condition. In case of restricted visibility the Rules provide only recommendations of a general nature and they do not cover all necessary conditions of the real process. Therefore, in the light of the legal regulations, the real ship passing process occurs under the conditions of indefiniteness and conflict accompanied by an imprecise co-operation among the ships.

Consequently, it is reasonable for ship operational purposes, to present this process and to develop and examine methods for a safe steering of the ship, by applying the rules of the game theory.

A necessity to consider simultaneously the strategies of the encountered objects and the dynamic properties of the

ships as the steering objects is a good reason to apply the differential game model, often called the dynamic game, for description of the processes [12,15,18].

## PROCESSES OF GAME CONTROL

It is assumed that the dynamic movement of the ships in time occurs under the influence of the appropriate sets of steering:

$$[\Theta_o^{(\beta)}, \Theta_j^{(\beta)}] \quad (5)$$

where:

$\Theta_o^{(\beta)}$  - a set of the own ship's strategies,

$\Theta_j^{(\beta)}$  - a set of the j-th ship's strategies,

$\beta = 0$  - denotes course and trajectory stabilisation,

$\beta = 1$  - denotes the execution of the anti-collision manoeuvre in order to minimize the risk of collision, which in practice is achieved by satisfying the following inequality:

$$D_{\min}^j = \min D_j(t) \geq D_s \quad (6)$$

$D_{\min}^j$  - the smallest distance of approach of the own ship and the j-th encountered object,

$D_s$  - safe approach distance in the prevailing conditions depending on the visibility conditions at sea, the COLREG Rules and the ship's dynamics.

$D_j$  - current distance to the j-th object taken from the ARPA anti-collision system.

$\beta = -1$  - refers to the manoeuvring of the ship in order to achieve the closest point of approach, for example during the approach of a rescue vessel, transfer of cargo from ship to ship, destruction of the enemy's ship, etc.).

Using the adopted describing symbols we can distinguish the following type of steering the ship in order to achieve a determined goal:

- basic type of steering- stabilization of the course or trajectory:  $[\Theta_o^{(0)}, \Theta_j^{(0)}]$

- avoidance of a collision by executing:

a) own ship's manoeuvres:  $[\Theta_o^{(1)}, \Theta_j^{(0)}]$

b) manoeuvres of the j-th ship:  $[\Theta_o^{(0)}, \Theta_j^{(1)}]$

c) co-operative manoeuvres:  $[\Theta_o^{(1)}, \Theta_j^{(1)}]$

- encounter of the ships:  $[\Theta_o^{(-1)}, \Theta_j^{(-1)}]$

- situations of a unilateral dynamic game:

$$[\Theta_o^{(-1)}, \Theta_j^{(0)}] \quad \text{and} \quad [\Theta_o^{(0)}, \Theta_j^{(-1)}]$$

Dangerous situations resulting from a faulty assessment of the approaching process by one of the party with the other party's failure to conduct observation - one ship is equipped with a radar or an anti-collision system, the other with a damaged radar or without such device.

- chasing situations which refer to a typical conflicting dynamic game:  $[\Theta_o^{(-1)}, \Theta_j^{(1)}]$  and  $[\Theta_o^{(1)}, \Theta_j^{(-1)}]$ .

The first case usually represents regular optimum control, the second and third are unilateral games while the fourth

and fifth cases represent the conflicting games

## BASIC MODEL

As the process of steering the ship in collision situations, when a greater number of objects is encountered, often occurs under the conditions of indefiniteness and conflict, accompanied by an inaccurate co-operation of the ships within the context of COLREG Regulations, therefore the most adequate model of the process which has been adopted, is a model of a dynamic game of  $j$  tracked ships, in general, as objects of steering.

The diversity of selection of possible models directly affects the synthesis of the ship's handling algorithms which are afterwards effected by the ship's handling device directly linked to the ARPA system and, consequently, determines the effects of the safe and optimum control.

The most general description of the own ship passing the  $j$ - number of other encountered ships is the model of a differential game of a  $j$ - number of objects, shown in Fig. 5.

The properties of the process are described by the state equation:

$$\dot{\bar{x}}_i = f_i [ x_{0,\vartheta_0}, x_{1,\vartheta_1}, \dots, x_{j,\vartheta_j}, \dots, x_{m,\vartheta_m} ] ( u_{0,v_0}, u_{1,v_1}, \dots, u_{j,v_j}, \dots, u_{m,v_m} ] \quad (7)$$

$$i = 1, \dots, (j \cdot \vartheta_j + \vartheta_0) \quad j = 1, \dots, m$$

where:

$\bar{x}_{0,\vartheta_0}(t)$  -  $\vartheta_0$  dimensional vector of the process state of the own ship determined in a time span  $t \in [t_0, t_k]$ ,

$\bar{x}_{j,\vartheta_j}(t)$  -  $\vartheta_j$  dimensional vector of the process state for the  $j$ -th ship,

$\bar{u}_{0,v_0}(t)$  -  $v_0$  dimensional control vector of the own ship,

$\bar{u}_{j,v_j}(t)$  -  $v_j$  dimensional control vector of the  $j$ -th ship.

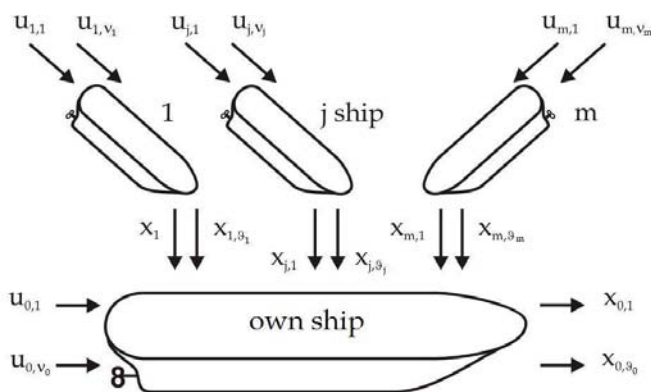


Fig. 5. Block diagram of a basic dynamic game model

Taking into consideration the equations reflecting the own ship's hydromechanics and equations of the own ship's movement relative to the  $j$ -th encountered ship, the equations of the general state of the process (7) take the form (8).

$$\begin{aligned} \dot{x}_{0,1} &= x_{0,2} \\ \dot{x}_{0,2} &= a_1 x_{0,2} x_{0,3} + a_2 x_{0,3} |x_{0,3}| + b_1 x_{0,3} |x_{0,3}| u_{0,1} \\ \dot{x}_{0,3} &= a_4 x_{0,3} |x_{0,3}| x_{0,4} |x_{0,4}| (1 + x_{0,4}) + a_5 x_{0,2} x_{0,3} x_{0,4} |x_{0,4}| + \\ &\quad + a_6 x_{0,2} x_{0,3} x_{0,4} + a_7 x_{0,3} |x_{0,3}| + a_8 x_{0,5} |x_{0,5}| x_{0,6} + \\ &\quad + b_2 x_{0,3} x_{0,4} |x_{0,3}| u_{0,1} \\ \dot{x}_{0,4} &= a_3 x_{0,3} x_{0,4} + a_4 x_{0,3} x_{0,4} |x_{0,4}| + a_5 x_{0,2} x_{0,2} + a_9 x_{0,2} + \\ &\quad + b_2 x_{0,3} u_{0,1} \end{aligned} \quad (8)$$

$$\dot{x}_{0,5} = a_{10} x_{0,5} + b_3 u_{0,2}$$

$$\dot{x}_{0,6} = a_1 x_{0,6} + b_4 u_{0,3}$$

$$\dot{x}_{j,1} = -x_{0,3} + x_{j,2} x_{0,2} + x_{j,3} \cos x_{j,3}$$

$$\dot{x}_{j,2} = -x_{0,2} x_{j,1} + x_{j,3} \sin x_{j,3}$$

$$\dot{x}_{j,3} = -x_{0,2} + b_{4+j} x_{j,3} u_{j,1}$$

$$\dot{x}_{j,4} = a_{1+j} x_{j,4} |x_{j,4}| + b_{5+j} u_{j,2}$$

The state variables are represented by the following values:

$x_{0,1} = \psi$  - course of the own ship,

$x_{0,2} = \dot{\psi}$  - angular turning speed of the own ship,

$x_{0,3} = V$  - speed of the own ship,

$x_{0,4} = \beta$  - drift angle of the own ship,

$x_{0,5} = n$  - rotational speed of the screw propeller of the own ship,

$x_{0,6} = H$  - pitch of the adjustable propeller of the own ship,

$x_{j,1} = D_j$  - distance to  $j$ -th object, or  $x_j$  - its coordinate,

$x_{j,2} = N_j$  - bearing of the  $j$ -th object, or  $y_j$  - its coordinate,

$x_{j,3} = \psi_j$  - course of the  $j$ -th object, or  $\beta_j$  - relative meeting angle,

$x_{j,4} = V_j$  - speed of the  $j$ -th object,

where:  $\vartheta_0 = 6$ ,  $\vartheta_j = 4$ .

While the control values are represented by:

$u_{0,1} = \alpha_r$  - reference rudder angle of the own ship, or  $\dot{\psi}$  - angular turning speed of the own ship, or  $\psi$  - course of the own ship, depending of a kind of approximated model of process,

$u_{0,2} = n_r$  - reference rotational speed of the own ship's screw propeller, or force of the propeller thrust of the own ship, or speed of the own ship,

$u_{0,3} = H_r$  - reference pitch of the adjustable screw propeller of the own ship,

$u_{j,1} = \psi_j$  - course of the  $j$ -th object, or  $\dot{\psi}_j$  - angular turning speed of the  $j$ -th object,

$u_{j,2} = V_j$  - speed of the  $j$ -th object, or force of the propeller thrust of the  $j$ -th object,

where:  $v_0 = 3$ ,  $v_i = 2$ .

Values of coefficients of the process state equations (8) for a 12 000 DWT container ship are given in Tab. 1.

**Tab. 1.** Coefficients of basic game model equations.

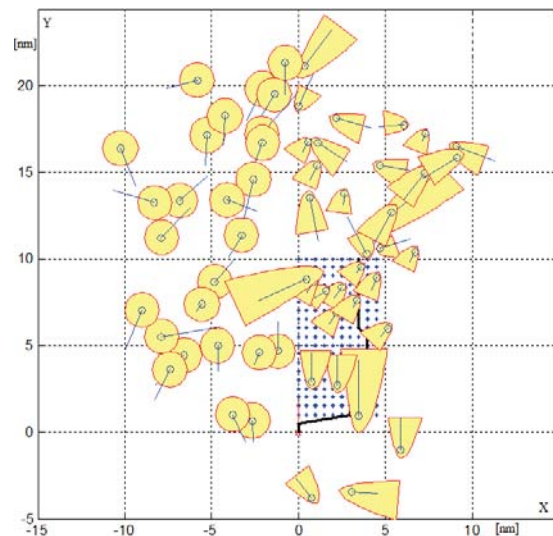
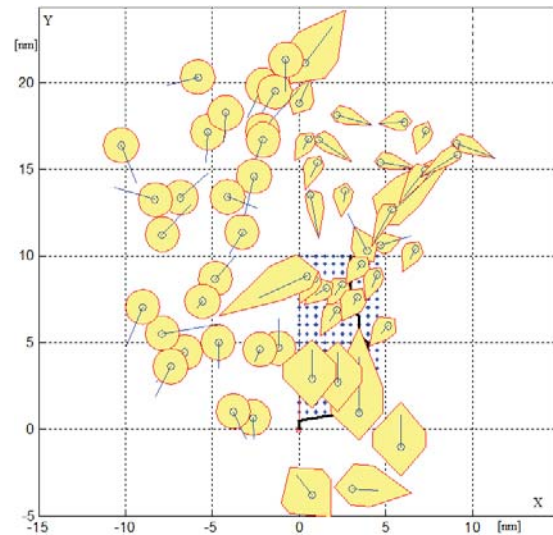
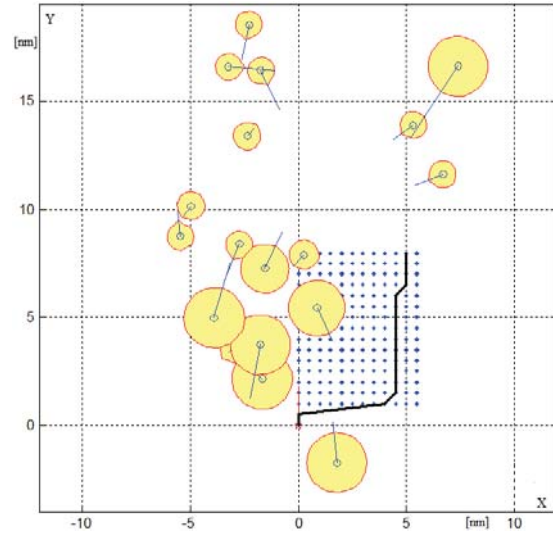
Coefficient	Measure	Value
$a_1$	$m^{-1}$	$-4.143 \cdot 10^{-2}$
$a_2$	$m^{-2}$	$1.858 \cdot 10^{-4}$
$a_3$	$m^{-1}$	$-6.934 \cdot 10^{-3}$
$a_4$	$m^{-1}$	$-3.177 \cdot 10^{-2}$
$a_5$	-	-4.435
$a_6$	-	-0.895
$a_7$	$m^{-1}$	$-9.284 \cdot 10^{-4}$
$a_8$	-	$1.357 \cdot 10^{-3}$
$a_9$	-	0.624
$a_{10}$	$s^{-1}$	-0.200
$a_{11}$	$s^{-1}$	-0.100
$a_{11+j}$	$s \cdot m^{-1}$	$-7.979 \cdot 10^{-4}$
$b_1$	$m^{-2}$	$1.134 \cdot 10^{-2}$
$b_2$	$m^{-1}$	$-1.554 \cdot 10^{-3}$
$b_3$	$s^{-1}$	0.200
$b_4$	$s^{-1}$	0.100
$b_{4+j}$	$m^{-1}$	$-3.333 \cdot 10^{-3}$
$b_{5+j}$	$m \cdot s^{-1}$	$9.536 \cdot 10^{-2}$

In the case of  $j=20$  met ships, the basic game model is represented by  $i=86$  state variables of process control.

The constraints of the control and the state of the process are connected with the basic condition for the safe passing of the objects at a safe distance  $D_s$  in compliance with COLREG Rules, which is generally expressed in the following form:

$$g_j(x_{j,9_j}, u_{j,v_j}) \leq 0 \quad (9)$$

The constraints referred to as *the ships domains* in the marine navigation, may take a shape of a circle, hexagon, parabola or ellipse, and be generated, for example, by an artificial neural network, as shown in Fig. 6, [2].



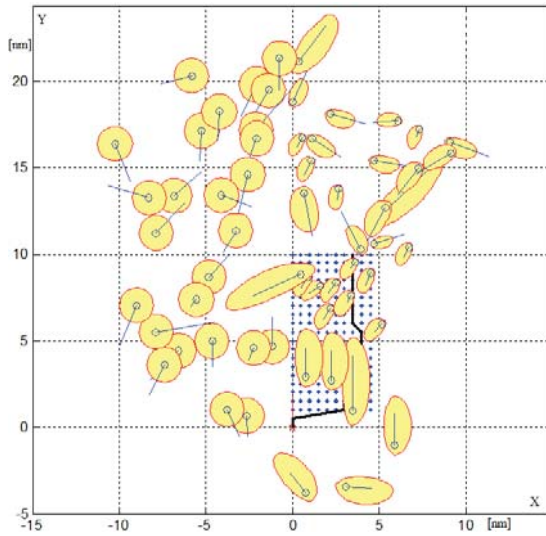


Fig. 6. The shapes of the neural domains: circle, hexagon, parabola and ellipse in the situation of 60 encountered ships in English Channel

The synthesis of the decision-making pattern of the object control leads to the determination of the optimum strategies of the players who determine the most favourable, under given conditions, conduct of the process. For the class of non-coalition games, often used in the control techniques, the most beneficial conduct of the own control object as a player with  $j$ -th object is the minimization of its goal function in the form of the payments – the integral payment and the final one:

$$I_{0,j} = \int_{t_0}^{t_k} [x_{0,9_0}(t)]^2 dt + r_j(t_k) + d(t_k) \rightarrow \min \quad (10)$$

The integral payment represents loss of way by the ship while passing the encountered objects and the final payment determines the final risk of collision  $r_j(t_k)$  relative to the  $j$ -th object and the final deflection of the ship  $d(t_k)$  from the reference trajectory.

Generally two types of the steering goals are taken into consideration - programmed steering  $u_0(t)$  and positional steering  $u_0[x_0(t)]$ . The basis for the decision-making steering are the decision-making patterns of the positional steering processes, the patterns with the feedback arrangement representing the dynamic games.

The application of reductions in the description of the own ship's dynamics and the dynamics of the  $j$ -th encountered ship and their movement kinematics leads to synthesis of game ship control algorithms in collision situations.

## ALGORITHMS OF GAME CONTROL

### Multi-stage positional game

The general model of dynamic game is simplified to the multi-stage positional game of  $j$  participants not co-operating with each other [7].

State variables and control values are represented by:

$$\left. \begin{aligned} x_{0,1} = X_0, x_{0,2} = Y_0, x_{j,1} = X_j, x_{j,2} = Y_j \\ u_{0,1} = \psi, u_{0,2} = V, u_{j,1} = \psi_j, u_{j,2} = V_j \\ j = 1, 2, \dots, m \end{aligned} \right\} \quad (11)$$

The essence of the positional game is to subordinate the strategies of the own ship to the current positions  $p(t_k)$  of the encountered objects at the current step  $k$ . In this way the process model takes into consideration any possible alterations of the course and speed of the encountered objects while steering is in progress. The current state of the process is determined by the co-ordinates of the own ship's position and the positions of the encountered objects:

$$\left. \begin{aligned} x_0 = (X_0, Y_0), x_j = (X_j, Y_j) \\ j = 1, 2, \dots, m \end{aligned} \right\} \quad (12)$$

The system generates its steering at the moment  $t_k$  on the basis of data received from the ARPA anti-collision system pertaining to the positions of the encountered ships:

$$p(t_k) = \begin{bmatrix} x_0(t_k) \\ x_j(t_k) \end{bmatrix} \quad j = 1, 2, \dots, m \quad k = 1, 2, \dots, K \quad (13)$$

It is assumed, according to the general concept of a multi-stage positional game, that at each discrete moment of time  $t_k$  the own ship knows the positions of the objects.

The constraints for the state co-ordinates:

$$\{x_0(t), x_j(t)\} \in P \quad (14)$$

are navigational constraints, while steering constraints:

$$u_0 \in \Theta_0, u_j \in \Theta_j \quad j = 1, 2, \dots, m \quad (15)$$

take into consideration: the ships' movement kinematics, recommendations of the COLREG Rules and the condition to maintain a safe passing distance as per relationship (6).

The closed sets  $\Theta_{0,j}$  and  $\Theta_{j,0}$ , defined as the sets of acceptable strategies of the participants to the game towards one another:

$$\{\Theta_{0,j}[p(t)], \Theta_{j,0}[p(t)]\} \quad (16)$$

are dependent, which means that the choice of steering  $u_j$  by the  $j$ -th object changes the sets of acceptable strategies of other ships.

### Multi-stage non-cooperative positional game algorithm pg\_nc

The optimum steering of the own ship  $u_0^*(t)$ , equivalent for the current position  $p(t)$  to the optimum positional control

$u_o^*(p)$ . The sets of acceptable strategies  $U_{j,0}[p(t_k)]$  are determined for the encountered ships relative to the own ship and initial sets  $U_{0,j}[p(t_k)]$  of acceptable strategies of the own ship relative to each one of the encountered ship. The pair of vectors  $u_j$  and  $u_{0,j}$  relative to each  $j$ -th ship is determined and then the optimum positional strategy for the own ship  $u_o^*(p)$  - from the condition (10).

$$I_0^* = \min_{u_0 \in \bigcap_{j=1}^m S_{0,j}} \max_{u_j \in S_j} \min_{u_{0,j} \in S_{0,j} t_0} \int_{t_0}^{t_k} u_0(t) dt = S_0^*(x_0, L_k) \quad (17)$$

The function  $S_0$  refers to the continuous function of the manoeuvring goal of the own ship, characterizing the distance  $S$  of the ship at the initial moment  $t_0$  to the nearest turning point  $L_k$  on the reference  $p_r(t_k)$  route of the voyage.

The optimum control of the own ship is calculated at each discrete stage of the ship's movement by applying the Simplex method to solve the problem of the triple linear programming, assuming the relationship (17) as the goal function and the control constraints (9).

#### Multi-stage cooperative positional game algorithm pg\_nc

The quality index of control for a cooperative game has the form:

$$I_0^* = \min_{u_0 \in \bigcap_{j=1}^m S_{0,j}} \max_{u_j \in S_j} \min_{u_{0,j} \in S_{0,j} t_0} \int_{t_0}^{t_k} u_0(t) dt = S_0^*(x_0, L_k) \quad (18)$$

#### Multi-step matrix game

When leaving aside the ship's dynamics equations, the general model of a dynamic game for the process of preventing collisions is reduced to the matrix game of  $j$ - participants non-co-operating with each other [17,20].

The state and steering variables are represented by the following values:

$$x_{j,1} = D_j, x_{j,2} = N_j, u_{0,1} = \psi, u_{0,2} = V, u_{j,1} = \psi_j, u_{j,2} = V_j \quad (19)$$

$j = 1, 2, \dots, m$

The game matrix  $R = [r_j(u_j, u_0)]$  includes the values of the collision risk  $r_j$  determined from relation (1) on the basis of data obtained from the ARPA anti-collision system for the acceptable strategies  $u_0$  of the own ship and acceptable strategies  $u_j$  of any particular number of  $j$  - encountered objects.

The problem of determining an optimum strategy may be reduced to the task of solving Simplex dual linear programming method. Mixed strategy components express the distribution of probability  $p_j(u_0, u_j)$  of using pure strategies by the players.

#### Multi-step non-cooperative matrix game algorithm mg\_nc

As a result of using the following form for the control goal:

$$I_0^* = \min_{u_0} \max_{u_j} r_j \quad (20)$$

the probability matrix  $P = [p_j(u_0, u_j)]$  of using particular pure strategies may be obtained.

The solution for the control problem is the strategy representing the highest probability:

$$u_0^* = u_0 \{ [p_j(u_0, u_j)]_{\max} \} \quad (21)$$

#### Multi-step cooperative matrix game algorithm mg\_c

The quality index of control for a cooperative game has the form:

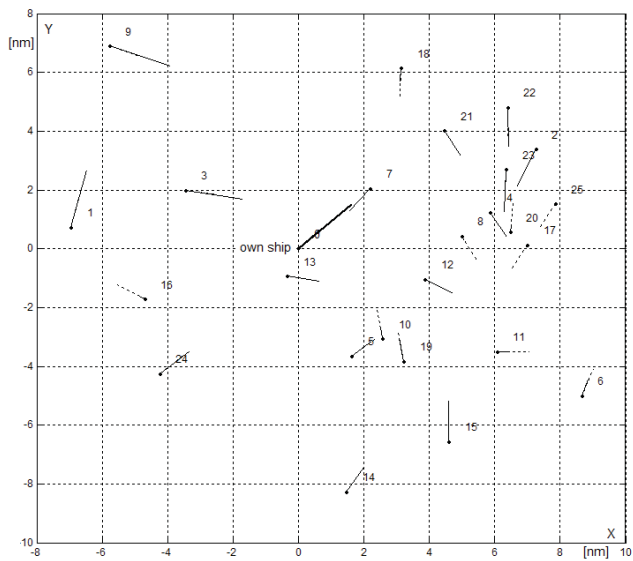
$$I_0^* = \min_{u_0} \min_{u_j} r_j \quad (22)$$

## COMPUTER SIMULATION

Computer simulation of control game algorithms were carried out on an example of a real navigational situations of passing  $j=25$  encountered ships. The situations were registered, in Kattegat Strait on board r/v HORIZONT II, owned by Gdynia Maritime University, on the radar screen of the ARPA anti-collision system Raytheon (Fig. 7 and 8).

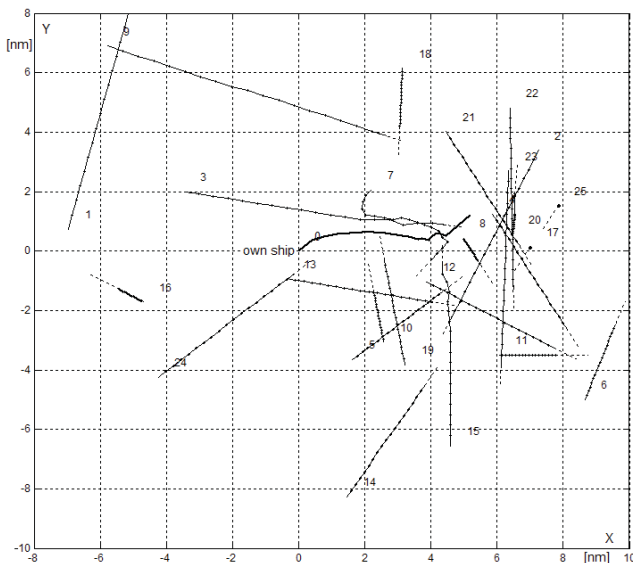


Fig. 7. The place of identification of navigational situation in Kattegat Strait



**Fig. 8.** The 12- minute speed vectors of own ship and 25 encountered ships in a navigational situation in Kattegat Strait

Examples of safe positional game trajectories are shown in Fig. 9 and 10.



**Fig. 9.** Computer simulation of multi-stage, non-cooperative positional game algorithm *pg\_nc* for safe own ship control in situation of passing 25 encountered ships,  $D_s=0,5$  nm,  $d(t_k)=2,65$  nm (nautical mile)

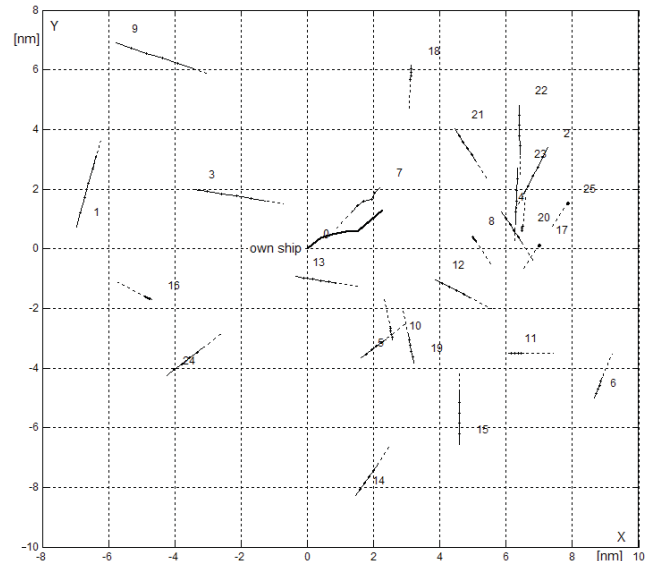


**Fig. 10.** Computer simulation of multi-stage cooperative positional game algorithm *pg\_c* for safe own ship control in situation of passing 25 encountered ships,  $D_s=0,5$  nm,  $d(t_k)=0,60$  nm (nautical mile)

Examples of safe matrix game trajectories are shown in Fig. 11 and 12.

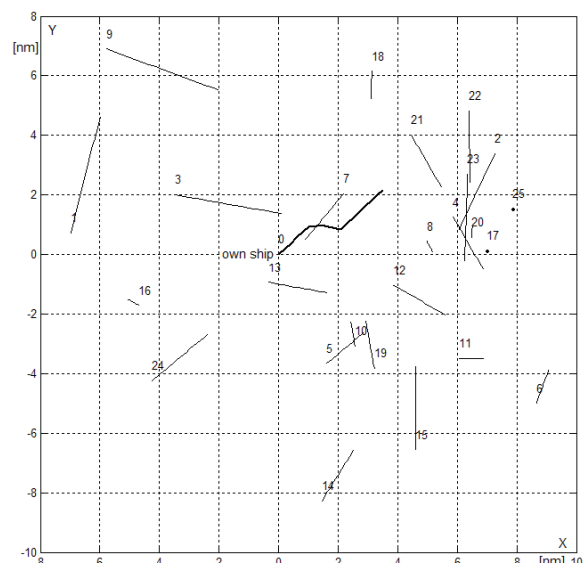


**Fig. 11.** Computer simulation of multi-step, non-cooperative matrix game algorithm *mg\_nc* for safe own ship control in situation of passing 25 encountered ships,  $D_s=0,5$  nm,  $d(t_k)=0,88$  nm (nautical mile)

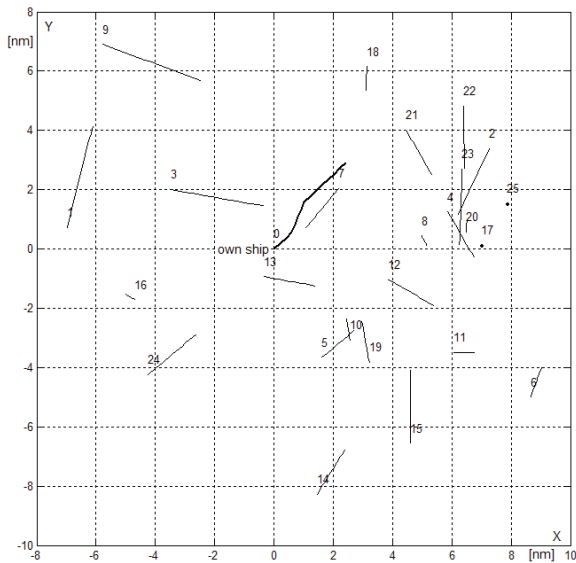


Fig. 12. Computer simulation of multi-step, cooperative matrix game algorithm *mg\_c* for safe own ship control in situation of passing 25 encountered ships,  $D_s=0,5$  nm,  $d(t_k)=0,48$  nm (nautical mile)

Fig. 13 shows a comparison of the own ship safe trajectory designated by four algorithms of dynamic game.

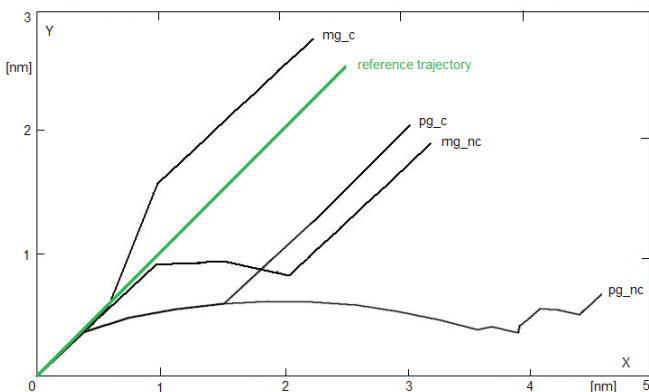


Fig. 13. Comparison of own ship safe trajectories in situation of passing 25 encountered ships

The biggest impact on the amount of the final game payment considered as the final deviation from the reference trajectory, has a degree of co-operation of ships in avoiding collision.

## CONCLUSIONS

The application of the models of a game theory for the synthesis of an optimum manoeuvring makes it possible to determine the safe game trajectory of the own ship in situations when she passes a greater number of the encountered ships.

The developed algorithms takes also into consideration the COLREGS Rules and the advance time of the manoeuvre approximating ship's dynamic properties and evaluates the

final deviation of the real trajectory from the reference one.

The positional game control algorithms determine game and safe trajectory of the own ship with relation to all encountered ships.

The matrix game control algorithms determine game and safe trajectory of the own ship with relation to the most dangerous ship.

To sum up, it may be stated that the control methods considered in this study are, in certain sense, formal models for the thinking processes of a navigating officer steering own ship and making decisions on manoeuvres.

Therefore they may be applied to the construction of a new model of ARPA system containing a computer which supports the navigator's decision-making process.

## BIBLIOGRAPHY

1. Basar T., Olsder G.J.: *Dynamic noncooperative game theory*. Siam, Philadelphia, 2013.
2. Baba N. and Jain L.C.: *Computational intelligence in games*. Physica-Verlag, New York, 2001.
3. Bist D.S.: *Safety and security at sea*. Butterworth Heinemann, Oxford-New Delhi, 2000.
4. Bole A., Dineley B., Wall A.: *Radar and ARPA manual*. Elsevier, Amsterdam-Tokyo, 2006.
5. Cahill R.A.: *Collisions and their causes*. The Nautical Institute, London, 2002.
6. Cockcroft A.N., Lameijer N.F.: *Collision avoidance rules*. Elsevier, Amsterdam-Tokyo, 2006.
7. Engwerda J.C.: *LQ dynamic optimization and differential games*. John Wiley and Sons, West Sussex, 2005.
8. Gluver H., Olsen D.: *Ship collision analysis*. Balkema, Rotterdam, 1998.
9. Isaacs R.: *Differential games*. John Wiley and Sons, New York, 1965.
10. Millington I. and Funge J.: *Artificial intelligence for games*. Elsevier, Amsterdam-Tokyo, 2009.
11. Modarres M.: *Risk analysis in engineering*. Taylor and Francis Group, Boca Raton, 2006.
12. Nisan N., Roughgarden T., Tardos E., Vazirani V.V.: *Algorithmic game theory*. Cambridge University Press, New York, 2007, p. 717-733.
13. Nise N.S.: *Control systems engineering*. John Wiley and Sons, New York, 2011.
14. Nowak A.S., Szajowski K.: *Advances in dynamic games, applications to economics, finance, optimization and stochastic control*. Birkhauser, Boston, Basel, Berlin, 2000.
15. Osborne M.J.: *An introduction to game theory*. Oxford University Press, New York, 2004.
16. Pietrzykowski Z.: *The navigational decision support system on a sea-going vessel*. Maritime University, Szczecin, 2011.
17. Radzik T.: *Characterization of optimal strategies in matrix games with convexity properties*. Game Theory, Vol. 29, No 2, 2000, p. 211-228.
18. Straffin P.D.: *Game theory and strategy*. Scholar,

Warszawa, 2001 (in Polish).

19. Szłapczyński R., Śmierchalski R.: *Supporting navigators decisions by visualizing ship collision risk*. Polish Maritime Research, Vol. 59, No 1, 2009, p. 83-88.
20. Zio E.: *Computational methods for reliability and risk analysis*. Quality, Reliability and Engineering Statistics, No 14, World Scientific, New Jersey-Chennai, 2009, p. 295-334.

### **CONTACT WITH THE AUTOR**

Józef Lisowski, Prof.  
Faculty of Marine Electrical Engineering,  
Gdynia Maritime University,  
Morska 81-87  
81-225 Gdynia, POLAND  
e-mail: jlis@am.gdynia.pl

# Dynamic positioning system for a ship on harbour manoeuvring with different observers. Experimental results

Mirosław Tomera, Ph. D.  
Gdynia Maritime University

## ABSTRACT

*In cases when the navigational space of the manoeuvre performed by the ship is severely limited, the procedures making use of the rudder blade, propeller screw, and thrusters are very complicated. Such situations take place when the ship manoeuvres inside the harbour area and in those cases the structure of the control system is very complex. The article describes the algorithm of multivariable control of ship motion over the water surface, which makes use of the state vector consisting of 6 variables. Three of them, which are the position coordinates  $(x, y)$  measured by the DGPS system and the ship heading  $\psi$  measured by gyro-compass, were obtained experimentally. The three remaining variables, which are the velocities in surge  $u$ , sway  $v$ , and yaw  $r$  directions, were estimated by Kalman filter, Kalman-Bucy filter and extended Kalman filter, respectively.*

*The control algorithms making use of these observers were examined using the training ship „Blue Lady” which was navigated on the lake Silm in Ilawa/Kamionka in the Ship Handling Research and Training Centre owned by the Foundation for Safety of Navigation and Environment Protection. The experimental results obtained using control systems with three observers were finally compared between each other.*

**Keywords:** Dynamic positioning system, Manoeuvring control, Observers, Real-time experiments.

## INTRODUCTION

Ship manoeuvring in the harbour area is one of most complicated and dangerous types of ship motion control. For this purpose all available actuators are used, including the rudder blade, propeller screw and thrusters. Due to low speed, nonlinear ship dynamics, wide ranges of manoeuvring movements, and complicated harbour environment, the safety of manoeuvring inside the harbour area is of extreme importance, especially in case of large ships. Therefore from the point of view of economy and safety an important issue is designing robust and efficient ship control systems for harbour manoeuvring.

Ship manoeuvring includes selection of the required passing trajectory, complemented by the requirements concerning the expected speed of ship motion along this trajectory. During ship manoeuvring, ship movements in the horizontal plane in surge, sway and yaw directions are to be taken into account. Since all sensors and actuators are used in ship manoeuvring inside the harbour, the controller performing this operation is to be a control system with a number of inputs and outputs. In the automatic control theory such systems bear the name of multivariable control

systems. Due to large ship inertia and low speeds near the pier, the environmental disturbances such as wind and water currents affect remarkably the safety of the manoeuvring operations.

The manoeuvring control makes use of techniques developed in dynamic ship positioning systems (DP). The tasks of the DP systems include keeping the ship position constant with the aid of the actuators only, and/or with the aid of mooring lines, and slow tracking of the reference velocity [1, 2].

Until the late 1970s, attempts to develop the control systems for sea going vessels were focused on designing various autopilots. The autopilot is a controller which keeps the ship course constant using the rudder blade for ship steering along the assumed direction. In this system the course was measured by a gyro-compass [3]. In the 1980s, commercial autopilot versions appeared on the market which were based on classical course controllers ([4, 5, 6].

With the introduction of precise devices for measuring ship position coordinates in the 1980s, the systems which controlled the ship motion along an assumed trajectory, so-called track-keeping control systems, started to be examined. The track-keeping system could be obtained

from a conventional ship course control system by simple use of the information coming from the positioning system [7]. A number of complicated controllers were designed to improve the operation of such autopilots, including the adaptive control [8, 9], self-tuning [10], LQG [11, 12],  $H_\infty$  [13] and those making use of fuzzy logic [14, 15] and artificial neural networks [16].

In the 1980s, along with the track-keeping systems as automatic systems focusing on manoeuvres performed inside the harbour and automatic mooring started to be analysed. Solving this problem required a mathematical model of a ship which would model the manoeuvring movements inside the harbour, complemented by a relevant control method. The discussion on an accurate mathematical model of a ship which could be used for manoeuvring control can be found in [17, 18, 19, 20, 21, 22].

In order to determine correct control, a number of methods were adapted which had been developed in the field of nonlinear and intelligent control. Shouji et al. [23] have formulated a mooring problem as nonlinear and limited by two point values, and used the optimal control techniques for designing the controller. Then the problem was solved in various manoeuvring situations using an iterative coupled gradient method [24, 25]. However these solutions could not be applied in online ship control systems due to excessively high calculation effort needed to obtain the optimal solution [26]. Sarioz and Narli performed simulation investigations to analyse the use of the manoeuvring control for controlling the motion of large tankers sailing through the Bosphorus Strait connecting the Marmara Sea with the Black Sea, the area in which numerous dangerous accidents have been recorded [27]. The manoeuvring task which ended with ship mooring in the harbour was also solved by developing multivariable neural networks and using them in a ship motion controller [28, 29]. Skjetne et al. have proposed an adaptive control method, which they examined by controlling the motion of the physical model of a ship bearing the name of Cybership II on shallow water in a laboratory shallow-water tank in Trondheim [30]. Gierusz et al. have developed a ship manoeuvring system which consisted of two different controllers switched on and off depending on the performed tasks [31]. Morawski and Nguyen Cong have developed a controller for ship manoeuvring inside the harbour area using fuzzy logic [32, 33]. Lee et al. have compared the quality of control of two controllers: the PID controller and the fuzzy controller during bringing the ship to harbour [34]. Bui et al. have proposed the use of four tug boats for ship manoeuvring in harbour, and the method of control of their movements [35].

The article presents the results of experimental investigations of a multivariable ship steering. The non-measured velocities as surge  $u$ , sway  $v$  and yaw  $r$ , were estimated using observer. Studies were conducted with three different observers: the discrete-time Kalman filter [36], the

continuous-time Kalman-Bucy filter [37] and the extended Kalman filter [38].

## THE MULTIVARIABLE SHIP MOTION CONTROL SYSTEM

The guidance system is used for planning the passing trajectory from the initial ship position to the target position. In the DP system the guidance system delivers a smooth trajectory with the position coordinates and the course leading to the next position.

When applied in low velocities, the controller calculates three assumed values, which are the longitudinal force, the lateral force and the rotating moment.

The propeller allocation processes the assumed forces and moment obtained from the controller to the required propeller settings, such as the rotational speed of the screw propeller, the blade setting angle, the rudder angle and the azimuth pitch propeller angle.

The main task of the observer is to deliver the low-frequency estimates of the ship's surge  $u$ , sway  $v$  and yaw  $r$  velocities.

### Guidance system

Guidance system was designed for tracking the set trajectory and consists in moving the ship along the reference trajectory. Figure 2 shows schematically sample ship motion from the initial position P to the target position K. To define this motion three coordinate systems were introduced. The first coordinate system is the Cartesian system  $x^n y^n$  fixed to the map of the water region in the tangential plane to the Earth surface in the area in which the manoeuvre is performed. In this system the  $x^n$  axis is directed north and the  $y^n$  axis is directed east. This reference system refers to the navigation over the Earth surface and, for simplicity, bears the name of the  $n$ -frame. The second coordinate system  $x^b y^b$  is movable and fixed to the moving ship. Here the  $x^b$  axis is directed along the longitudinal axis of the ship, from stern to bow, while the  $y^b$  axis is the lateral axis directed toward the starboard side. The ship position  $(x, y)$  and heading  $\psi$  are determined with respect to the stationary coordinate system ( $n$ -frame) and are collected in the position vector  $\eta = [x, y, \psi]^T$ , while the linear speeds  $(u, v)$  and the angular speed  $r$  are determined in the movable coordinate system  $x^b y^b$  and collected in the velocity vector  $v = [u, v, r]^T$ .

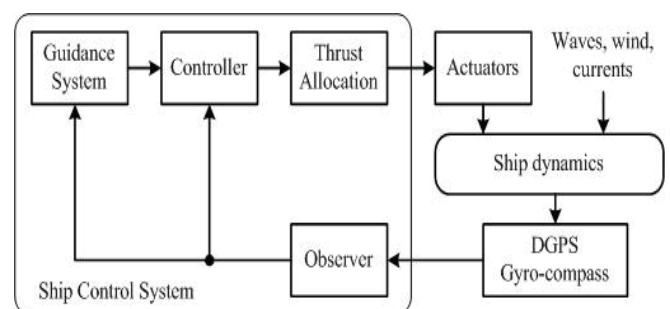


Fig. 1. Block diagram of ship control system and its major components

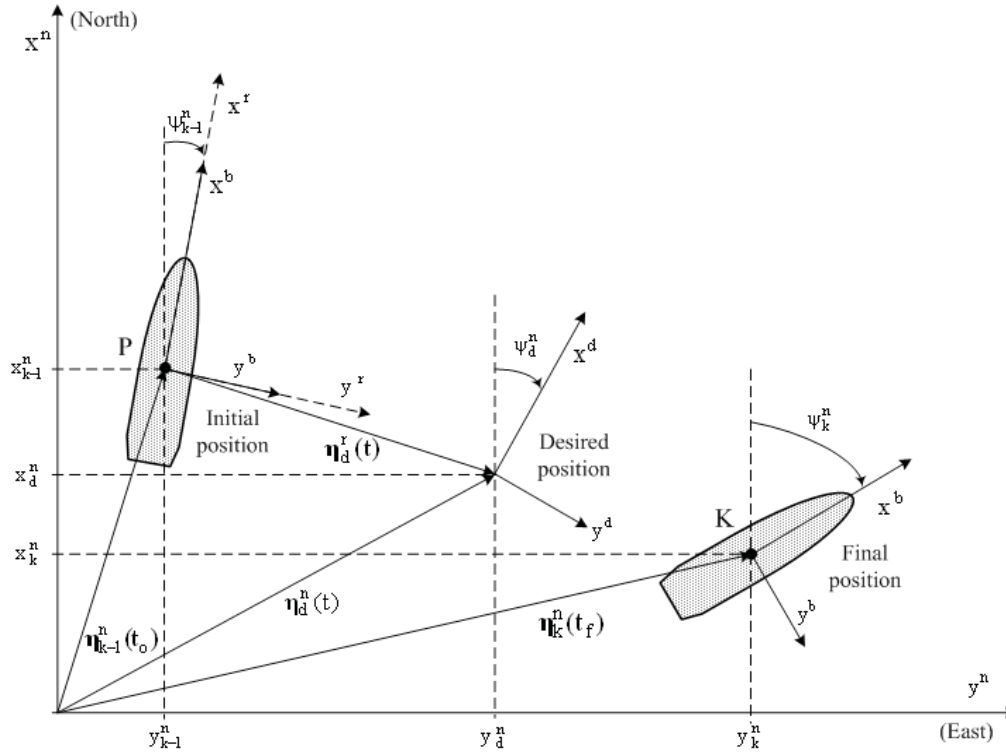


Fig. 2. Definition of the introduced reference systems and positions of the vehicle changing location [39]

The origin of the movable coordinate system is usually placed in the ship's centre of gravity. The motion of the ship changing the position is also described using the third coordinate system  $x^r y^r$  bearing the name of the reference coordinate system, the  $r$ -frame. This system is used for describing the ship motion from the initial point  $P$  to the final point  $K$ . This coordinate system has the same properties as the  $n$ -frame, with the only exception that the direction of the sense of the  $x^r$  axis changes and the coordinates of the origin of this system are each time shifted to the initial point  $P$  of the current trajectory segment.

$$\eta_k^r = (\eta_k^n - \eta_P^n) \cdot R(\psi_{k-1}^n) \quad (1)$$

where  $R(\phi)$  is the rotation matrix defined as

$$\mathbf{R}(\psi_{k-1}^n) = \begin{bmatrix} \cos \psi_{k-1}^n & \sin \psi_{k-1}^n & 0 \\ -\sin \psi_{k-1}^n & \cos \psi_{k-1}^n & 0 \\ 0 & 0 & 1 \end{bmatrix} \quad (2)$$

The coordinates of position  $\eta_d^r(t)$ , velocity  $\dot{\eta}_d^r(t)$  and acceleration  $\ddot{\eta}_d^r(t)$  of the virtual ship moving from the initial point  $P$  to the final point  $K$  are calculated in the reference system shown in Fig. 3.

### Mathematical model of ship dynamics

The object of control for which the presented control algorithm was prepared is the training ship bearing the name of "Blue Lady", which sails on the lake Silm near Ilawa in

the Ship Handling Research and Training Centre owned by the Foundation for Safety of Navigation and Environment Protection [40]. This ship is used for training captains to perform complicated and difficult manoeuvres with large ship in various navigational situations and on various water regions (harbours, narrow navigational channels, shallows, rivers, etc.). "Blue Lady" is an isomorphic model of a VLCC (Very Large Crude Carrier) tanker, the displacement of which is 176 000 DWT. The model is made of epoxide laminate in scale 1:24 (Fig. 4). The main particulars of "Blue Lady" are collected in Table 1.

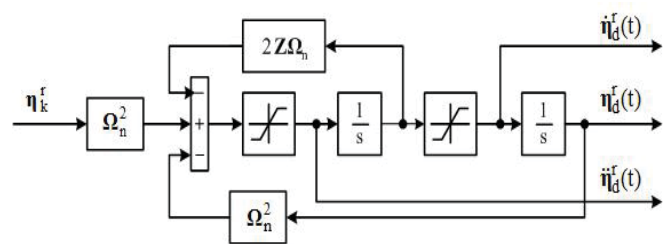


Fig. 3. Reference system command generator for DP controller [39]



Fig. 4. The view of the ship "Blue Lady" [40]

The manoeuvring system of "Blue Lady" consists of one rudder blade, one propeller screw, two tunnel thrusters (one at bow and one at stern), and two rotating thrusters (one at bow and one at stern). The locations of all installed propellers are shown in Fig. 5.

The control of all these propellers makes use of a set of eight commands:

- rudder blade angle deflection –  $\delta_c$  (deg),
- revolutions of the main propeller –  $n_{1c}$  (rpm),
- relative revolutions of a propeller of the bow (stern) tunnel thruster –  $p_{2c}$  ( $p_{3c}$ ),
- turn angle of the movable bow (stern) thruster –  $\alpha_{bc}$  ( $\alpha_{sc}$ ) (deg),
- relative revolutions of a propeller of the movable bow (stern) thruster –  $p_{bpc}$  ( $p_{spc}$ ) (-).

In the developed multivariable control system only three propellers are used, which are the main propeller, and the two tunnel thrusters. The complex mathematical model of "Blue Lady" dynamics, including the modelled actuators,

Tab. 1. Main particulars of the ship "Blue Lady"

Overall length ( $L_{0A}$ ) [m]	13.78
Length between perpendiculars [m]	13.50
Breadth [m]	2.38
Mean draught (full load) [m]	0.86
Displacement (full load) [m <sup>3</sup> ]	22.83
Nominal x coordinate of CG ( $x_c$ ) [m]	0.00
Maximal speed [knots]	3.10

which well reflects real behaviour of the training ship, was worked out by Gierusz [19].

The dynamic positioning system is designed for controlling the low-speed ship motion. The proposed multivariable

controller applied in the DP system will be determined based on the mathematical model of the ship at low speeds, described by the following formulas [3].

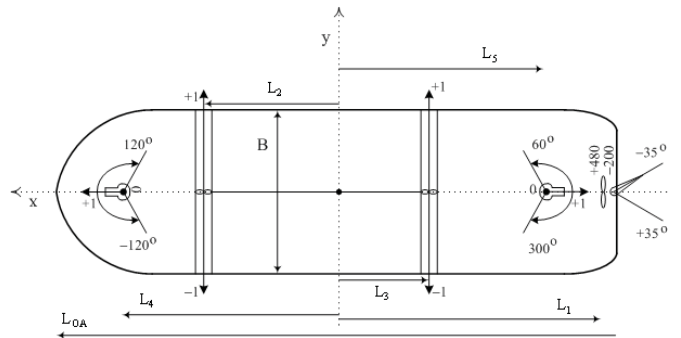


Fig. 5. Thrusters location on "Blue Lady" [39]

$$\dot{\eta} = R(\psi)v \quad (3)$$

$$M\dot{v} + D_L v = \tau \quad (4)$$

where  $R(\psi)$  is the rotation matrix:

$$R(\psi) = \begin{bmatrix} \cos \psi & -\sin \psi & 0 \\ \sin \psi & \cos \psi & 0 \\ 0 & 0 & 1 \end{bmatrix} \quad (5)$$

The matrix  $M$  includes the inertia parameters of a rigid body: its dimensions, weight, mass distribution, volume, etc. and the added mass coefficients.

$$M = \begin{bmatrix} m - X_{\dot{u}} & 0 & 0 \\ 0 & m - Y_{\dot{v}} & mx_G - Y_{\dot{r}} \\ 0 & mx_G - N_{\dot{v}} & I_z - N_{\dot{r}} \end{bmatrix} \quad (6)$$

The linear damping matrix  $D_L$  refers to hydrodynamic damping forces and is calculated for a given low and constant longitudinal speed  $v = v_0 \approx [u_0, 0, 0]^T$  [41].

$$D_L = \begin{bmatrix} -X_u & 0 & 0 \\ 0 & -Y_v & -Y_r \\ 0 & -N_v & -N_r \end{bmatrix} \quad (7)$$

It is assumed that the position vector  $\eta$  and the speed vector  $v$  are measured. The parameters calculated for the "Blue Lady" model ship at the speed  $u_0 = 0.1$  (m/s), are collected in Table 2.

**Tab. 2.** Parameters of the simplified mathematical model of "Blue Lady"

No	Variable	Value	No	Variable	Value
1.	$X_{\dot{u}}$	-730.50	6.	$X_u$	-21.10
2.	$Y_{\dot{v}}$	-1896.20	7.	$Y_v$	-259.80
3.	$Y_{\dot{r}}$	-18351.90	8.	$Y_r$	-855.40
4.	$N_{\dot{v}}$	0.00	9.	$N_v$	-855.40
5.	$N_{\dot{r}}$	0.00	10.	$N_r$	-6130.50

The following mathematical models of propellers used in the control system were analysed for low speed. The thrust force for the main propeller is

$$F_1 = k_1 |n_1| n_1 \quad (8)$$

where  $k_1 = 1.9589$  and  $n_1$  is the revolution of the screw propeller. The thrust forces:  $F_2$  for the bow tunnel thruster and  $F_3$  for the stern tunnel thruster are given by the formulas

$$F_i = k_i p_i, \quad i \in \{2, 3\} \quad (9)$$

where  $k_2 = k_3 = 44145$ , while  $p_2$  and  $p_3$  are the relative revolutions of propellers.

The forces generated by the thrusters are the following

$$\mathbf{u}_c = [F_1 \quad F_2 \quad F_3]^T \quad (10)$$

The vector of forces acting on the ship in relation with these thrusters are

$$\boldsymbol{\tau}_c = \mathbf{T} \mathbf{u}_c \quad (11)$$

$$\begin{bmatrix} \tau_X \\ \tau_Y \\ \tau_N \end{bmatrix} = \begin{bmatrix} 1 & 0 & 0 \\ 0 & 1 & 1 \\ 0 & L_2 & -L_3 \end{bmatrix} \cdot \begin{bmatrix} F_1(p_1) \\ F_2(p_2) \\ F_3(p_3) \end{bmatrix} \quad (12)$$

where  $L_2 = 3.24$  [m],  $L_3 = 2.376$  [m]. The matrix  $\mathbf{T}$  is the propeller configuration matrix.

### Multivariable controller

The control task consists in keeping track of the required smooth trajectory  $(\eta_d^r(t), \dot{\eta}_d^r(t), \ddot{\eta}_d^r(t))$  delivered by the ship navigation system. In the control systems the deviations from the set values will be calculated, out of which the position deviation  $\eta_e$  will be calculated in the stationary r-frame, while the speed and acceleration deviations will be determined in the movable b-frame fixed to the moving ship.

$$\eta_e^r = \eta^r - \eta_d^r \quad (13)$$

$$\dot{\eta}_e^b = \dot{\eta}^b - \dot{\eta}_d^b = \dot{\eta} - \mathbf{R}^T(\psi_e) \cdot \dot{\eta}_d^r \quad (14)$$

$$\ddot{\eta}_e^b = \ddot{\eta}^b - \ddot{\eta}_d^b = \ddot{\eta}^b - \dot{\psi}_e \mathbf{S}^T \mathbf{R}^T(\psi_e) \cdot \dot{\eta}_d^r - \mathbf{R}^T(\psi_e) \cdot \ddot{\eta}_d^r \quad (15)$$

where  $\psi_e = \psi - \psi_d$ , and the rotation matrix  $\mathbf{R}(\psi_e)$  is calculated using formula (5). The matrix  $\mathbf{S}$  has the following form:

$$\mathbf{S} = \begin{bmatrix} 0 & -1 & 0 \\ 1 & 0 & 0 \\ 0 & 0 & 0 \end{bmatrix} \quad (16)$$

In the DP control system a controller will be used which will stabilise the dynamics of the deviation, i.e.

$$\dot{\xi}_e^r = \eta_e^r \quad (17)$$

$$\ddot{\eta}_e^b + K_D \dot{\eta}_e^b + K_P \eta_e^r + K_I \xi_e^r = 0 \quad (18)$$

After determining the ship acceleration  $\ddot{\eta}^b$  from formula (18) we arrive at:

$$\ddot{\eta}^b = \ddot{\eta}_d^b - K_D \dot{\eta}_e^b - K_P \eta_e^r - K_I \xi_e^r \quad (19)$$

Based on equation (4), the proposed law of control will be given by the formula

$$\boldsymbol{\tau}_c = \mathbf{M} \dot{\mathbf{v}} + \mathbf{D}_L \mathbf{v} \quad (20)$$

The velocity vector derivative  $\dot{\mathbf{v}}$  in equation (20) is determined via differentiation of the kinetic equation (3) with respect to time, which gives us the searched relation

$$\dot{\mathbf{v}} = \mathbf{R}^{-1}(\psi) [\dot{\eta}^b - \dot{\mathbf{R}}(\psi) \mathbf{v}] \quad (21)$$

The derivative of the rotation matrix  $\mathbf{R}(\psi)$  is calculated from the formula

$$\dot{\mathbf{R}}(\psi) = r \mathbf{R}(\psi) \mathbf{S} \quad (22)$$

where  $r = \dot{\psi}$ . After placing the relation (19) to equation (21), and then to the proposed law of control (20), we arrive at the formula describing the algorithm of operation of the multivariable DP controller

$$\boldsymbol{\tau}_c = \mathbf{M} \mathbf{R}^{-1}(\psi) [\ddot{\eta}_d^b - K_D \dot{\eta}_e^b - K_P \eta_e^r - K_I \xi_e^r - r \mathbf{R}(\psi) \mathbf{S} \mathbf{v}] + \mathbf{D}_L \mathbf{v} \quad (23)$$

### Allocation of propellers

The control allocation problem appears when the number

of actuators is larger than the number of controlled degrees of freedom. The algorithm can be executed in two steps, as shown in Fig. 6.

In the first step, bearing the name of force allocation, the set generalised force  $\tau_c$  is decomposed into all propellers of interest. The quality of the decision made at this step depends on how good the force allocation algorithm is. The second step consists in finding settings for the actuators which will lead to the generation of the required forces  $F$ . This step is called the inverse transformation, as it consists in finding the inverse characteristics of the actuators.

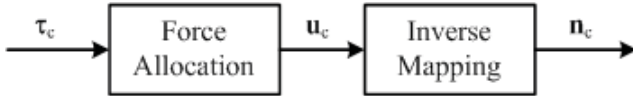


Fig. 6. The thrust allocation problem considered as a two-step process [39]

In the analysed DP system three propellers having the configuration shown in Fig. 2 were used for ship motion control. In this case the force allocation consists in solving the equation

$$u = T^{-1} \tau_c \quad (24)$$

$$\begin{bmatrix} F_1 \\ F_2 \\ F_3 \end{bmatrix} = \begin{bmatrix} 1 & 0 & 0 \\ 0 & 1 & 1 \\ 0 & L_2 & -L_3 \end{bmatrix}^{-1} \begin{bmatrix} \tau_X \\ \tau_Y \\ \tau_N \end{bmatrix} \quad (25)$$

After decomposing the forces into particular propellers, the transformation of formulas (8) and (9) gives the command values for the main propulsion propeller

$$n_{1c} = \text{sgn}(F_1) \sqrt{F_1/k_1} \quad (26)$$

and for the tunnel thrusters

$$p_{ic} = F_i/k_i, \quad i \in \{2,3\} \quad (27)$$

The command revolution of the main propeller ( $n_{1c}$ ) is to be limited to the physically existing range  $-200...+480$  (rpm), while the desired relative revolution of propellers for the bow ( $p_{2c}$ ) and stern ( $p_{3c}$ ) tunnel thrusters are to be kept within the range  $\pm 1$  (-).

## OBSERVERS USED FOR ESTIMATING THE SHIP VELOCITIES

The problems of filtration and state estimation are of high importance in dynamic positioning systems. In many cases the ship velocity measurements are not available and in those cases the velocity estimates should be determined by the stateobserver based on the noised measurements of ship's position and heading.

The first observer used to estimate the unmeasured velocities of the ship ( $u, v, r$ ) in multivariable control system shown in Figure 1, was a nonlinear observer [38]. However, during preliminary simulation studies of designed

multivariable control system that uses a nonlinear observer, problems with the stability of the overall control system appeared.

For this reason, the search for new observers to replace the nonlinear observer began. Author reached for observers based on the Kalman filter, using observers such as discrete Kalman filter, continuous Kalman filter and extended Kalman filter to estimate the unmeasured velocities. During the experimental tests carried out on the lake Silm in Ilawa/Kamionka, the control system that uses a nonlinear observer was unstable, while other control systems with observers based on the Kalman filter worked steadily. For this reason, in the following discussion nonlinear observer is omitted.

### Discrete-time Kalman filter

The discrete-time Kalman filter tries to estimate optimally the state vector of the controlled process, which is modelled by the linear, stochastic difference equation having the form [42].

$$\mathbf{x}_{k+1} = \mathbf{F}_k \mathbf{x}_k + \mathbf{G}_k \mathbf{w}_k \quad (28)$$

The observations (measurements) of the process are done at discrete times and are described by the following linear relation

$$\mathbf{y}_k = \mathbf{H}_k \mathbf{x}_k + \mathbf{v}_k \quad (29)$$

where  $\mathbf{x}_k$  is the state vector of the process at time  $t_k$ ,  $\mathbf{F}_k$  is the matrix which refers  $\mathbf{x}_k$  to  $\mathbf{x}_{k+1}$  at the absence of the exciting force,  $\mathbf{w}_k$  are the random disturbances affecting the process,  $\mathbf{G}_k$  is the matrix which scales the amplitude of the process disturbances,  $\mathbf{y}_k$  is the vector of the values measured at time  $t_k$ ,  $\mathbf{H}_k$  is the matrix linking the measurements with the state vector at time  $t_k$  and  $\mathbf{v}_k$  describes the measurement errors. It is assumed that the signals  $\mathbf{v}_k$  and  $\mathbf{w}_k$  have the mean value equal to zero and that there is no correlation between them [42].

Details concerning the derivation of the algorithm based on which the discrete Kalman filter works, and the way in which the estimation of ship velocity is performed can be

Tab. 3. Discrete-time Kalman filter [36, 43]

Design matrices	$\mathbf{Q}_k = \mathbf{Q}_k^T > 0, \mathbf{R}_k = \mathbf{R}_k^T > 0$
Initial conditions	$\bar{\mathbf{x}}(0) = \mathbf{x}_0, \bar{\mathbf{P}}(0) = \mathbf{P}_0$
Kalman gain matrix	$\mathbf{L}_k = \bar{\mathbf{P}}_k \mathbf{H}_k^T [\mathbf{H}_k \bar{\mathbf{P}}_k \mathbf{H}_k^T + \mathbf{R}_k]^{-1}$
State estimate update	$\hat{\mathbf{x}}_k = \bar{\mathbf{x}}_k + \mathbf{L}_k [\mathbf{y}_k - \mathbf{H}_k \bar{\mathbf{x}}_k]$
Error covariance update	$\hat{\mathbf{P}}_k = \bar{\mathbf{P}}_k - \bar{\mathbf{P}}_k \mathbf{H}_k^T [\mathbf{H}_k \bar{\mathbf{P}}_k \mathbf{H}_k^T + \mathbf{R}_k]^{-1} \mathbf{H}_k \bar{\mathbf{P}}_k$
State estimate propagation	$\bar{\mathbf{x}}_{k+1} = \mathbf{F}_k \hat{\mathbf{x}}_k$
Error covariance propagation	$\bar{\mathbf{P}}_{k+1} = \mathbf{F}_k \hat{\mathbf{P}}_k \mathbf{F}_k^T + \mathbf{G}_k \mathbf{Q}_k \mathbf{G}_k^T$

Tab. 4. Continuous-time Kalman-Bucy filter [37,43]

Design matrices	$\mathbf{Q}(t) = \mathbf{Q}^T(t) > 0, \quad \mathbf{R}(t) = \mathbf{R}^T(t) > 0,$
Initial conditions	$\mathbf{x}(0) = \mathbf{x}_0, \quad \mathbf{P}(0) = \mathbf{P}_0,$
Kalman gain matrix propagation	$\mathbf{L}(t) = \mathbf{P}(t)\mathbf{H}^T(t)\mathbf{R}^{-1}(t)$
State estimate propagation	$\dot{\hat{\mathbf{x}}}(t) = \mathbf{A}(t)\hat{\mathbf{x}}(t) + \mathbf{L}(t)[y(t) - \mathbf{C}(t)\hat{\mathbf{x}}(t)]$
Error covariance propagation	$\dot{\mathbf{P}}(t) = \mathbf{A}(t)\mathbf{P}(t) + \mathbf{P}(t)\mathbf{A}(t) + \mathbf{G}(t)\mathbf{Q}(t)\mathbf{G}(t) - \mathbf{P}(t)\mathbf{C}(t)\mathbf{R}^{-1}(t)\mathbf{C}(t)\mathbf{P}(t)$

found in [36]. The discrete-time Kalman filter algorithm is given in table 3.

Recursively determined gains of discrete-time Kalman filter  $\mathbf{L}$  according to an algorithm contained in Table 3 are steady-state within the first twelve seconds. To simplify the program code implementing the algorithm of discrete-time Kalman filter in calculations of estimates fixed values of gains obtained by using the function dlqr contained in the Matlab were used. In particular tracks of estimation the following gain values were applied

$$\mathbf{L}_x = \mathbf{L}_y = \mathbf{L}_\psi = \begin{bmatrix} 0.07945 \\ 0.36868 \end{bmatrix} \quad (30)$$

### Continuous-time Kalman-Bucy filter

The equation describing the continuous Kalman-Bucy filter are obtained from those describing the discrete Kalman filter by decreasing the sampling interval  $\Delta t \rightarrow 0$ . This

continuous process is described by the equation

$$\dot{\mathbf{x}}(t) = \mathbf{A}(t)\mathbf{x}(t) + \mathbf{G}(t)\mathbf{w}(t) \quad (31)$$

$$\mathbf{y}(t) = \mathbf{C}(t)\mathbf{x}(t) + \mathbf{v}(t) \quad (32)$$

where  $\mathbf{w}$  and  $\mathbf{v}$  are zero-mean Gaussian white noise processes. Details concerning the derivation of the equations describing the continuous Kalman-Bucy filter and the way in which it was used for estimating ship velocities can be found in [37].

In paper were used the steady-state solution for continuous-time Kalman filter given by

$$\mathbf{L}(t) = \mathbf{L}_\infty = \mathbf{P}_\infty \mathbf{C}^T \mathbf{R}^{-1} \quad (33)$$

where  $\mathbf{P}_\infty = \mathbf{P}_\infty^T > 0$  is the positive definite solution of the algebraic matrix Riccati equation

$$\mathbf{A}\mathbf{P}_\infty + \mathbf{P}_\infty \mathbf{A}^T + \mathbf{G}\mathbf{Q}\mathbf{G}^T - \mathbf{P}_\infty \mathbf{C}^T \mathbf{R}^{-1} \mathbf{C}\mathbf{P}_\infty = 0 \quad (34)$$

The steady-state values of gains  $\mathbf{L}_\infty$  were determined by the function lqr from the library of Matlab. In particular tracks of estimation the following gain values were used

$$\mathbf{L}_{x\infty} = \mathbf{L}_{y\infty} = \mathbf{L}_{\psi\infty} = \begin{bmatrix} 0.1 \\ 0.45826 \end{bmatrix} \quad (35)$$

### Extended Kalman filter

A design of the extended Kalman filter for the multivariable system of ship motion control will be based on the nonlinear model having the following form:

$$\dot{\mathbf{x}}(t) = \mathbf{f}(\mathbf{x}(t)) + \mathbf{E}\mathbf{w}(t) \quad (36)$$

$$\mathbf{y}(t) = \mathbf{H}\mathbf{x}(t) + \mathbf{v}(t) \quad (37)$$

where the matrices  $\mathbf{f}(\mathbf{x}(t))$ ,  $\mathbf{E}$  and  $\mathbf{H}$  take the following forms [38]

$$\mathbf{f}(\mathbf{x}(t)) = \begin{bmatrix} \mathbf{R}(\psi(t))\mathbf{v}(t) \\ -\mathbf{M}^{-1}\mathbf{D}_L\mathbf{v}(t) + \mathbf{M}^{-1}\mathbf{R}^T(\boldsymbol{\eta}(t)) \\ -\mathbf{T}_b^{-1} \end{bmatrix} \quad (38)$$

$$\mathbf{E} = \begin{bmatrix} \mathbf{0}_{3 \times 3} \\ \mathbf{0}_{3 \times 3} \\ \mathbf{E}_b \end{bmatrix} \quad (39)$$

$$\mathbf{H} = [\mathbf{I}_{3 \times 3} \quad \mathbf{0}_{3 \times 3} \quad \mathbf{0}_{3 \times 3}] \quad (40)$$

Here:  $\mathbf{x} = [\boldsymbol{\eta} \quad \mathbf{v} \quad \mathbf{b}]^T$ ,  $\mathbf{w} = \mathbf{w}_b$ . The matrix  $\mathbf{f}(\mathbf{x}(t))$  is a nonlinear vector field.

The extended Kalman filter is derived in the discrete form. For this purpose the linearized state equation (36) and the output equation (37) are written in the following discrete form

$$\mathbf{x}_{k+1} = \mathbf{F}_k \mathbf{x}_k + \mathbf{G}_k \mathbf{w}_k \quad (41)$$

$$\mathbf{y}_k = \mathbf{H}\mathbf{x}_k + \mathbf{v}_k \quad (42)$$

Tab. 5. Discrete-time extended Kalman Filter [38, 43]

Design matrices	$\mathbf{Q}_k = \mathbf{Q}_k^T > 0, \quad \mathbf{R}_k = \mathbf{R}_k^T > 0$
Initial conditions	$\bar{\mathbf{x}}(0) = \mathbf{x}_0, \quad \bar{\mathbf{P}}(0) = \mathbf{P}_0$
Kalman gain matrix	$\mathbf{L}_k = \bar{\mathbf{P}}_k \mathbf{H}_k^T [\mathbf{H}_k \bar{\mathbf{P}}_k \mathbf{H}_k^T + \mathbf{R}_k]^{-1}$
State estimate update	$\hat{\mathbf{x}}_k = \bar{\mathbf{x}}_k + \mathbf{L}_k [y_k - \mathbf{H}_k \bar{\mathbf{x}}_k]$
Error covariance update	$\hat{\mathbf{P}}_k = \bar{\mathbf{P}}_k - \bar{\mathbf{P}}_k \mathbf{H}_k^T [\mathbf{H}_k \bar{\mathbf{P}}_k \mathbf{H}_k^T + \mathbf{R}_k]^{-1} \mathbf{H}_k \bar{\mathbf{P}}_k$
State estimate propagation	$\bar{\mathbf{x}}_{k+1} = \mathbf{O}(\hat{\mathbf{x}}_k)$
Error covariance propagation	$\bar{\mathbf{P}}_{k+1} = \mathbf{F}_k \hat{\mathbf{P}}_k \mathbf{F}_k^T + \mathbf{G}_k \mathbf{Q}_k \mathbf{G}_k^T$

where matrices  $\mathbf{F}_k$  and  $\mathbf{G}_k$  can be determined using the Euler forward method and the following relations

$$\Phi(\hat{\mathbf{x}}(k)) = \mathbf{x}(k) + T \cdot f(\hat{\mathbf{x}}(k)) \quad (43)$$

$$\mathbf{F}_k = \mathbf{I}_{n \times n} + T \left. \frac{\partial f_k(\mathbf{x}_k)}{\partial \mathbf{x}_k} \right|_{\mathbf{x}_k = \hat{\mathbf{x}}_k} \quad (44)$$

$$\mathbf{G}_k = T \cdot \mathbf{E} \quad (45)$$

where  $T > 0$  is the sample time. This system includes  $n = 9$  states, the process noise covariance weight matrix  $\mathbf{Q}_k = E(\mathbf{w}_k^T \mathbf{w}_k) \in \mathfrak{R}^{n \times n}$  and the ship position and heading measurement noise covariance matrix  $\mathbf{R}_k = E(\mathbf{v}_k^T \mathbf{v}_k) \in \mathfrak{R}^{3 \times 3}$ . These matrices usually exist in the diagonal form. For this system, the state vector was estimated using the algorithm of discrete-time extended Kalman filter (EKF) placed in table 5.

### CASE OF STUDY

Simulation and experimental tests were performed to assess the quality of the designed control system with different observers. The experimental tests were performed on the training ship "Blue Lady", the characteristics of which were given earlier. During the tests the ship position coordinates  $(x, y)$  were measured by the DGPS system, while the ship heading  $\psi$  was recorded by the gyro-compass. The velocities as surge  $u$ , sway  $v$  and yaw  $r$  were estimated by the observer.

The complete control system, shown in Fig. 1, was modelled in the Matlab/Simulink environment, in which the simulation tests were performed. All blocks belonging to this scheme (navigation system, controller, propeller allocation, observer, ship) were recorded in the form of S-functions as M-files. The next step was the translation of all S-functions into the C language and their compilation to the form of MEX-files. During the simulation tests, following parameters of the PID-type multivariable controller were selected

$$\mathbf{K}_p = \text{diag}(1 \quad 1 \quad 1) \quad (46)$$

$$\mathbf{K}_i = \text{diag}(0.01 \quad 0.01 \quad 0.01) \quad (47)$$

$$\mathbf{K}_d = \text{diag}(100 \quad 100 \quad 100) \quad (48)$$

The designed extended Kalman filter was based on the following mathematical model of "Blue Lady"

$$\mathbf{M} = \text{diag}(23664.9 \quad 24830.6 \quad 455182.1) \quad (49)$$

$$\mathbf{D}_L = \begin{bmatrix} 21.10 & 0 & 0 \\ 0 & 259.8 & -855.4 \\ 0 & -855.4 & 6130.5 \end{bmatrix} \quad (50)$$

The time constants for the bias were selected in the following way

$$\mathbf{T}_b = \text{diag}(1000 \quad 1000 \quad 1000) \quad (51)$$

The process noise covariance weight matrix

$$\mathbf{Q} = \text{diag}(0.1 \quad 0.1 \quad 0.1) \quad (52)$$

and the ship position and heading measurement noise covariance matrix

$$\mathbf{R} = \text{diag}(0.1 \quad 0.1 \quad 0.1) \quad (53)$$

The simulation tests consisted in ship manoeuvring along different trajectories inside the harbour area in different weather conditions. The system was tested with different observers described earlier. Estimating the ship velocity components  $u, v, r$  from the position coordinates  $(x, y)$  measured by the DGPS and the ship course measured by the gyro-compass took into account the measurement noise.

After completing the simulation tests and confirming the correctness of system operation in various manoeuvring tasks performed with different observers, the next step was to initiate the designed control algorithm on a real ship. For this purpose the control and measurement system worked out in the Department of Ship Automation, Gdynia Maritime University was used [44]. The system makes use of Mathworks programmes and works in the xPC Target mode, which requires two computers. The software installed in the first computer, referred to as 'Host', includes Matlab with toolboxes: Simulink, Real Time Workshop and xPC-Target. The designed control algorithm comprising the navigation system, the controller, the propeller allocation and the observer is recorded in Simulink in the form of blocks with S-functions as C-MEX files, which were earlier tested in simulation tests. The second computer, bearing the name of 'Target' is equipped with an I/O card with analogue and numerical inputs and outputs and serial transmission ports (RS232/422/485) designed for communication with external devices. The communication between 'Host' and 'Target' is realised via Ethernet.

The Real Time Workshop generates the code ANSI/ISO C from the block diagram stored in the Simulink and containing C-MEX files with the control system algorithm. The code generated in the above way is then compiled to the executable form and sent to 'Target'. After starting the scheme in Simulink stored in 'Host' the initiation of the real-time control takes place.

To assess the quality of operation of the designed control system, the test consisting in changing the ship position inside the harbour area was performed, as shown in Fig. 7.

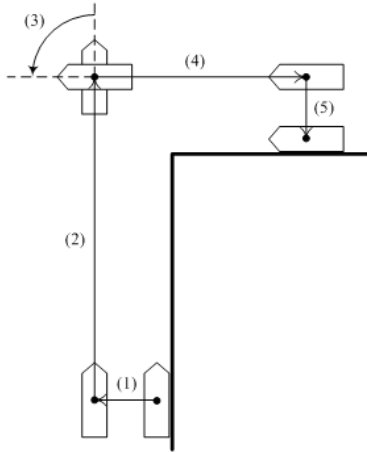


Fig. 7. Schematic overview of the performed manoeuvres

The test task included the following manoeuvres:

- (1) lateral ship movement to port side by 7 (m),
- (2) longitudinal ship movement forward by 38 (m),
- (3) ship rotation by 90 degrees,
- (4) longitudinal ship movement backward by 15 (m),
- (5) lateral ship movement to port side by 3 (m).

The change of the performed manoeuvre was done when the ship was at a distance of 1 m from the turning point and the course difference was smaller than 5 degrees.

During the tests performed on the lake Silm the wind blew from the average direction  $\psi_w = 300$  (deg) and at the average speed  $V_w = 3$  (m/s).

In Figure 8, the trajectory of the training ship “Blue Lady” is shown selected as reflected, successive positions of the hull, recorded by an electronic map of the water basin where the manoeuvres were performed.

Figures 9-11 present the results of the experimental tests performed using the control system shown in Fig. 1 with three observers (the discrete Kalman filter, the continuous Kalman-Bucy filter, and the extended discrete Kalman filter). The desired and measured vector position of the ship  $\eta = [x, y, \psi]^T$  in r-frame were shown in the left columns, whereas the desired and estimate ship velocity vector  $v = [u, v, r]^T$  in surge, sway and yaw were shown in the right columns.

The quality of operation of the control systems with different observers was assessed by calculating the accuracy of ship position control. To assess the accuracy of the ship position control, three coefficients were calculated in form:

$$x_E = \frac{1}{N} \sum_{k=1}^N |x_d^r(k) - x^r(k)| \quad (54)$$

$$y_E = \frac{1}{N} \sum_{k=1}^N |y_d^r(k) - y^r(k)| \quad (55)$$

$$\psi_E = \frac{1}{N} \sum_{k=1}^N |\psi_d^r(k) - \psi^r(k)| \quad (56)$$

where  $x_d^r, y_d^r, \psi_d^r$  are the set position coordinates, and the variables  $x^r, y^r, \psi^r$  represent the values measured by the

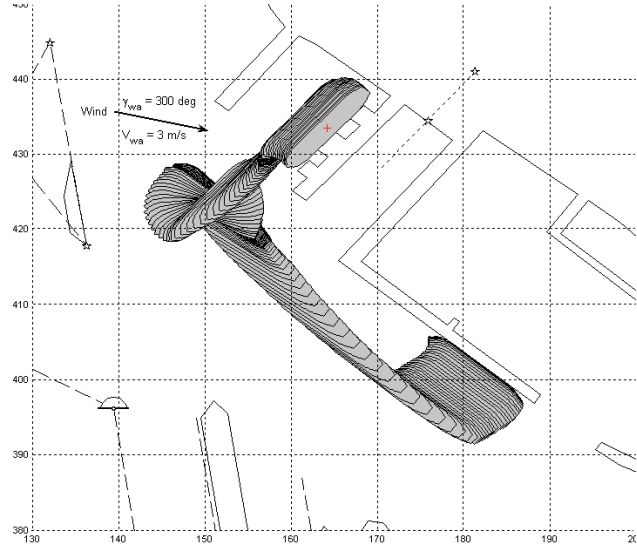


Fig. 8. The analysed ship motion trajectory on the lake Silm, where  $\gamma_{wa}$  is the average wind direction,  $V_w$  is the average wind speed

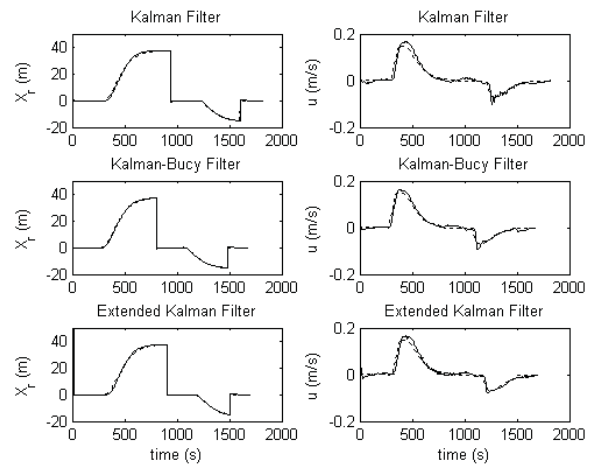


Fig. 9. Left column: coordinate X of ship position in r-frame, desired values (dashed line), measured values (solid line). Right column: surge ship speed u in b-frame, desired values (dashed line), estimated values (solid line)

ship position deviations the functional having the following form was calculated

$$J_c = \lambda_1 x_E + \lambda_2 y_E + \lambda_3 \psi_E \quad (57)$$

where  $\lambda_1 = 1.0$ ,  $\lambda_2 = 1.0$ ,  $\lambda_3 = 0.01$  are the weight coefficients. The results of obtained in the tests performed on the lake Silm are given in Table 6.

## REMARKS AND CONCLUSIONS

In the article the quality of ship motion control was analysed for the case when the ship performs the position change manoeuvre inside the harbour area from one berth to another. The manoeuvre was performed using three different observers for estimating the ship velocity components, i.e. surge  $u$ , sway  $v$  and yaw  $r$ , and was completed independently on the used observer.

Analysing the results collected in Table 6 leads to the conclusion that the best quality of control was obtained when the continuous-time Kalman-Bucy filter was used as the observer. The designed control system equipped with this observer reveals the highest accuracy of control.

## BIBLIOGRAPHY

1. Strand J.P.: *Nonlinear position control systems design for marine vessels*, Ph.D. Thesis, Norwegian University Science and Technology, Department of Engineering Cybernetics, Trondheim, Norway, 1999.
2. Lindegaard K.-P.: *Acceleration Feedback in Dynamic Positioning*, Ph.D. Thesis, Norwegian University Science and Technology, Department of Engineering Cybernetics, Trondheim, Norway, 2003.
3. Fossen T.I., 1994. *Guidance and control of ocean vehicles*, John Wiley and Sons, Chichester, UK, 1994.
4. Amerongen J.V.: *Adaptive Steering of Ships - Model Reference Approach*, Automatica, Vol. 20, No 1, 1984, pp. 3-14.
5. Saelid S., Svanes T., Onshus T., Jensen N.A.: *Design considerations, analysis and practical experience with an adaptive ship's autopilot*, In: Proceedings of the 9<sup>th</sup> IFAC World Congress, Budapest, Hungary, 1984, pp. 35-40.
6. Holzhtuter T., Strauch H.: *A Commercial Adaptive Autopilot for Ships: Design and Operational Experiences*, In: Proceedings of the 10<sup>th</sup> IFAC World Congress, Munich, Germany, 1987, pp. 226-230.
7. Amerongen J.V., Nauta Lemke H.R.V.: *Recent development in automatic steering of ships*, Journal of Navigation, Vol. 39, No 3, 1986, pp. 349-362.
8. Amerongen J.V., Land E.F.A.: *An adaptive autopilot for track-keeping*, Ship Operation Automation, III, Editor J. Vlietstra, North-Holland Publishing Company, 1980, pp. 105-114.
9. Chocianowicz W., Pejaś J.: *Adaptive control system for steering the ship along the desired trajectory - based on the optimal control and filtering theory*, In: Proceedings of the Control Applications in Marine Systems (CAMS-92),

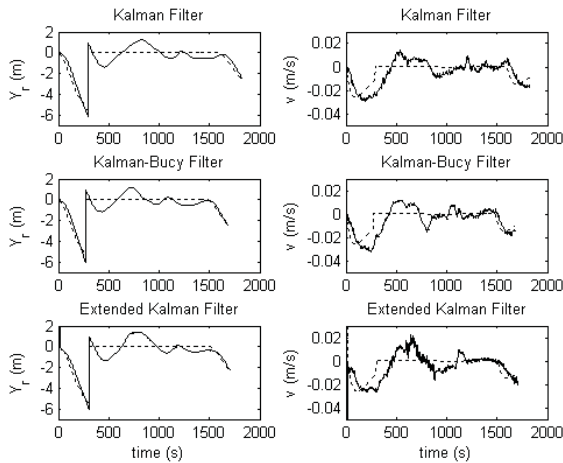


Fig. 10. Left column: coordinate  $Y$  of ship position in  $r$ -frame, desired values (dashed line), measured values (solid line). Right column: sway ship speed  $v$  in  $b$ -frame, desired values (dashed line), estimated values (solid line)

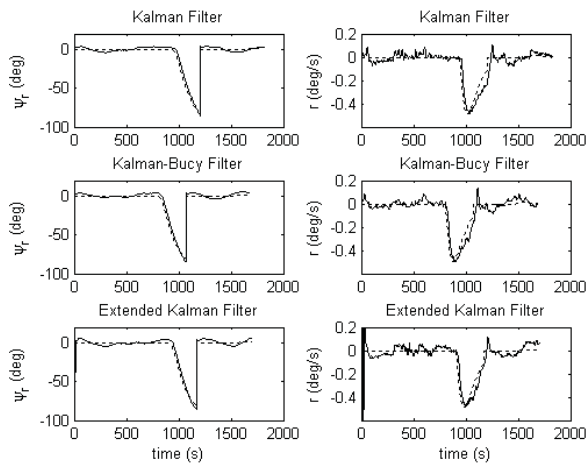


Fig. 11. Left column: ship heading  $\psi$  in  $r$ -frame, desired values (dashed line), measured values (solid line). Right column: yaw ship speed  $r$  in  $b$ -frame, desired values (dashed line), estimated values (solid line)

Tab. 6. Quality coefficients calculated based on the results obtained in experimental tests performed on the lake Silm

	$x_E$	$y_E$	$\psi_E$	$J_c$
Discrete Kalman Filter	1.3523	0.4163	377.0888	5.5395
Continuous Kalman-Bucy Filter	0.2376	0.2984	402.5533	4.5615
Extended Kalman Filter	1.3774	0.4738	387.4744	5.7259

DGPS system and the gyro-compass in  $r$ -frame with sampling time equal 1 (s). Based on the calculated mean values of the

- Genova, Italy, 1992, pp. 319-335.
10. Lu X.R., Jiang J.H., Huang Y.X.: *Design of a self-tuning adaptive track-keeping control system for ships*, In: Proceedings of the International Conference on Modelling and Control of Marine Craft, University of Exeter, U.K., 1990, pp. 178-192.
  11. Holzhüter T.: *LQG approach for the high-precision track control of ships*, IEE Proceedings: Control Theory Application, Vol. 144, No 2, 1997, pp. 121-127.
  12. Bertin D.: *Track-keeping controller for a precision manoeuvring autopilot*, In: Proceedings of the IFAC Conference Control Application in Marine Systems (CAMS-98), Fukuoka, Japan, 1998, pp. 155-160.
  13. Messer A.C., Grimble M.J.: *Robust Track-keeping Control*, Proceedings of IFAC Workshop on Control Applications in Marine Systems (CAMS-92), Genova, Italy, 1992, pp. 371-380.
  14. Vukic Z., Omerdic E., Kuljaca L.: *Improved fuzzy autopilot for track-keeping*, In: Proceedings of IFAC Conference on Control Application in Marine Systems (CAMS-98), Fukuoka, Japan, 1998, pp. 135-140.
  15. Velagic J., Vukic Z., Omerdic E.: *Adaptive fuzzy ship autopilot for track-keeping*, Control Engineering Practice, Vol. 11, No 4, 2003, pp. 433-443.
  16. Zhang Y., Hearn G.E., Sen P.: *A Neural Network Approach to Ship Track-Keeping Control*, IEEE Journal of Ocean Engineering, Vol. 21, No 4, 1996, pp. 513-527.
  17. Galbas J.: *Synthesis of precise ship steering system making use of thrusters*, Ph.D. Thesis, Technical University of Gdańsk, Poland, 1988. (in Polish)
  18. Hasegawa K., Kitera K.: *Mathematical Model of Manoeuvrability at Low Advance Speed and its Application to Berthing Control*, In: Proceedings of the 2<sup>nd</sup> Japan-Korea Joint Workshop of Ship and Marine Hydrodynamics, Osaka, Japan, 1993, pp. 144-153.
  19. Gierusz W.: *Simulation model of the shiphandling training boat "Blue Lady"*, In: Proceedings of the 5<sup>th</sup> IFAC Conference on Control Application in Marine Systems (CAMS-01), 2001, Glasgow, Scotland.
  20. Skjetne R., Smogeli O., Fossen T.I.: *A nonlinear ship maneuvering model: Identification and adaptive control with experiments for a model ship*, Modeling, Identification and Control, Vol. 25, No 1, 2004, pp. 3-27.
  21. Obreja D., Nabergoj R., Crudu L., Pacuraru-Popoiu S.: *Identification of hydrodynamic coefficients for manoeuvring simulation model of a fishing vessel*, Ocean Engineering, Vol. 37, No 7-8, 2010, pp. 678-687.
  22. Herrero R.R., Gonzales F.J.V.: *Two-step identification of non-linear manoeuvring models of marine vessels*, Ocean Engineering, Vol. 53, No 10, 2012, p. 72-82.
  23. Shouji K., Ohtsu K., Mizoguchi S.: *An Automatic Berthing Study by Optimal Control Techniques*, In: Proceedings of the IFAC Workshop on Control Application in Marine Systems (CAMS-92), Genova, Italy, 1992, pp. 185-194.
  24. Ohtsu K., Shouji K.: *Minimum-time maneuvering of ships with wind disturbances*, Control Engineering Practice, Vol. 4, No 3, 1996, pp. 385-392.
  25. Okazaki T., Ohtsu K., Shouji K.: *A study of minimum time berthing solution*, In: Proceedings of the 5<sup>th</sup> IFAC Conference on Manoeuvring and Control of Marine Craft (MCMC-2000), Aalborg, Denmark, 2000, pp. 135-139.
  26. Mizuno N., Kuroda M., Okazaki T., Ohtsu K.: *Minimum time ship manoeuvring method using neural network and nonlinear model predictive compensator*, Control Engineering Practice, Vol. 15, No 6, 2007, pp. 757-765.
  27. Sarioz K., Narli E.: *Assessment of manoeuvring performance of large tankers in restricted waterways: a real-time simulation approach*, Ocean Engineering, Vol. 30, No 12, 2003, pp. 1535-1551.
  28. Zhang Y., Hearn G.E., Sen P.: *A Multivariable Neural Controller for Automatic Ship Berthing*, Journal of IEEE Control System, Vol. 17, No 8, 1997, pp. 31-44.
  29. Im N., Keon L.S., Do B.H.: *An application of ANN to automatic ship berthing using selective controller*, TransNav – International Journal of Marine Navigation and Safety of Sea Transportation, Vol. 1, No 1, 2007, pp. 101-105.
  30. Skjetne R., Fossen T.I., Kokotovic P.V.: *Adaptive maneuvering, with experiments, for a model ship in a marine control laboratory*, Automatica, Vol. 41, No 2, 2005, pp. 289-298.
  31. Gierusz W., Nguyen Cong V., Rak A.: *Maneuvering control and trajectory tracking of very large crude carrier*, Ocean Engineering, Vol. 34, No 7, 2007, pp. 932-945.
  32. Morawski L., Nguyen Cong V.: *Ship Control in Manoeuvring Situation with Fuzzy Logic Controllers*, TransNav – International Journal of Marine Navigation and Safety of Sea Transportation, Vol. 2, No 1, 2008, pp. 77-84.
  33. Morawski L., Nguyen Cong V.: *Problem of Stopping Vessel at the Waypoint for Full-Mission Control Autopilot*, TransNav – International Journal of Marine Navigation and Safety of Sea Transportation, Vol. 4, No 2, 2010, pp. 151-156.
  34. Lee G., Surendran S., Kim S.-H.: *Algorithms to control the moving ship during harbour entry*, Applied Mathematical Modelling, Vol. 33, No 5, 2009, pp. 2474-2490.
  35. Bui V.P., Kawai H., Kim Y.B., Le K.S.: *A ship berthing system design with four tug boats*, Journal of Mechanical Science and Technology, Vol. 25, No 5, 2011, pp. 1257-1264.
  36. Tomera M.: *Discrete Kalman filter design for multivariable ship motion control: experimental results with training ship*, Joint Proceedings of Gdynia Maritime Academy and Hochschule Bremerhaven, Bremerhaven, 2010, pp. 26-34.
  37. Tomera M.: *Kalman-Bucy filter design for multivariable ship motion control*, TransNav – International Journal of Marine Navigation and Safety of Sea Transportation, Vol. 5, No 3, 2011, pp. 345-355.
  38. Tomera M.: *Nonlinear observers design for multivariable ship motion control*, Polish Maritime Research, Issue Special, Vol. 19, No 74, 2012, pp. 50-56.
  39. Tomera M.: *Dynamic positioning system for „Blue Lady”. Simulation tests*, Polish Maritime Research, Issue

Special, Vol. 19, No 74, 2012, pp. 57-65.

40. *Foundation for Safety of Navigation and Environment Research*, 2012. <[www.ilawashiphandling.com.pl](http://www.ilawashiphandling.com.pl)>
41. Fossen T.I.: *Marine Control Systems: Guidance, Navigation, and Control of Ships, Rigs and Underwater Vehicles*, Marine Cybernetics, Trondheim, Norway, 2002.
42. Brown R.G., Hwang P.Y.C.: *Introduction to Random Signals and Applied Kalman Filtering with Matlab Exercises and Solutions*, Third Edition, John Wiley & Sons, Inc, 1997.
43. Fossen T.I.: *Handbook of Marine Craft Hydrodynamics and Motion Control*, John Wiley & Sons, 2011.
44. Pomirski J., Rak, A., Gierusz W.: *Control system for trials on material ship model*, Polish Maritime Research, Special Issue, Vol. 19, No 74, 2012, pp. 25-30.

#### **CONTACT WITH THE AUTHOR**

Mirosław Tomera, Ph. D.  
Gdynia Maritime University,  
Faculty of Marine Electrical Engineering,  
Department of Ship Automation,  
Morska 81/87 Str.  
81-225 Gdynia, POLAND  
e-mail: [tomera@am.gdynia.pl](mailto:tomera@am.gdynia.pl)

# LATITUDE ERROR IN COMPASS DEVIATION

## MATHEMATICAL METHOD TO DETERMINE THE LATITUDE ERROR IN MAGNETIC COMPASS DEVIATION

**Imanol Basterretxea Iribar**<sup>1</sup>, Ph.D.

University of Basque Country, Spain

**Jesús Angel Vila Muñoz**<sup>1</sup>, Ph.D.

University of Basque Country, Spain

**Carlos Angel Pérez Labajos**, Ph.D.

University of Cantabria, Spain

### ABSTRACT

*This article aims to provide the seafarer with a tool to calculate the deviation for a righted ship in any geographical position using only the information available on board. In this way the accidental errors in the deviation card are reduced and the latitude error is made negligible. Moreover, an experimental application of this method is carried out on board a tanker to compare the latitude error in different positions at sea.*

**Keywords:** optimal exact coefficients, average deviation, latitude error

### INTRODUCTION

Today the magnetic compass is a secondary navigation system compared to other electronic or electro-mechanic compasses on board ships. However, the magnetic compass relies solely on the existence of a magnetic field and, therefore, has a advantage over the gyroscopic or satellite compasses: it works without the help of a source of energy. That is the reason why the magnetic compass is part of the necessary navigation equipment on board the current merchant ships according to SOLAS (Safety of Life at Sea) Convention.

When the magnetic compass is located in a place isolated from magnetic materials, the needle is guided only by the earth's magnetic field  $B_E$  which is split up into the horizontal and vertical components represented by the symbols  $B_{EH}$  and  $B_{EZ}$ , respectively, traditionally known as H and Z. The compass' needle will follow the component  $B_{EH}$  parallel to the magnetic meridian and the angle between the needle and the geographical meridian is called magnetic declination. If the magnetic compass is placed on board a ship, the steel of which she is built will act as a magnet creating a ship's magnetic field which makes the needle separate from the magnetic meridian an angle, called deviation. As a result, the magnetic compass course has to be corrected by the magnetic declination and deviation to obtain the true course that is parallel to the geographical meridian.

Given that the component  $B_{EH}$  changes intensity and direction depending on the geographical coordinates of the place where the compass is located, the magnetic declination will be altered when the ship is moving along the whole earth's surface. In the same way, the changes in the earth's magnetic field will affect the magnetism of the ship's steel and the deviation angle will not be the same in different positions at sea. The variations in the magnetic declination

are obtained easily from nautical charts or IGRF (International Geomagnetic Reference Field) models (Zmuda 1971). However, the deviation has to be reduced by the well-known practical method called compass' adjustment since; unlike the magnetic declination, it also varies with the direction of the bow. The reduced deviations obtained after the adjustment are registered for various courses in a sheet called magnetic compass table (also deviation card) that is placed in the bridge close to the chartroom. However, the actual deviations may change from those registered in the table when the ship moves from one port to another and it is not usual for deck officers to correct this [10]. We refer to this error as latitude error or variation in deviation. Obviously, this error will increase as the ship gets closer to the magnetic poles, whose current geographical coordinates are  $85^{\circ} 18' N$  &  $136^{\circ} 29.4' W$  for North Pole and  $64^{\circ} 24.4' S$  &  $137^{\circ} 12.3' E$  for South Pole (on date 01.01.2011) [13].

The aim of this article is to develop a mathematical method to obtain the deviations in any geographical position correcting in this way the latitude error. In addition the deviations from the magnetic compass table will be compared graphically to those obtained by this method at different positions. The data for the comparison were collected from a 150,000 dwt crude tanker named "MONTE TOLEDO".

### CALCULATING THE OPTIMAL EXACT COEFFICIENTS FOR A RIGHTED SHIP

The exact deviation for a righted ship ( $\delta$ ) may be calculated by the well-known equation of Archibald Smith and Evans [4]:

$$\tan \delta = \frac{A' + B' \cdot \sin \zeta + C' \cdot \cos \zeta + D' \cdot \sin 2\zeta + E' \cdot \cos 2\zeta}{1 + B' \cdot \cos \zeta - C' \cdot \sin \zeta + D' \cdot \cos 2\zeta - E' \cdot \sin 2\zeta} \quad (1)$$

The symbols  $\zeta$  and  $\zeta'$  denote the magnetic and compass

course, respectively, whereas A', B', C', D' and E' indicate in this article the exact coefficients that were expressed originally by Archibald-Smith as A, B, C, D y E.

This equation may be also expressed as follows [3]:

$$\sin \delta = A' \cdot \cos \delta + B' \cdot \sin \zeta' + C' \cdot \cos \zeta' + D' \cdot \sin(2\zeta' + \delta) + E' \cdot \cos(2\zeta' + \delta) \quad (2)$$

On the other hand, the formula in (3) lets us calculate the deviation in degrees by a simple way although various trigonometric estimations turned it into a rough equation. Nevertheless, this approximate deviation ( $\Delta$ ) is normally used to adjust the magnetic compass [2].

$$\Delta = A + B \cdot \sin \zeta' + C \cdot \cos \zeta' + D \cdot \sin 2\zeta' + E \cdot \cos 2\zeta' \quad (3)$$

The symbols A, B, C, D and E are known as approximate coefficients and their values match up with the sine of the exact coefficients. Both coefficients may be considered constant for a long time. However this may not always be the case, since a bolt of lightning or a shipment of steel cargo may affect the ship magnetism [8].

If the deviation were very high (more than five degrees), it should be reduced to near zero by moving the correctors set in the binnacle. The compass adjuster is the specialized person who carries out this work. He draws up a magnetic compass table where the reduced deviations are registered for n courses. The practical method for evaluating the deviation is based on the execution of a complete compass swing circulation [7]. Nevertheless there are also other simpler methods to calculate the deviation even at single any course [11]. The magnetic and compass bearings are usually compared on 24 or 36 equidistant courses (each 15° or 10° degrees respectively). Then, by using the traditional formula in (4), the deviation ( $\delta_i$ ) is obtained for each individual course.

$$\delta_i = \zeta_i - \zeta_i', i \in \overline{1, n} \quad (4)$$

Therefore, the vectors of the magnetic course ( $\zeta_i$ ), the compass course ( $\zeta_i'$ ) and the deviation sine, where  $i = 1$  to  $n$ , can be created as it shown in (5). The subscript i denote the course to which the deviation is obtained.

$$\zeta_i = \begin{pmatrix} \zeta_1 \\ \zeta_2 \\ \zeta_3 \\ \vdots \\ \zeta_n \end{pmatrix} \quad \zeta_i' = \begin{pmatrix} \zeta_1' \\ \zeta_2' \\ \zeta_3' \\ \vdots \\ \zeta_n' \end{pmatrix} \quad D(i) = \begin{pmatrix} \sin \delta_1 \\ \sin \delta_2 \\ \sin \delta_3 \\ \vdots \\ \sin \delta_n \end{pmatrix} \quad (5)$$

Thus the equation in (2) may be written in matrix form as follows:

$$D(i) = K \cdot T_n(i) \quad (6)$$

Where  $T_n(i)$  and K have the forms in (7) and (8) respectively:

$$T_n(i) = \begin{pmatrix} \cos \delta_1 & \sin \zeta_1' & \cos \zeta_1' & \sin(\zeta_1' + \delta_1) & \cos(\zeta_1' + \delta_1) \\ \cos \delta_2 & \sin \zeta_2' & \cos \zeta_2' & \sin(\zeta_2' + \delta_2) & \cos(\zeta_2' + \delta_2) \\ \cos \delta_3 & \sin \zeta_3' & \cos \zeta_3' & \sin(\zeta_3' + \delta_3) & \cos(\zeta_3' + \delta_3) \\ \vdots & \vdots & \vdots & \vdots & \vdots \\ \cos \delta_n & \sin \zeta_n' & \cos \zeta_n' & \sin(\zeta_n' + \delta_n) & \cos(\zeta_n' + \delta_n) \end{pmatrix} \quad (7)$$

$$K = \begin{pmatrix} A' \\ B' \\ C' \\ D' \\ E' \end{pmatrix} \quad (8)$$

## CORRECTING THE DEVIATION OBTAINED BY THE SHIP'S SWING CIRCULATION

Frequently the readings of courses during the swing circulation are not very exact and consequently the deviations obtained from them and registered in the magnetic compass table may be erratic. This may be due to mistakes made by the adjuster, to Gaussin errors, to magnetic cargo carried on board, electrical devices, hoisting booms, magnetic objects near the binnacle or to any other reason that may accidentally affect the compass. Therefore the corresponding deviation curve becomes very rough and has to be smoothed by the application of least squares method [1]. The optimal exact coefficients (K) are calculated in (9) by means of the least squares method to reduce the possible deviation errors observed during the compass swing circulation [5]. All of these coefficients are constant except B' and C' which change with the geographical position.

$$K = [T_n^T(i) \cdot T(i)]^{-1} \cdot T^T(i) \cdot D(i) \quad (9)$$

Once the optimal exact coefficients are calculated, an average deviation is obtained by the formula in (6). Figure 1 shows the difference between the average deviation calculated by least squares method (soft curve) and the deviation collected from the magnetic compass table (rough curve) on board M/T "MONTE TOLEDO".

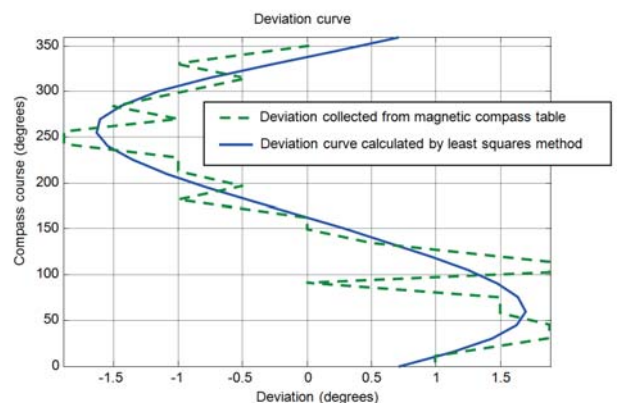


Fig. 1. Difference between average deviation (blue continuous curve) and magnetic table deviation (green discontinuous curve) on board M/T "MONTE TOLEDO".

## PERMANENT AND INDUCED MAGNETISM IN RIGHTED SHIP

In order to study the magnetism on board, a righted ship may be plotted into a Cartesian coordinate system where the origin is placed in the centre of the rose, the axis X is on

fore-and-aft line and Y on the starboard-and-port line (both on the plane of horizon), and Z on the zenith-and-nadir (vertical) line. The ship magnetism may be divided into the permanent magnetism caused by the ship's hard irons and the induced magnetism created by the ship's soft irons. The permanent magnetism ( $B_p$ ) may be expressed by the vector in (10) where  $B_{PX}$ ,  $B_{PY}$  and  $B_{PZ}$  are its components in the X, Y and Z axis, respectively, which have been called traditionally P, Q and R. The formula in (11) indicates the induced magnetism ( $B_I$ ) where the parameters  $B_{EX}$  and  $B_{EY}$  are the components of  $B_{EH}$  in the X and Y axis, respectively, and the matrix  $\chi$  indicates the susceptibility tensor of the induced magnetism, assuming the ship has an anisotropic susceptibility [9].

$$B_p = \begin{pmatrix} B_{PX} \\ B_{PY} \\ B_{PZ} \end{pmatrix} \quad (10)$$

$$B_I = \chi \cdot \begin{pmatrix} B_{EX} \\ B_{EY} \\ B_{EZ} \end{pmatrix} = \begin{pmatrix} \chi_{x,x} & \chi_{x,y} & \chi_{x,z} \\ \chi_{y,x} & \chi_{y,y} & \chi_{y,z} \\ \chi_{z,x} & \chi_{z,y} & \chi_{z,z} \end{pmatrix} \cdot \begin{pmatrix} B_{EX} \\ B_{EY} \\ B_{EZ} \end{pmatrix} \quad (11)$$

If the ship is up righted, the vertical component  $B_{PZ}$  and the coefficients  $\chi_{z,x}$ ,  $\chi_{z,y}$  and  $\chi_{z,z}$  will not have an influence in the deviation. They are only noted as an additional deviation (heeling deviation) in sailing vessels with a permanent list and as compass' needle oscillations in motor ships navigating in rough seas with large rolling movements.

### DETERMINING B' & C' COEFFICIENTS AND THE DEVIATION WHEN THE SHIP'S POSITION CHANGES

The exact coefficients may be expressed by the horizontal components belonging to the earth's field and permanent magnetism, as well as the horizontal coefficients from the susceptibility tensor representing the induced magnetism,  $\lambda$  being the shielding factor.

$$A' = \frac{\chi_{x,y} - \chi_{x,y}}{2 \cdot \lambda} \quad B' = \frac{1}{\lambda \cdot B_{EH}} \cdot (B_{PX} + \chi_{x,z} \cdot B_{EZ})$$

$$C' = \frac{1}{\lambda \cdot B_{EH}} \cdot (B_{PY} + \chi_{y,z} \cdot B_{EZ}) \quad D' = \frac{\chi_{x,x} - \chi_{y,y}}{2 \cdot \lambda} \quad (12)$$

$$E' = \frac{\chi_{y,x} + \chi_{x,y}}{2 \cdot \lambda}$$

As can be seen in (12) only the coefficients B' and C' depend on  $B_{EX}$  and  $B_{EY}$ , which indicates that the value of these coefficients will change for different positions along the earth's surface due to the variations in the components of earth's magnetism. Nevertheless, the rest of the coefficients will remain constant in spite of these changes. This means that the values of  $B_{EX}/\lambda$ ,  $B_{EY}/\lambda$ ,  $\chi_{x,z}/\lambda$  and  $\chi_{y,z}/\lambda$  have to be obtained independently from each position in order to proceed to the

calculation of the different coefficients B' and C'.

The values  $\chi_{x,z}$  and  $\chi_{y,z}$  belonging to the induced magnetism may be calculated by the traditional formulae in (13) and (14) [12] where the coefficients  $B_2'$  and  $C_2'$  are obtained respectively by steering the ship to the North or South and to the East or West in a position where the components of the earth's magnetism ( $B_{EH}$  and  $B_{EZ}$ ) are quite different from the same components in the place where the coefficients B' and C' were obtained ( $B_{EH}$  and  $B_{EZ}$ ).

$$\chi_{x,z} = \lambda \cdot \frac{B_{EH} \cdot \sin B' - B_{EH} \cdot \sin B_2'}{B_{EZ} - B_{EZ}'} \quad (13)$$

$$\frac{\chi_{x,z}}{\lambda} = \frac{B_{EH} \cdot \sin B' - B_{EH} \cdot \sin B_2'}{B_{EZ} - B_{EZ}'}$$

$$\chi_{y,z} = \lambda \cdot \frac{B_{EH} \cdot \sin C' - B_{EH} \cdot \sin C_2'}{B_{EZ} - B_{EZ}'} \quad (14)$$

$$\frac{\chi_{y,z}}{\lambda} = \frac{B_{EH} \cdot \sin C' - B_{EH} \cdot \sin C_2'}{B_{EZ} - B_{EZ}'}$$

Later, the values of  $B_{PX}/\lambda$  and  $B_{PY}/\lambda$  may be calculated using the formulae in (15) and (16):

$$\frac{B_{PX}}{\lambda} = B_{EH} \cdot B' - \frac{\chi_{x,z}}{\lambda} \cdot B_{EZ} \quad (15)$$

$$\frac{B_{PY}}{\lambda} = B_{EH} \cdot C' - \frac{\chi_{y,z}}{\lambda} \cdot B_{EZ} \quad (16)$$

Once the value of  $B_{PX}/\lambda$ ,  $B_{PY}/\lambda$ ,  $\chi_{x,z}$  and  $\chi_{y,z}$  are calculated, the value of the new optimal exact coefficients B' and C' at any other position may be obtained by the application of formulae in (12). Then the deviation at any geographical position can be calculated by executing repeatedly the equation in (2) within a do-while iterative block, until the difference between both deviation values of the equation is reduced to near zero. The approximate deviation ( $\Delta$ ) obtained from (3) may be used as first value to be evaluated in the block.

### APPLICATION ON BOARD A SHIP

In this section the mathematical method to obtain the deviation is put into practice on board a 150,000 dwt crude tanker. The deviation calculated for the 1<sup>st</sup> of January 2011 in different geographical positions is compared to the deviation at the position where the compass was adjusted the last time (27° N & 091° W). The values of  $B_{EH}$  and  $B_{EZ}$  are determined by using the on-line calculator based on the 11<sup>th</sup> generation IGRF model [6]. The compass is located 20 meters above the sea in order to input the data required by this calculator. In any case, a difference of 20 meters in height only gives an error of less than one thousandth gauss in the geomagnetic components.

The figures 2 and 3 show a geographical map in three-dimensional form concerning the components  $B_{EH}$  and  $B_{EZ}$  on the 1<sup>st</sup> of January 2011, respectively. Their values have been obtained from a geomagnetic model and local magnetic anomalies may be not shown. This occurs, for example, in the Baltic Sea where the mathematical model of the Earth's magnetic field does not consider local magnetic anomalies [14]. As can be seen in these figures, the values of these components are not only changing with the geographical latitude but also with the geographical longitude and, although the latitude affects in a greater degree, the term "latitude error" would not be considered absolutely correct. This is partly due to the variation of longitude is caused by the slight inclination of the magnetic equator with respect to the geographical equator. Another cause has to do with the fact that the earth's magnetic field is non-homogeneous.

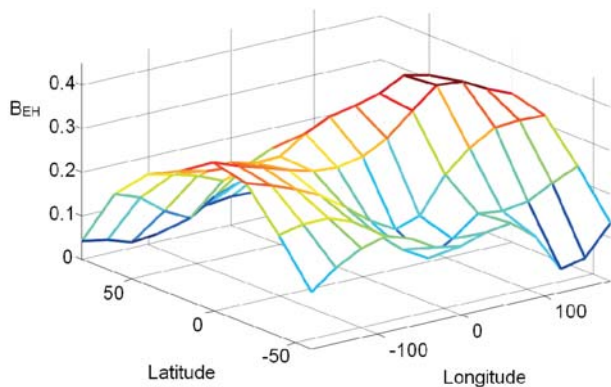


Fig. 2. Value of  $B_{EH}$  component (in gauss) on 01.01.2011.

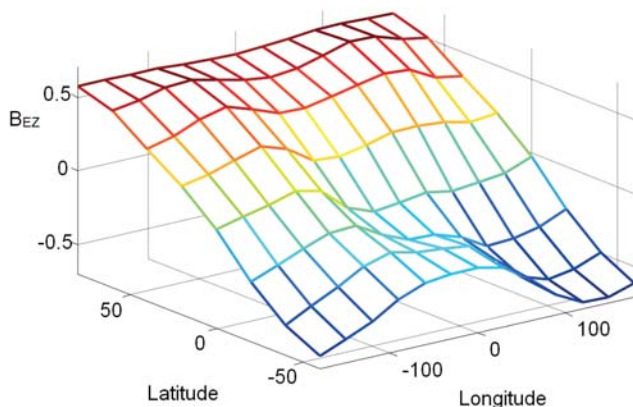


Figure 3. Value of  $B_{EZ}$  component (in gauss) on 01.01.2011.

Table 1 shows the optimal exact coefficients that result from the application of the least squares method, as well as the components of the coefficients  $B'$  and  $C'$  obtained by changing the ship's position in accordance with the method defined in section 4. As far the calculation of these components, the ship navigated a long passage to vary the latitude around  $25^\circ$  until she reached a difference close to 0.10 and 0.40 gauss in the earth's components  $B_{EH}$  and  $B_{EP}$ , respectively. The low value of the coefficient  $A'$  indicates that the binnacle is properly installed at centreline, which means that the North of the verge ring and the fore-and-aft line coincide. The existence of the

$E'$  coefficient suggests that the ship contains unsymmetrical arrangements of horizontal soft iron. On the other hand, the higher values of  $B'$  and  $C'$  indicate that the deviation curve is mainly semicircular, as shown in figure 1.

Table 1.  $B_{PX}$ ,  $B_{PY}$ ,  $\chi_{x,z}$  and  $\chi_{y,z}$  parameters and optimal exact coefficients of "MONTE TOLEDO" at the last place of compass adjustment.

Date: 01.01.2011.

Parameters	Optimal exact coefficients
$\chi_{x,z}/\lambda = 0,0143$	$A' = 0,0007$
$\chi_{y,z}/\lambda = -0,0044$	$B' = 0,0271$
$B_{PX}/\lambda = 0,0012$	$C' = 0,0100$
$B_{PY}/\lambda = 0,0042$	$D' = 0,0017$
	$E' = 0,0018$

Figures 4 to 12 show the deviation curve at the place of the last adjustment (in blue colour) and at other positions (in red colour). These curves allow us to compare how the deviation is changing throughout all the navigational waters of the earth's surface when the ship changes her geographical position. It should be noted that the calculations were carried out on 1<sup>st</sup> January 2011.

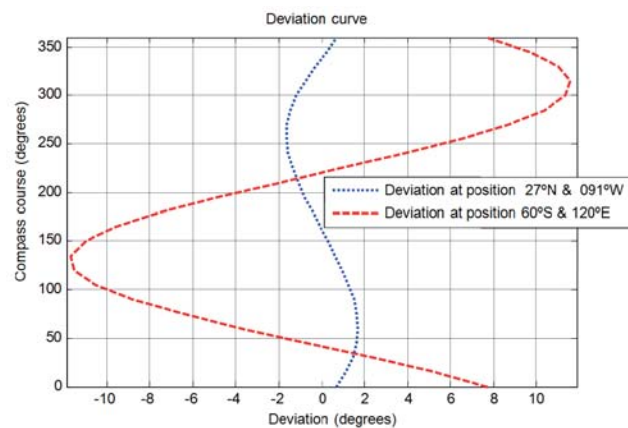


Fig. 4. Deviations comparative at 600S & 1200E

According to figure 4 the variation in deviation may reach a little more than  $12^\circ$  when the ship is navigating at geographical position  $60^\circ S$  and  $120^\circ E$ . Bearing in mind that, in this case, the ship is sailing nearest to the magnetic pole (only around 680 miles away), this variation should be the highest in the test.

This seems to be confirmed in figures 5 and 6 (position  $40^\circ S$ ) since the maximum variation in deviation is reduced to only  $4^\circ$ . On the other hand, both deviation curves are out of phase (nearly  $180^\circ$ ) in these figures, which makes the variation greater.

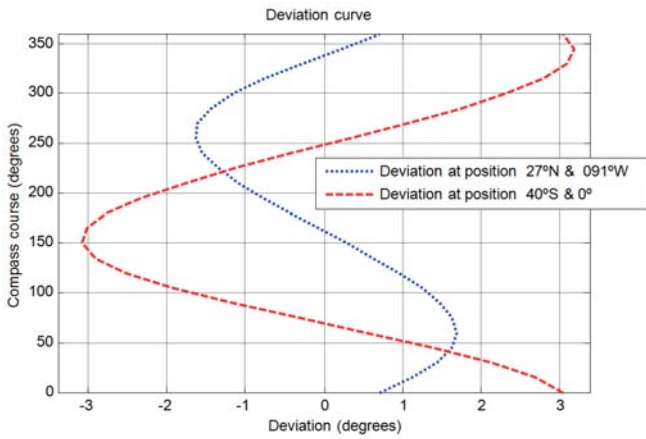


Fig. 5. Deviations comparative at 40°S & 0°

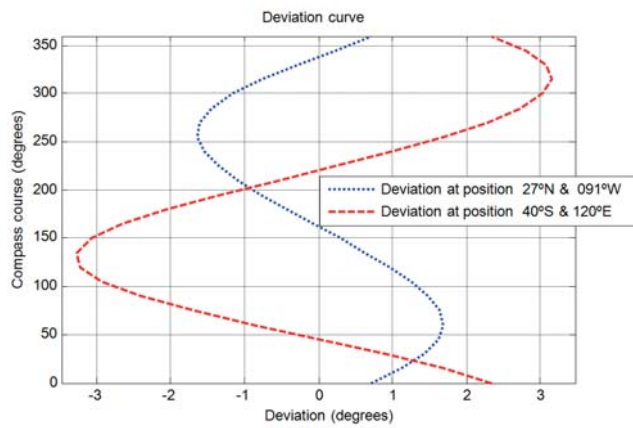


Fig. 6. Deviations comparative at 40°S & 120°E

As the ship gets nearer the geographical equator, the variation in deviation is gradually reduced to slightly less than 2° at geographical latitude 20°S and 1° at the geographical equator (figures 7 and 8). Moreover, it is also noted that the phases of both curves are approaching.

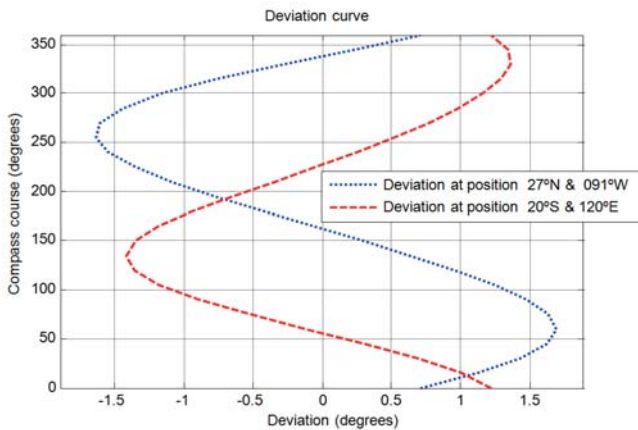


Fig. 7. Deviations comparative at 20°S & 120°E

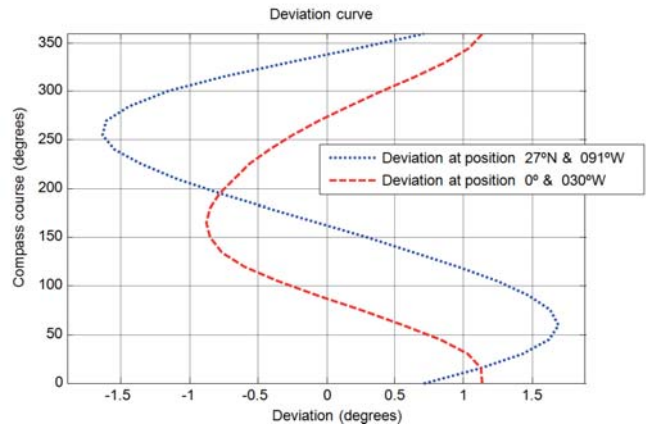


Fig. 8. Deviations comparative at 0°S & 30°W

In figures 9 and 10 the maximum variation is less than 1° due to the fact that the ship is near the position where the magnetic compass was last adjusted. By comparing both figures, it emerges that the curves in figure 10 are nearer than in figure 9 notwithstanding that the distance between positions in figure 10 is longer than in figure 9. This is due to the longitude influence, since the difference of the earth's magnetic components between the red and blue curves in figure 9 ( $B_{EH} = 0,04$  and  $B_{EZ} = 0,17$  gauss) are higher than in figure 11 ( $B_{EH} = 0,02$  and  $B_{EZ} = 0,05$  gauss).

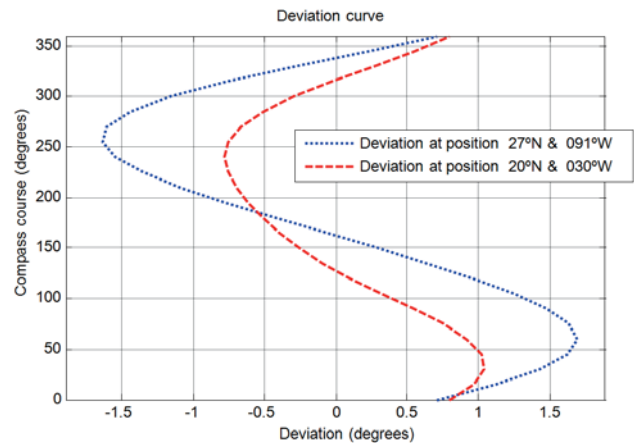


Fig. 9. Deviations comparative at 20°N & 30°W

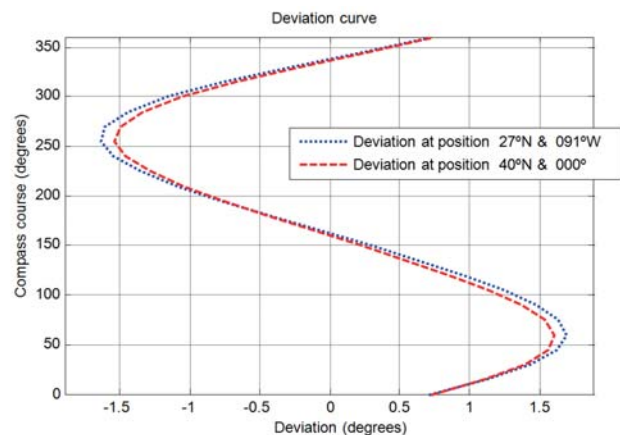


Fig. 10. Deviations comparative at 40°N & 000°

In figure 12 the variation in deviation reaches only  $6^{\circ}$  despite the fact that the ship is sailing in geographical latitude near the North Pole. This variation is not as high as in figure 4 due to the geographical longitude difference is near to  $180^{\circ}$ . Obviously, the maximum variation in deviation in figure 11 is only near to  $3^{\circ}$  since the latitude is not so near the pole's geographical latitude as in figure 12.

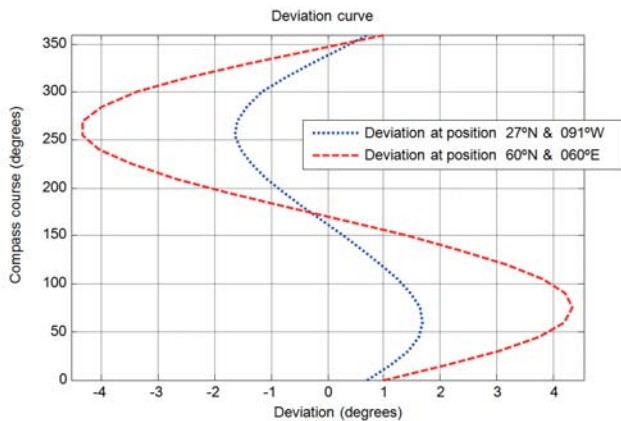


Fig. 11. Deviations comparative at  $60^{\circ}\text{N}$  &  $60^{\circ}\text{E}$

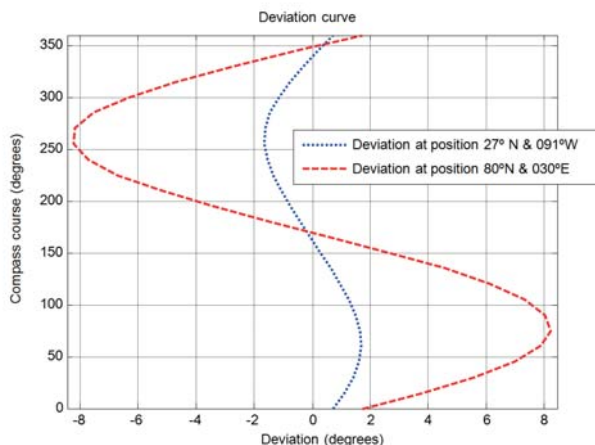


Fig. 12. Deviations comparative at  $80^{\circ}\text{N}$  &  $30^{\circ}\text{E}$

## CONCLUSIONS

The mathematical method presented in this article is easily programmable, and may help ship officers carry out a program of latitude error calculation in their computers. It is only necessary to be in possession of the last magnetic compass table and the deviation for the cardinal compass courses at places where the earth's magnetic components have changed considerably.

According to the results of the experimental application, the latitude error for a properly installed magnetic compass may reach  $12^{\circ}$  when the ship is 600-700 miles away from the magnetic pole. But it decreases rapidly when the ship strays from this point. Thus the error is less than  $4^{\circ}$  for the zone between parallels  $60^{\circ}\text{N}$  and  $40^{\circ}\text{S}$  covering the most of navigational waters. Moreover, it is also important to take

into account the position of the port where the compass was last adjusted, since the latitude error in deviation depends on the distance to this port. In this sense, it is preferable that the compass adjustment would be carried out in a port placed at mid-latitude of waters where the ship usually navigates.

## BIBLIOGRAPHY

1. Admiralty Compass Observatory, The Theory of the Deviations of the Magnetic Compass. H.M. Stationery Office, 1948.
2. Barber, G.W. and Arrott, A.S., History and magnetics of compass adjusting., IEEE Transactions on Magnetics, 24, no.6, pp. 2883-2885, 1988.
3. Denne, W. Magnetic Compass Deviation and Correction. Brown, Son & Ferguson, Ltd, 1998.
4. Evans, F.J. and Archibald-Smith, Admiralty Manual for Ascertaining and Applying the Deviations of the Compass Caused by the Iron in a Ship. Hydrographic Office of Admiralty, 1863.
5. Felski, A., Application of the Least Squares Method for Determining Magnetic Compass Deviation. Journal of Navigation, 52, pp. 388-393, 1999.
6. NOAA, Magnetic fields values calculator. Available: <http://www.ngdc.noaa.gov/geomag/>, 2011-09-20-last updated.
7. Jenkins, J.A., Binnacles and Swinging Ship. Bureau of Navigation, 1869.
8. Kemp, J., Experiences with Compasses in the Mid-20th Century. Journal of Navigation, 63, pp. 545-556, 2010.
9. Lesur, V., Clark, T.; Turbitt, C. & Flowers, S., A Technique for Estimating the Absolute Vector Geomagnetic Field from a Marine Vessel. Journal of Geophysics and Engineering, 1, pp. 109-115, 2004.
10. Lushnikov, E.M., The Problem of Magnetic Compass Deviation at Contemporary Conditions. Transnav, the International Journal of Marine Navigation and Safety of sea Transportation, 4, no. 1, pp. 65-66, 2010.
11. Lushnikov, E.M., Compensation of Magnetic Compass Deviation at Single Any Course. Transnav, the International Journal of Marine Navigation and Safety of sea Transportation, 5, no. 3, pp. 303-307, 2011.
12. National Geospatial-intelligence Agency, Handbook of Magnetic Compass Adjustment. Defence Mapping Agency Hydrographic/Topographic Center, 2004.
13. Thomas, A.V., The Use of Compasses in High Latitudes. Journal of Navigation, 4, pp. 135-148, 1951.
14. Woloszyn, M., Detection of ferromagnetic objects in local magnetic anomaly of the Baltic Sea. Polish Maritime Research, 15, pp. 77-82, 2008.
15. Zmuda, A.J., The International Geomagnetic Reference Field: Introduction. Bulletin International Association of Geomagnetism and Aeronomy, 28, pp. 148-152, 1971.

## **CONTACT WITH THE AUTOR**

**Imanol Basterretxea Iribar<sup>1</sup>**  
**1 E.T.S. de Náutica y Máquinas Navales**  
**University of Basque Country**  
**UPV/EHU, Portugalete**  
**Bizkaia**  
**Spain**

**Jesús Angel Vila Muñoz<sup>1</sup>**  
**1 E.T.S. de Náutica y Máquinas Navales**  
**University of Basque Country**  
**UPV/EHU, Portugalete**  
**Bizkaia**  
**Spain**

**Carlos Angel Pérez Labajos**  
**2 E.T.S. de Náutica**  
**University of Cantabria**  
**UC, Santander**  
**Cantabria**  
**Spain**

# Numerical Analysis of the Unsteady Propeller Performance in the Ship Wake Modified By Different Wake Improvement Devices

Tomasz Bugalski, Ph.D.

Ship Design and Research Centre CTO, Poland

Jan A. Szantyr, Prof.

Gdańsk University of Technology, Poland

## ABSTRACT

*The paper presents the summary of results of the numerical analysis of the unsteady propeller performance in the non-uniform ship wake modified by the different wake improvement devices. This analysis is performed using the lifting surface program DUNCAN for unsteady propeller analysis. The object of the analysis is a 7000 ton chemical tanker, for which four different types of the wake improvement devices have been designed: two vortex generators, a pre-swirl stator, and a boundary layer alignment device. These produced five different cases of the ship wake structure: the original hull and hull equipped alternatively with four wake improvement devices. Two different propellers were analyzed in these five wake fields, one being the original reference propeller P0 and the other - a specially designed, optimized propeller P3. The analyzed parameters were the pictures of unsteady cavitation on propeller blades, harmonics of pressure pulses generated by the cavitating propellers in the selected points and the fluctuating bearing forces on the propeller shaft. Some of the calculated cavitation phenomena were confronted with the experimental. The objective of the calculations was to demonstrate the differences in the calculated unsteady propeller performance resulting from the application of different wake improvement devices. The analysis and discussion of the results, together with the appropriate conclusions, are included in the paper.*

**Keywords:** ship wake improvement devices, unsteady propeller performance, numerical analysis

## INTRODUCTION

The research presented in this paper is related to two recent EU projects: PREFUL and STREAMLINE. Within the project PREFUL an extensive modernization of the computer program DUNCAN [1,2] was undertaken. This program is based on the unsteady lifting surface theory and it may be applied to the analysis of unsteady propeller operation in the non-uniform velocity field of the ship's wake. The program DUNCAN can analyse both open and ducted propellers, delivering the time-dependent cavitation extent, unsteady blade and shaft forces and pulsating pressure induced by the cavitating propeller in the prescribed points.

The project STREAMLINE was concerned with the hydrodynamic performance of a 7000 ton chemical tanker [3,4]. The model of this ship was equipped with several different flow-modifying devices and tested in a model basin. The tests covered the resistance and propulsion performance of the ship and the unsteady aspects of propeller operation. This paper concentrates on the influence of the wake-improvement devices, such as: vortex generators, pre-swirl stators and boundary layer alignment devices, on the unsteady propeller operation. Altogether five different wake fields are considered in the analysis: the original hull wake, two vortex generators, a pre-swirl stator and a boundary layer alignment device. The objective of the analysis was to determine and compare different aspects of unsteady propeller operation in these wakes, including unsteady cavitation, fluctuating shaft forces and induced pressure pulses. Two propellers were included

in the analysis: the reference propeller P0 originally designed for the ship and the propeller P3 as a modified, improved design.

The analysis was performed almost entirely by numerical computations. Only the calculations for the original hull equipped with propeller P0 could be directly compared with the unsteady cavitation photographs and pressure pulses measured on the ship model in a circulating water channel. The results of the analysis are presented in the following sections of this paper. All results given in this paper refer to model scale and the scale of the models is 1:16.5.

## WAKE IMPROVEMENT DEVICES AND THEIR EFFECT ON THE WAKE STRUCTURE

The ship considered in this analysis is the 7000 ton chemical tanker with the length between perpendiculars of 94.0 [m], breadth of 15.4 [m], draft of 6.0 [m], block coefficient of 0.786 and the volume displacement of 6826.9 [m<sup>3</sup>]. The hull geometry is shown in Fig. 1.

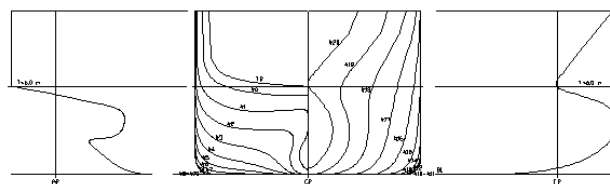


Fig. 1. Geometry of the hull of the chemical tanker

The photograph of the stern part of the original hull H0 and the map of the resulting wake velocity field are shown in Fig. 2. The velocity field of the wake seems to be typical for this category of ships and it is reasonably favourable from the point of view of unsteady propeller operation. Consequently, no high intensity of unsteady cavitation phenomena and high induced pressure pulses may be expected.

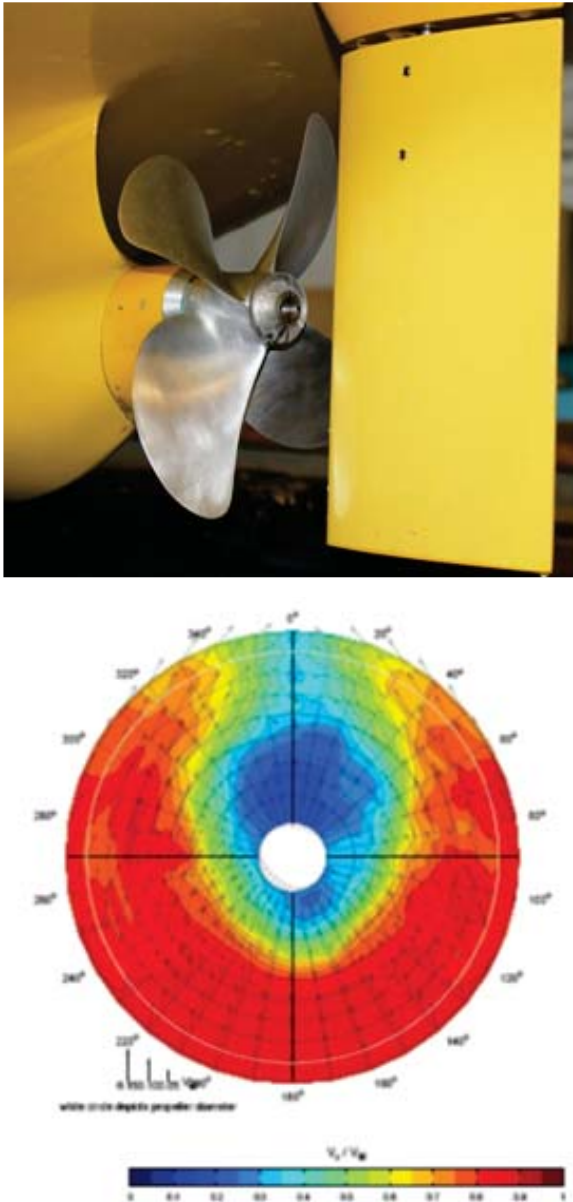


Fig. 2 Photograph of the original hull H0 with propeller P0 and basic rudder and map of the measured wake velocity field

The vortex generators (VG) were the first tested devices aiming at modification of the wake velocity field. They were fitted both on port and starboard side of the stern in the same positions. The vortex generators VG2 were inclined at an angle of 23 degrees with respect to the waterline. The photograph of the hull equipped with vortex generators VG2 is shown in Fig. 3, together with map of the resulting wake velocity field. The generators have modified the upper part of the wake quite significantly.

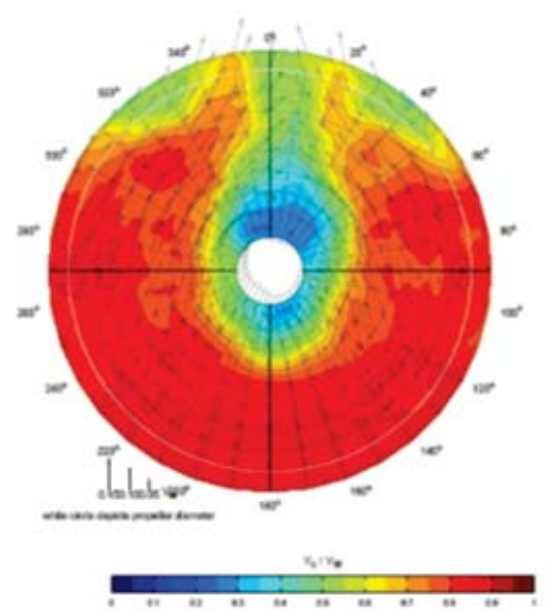


Fig. 3. Photograph of the hull with vortex generators VG2 and map of the measured wake velocity field

The central wake peak was reduced in extent and intensity, particularly in the region right above the shaft, and two additional weak peaks have been added on both sides. These changes should have a positive effect on the unsteady performance of propeller.

The vortex generators VG6 were placed in the same positions as VG2, but they were inclined at an angle of 9 degrees with respect to the waterline. The photograph of the stern with vortex generators VG6 is shown in Fig. 4, together with the map of the resulting wake velocity field. Now the three separate wake peaks visible in the upper part of the wake in Fig. 3 are melted together, creating a wide region of almost uniform velocity. Moreover, the iso-wake lines in this region have an almost circumferential direction. This should have a marked positive effect on the unsteady operation of propellers.

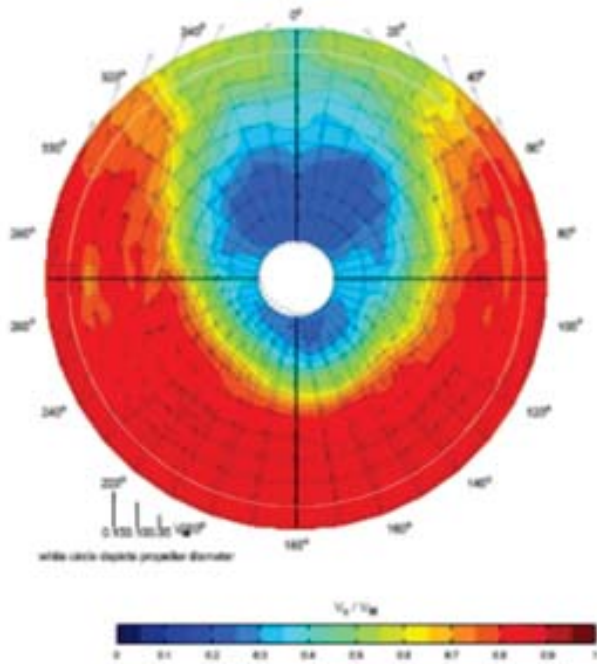


Fig. 4. Photograph of the hull with vortex generators VG6 and map of the measured wake velocity field

Another type of wake improving devices were the Pre-Swirl Stators (PSS), which were intended first of all to increase the propulsive efficiency. Several configurations of these were tested and finally the one with three stator vanes fitted on the port side of the hull was selected. The photograph of the stern with PSS is shown in Fig. 5, together with the map of the resulting wake velocity field.

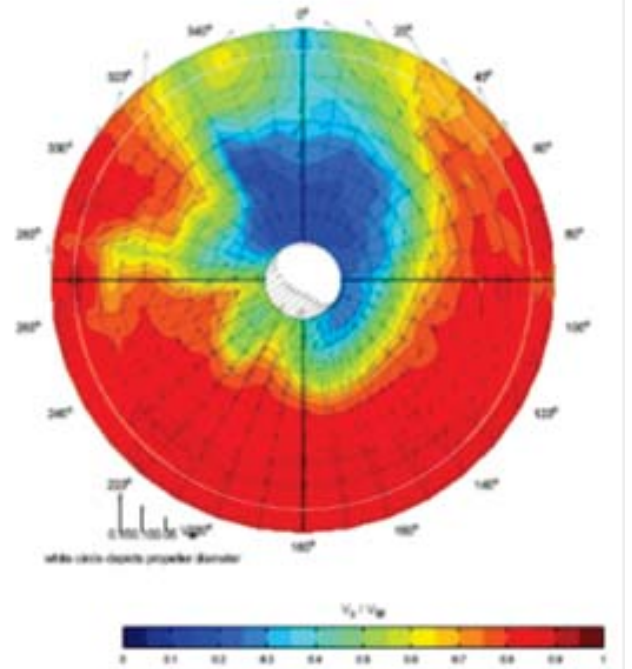


Fig. 5. Photograph of the hull with Pre-swirl Stator PSS and map of the measured wake velocity field

Now the main upper peak of the wake is weaker in the top region, but much more intensive and extended towards the starboard side in the region right above the shaft.

At the same time an additional peak has appeared of the port side at approximately 270 degrees position. This should not result in the rise of unsteady cavitation and induced pressure pulses, but it may amplify higher harmonics of the unsteady shaft forces.

Another type of wake improvement devices was the Boundary Layer Alignment Device (BLAD). It consisted of a couple of spoilers fitted to both sides of the stern part of the hull. Their objective was to prevent thickening of the hull boundary layer in front of the propellers. The photograph of the stern equipped with BLAD is shown in Fig. 6, together with the map of the resulting wake velocity field. The map of the wake does not indicate any decrease on the hull boundary layer thickness. At the same time a quite wide area of retarded flow has appeared in the region right above the shaft. These modifications of the original wake distribution cannot be regarded as positive from the point of view of the unsteady propeller operation.

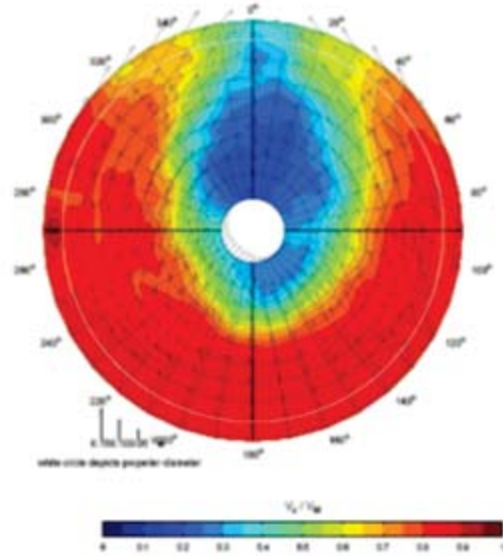
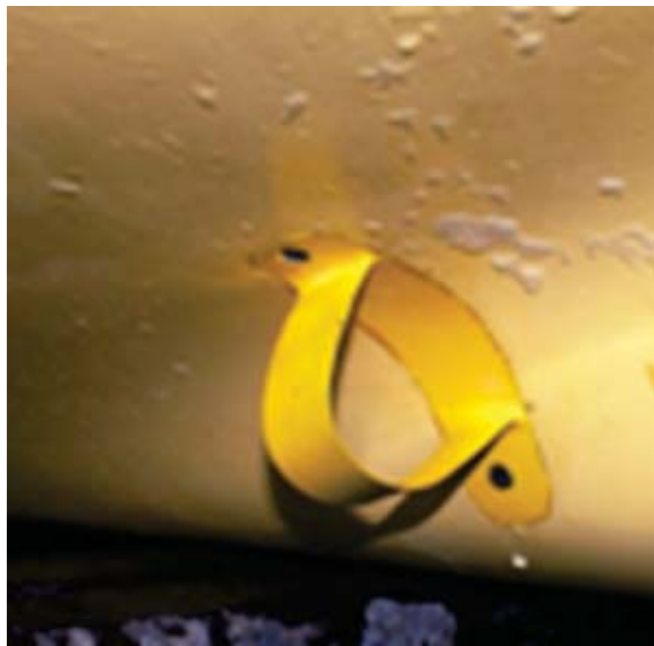


Fig. 6. Photograph of the hull with Boundary Layer Alignment Device BLAD and map of the measured wake velocity field

### PROPELLERS INCLUDED IN THE ANALYSIS

Both propellers considered in the analysis were four bladed and they had the same full scale diameter of 3.8 [m]. Their detailed geometry is presented in Figs. 7 and 8. Comparison of both propeller designs shows that the most significant difference between them is the higher hydrodynamic blade tip loading of propeller P3 with respect to the propeller P0. It is visible both in the increased blade pitch and increased mean line camber of the blade sections in this region. This increases the risk of unsteady cavitation. This risk may be further aggravated by a reduction of the expanded blade area ratio from 0.5809 for the propeller P0 to 0.5208 for the propeller P3 and it may cause an inferior unsteady performance of propeller P3.

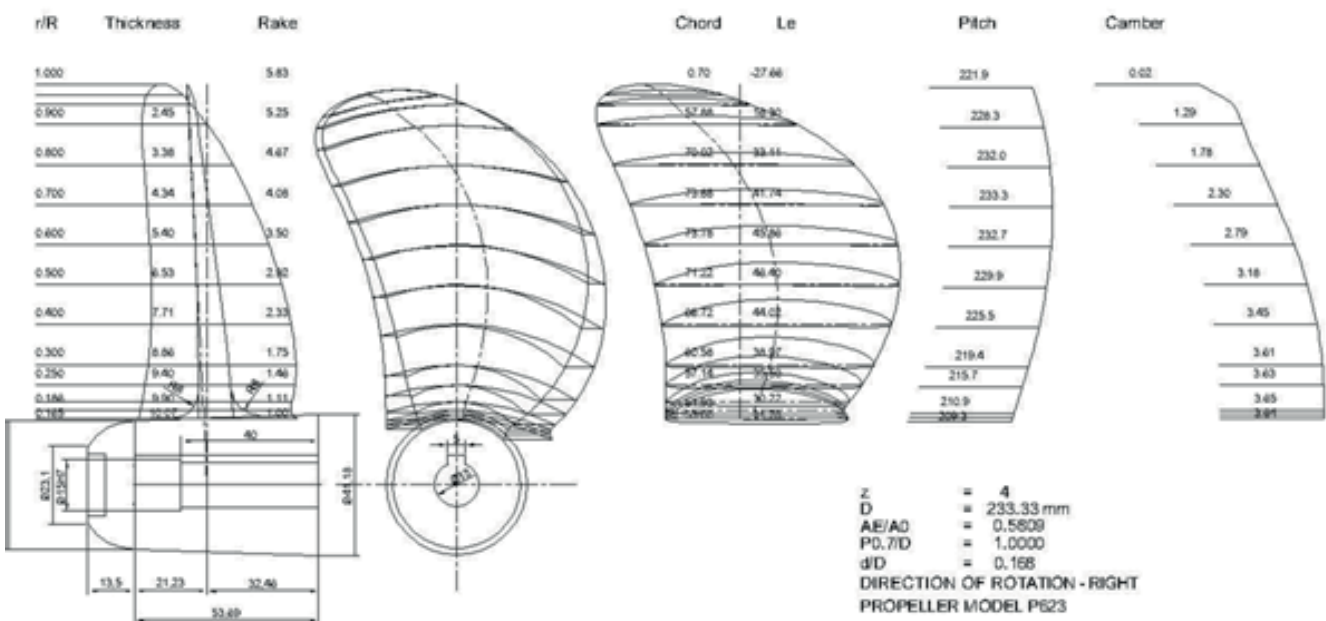


Fig. 7. Drawing of the reference propeller P0

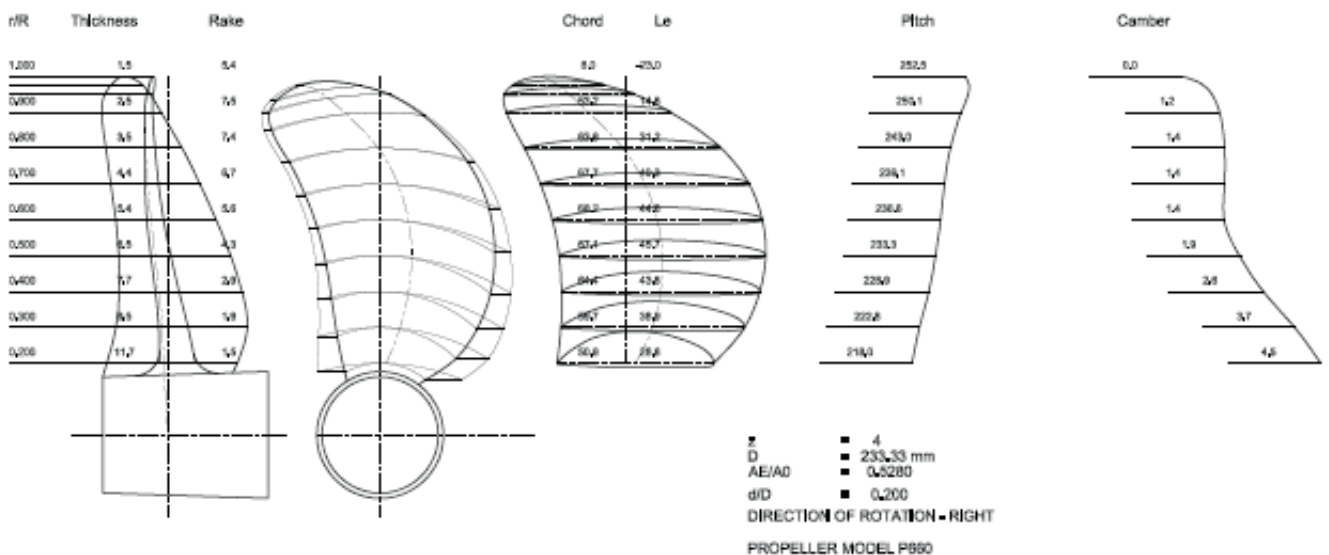


Fig. 8. Drawing of the designed propeller P3

## RESULTS OF CALCULATIONS AND COMPARISON WITH EXPERIMENTS

Calculations reported in this paper were performed using the newly modified computer program DUNCAN. This program is based on the deformable lifting surface theory and it is capable of calculating for the propeller operating in the three-dimensional non-uniform velocity field the time-dependent pressure distribution of the propeller blades, the unsteady cavitation extent on the propeller including sheet, bubble and vortex cavitation, the fluctuating bearing forces and the pressure pulses generated by the cavitating propeller in the prescribed points. The program uses a vortex lattice model with 165 bound vortex elements and 180 trailing vortex elements to represent each propeller blade.

Unfortunately, the corresponding experimental results in model scale were available only for the hull H0 with propeller P0. In these experiments the observations of unsteady cavitation on propeller blades were performed together with the measurements of the pressure pulsations in 17 points on the stern part of the ship hull. The locations of these points are shown in Fig. 9. As the program allowed for 16 computation points only, and furthermore, the measurements were performed with the rudder in place while the computations did not include the rudder, it was decided to disregard in calculations point no. 1, located closest to the rudder.

All calculations were performed for the ship speed of 15.0 knots and the cavitation number equal to  $\sigma_N=2.632$ . This cavitation number is defined in the following way:

$$\sigma_N = \frac{p - p_v}{0.5\rho(nD)^2}$$

- where:  $p$  - local static pressure in [Pa],  
 $p_v$  - water boiling pressure in [Pa],  
 $\rho$  - water density in [ $\text{kg}/\text{m}^3$ ],  
 $n$  - propeller number of revolutions per second,  
 $D$  - propeller diameter in metres.

During calculations in the different wake velocity fields the input ship speed was adjusted to produce the same thrust coefficient equal to  $K_T=0.2649$ . In this way all the computations of the unsteady parameters of operation of both propellers in all analysed wake fields may be regarded as comparable.

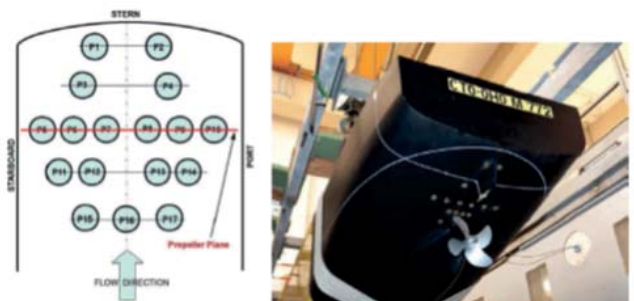


Fig. 9. Location of points for measurement and calculation of the propeller-induced pressure pulses

The observations of cavitation showed some inconsistency in the results, namely in the upper top position of the blade sheet cavitation appeared only occasionally (i.e. in some moments there was no cavitation on the blade in this position, while in the other moments the sheet cavity at the leading edge was clearly visible), leading to a suspicion that there may exist a region of flow separation on the stern part of the hull, generating some unsteadiness of the wake velocity field. Anyway, the calculations indicated a small region of sheet cavitation on the blade in the upper top position, which agrees reasonably well with that observed experimentally at the maximum sheet cavity extent (cf. Fig. 10).

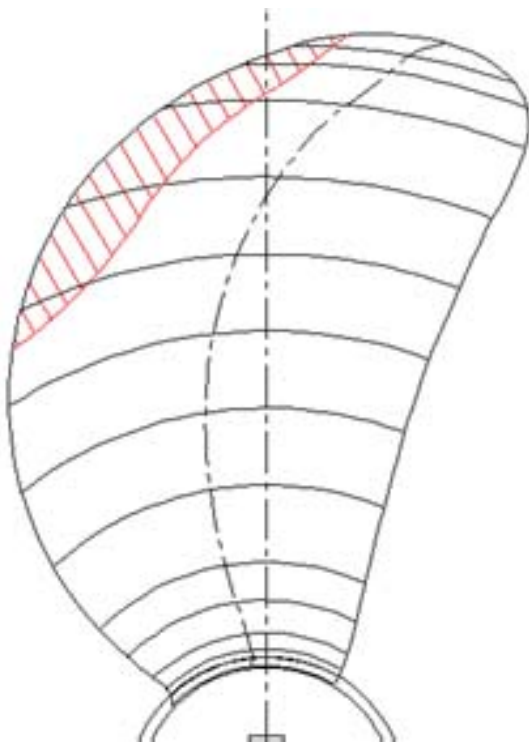
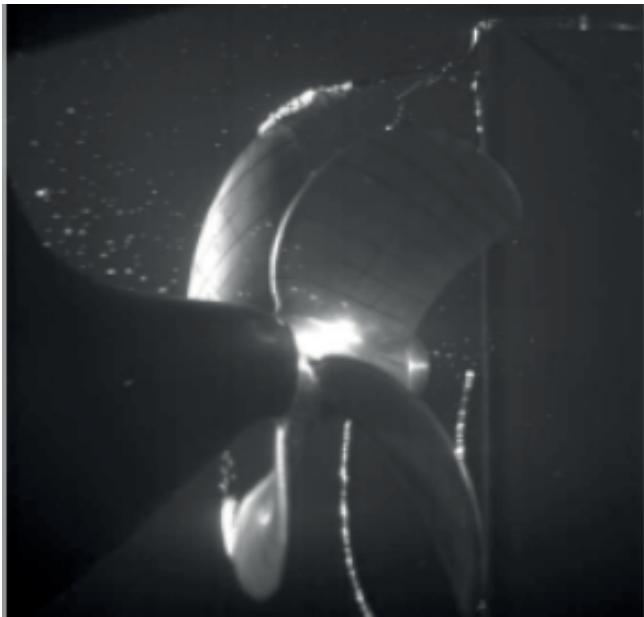


Fig. 10. Comparison of the observed and calculated sheet cavity extent on the blade of propeller P0 in the vertical position

Fig. 11 shows the comparison of the calculated and experimentally measured blade frequency harmonic amplitudes of the pressure pulses in model scale. The calculated results are visibly higher than the results of corresponding measurements, however both sets of results give values which are well within the acceptable range for this kind of ship. Several reasons for the discrepancy between measurements and calculations may be suggested:

- overestimation of the maximum extent and volume of the pulsating sheet cavity in the calculations, which leads to an overestimation of the maximum amplitudes of the pressure pulses,

- absence of the rudder in the calculations,

- measurements were conducted in the limited space of the circulating water channel, while the calculations assumed unlimited space (except hull surface as the only rigid boundary).

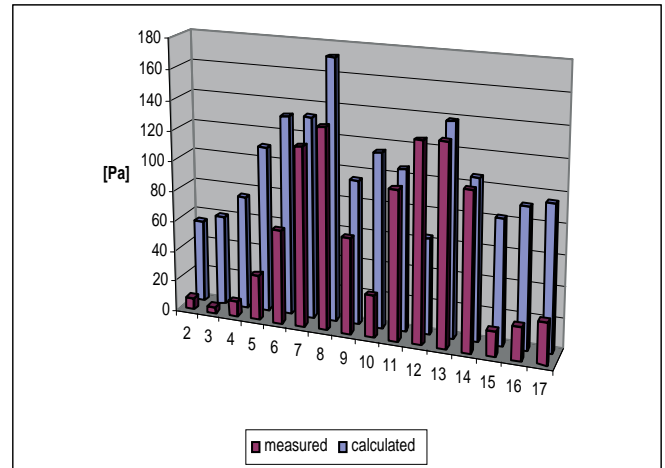


Fig. 11. Comparison of the measured and calculated blade frequency amplitudes of the pressure pulses generated by the propeller P0 behind the hull H0

The following figures, Figs. 12 to 17, show only the results of calculations. As the unsteady performance of marine propellers is strongly influenced by the cavitation phenomena, Fig. 12 shows the variation of sheet cavity volume, calculated for propeller P0 in model scale for all five wake fields and presented as function of the blade position angle. Blade position angle equal to 0 denotes the upper top position of the blade. The rate of change of the cavity volume with time is the factor primarily responsible for generation of the pressure pulses. The results shown in Fig. 12 may be compared and analysed together with the pressure pulses presented in Fig. 13.

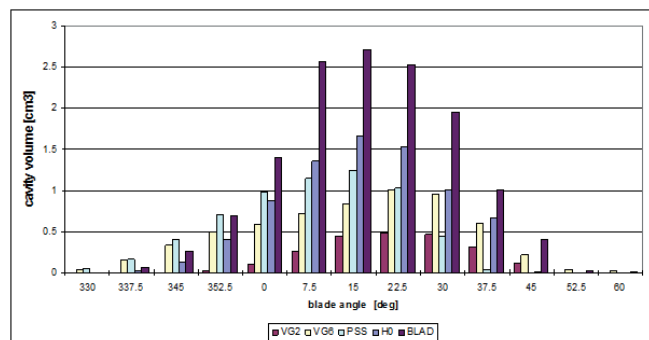


Fig. 12. Calculated cavity volume variation in model scale for propeller P0

The figures 13 and 14 present the comparison of the blade frequency harmonic amplitudes of the pressure pulses and the blade frequency harmonic amplitudes of the bearing forces for the propeller P0 in all analysed wake velocity fields H0, VG2, VG6, PSS and BLAD.

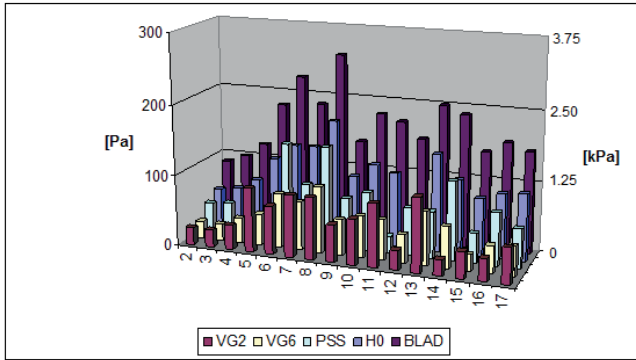


Fig. 13. Comparison of the calculated blade frequency amplitudes of the pressure pulses generated by the propeller P0 behind the hulls H0, VG2, VG6, PSS and BLAD in model scale ([Pa]) and in full scale ([kPa])

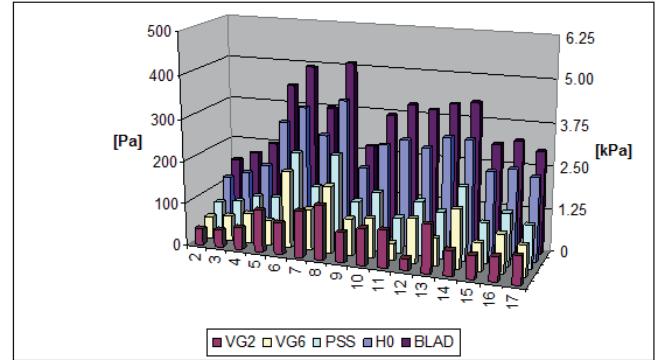


Fig. 16. Comparison of the calculated blade frequency amplitudes of the pressure pulses generated by the propeller P3 behind the hulls H0, VG2, VG6, PSS and BLAD in model scale ([Pa]) and in full scale ([kPa])

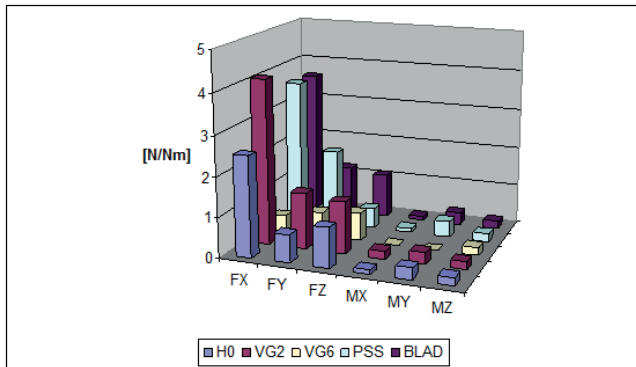


Fig. 14. Comparison of the calculated blade frequency amplitudes of the shaft forces generated on the propeller P0 behind hulls H0, VG2, VG6, PSS and BLAD

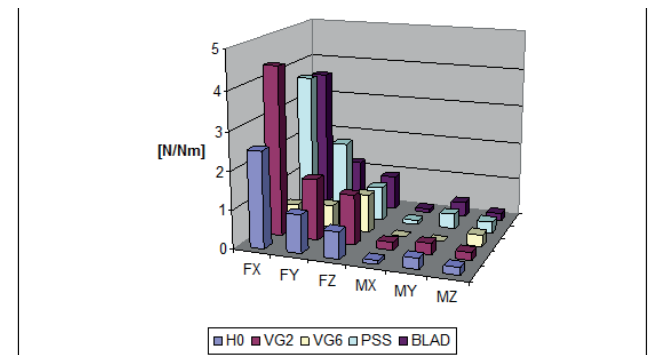


Fig. 17. Comparison of the calculated blade frequency amplitudes of the shaft forces generated on the propeller P3 behind hulls H0, VG2, VG6, PSS and BLAD

Fig. 15 shows the variation of sheet cavity volume, calculated for propeller P3 in model scale for all five wake fields and presented as a function of the blade position angle. Similarly as in the case of propeller P0, the results shown in Fig. 15 may be compared and analysed together with the pressure pulses presented in Fig. 16.

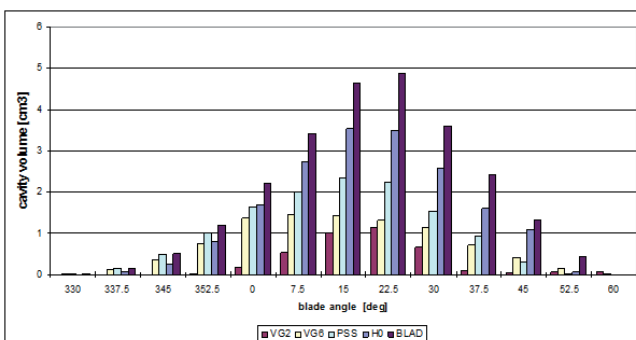


Fig. 15. Calculated cavity volume variation in model scale for propeller P3

## CONCLUSION

The following conclusions may be drawn from the analysis of the above presented results:

- Both computations and experimental observations show very little cavitation on the propeller blades.
- The computed blade frequency harmonic amplitudes of the pressure pulses for the hull H0 and propeller P0 are visibly higher than the values measured experimentally in the circulating water channel. However, both computed and measured amplitude values are rather low and they would be regarded as acceptable for this type of ship.
- The spatial distribution of pressure pulses amplitudes over the stern area in calculations and measurements shows visible differences. The calculated results are much closer to the measured values in the points located near the propeller, while the calculations overestimate the pressure amplitudes more significantly in the regions farther from the propeller. This may result from an overestimation of the maximum size of the pulsating

sheet cavity. The pressure signal generated by such a cavity fades with distance less rapidly than a signal generated by rotating blades and their variable hydrodynamic loading.

- The calculated variation of the sheet cavity volume with blade position showed a strong dependence of this process on the application of respective wake improvement devices. Application of these devices could reduce the cavity volume below the values obtained for the original hull as well as increase it over these values. The best results were achieved for VG2 and the worst for BLAD.

- The most effective reduction of the blade frequency harmonic amplitudes of the pressure pulses is achieved with the vortex generators VG2. Next best results are obtained with vortex generators VG6 and the Pre-Swirl Stator. Application of the Boundary Layer Alignment Device BLAD increases the blade frequency harmonic amplitudes.

- In all cases the blade frequency harmonic amplitudes of the pressure pulses for the propeller P3 are significantly higher than the corresponding values for the original propeller P0. This follows from a rather unusual geometry of the propeller P3 as compared to the propeller P0.

- The most effective reduction of the blade frequency amplitude of the bearing forces (practically the fluctuation of thrust is a decisive factor here) is achieved with the vortex generator VG6 for both propellers. As far as the fluctuating bearing forces are concerned, both propellers P0 and P3 are fully comparable. The general level of fluctuation of the bearing forces should be regarded as low and fully acceptable in all analysed cases.

- Considering all results of calculations presented in this paper the vortex generator VG6 should be considered as the most effective device as far as the unsteady performance of the propeller is concerned.

## ACKNOWLEDGEMENT

The experimental results presented in this paper have been obtained in STREAMLINE project. The STREAMLINE project is a collaborative R&D project, partly funded by the 7th Framework Programme of the European Commission. The authors would like to express their gratitude for the possibility of using these results in preparation of this paper.

## BIBLIOGRAPHY

1. Glover E.J., Szantyr J. A.: The Analysis of Unsteady Propeller Cavitation and Hull Surface Pressures for Ducted Propellers, Trans. RINA, Vol. 132, 1990.
2. Szantyr J. A.: User Instructions for the Program DUNCAN2012 for the Analysis of Ducted Propeller Operation in the Non-uniform Velocity Field, Technical Report of CTO SA No RH-2012/T-123 (in Polish), 2012.
3. Di Felice F., Salvatore F., Dymarski P., Pereira F.: Deliverable D21.1 -Results of Model Tests on Reference Configurations. STREAMLINE project Technical report, INSEAN and CTO, 2011.
4. Di Felice F., Falchi M., Aloisio G., Pecoraro A., Salvatore F., Bugalski T.: Deliverable D21.11 -Results of Model Tests on Optimized Configurations. STREAMLINE project Technical report, INSEAN and CTO, 2013.

## CONTACT WITH THE AUTHORS

Tomasz Bugalski, Ph.D.

Ship Design and Research Centre CTO  
Szczecińska 65  
80-392 Gdańsk,  
Poland

email: tomasz.bugalski@cto.gda.pl

Jan Szantyr, Prof.

Gdańsk University of Technology  
11/12 Narutowicza Street  
80-233 Gdańsk,  
Poland

email: jas@pg.gda.pl

# CFD and FEM model of an underwater vehicle propeller

Tadeusz Chruściel, MSc  
Ewelina Ciba, MSc  
Julita Dopke, MSc  
Gdańsk University of Technology

## ABSTRACT

*Within the framework of the project for design and optimization of the Remotely Operated Vehicle (ROV), research on its propulsion has been carried out. The entire project was supported by CFD and FEM calculations taking into account the characteristics of the underwater vehicle. One of the tasks was to optimize the semi-open duct for horizontal propellers, which provided propulsion and controllability in horizontal plane. In order to create a measurable model of this task it was necessary to analyze numerical methodology of propeller design, along with the structure of a propellers with nozzles and contra-rotating propellers. It was confronted with theoretical solutions which included running of the analyzed propeller near an underwater vehicle. Also preliminary qualitative analyses of a simplified system with contra-rotating propellers and a semi-open duct were carried out. The obtained results enabled to make a decision about the ROVs duct form. The rapid prototyping SLS (Selective Laser Sintering) method was used to fabricate a physical model of the propeller. As a consequence of this, it was necessary to verify the FEM model of the propeller, which based on the load obtained from the CFD model. The article contains characteristics of the examined ROV, a theoretical basis of propeller design for the analyzed cases, and the results of CFD and FEM simulations.*

**Keywords:** ROV, ROV propeller, semi-open duct for horizontal propellers, rapid prototyping propeller

## Introduction

Evolution in the design of underwater vehicles of ROV type requires exploration of new solutions oriented on improving the quality of the offered products. One of them is a semi-open duct of horizontal thrusters that has been applied in a prototype of multitasking underwater robot developed within the framework of a research project conducted by the Department of Underwater Technology, Faculty of Ocean Engineering and Ship Technology, Gdansk University of Technology. One of the main tasks of the robot is to explore the seabed for geological purposes and evaluate the suitability of a land for the wind farm construction. This task implies the need for a high operating speed and high manoeuvrability when operating on a geological object. Providing both of these features while ensuring planned functionality require

the support for the design process throughout its range by numerical modelling in both CFD and FEM fields. One of tasks which have been implemented was to optimize the shape of semi-open ducts of horizontal thrusters (fig. 1).

The analysis of such an extensive issue started by checking the level of convergence between the prepared numerical models and the theoretical calculations for two cases: a free propeller and a propeller in the nozzle. In the next step the numerical model was extended by the disorder coming from the drive motor. The results obtained from the numerical analysis were compared with those recorded on the real object.

This enabled to refine faster the numerical model extended by the variable disorder derived from the semi-open ducts and the interference between the propellers.

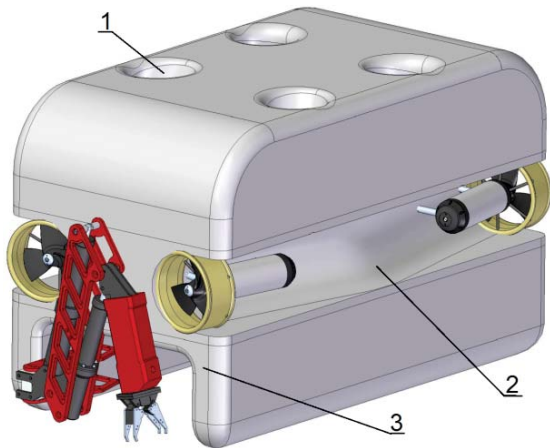


Fig. 1. ROV with semi-open duct for horizontal propellers (1 - duct for vertical propeller; 2 - semi-open duct for horizontal propeller; 3 - manipulating module)

The structure of the full model of the semi-open ducts for horizontal thrusters not only had to provide the information about the effectiveness of the solutions but also to make a basis for the analysis of the operational capacity of the ROV. Another aspect of the vehicle's propellers was the strength of the applied materials. Due to the fact that when designing the vehicle demonstrator a decision was made to use the technology of rapid manufacturing of prototype propellers, there was also a need to analyze their work using the FEM model. The loading force on the propeller was assessed using the pressure generated in the CFD analysis of the free propeller.

### Theoretical overview of the issue

Due to the lack of publicly available theoretical solutions and guidelines for designing a system based on the semi-open ducts, a decision was made to build a numerical model that allows at least determining the quality of the proposed solution. At the beginning, the reference point of the thrust characteristics of the designed propeller working in the nozzle was adopted. These data were used to check the propeller in the numerical model in two basic operating states, i.e. as the free arrangement and in the nozzle. The characteristics of the propeller are discussed in Section "Free propeller and nozzle". Further steps of solving the problem included complementing the CFD model by disorders generated by the propeller and confronting it with the results of the tests performed on a real object. These considerations were supplemented by FEM model calculations, which are discussed in Section "FEM model".

### Free propeller and nozzle

The design stage was based on the database of the functional components of a previously developed ROV bearing the name of Morświn. A group of the elements used to develop the numerical models and build the test bench in order to determine the suitability of design solutions,

included the propeller, the nozzle, and the drive motor. The nominal rotational speed of the propeller was 40 rps. The geometric parameters of the propeller which constituted the reference point are listed below, while the indicative geometric characteristics of the nozzle for this propeller are shown in Fig. 2

Geometric parameters of the propeller:

- propeller diameter:  $D = 0.22\text{m}$
- hub diameter:  $DH = 0.04\text{m}$
- number of wings:  $z = 3$
- surface coefficient:  $AE/AO = 0.65$
- pitch coefficient for 0.7R:  $P/D = 0.9845$
- profiles type: NACA16

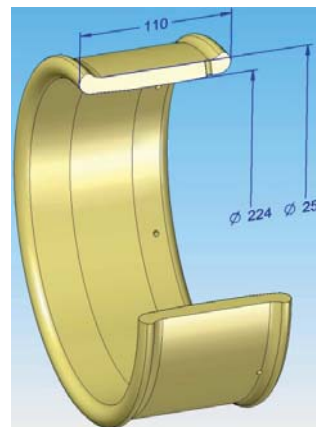


Fig. 2. The nozzle

According to the theory, the system being a combination of the propeller and the nozzle improves the thrust characteristics, as can be seen in Figs. 3 and 4.

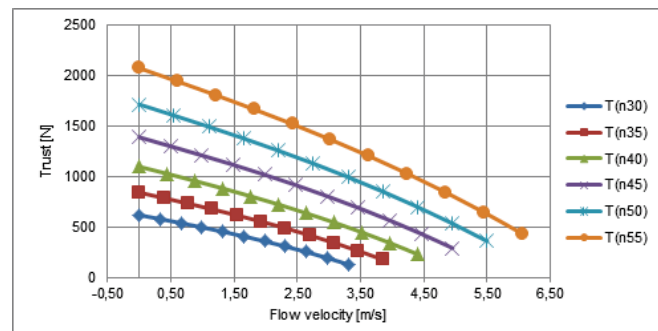


Fig. 3. Thrust of the free propeller

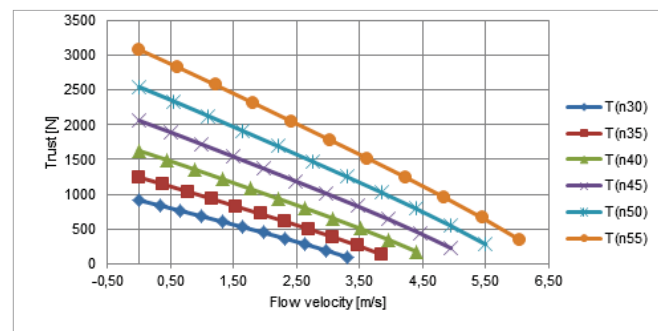


Fig. 4. Thrust of the propeller with the nozzle

The above characteristics were determined during the design of the propeller for earlier project. In Section 3.1 they will be discussed in more detail with the reference to the results obtained from CFD calculations.

### CFD model

While working on improving the flow model of the rotor, which in this case is the propeller of ROV, modelling making use of a frozen rotor rotary domain in quasi stationary systems has been applied. The use of this model made it possible to shorten the computation time, which was an important aspect in the context of time restrictions related to the implementation of the project. The expense for reducing the computing time demand was lower accuracy associated with model simplifications resulting from this method of modelling. The main disadvantage of this method of the calculation model included the lack of modelling the transition state, the transitions between the steady state and the turbulent state, and the state of merging of these two types of flows.

As already mentioned in the model with respect to the CFD, three models of varying degrees of sophistication were built. The domain for the first model calculations is shown in Fig. 5.

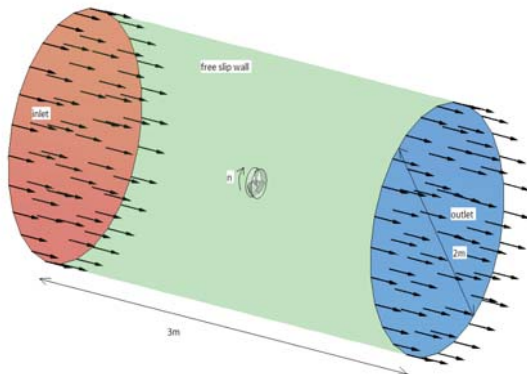


Fig. 5. Domain of the free propeller model

The propeller with a part of the rotating domain was placed in the middle of the span of the main domain. The results obtained using the above model are discussed in the initial part of Section 3.1.

The second model, whose results were compared with the solution of the theoretical model, was supplemented by a nozzle. This model uses the same size of the main domain, and the propeller together with the nozzle is placed in the middle of the span of the domain. In order to take into account the effect of the nozzle on the working surface of the propeller, the division between the main domain and the rotating domain is placed on the inner cylindrical surface of the nozzle. This is illustrated by Fig. 6, in which the division surface is highlighted in orange.

The third model, which was most complex in geometrical terms, was the model of the propeller in the nozzle complemented by a drive motor and the objects of the measuring devices mounted of a real bench.

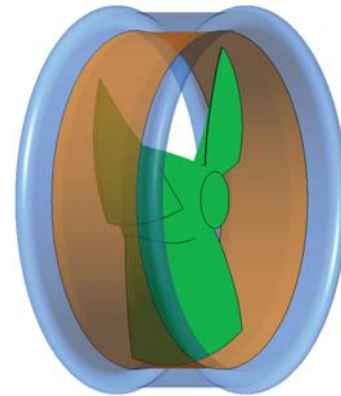


Fig. 6. Wall counter rotate velocity

The interface areas were introduced in this model in the same way as in the model based solely on the propeller and the nozzle. A detailed description of the method of measurement and the test bench is given in Section 2.4. The following is a sketch of the modelled system in a natural way simplified for the purposes of CFD.

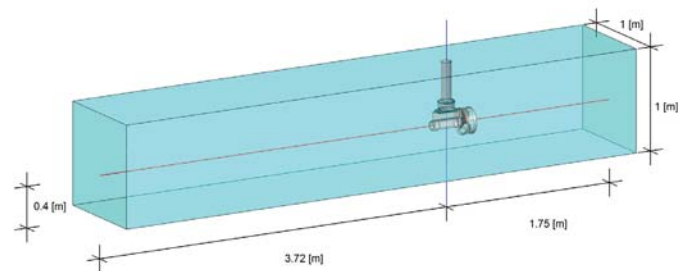


Fig. 7. Geometric parameters of CFD model No. 3

Dimensions of the domain cross section and the location of the thruster resulted from the dimensions of the circulating water channel which was available for the tests.

### FEM model

The reason to create the FEM model for propeller loaded with pressure imported from the CFD model was, above all, a desire to see how large the strength reserve made by rapid prototyping item is. The rapid prototyping method that has been used to produce designed propellers was Selective Laser Sintering (SLS). It involves successive sintering of layers of powdered base metal. In the case of the tested propeller it was Alumide whose parameters are included in Table 1.

Table 1. Parameters of alumide

Parameter	Value
Density	1360 kg/m <sup>3</sup>
Young module	3800 MPa
Poisson number	0.4
Tensile strength	48 MPa

The SLS method allows to produce a fully functional device from many different materials. In the literature there is no clear information concerning the real strength level of products made based on this kind of rapid prototyping. The only information that can be found refers to on simple material parameters of the base material. However, observing the structure of the material made using this technology a question arises what is the safe load that this propeller can carry and what is the level of internal stress in the structure. Then, assuming a safety factor of 2 we can decide, in the engineering way, whether the designed item can safely carry the load.

The model was built based on the load taken from the quasi static CFD model and complemented by the hydrostatic pressure acting on the object at a depth of 200m. The dynamic load was assumed for the propeller rotating with the rotational speed of 55 rps in the flow with the linear speed of 3 m/s. In these conditions, the thrust force generated by the propeller was approximately equal to 1368 N. The type of the analysis was static analysis making use of the solid model and solid elements of solid187 type (10-node element with three degrees of freedom at each node UZ, UY, UZ). The main mesh with parts of 1.5mm in size was locally concentrated to 0.5mm within the passageway of the propeller blades to the hub (Fig. 8).

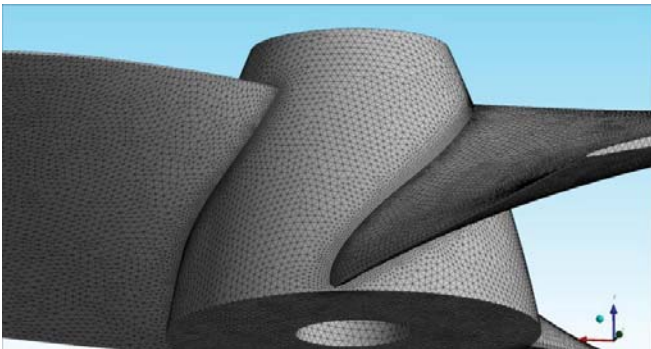


Fig. 8. Model mesh with local concentrations

### Experimental model

The experimental model consisted of a drive unit equipped with a propeller in a nozzle, a dynamometer, and the circulating water channel in which the test was performed for flow rates of 0.0; 0.2; 0.5; 0.7 and 1.0 m/s. The tests were performed for work angles at 0; 22.5 and 45deg, at two stages of propeller operation, i.e. the nominal operating condition (right rotation - push system) and the backward operating condition (left rotation - pull system). In the push system the water first passed through the drive motor, and then the disrupted flow reached the propeller. In the pulling system, the undisturbed stream of water first reached the propeller and then encountered the drive motor. The measurement system used in this test is shown in Fig. 9, while its orientation relative to the flow direction is given in Fig. 10.



Fig. 9. Experimental model



Fig. 10. Experimental model orientation

In order to minimize the impact of the test structure on the measured magnitude of the thrust force generated by the testing setup, the x-axis was bound with the drive motor, which allowed direct measurement of the thrust forces in tests with angles with respect to the axis of movement without the need to set the value of the components. Another procedure to remove forces generated at the test bench from the value measured for different flow velocities was calibration of the dynamometer each time the flow speed was stabilized. The calibration was performed before starting the motor, which allowed directly to record the change of the thrust as a function of propeller speed rotation.

### Analysis of solutions

The main purpose of the construction of CFD models was to gain knowledge on how to model the discussed issue, and to confront the simulation results with the theoretical and experimental results. The applied computational method was verified by comparing with theoretical characteristics of the Series B-Wageningen. The level of coincidence of the compared values ranged from 1 to 5%, and the variation of the characteristics of the determined parameters coincide with the theoretical values.

The promising results of the analysis gave rise to the application of this method for modelling the phenomenon of the real object. The following sections present the obtained results in relation to theoretical calculations and modelling studies.

## Solution of theoretical, CFD, and experimental models

The discrepancy between the results of the theoretical calculations and numerical simulation for the free propeller did not exceed 5%. Figure 11 shows sample comparison of the thrust generated on the propeller.

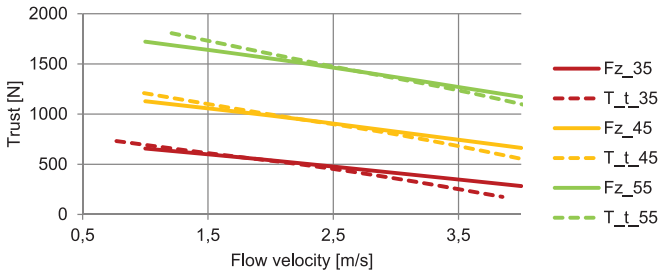


Fig. 11. Thrust of the free propeller:  $T_t$  - theoretical solution;  $F_z$  - numerical solution

The above presented convergence level of the free propeller model was considered sufficient in the context of the task at hand. In the next step the CFD model was supplemented by the effect of the nozzle. Extensive simulation calculations allowed to obtain results revealing similar convergence to the free propeller model.

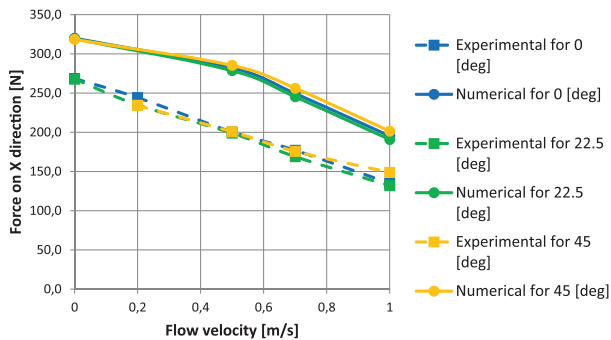


Fig. 12. Push configuration for 25 [rps]

At the same time, laboratory tests were performed for the configuration shown in section 2.4, along with simulations corresponding to flow conditions in the circulating water channel. The results of sample numerical solutions and experimental studies are summarised below in Figs. 12 and 13. They reveal that the method needs further development in order to obtain proper model of disturbances coming from the structure. In addition, the analysis of images of pressure fields behind the CFD model of the propeller has made it possible to observe swirls flowing down from propeller blades, what coincides with relevant information in the literature and testifies to the correctness of operation of the method.

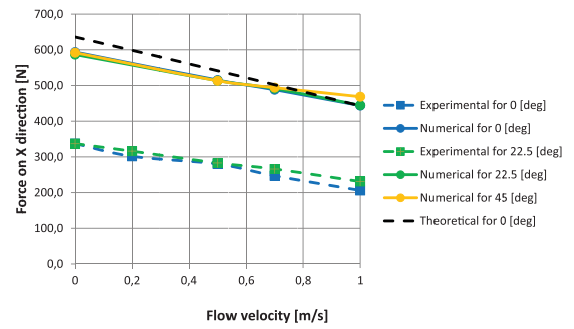


Fig. 13. Pull configuration for 25 [rps]

## Solution of FEM model

The load imported from the CFD model for the push side and the pull side of the propeller blade does not exceed  $4.5e5$  Pa. The distribution of the load on the respective sides of the propeller's blades is given in Fig. 14.

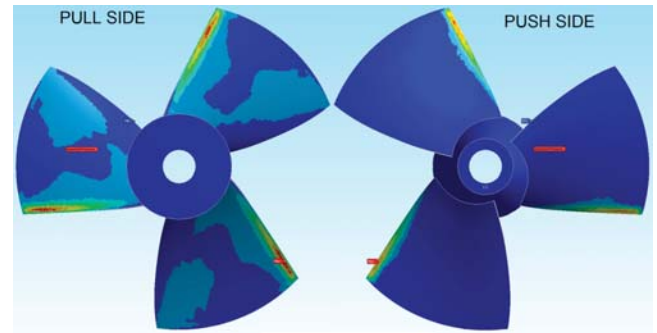


Fig. 14. Load from CFD model

The defined load supplemented by the hydrostatic pressure equal to 200m H<sub>2</sub>O (this value reflects the maximum depth of operation of the vehicle) resulted in the maximum global strain equal to 0.0095m.

As expected, the most strenuous region of the propeller proved to be the central parts of the propeller blades at the area of connection with the hub, which is presented in a picture of stresses reduced by the von-Mises hypothesis (Fig. 15). The values of these stresses ranged from  $2.8e4$  Pa to  $8e7$  Pa.

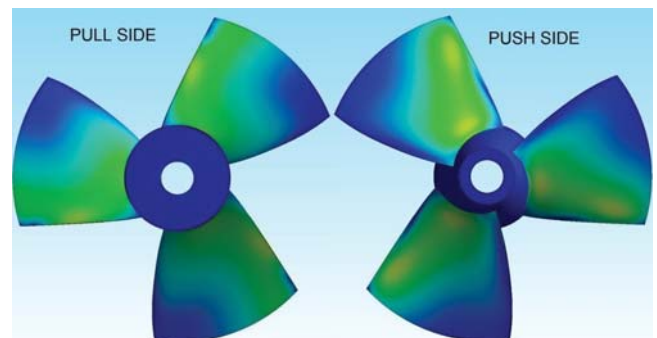


Fig. 15. Equivalent (von-Mises) stress

## Conclusions

Referring to the results obtained from the FEM model and the assumed safety factor of 1.5, it was found that propeller made of alumide using the method of rapid prototyping (SLS) can transfer safely the dynamic load generated during its operation. In addition, a small deformation of the material should not significantly affect the efficiency of the propeller and change its hydrodynamic parameters.

In order to verify the performance of products manufactured by a rapid prototyping method, measures have been taken to develop a computational method based on FEM for structures made in the above process. Ultimately, this method is going to be verified in further experimental strength tests.

A conclusion from the experimental studies on the task in question performed from the point of view of hydrodynamics phenomena is that the proposed method of calculation needs further development, primarily in the field of modelling the interference of the nozzle and the propeller. However, the presently obtained results are satisfactory considering that further stages of the project will include assessing the ROV design solution, in which applying a semi-open ducts for horizontal thrusters will be based on the analysis of qualitative rather than quantitative analysis.

## Acknowledgements

The work presented in this paper was funded by The National Centre for Research and Development, Warsaw, Poland. Project No PBS1/B9/12/2012.

The calculations were carried out at the Academic Computer Centre in Gdańsk.

## References

1. Bielewicz E., *Wytrzymałość materiałów*, Wydawnictwo Politechniki Gdańskiej, Gdańsk 1992.
2. Bielski J., *Inżynierskie zastosowania sytemu MES*, Wydawnictwo Politechniki Krakowskiej, Kraków 2013
3. Bielski J., *Wprowadzenie do inżynierskich zastosowań MES*, Wydawnictwo Politechniki Krakowskiej, Kraków 2010
4. Jarzyna H., Koronowicz T., Szantyr J., *Design of Marine Propellers, Selcted Problems*, PAN, Wrocław, Warszawa, Kraków 1996
5. Kobyliński L., *Śruby okrętowe*, Wydawnictwo Komunikacyjne, Warszawa 1955
6. Timoshenko S., Goodier J. N., *Teoria sprężystości*, Arkady, Warszawa 1962
7. Zagrajek T., Krzesiński G., Marek P., *Metoda elementów skończonych w mechanice konstrukcji*, Oficyna Wydawnicza Politechniki Warszawskiej, Warszawa 2006
8. CFX-Solver Theory Guide for Ansys 14.5

## CONTACT WITH THE AUTHORS

Tadeusz Chruściel, MSc  
email: tadeusz.chrusciel@pg.gda.pl

Ewelina Ciba, MSc  
email: eweciba@pg.gda.pl

Julita Dopke, MSc  
email: dopke.julita@gmail.com

Gdańsk University of Technology  
11/12 Narutowicza Street  
80-233 Gdańsk,  
Poland

# Numerical simulation of tonal and broadband hydrodynamic noises of non-cavitating underwater propeller

B. Mousavi, Ph. D.

A. Rahrovi, Prof.

S. Kheradmand, Asso. Prof.

University of Technology, Shahin-shahr, Iran

## ABSTRACT

*The objective of the study was to carry out numerical simulation of the hydrodynamic noise generated by the flow around a non-cavitating underwater propeller. To achieve this goal, hydrodynamic simulation of flow around the propeller was initially done. The unsteady 3-D flow was modelled numerically along with the LES turbulence model. The hydrodynamic parameters calculated for different advance coefficients are visibly in line with the previous experimental works. The turbulent quantities of the hydrodynamic study and the FWH model were used to find spectral distributions of flow noise for different advance coefficients. The results of the acoustic investigation were compared against other numerical results. An array of 100 hydrophones was used to find the directional distribution of the noise around the propeller. The obtained results indicate that, for different advance coefficients, the highest intensity of the noise recorded by different receivers around the propeller occurs in BPF. Furthermore, it has been found that the noise is directionally as well as intensively distributed around the propeller. Noise distributions of noise are presented and discussed for different regimes of propeller rotation. The analysis of the expanded spectrum (broadband analysis) of noise on the propellers has also been done and the contribution of all parts of the propeller to hydrodynamic noise generation are presented.*

## INTRODUCTION

The noise generated by the propeller of a submarine is the most principal factor in its recognition by enemy's sonar contacts. The noise also pollutes the subsea environment. Hence, it seems vital to measure the noise and lower its intensity. The noise produced by the propeller can be divided into that of cavitation and non-cavitation nature. Although most propellers experience cavitation and generate enormous noise due to the destruction of bubbles, in deep sea conditions propellers are still noisy without cavitation.

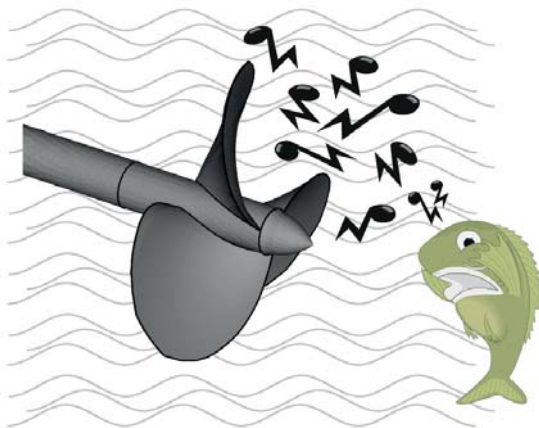


Fig. 1. Underwater propeller DTMB 4119

The hydrodynamic analysis of the flow around the propeller is the prerequisite of its acoustic analysis. Propellers rotate in a highly turbulent wake behind vessels, therefore the flow pattern around them is truly complicated and hard to resolve. It seems necessary to precisely simulate the turbulent quantities. In the present study, the flow around the propellers is analysed both numerically and experimentally. Many researchers measured experimentally propellers performance [1-4]. Unfortunately, these methods require complex laboratory equipment and are very expensive, especially when fluctuating quantities are to be measured. On the other hand, numerical simulations (making use of both inviscid [5-10] and viscous flow methods [11-15]) are also widely represented in the literature.

Turbulence modelling is the most challenging problem of propeller hydrodynamic studies. Many researchers use RANS equations including 0, 1, 2 and multi-equation methods to resolve the closure problem [11-15]. In a pure hydrodynamic study oriented on determining certain integral quantities including  $K_1$  or  $K_Q$ , the given methods lead to acceptable results. However, in the noise studies where temporal and space distributions of fluctuating quantities, such as pressure for instance, should be found, more accurate models are required. Here, DNS [16], DES [17] and LES [18] are the candidates to model the turbulence. LES is more commonly used to setup hydrodynamic parameters for acoustic investigations, because of its precision and moderate computational cost [19-22].

The noise detected in the fluid can be generated by either a vibrating structure or fluid fluctuations. Although the structural noise is very important and is studied by many researchers [23-25], in the present work the vibration of the propeller structure is not considered and only the flow noise is studied.

Sound propagation is related to the media in which the noise is propagated. Although the subject studied by most flow noise researches falls into the category of aero-acoustic noise (in gas media) [26], the hydrodynamic noise has also been the object of interest of some researches [27]. Regardless of the media, basically there are two kinds of methods to model the flow noise numerically, which are the direct methods [28] and those based on the acoustic analogy [29]. Beside the acoustic analogy, some methods, such as the Linearised Euler Equation [30-32], the Acoustic Perturbation Equation [33] and the Linearised Perturbed Compressible Equation make use of perturbation quantities [34].

In the present study, the flow-noise of a rotating submerged propeller is predicted by a 3D numerical simulation. For the near-field, the Navier-Stocks Equations are used for modelling the flow and the LES model to model the turbulence, while for the far-field acoustic, the FWH model is applied. Equations are presented in Section 2, and the obtained results including the hydrodynamic and tonal noise results are presented in Section 3. Broadband noise results are presented in Section 4 and, finally, in Section 5 concluding remarks are depicted.

## EQUATIONS AND NUMERICAL SOLUTION

In the hydrodynamic analysis of the flow, the flow field can be predicted by solving the continuity and momentum equations (Equations 1 & 2) [18].

$$\frac{\partial \rho}{\partial t} + \frac{\partial}{\partial x_i} (\rho u_i) = 0 \quad 1$$

$$\frac{\partial}{\partial t} (\rho u_i) + \frac{\partial}{\partial x_k} (\rho u_k u_i) = \rho g_i - \frac{\partial P}{\partial x_i} + \frac{\partial \tau_{ij}}{\partial x_j} \quad 2$$

where  $u_i$  are velocity components of water,  $\rho$  is density,  $P$  is pressure, and  $\tau_{ij}$  is the shear stress tensor.

For the acoustic analysis of the propeller the integral equation FWH (Equation 3) is solved to find the far-field sound of the propeller [35].

$$\begin{aligned} \frac{1}{a_0^2} \frac{\partial^2 p'}{\partial t^2} - \nabla^2 p' &= \frac{\partial^2}{\partial x_i \partial x_j} \{T_{ij} H(f)\} - \frac{\partial}{\partial x_i} \{[P_{ij} + \rho u_i (u_n - v_n)] \delta(f)\} \\ &+ \frac{\partial}{\partial t} \{[\rho_0 v_n + \rho (u_n - v_n)] \delta(f)\} \end{aligned} \quad 3$$

In Equation 3  $p'$  is the pressure fluctuation and  $T_{ij}$  is the Lighthill stress tensor. The following equation is referred to as the Lighthill's equation in which the first right-side term stands for the generation source of the monopole noise, the second term represents the dipole noise, and the third term accounts for the quadrupole noise[35].

$$\frac{\partial^2 \rho}{\partial t^2} - c^2 \frac{\partial^2 \rho}{\partial x_i^2} = \frac{\partial q}{\partial t} - g_i \frac{\partial \rho}{\partial x_i} + \frac{\partial f_i}{\partial x_i} - \frac{\partial^2 \tau_{ij}}{\partial x_i \partial x_j} \quad 4$$

In this study, the noise caused by the rotating propeller forms the monopole thickness noise. The noise of the pressure level and propeller suction shapes the dipole loading noise. As the Mach number of the propeller rotation is small, the volume noise is ignored. Using the Lighthill analogy, Proudman proposed the following formula to compute the acoustic power of the turbulent flow, regardless of the average flow [36].

$$P_A = \alpha \rho_0 \left( \frac{u^3}{l} \right) \frac{u^5}{a_0^5} \quad 5$$

In the above equation,  $u$  and  $l$  are the turbulence velocity and the length scale, respectively, while  $a_0$  and  $\alpha$  are the sound speed and a coefficient.

For the simulation of the broadband noise, the acoustic power on the propeller surface ( $L_p$ ) is derived from Equation 6.

$$L_p = 101 \log \left( \frac{P_A}{P_{ref}} \right) \quad 6$$

In the above equation,  $P_{ref}$  is the reference acoustic power and equals 10-12W/m<sup>3</sup>.

The studied propeller is a real size DTMB 4119 propeller. All flow simulations are done using the OpenFOAM software and acoustic post processing of the data are performed with a homemade code for noise calculations. Figure 2 (on the right) shows the cylinder-shaped computational domain around the propeller. As shown in the figure, a small cylinder with the length of 0.385 D and diagonal of 1.1 D is placed around the propeller. The cylinder is used to revolve the propeller in the rotating reference frame. Figure 5(right) clarifies the dimensions of the solution (see the table for boundary conditions of the issue). The open water condition is applied to the inlet. To employ the LES model of turbulence for the acoustic analysis, the study employed an extensively fine grid (total number of 2 750 000 cells) upon and around the propeller, in particular where the flow vortex is generated (figure 2 left). The sliding mesh technique is used to model the rotation of the propeller. The small cylinder in figure 2 around the propeller rotates at the propeller speed.

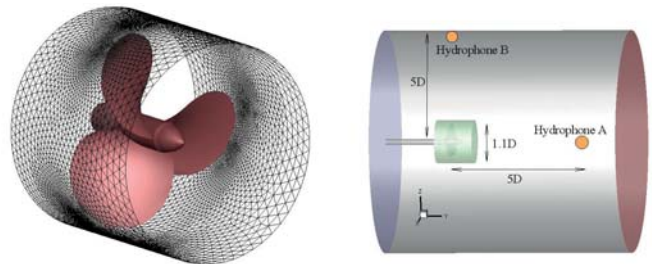


Fig. 2. Computational domain (right) and sliding portion of the domain with unstructured grid (left)

## HYDRODYNAMIC FINDINGS

Figure 3 shows the graphs comparing the hydrodynamic coefficients as a function of the advance coefficients obtained in the present study and recorded as the laboratory findings [37]. The results are visibly in line with each other. As the graph indicates, for all advance coefficients the thrust and moment coefficients are close to each other and their difference is less than 9 %. The value of the advance coefficients was derived from Equation 7.

$$J = \frac{V_s}{N_p D_p} \quad 7$$

where J is the advance coefficient, Vs is the advance velocity, Np and Dp are the angular velocity and the diameter of the propeller.

Figures 4 & 5 show the pressure coefficients of the propeller blade as functions of d<sub>le</sub> for two different value of dr (0.5 and 0.7) for J=0.83. Here dr is defined as dr=r/R in which r is the radial distance from the propeller axis and R is the propeller radius. d<sub>le</sub> represents the spatial distance from the propeller blade leading edge, non-dimensionalised by the propeller blade chord. The pressure coefficient value at this section was derived from Equation 8.

$$C_p = \frac{2p - 2p_0}{\rho V_s^2 \left[ 1 + \left( \frac{\pi d_r}{J} \right)^2 \right]} \quad 8$$

In the above equation, Cp is the pressure coefficient; p0 is the reference pressure and Vs is the advance velocity of the propeller. The numerical results of the present study were compared with those obtained by Pan et al. using the panel method, where the fluid was supposed to be inviscid [37]. The existing difference between these two cases is due to the fact that the boundary layer was not modelled in the panel method.

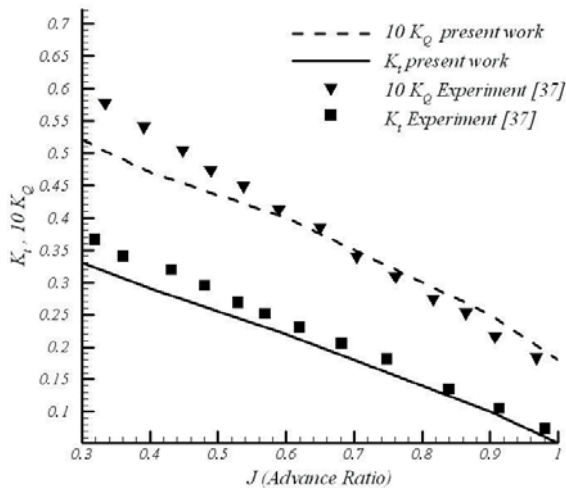


Fig. 3. Hydrodynamic performance of propeller in open water conditions

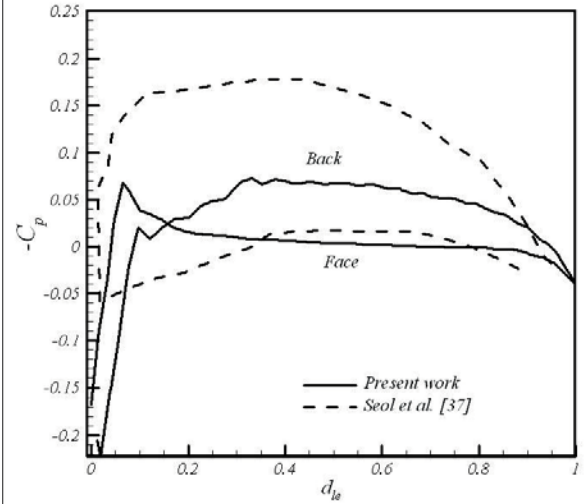


Fig. 4. Pressure coefficients for  $d_r = 0.5$

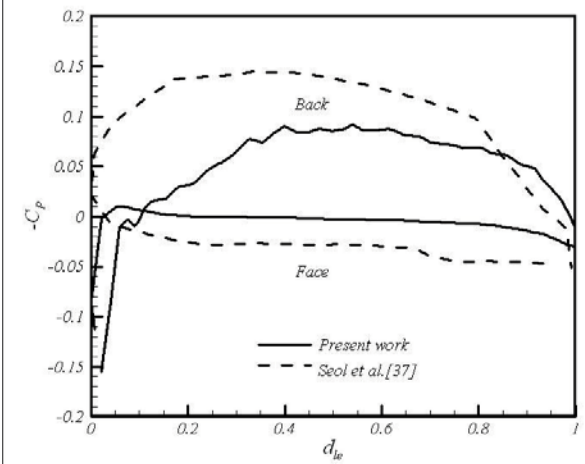


Fig. 5. Pressure coefficients for  $d_r = 0.7$

Figure 6 shows two views of axial distribution of water velocity, where the propeller is rotating with a constant angular velocity of 120 rpm. The figure shows the flow pattern in which every blade tip generates a high speed backward flow (regions marked red). At the same time a forward flow with lower axial velocity is also generated. These two reverse flows provoke a vertical flow around the blade tip. As the numerical value of the axial velocity indicates, the rotating direction of the eddy is clockwise.

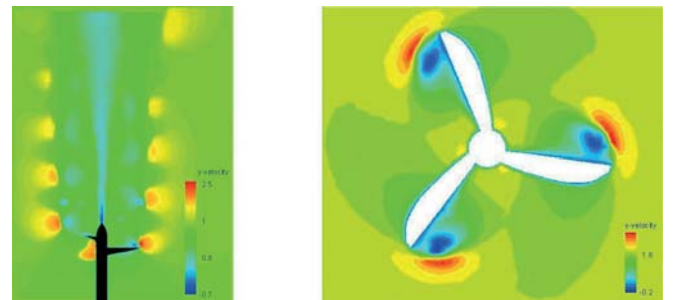


Fig. 6. Axial velocity distribution around propeller in horizontal plane (left) and propeller plane (right)

Figure 7 shows the planes of the same velocity around the propeller, demonstrating the creation of the radial and tangential flow and the velocity increase from the pure input axial velocity of 1.6 m/s to 1.65 m/s.

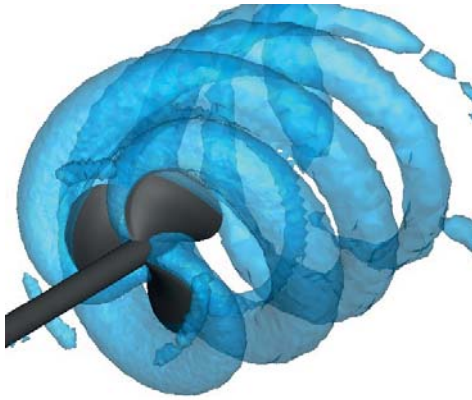


Fig. 7. Velocity isosurfaces, magnitude 1.6 m/s

Figure 8 shows vorticity contours in two perpendicular planes. As indicated in the figure, blades tips play the main role in vorticity generation. On the other hand it is evident from Figure 8 (left) that the propeller nose is also a source of vorticity. In this case, i.e. for the angular velocity of propeller equal to 120 rpm, the magnitude of the tip vorticity is higher than that generated by the propeller nose. The regions of vorticity generation are expected to be an active source of flow noise.

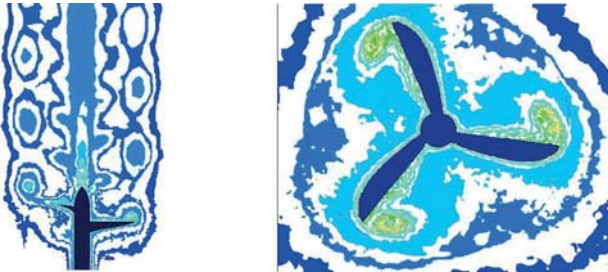


Fig. 8. Vorticity distribution around propeller in horizontal plane (left) and propeller plane (right)

### ACOUSTIC FINDINGS

In this section, the level of the noise generated by the propeller DTMB4119 is presented [38]. The water density and the speed of the sound were assumed as equal to 1026 kg/m<sup>3</sup> and 1500 m/s, respectively. The level of sound was computed using Equation 9.

$$SPL = 20 \times \log \frac{P_{acoustic}}{P_{ref}} \quad 9$$

In Equation 9, SPL stands for the decibel based Sound Pressure Level. The level of the reference pressure equals 1 x 10<sup>-6</sup> pa and P<sub>acoustic</sub> is the acoustic pressure.

Figures 9 & 10 show noise frequency spectra of two different receivers, one situated upon the hub axis in front of the propeller, at a distance of 10 times of the propeller radius (receiver A Figure 2), and the other located on the propeller rotation plane, above the propeller, also at a distance of 10 times of the propeller radius (receiver B Figure 2). The advance velocity was equal to 1/6 m/s and the rotational speed was equal to 120 rpm. Figures 9 & 10 evidently reveals substantial compatibility of the findings of the present study with the numerical findings of the study by Seol et al [38]. However, in receiver B, from 100 Hz on, the difference of 25 % can be observed in the results. This difference may be due to different methods used in two studies, i.e., the present study made use of the CFD method, while Seol et al., used the panel method.

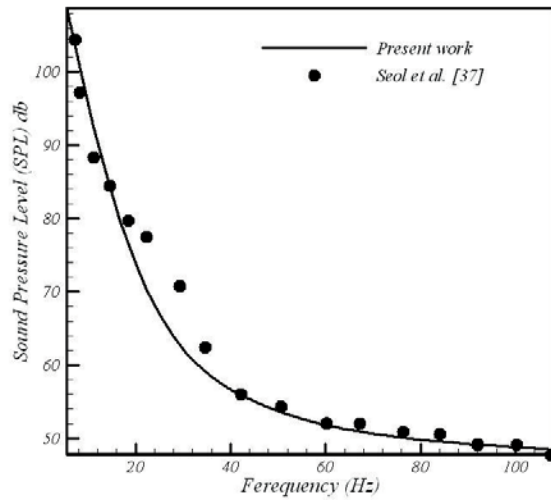


Fig. 9. Noise spectrum in receiver A

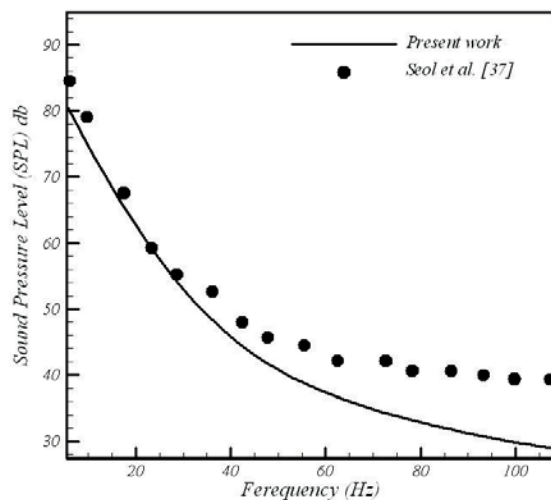


Fig. 9. Noise spectrum in receiver B

Time histories of the flow noise for different advance coefficients were studied as well. Figure 11 shows the time dependent values of the acoustic pressure, for two advance coefficients of 0.6 & 1, in the receiver B. The graph evidently indicates that the values of the acoustic pressure have reached the quasi-periodic state, thus approving the convergence of the solutions in the unsteady flow. The graph also reveals that increasing the advance coefficient (decreasing the rotational speed of the propeller), leads to the decrease of the pressure amplitude. The pressure amplitude for the case with  $J = 0.6$  is 3.5 times larger than that for  $J = 1.0$ .

Figure 12 shows the noise spectra for different advance coefficients in hydrophone B (Figure 2). For more clear presentation, the noise spectra for the optimal  $J$  and lower speeds are depicted in the left figure, while the high speed cases are presented on the right. What is prominent in this figure is that the level of noise intensity per advance coefficients reaches maximum for a given frequency. This frequency is referred to as BPF (Blade Passing Frequency) and is derived from the following equation:

$$BPF = N \times \frac{\omega}{2\pi} \quad 10$$

In the above equation  $N$  is the number of propeller blades and  $\omega$  is the angular velocity of the propeller, in radians per second. An anti-aliasing filter was used in these calculations.

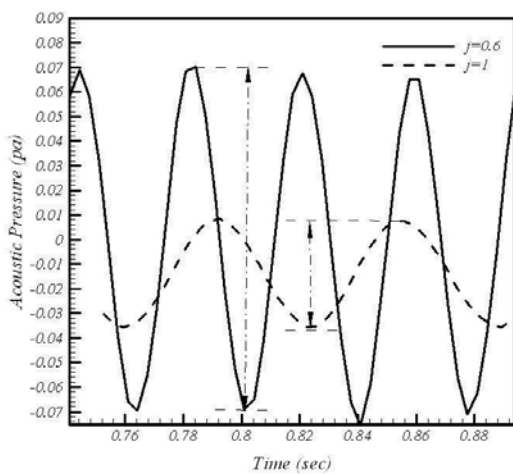


Fig.11. Time history of acoustic pressure wave for two advance coefficients

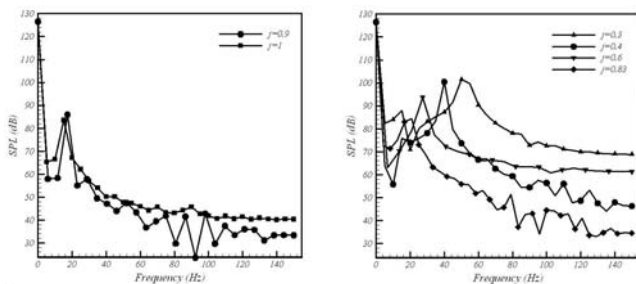


Fig. 12. Noise spectrum for different advance coefficients

## DIRECTIONAL DISTRIBUTION

In the previous Section all investigations were dedicated to two locations: A and B (Figure 2). In this section, the reported results refer to all directions around the propeller in order to understand better the directional behaviour of the flow noise. For this purpose an array of 100 microphones was arranged on a sphere. The propeller was located in the centre of the sphere with the microphones and the sphere radius was  $10R$ .

Figure 13 shows the 3D graph of the intensity level of the noise recorded by 100 receivers for the frequency equal to 2 Hz and the rotational speed equal to 120 rpm. It is clear from Figure 13 that the maximum of the acoustic pressure is detected in the horizontal plane and the minimum of SPL is around two poles of the sphere. Although the reported results have been obtained for one special case of 120 rpm and 2 Hz, they clarify the directional distribution of the propeller flow noise.

Figure 14 shows the directional distribution of noise intensity in an hour circle of the sphere containing the hydrophone array. In this figure, directional distributions for two advance coefficients of 0.3 & 0.4 are shown. According to the figure, lower advance coefficients (higher propeller speed) result in a higher level of noise in all directions. The directional distribution reveals that the highest levels of noise are upon the hub axis, while the lowest levels are on the plane perpendicular to the propeller axis. According to the report by Seol et al., the loading noise upon the hub axis and the thickness noise on the axis perpendicular to the hub axis (the rotating plane of the propeller) are the maximal ones. Thus, it is noteworthy that, due to drastic changes of the static pressure upon the levels of the propeller in conditions of high rotational speed and low advance coefficients, the noise mostly is of loading nature.

For high advance coefficients, the directional distribution process of the hydrodynamic noise is entirely reversed (Figure 15). It is observed that the lowest levels of noise intensity are located upon the propeller hub axis and the highest levels are placed on the axis perpendicular to the hub axis (the rotating plane of the propeller). This suggests that, in the conditions of high advance coefficients (low propeller speed), the hydrodynamic noise of the propeller is of monopole type (thickness noise), as the effect of the static pressure is lower than in the case of low rotations and most of the generated noise is caused by the periodic movement and rotation of the propeller, which produces the monopole noise.

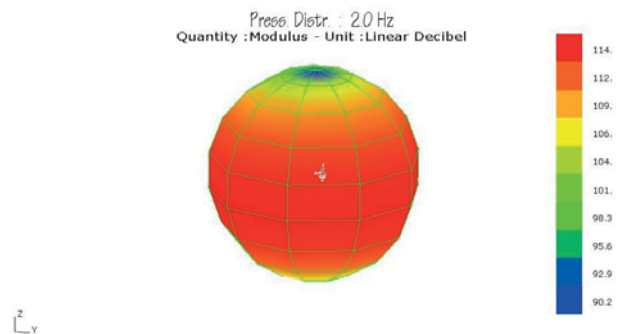


Fig. 13. SPL (2 Hz, 120 rpm) on the sphere around the propeller Noise spectrum for different advance coefficients

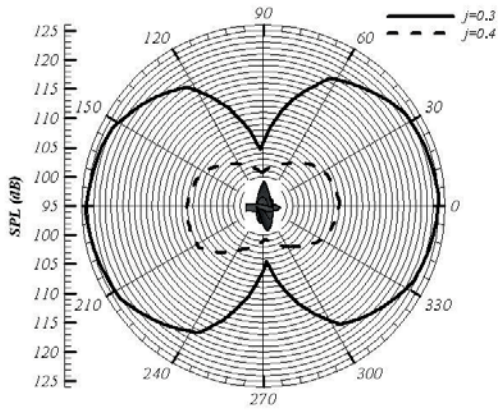


Fig. 14. Directional distribution of flow noise for low advance coefficients

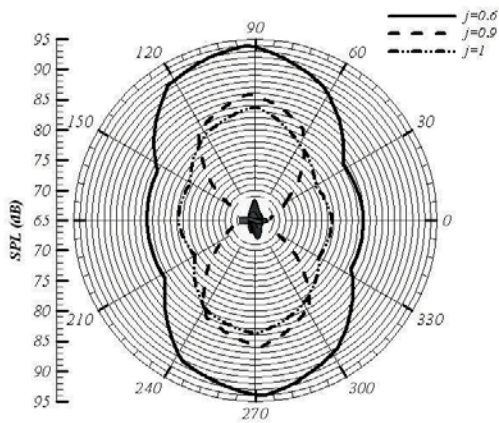


Fig. 15. Directional distribution of flow noise for high advance coefficients

### BROAD BAND NOISE OF THE PROPELLER

Another fruitful study in the area of flow noise is broadband noise investigation. In the broadband noise study regardless of the frequency, the total flow noise could be obtained. Figure 16 presents the decibel based broad band noise upon the propeller for different advance ratios. As is evident from the acoustic power distribution shown in Figure 16, the maximum sources of the generated noise are situated upon the leading edges, the blade-hub junction, and the hub tip. This is due to vortex shedding from the propeller and hub tip. We can notice that in the regions of drastic geometrical changes, a great amount of vorticity is generated (Figure 8) and subsequently large static pressure differences are observed. Thus, the maximal level of the dipole (loading) noise is produced. It is clear from the figure that as the advance ratio is increased (low speed cases), the level of noise is decreased. At  $J = 0.4$  the propeller hub is a source of noise while at  $J = 1.0$  the noise is only generated by the blades.

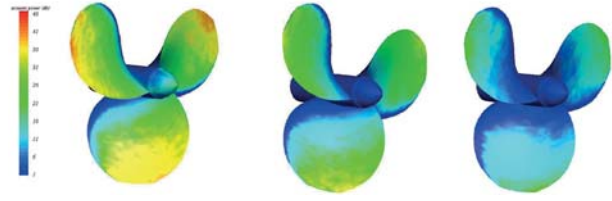


Fig. 16. Acoustic power distribution on propeller surface for  $J = 0.4$  (left),  $J = 0.6$  (middle) and  $J = 1.0$  (right)

### CONCLUSIONS

3D numerical simulation of the hydro-acoustic flow around a propeller has been performed and the following results have been concluded:

- With the aid of the LES model of turbulence, a fairly fine grid, and a sliding mesh, the hydrodynamic flow pattern can be captured and the fluctuating quantities can be derived for further use in acoustic models.
- The obtained hydrodynamic parameters have been compared against the experimental data for various advance coefficients. The observed level of agreement is satisfactory. The distributions of flow parameters such as velocity and vorticity are presented to understand better the flow.
- The tonal noise of the propeller was simulated using the FWH model and the results have been compared with other available numerical results.
- The effect of advance ratio has been studied and the advance ratio has been found to be a key parameter in noise propagation. Investigating the hydro-acoustic findings of the flow around the propeller has lead to the conclusion that decreasing the advance coefficients (increasing the propeller speed) increases the acoustic pressure range of the noise recorded in the receiver and decreases the period of the acoustic wave pressure.
- Looking into the frequency based SPL graphs for different advance coefficients indicates that each graph reaches the maximum at a given frequency. This frequency is referred to as BPF (Blade Passing Frequency).
- The directional distribution of the noise power level around the propeller should also be taken into consideration. In low advance coefficients (high speeds), the level of the noise around the hub axis of the propeller increases to the maximum, and drops to the minimum upon the axis perpendicular to the propeller axis within the rotating plane of the propeller. This is an indication of dipole (loading) noise maximisation in the examined cases. However, in high advance coefficients (low speed), the noise power within the rotating plane of the propeller increases to the maximum, and drops to the minimum upon the axis of the propeller hub. This is

an indication of the monopole (thickness) noise capability in these advance coefficients.

- A broadband study has been carried out on the propeller, and the regions with highest noise potential have been detected, see the 3D graph. It is noticeable that the flow pattern, especially the vorticity distribution is associated with the broadband noise.

- Examination of the broad band noise upon the propeller surface and the resultant graph of the acoustic power plainly demonstrate that regions in the vicinity of propeller hub and tip play a crucial role in the generation of vortices in the flow around the propeller, which are precisely the source of major part of the noise generated around the propeller. In these regions, due to drastic geometrical changes, high static pressure differences are observed.

## BIBLIOGRAPHY

1. Amini H., Steen S.: Experimental and Theoretical Analysis of Propeller Shaft Loads in Oblique Inflow, *Journal of Ship Research*, Vol. 55 No 4, pp. 268-288(21), 2011.
2. Juan J.A., Kazuo N., Claudio M.S., Julio C.A.: Experimental Investigation of the Hydrodynamic Coefficients of a Remotely Operated Vehicle Using a Planar Motion Mechanism, *Journal Offshore Mech. Arct. Eng.*, Vol. 134, Issue 2, 021601 (6 pages), 2012.
3. Ning L., Sande W., Tao G., Xiyong L., Ziyang Y.: Experimental research on the double-peak characteristic of underwater radiated noise in the near field on top of a submarine, *Journal of Marine Science and Application*, Vol. 10 No 2, 233-239, DOI: 10.1007/s11804-011-1049-2
4. Zhi-hua L, Ying X, Zhan-zhi W, Song W, Cheng x.: Numerical Simulation and Experimental Study of the new Method of Horseshoe Vortex Control, *Journal of Hydrodynamics*, Ser. B, Vol. 22, Issue 4, pp. 572–581, 2010.
5. Gaggero S., Villa D., Brizzolara S.: RANS and PANEL method for unsteady flow propeller analysis, *Journal of Hydrodynamics*, Vol. 22, Issue 5, Supplement 1, pp. 564–569, 2010.
6. Fang-wen H., Shi-tang D.: Numerical Analysis for Circulation Distribution of Propeller Blade, *Journal of Hydrodynamics*, Vol. 22, Issue 4, pp. 488–493, 2010.
7. Ghasseni H., Ghadimi P.: Numerical analysis of the high skew propeller of an underwater vehicle, *Journal of Marine Science and Application* Vol. 10 No. 3, 289-299, DOI: 10.1007/s11804-011-1071-4
8. Baltazar J., Falcão de Campos J.A.C.: An iteratively coupled solution of the cavitating flow on marine propellers using BEM, *Journal of Hydrodynamics*, Ser. B, Vol. 22, Issue 5, Supplement 1, pp. 838–843, 2010.
9. G. Kuiper.: New developments and propeller design, *Journal of Hydrodynamics*, Vol. 22, Issue 5, Supplement 1, pp. 7–16, 2010.
10. Bong-Jun C., Seokcheon G.: Study on a procedure for propulsive performance prediction for CRP-POD systems, *Journal of Marine Science and Technology*, Vol. 16 No. 1, pp.1-7, DOI: 10.1007/s00773-010-0108-8
11. Fang-wen H., Shi-tang D.: Numerical simulation of the structure of propeller's tip vortex and wake, *Journal of Hydrodynamics*, Vol. 22, Issue 5, Supplement 1, pp. 457–461, 2010.
12. Chao W., Sheng H., Xin C., Miao H.: Applying periodic boundary conditions to predict open water propeller performance, *Journal of Marine Science and Application*, Vol. 9 No. 3, 262-267, DOI: 10.1007/s11804-010-1005-6
13. Chun-yu G., Wen-ting H., Sheng H.: Using RANS to simulate the interaction and overall performance of propellers and rudders with thrust fins, *Journal of Marine Science and Application*, Vol. 9 No. 3, 323-327, DOI: 10.1007/s11804-010-1015-4
14. Wilson P.A., Molland, A.F., The development of hydrodynamics: 1860–2010. In, *The William Froude Conference: Advances in Theoretical and Applied Hydrodynamics, Past and Future*, Portsmouth, UK, 24 – 25, 2010.
15. Liu Z., Xiong Y., Tu C.: Numerical simulation and control of horseshoe vortex around an appendage–body junction, *Journal of Fluids and Structures*, Vol. 27, Issue 1, pp 23–42, 2011.
16. Alin N., Bensow R.E., Fureby C.; Huuva T., Svennberg U.: Current Capabilities of DES and LES for Submarines at Straight Course, *Journal of Ship Research*, Vol. 54, Number 3, pp. 184-196(13), 2010.
17. Jong-Yeon H., Kyung-Soo Y., Klaus B.: Direct Numerical Simulation of Turbulent Flow Around a Rotating Circular Cylinder, *J. Fluids Eng.*, Vol. 129, Issue 1, 40-47, doi:10.1115/1.2375133, 2007.
18. Wilcox D. C., *Turbulence Modeling for CFD*, 3rd edition, DCW Industries, Canada, 2006.
19. Yu-cun P., Huai-xin Z.: Numerical hydro-acoustic prediction of marine propeller noise, *Journal of Shanghai Jiaotong University (Science)*, Vol. 15 No. 6, 707-712, DOI: 10.1007/s12204-010-1073-4
20. Rickard E., B Bark., G Bark.: Implicit LES Predictions of the Cavitating Flow on a Propeller, *Journal Fluids Eng.*, -- Vol. 132, Issue 4, 041302 (10 pages) doi:10.1115/1.4001342, 2010.
21. Nai-xian L., Rickard E.B., Bark G.: LES of unsteady cavitation on the delft twisted foil, *Journal of Hydrodynamics*, Ser. B, Vol. 22, Issue 5, Supplement 1, pp. 784–791, 2010.
22. C Fureby.: ILES and LES of Complex Engineering Turbulent Flows, *Journal Fluids Eng.*, Vol. 129, Issue 12, 1514 (10 pages) doi:10.1115/1.2801370, 2007.
23. Oberai A., Ronaldkin F., Hughes T.: Computational procedures for determining structural-acoustic response due to hydrodynamic sources, *Comp. Methods Appl. Mech. Engineering* Vol. 190, pp. 345–361, 2000 .
24. Oberai A., Roknaldin F., Hughes T.J.R.: Computation of Trailing-Edge Noise due to Turbulent Flow over an Airfoil, *AIAA Aeroacoustics Journal* Vol. 40, pp.2206–2216, 2002.

25. Caro S., Ploumhans P., Gallez X.: A new formulation based on Lighthill's Analogy applied to an idealized Automotive HVAC Blower using AcuSolve and Actran/LA, Proceedings of 11th AIAA/CEAS Aeroacoustics Conference, No. 3015, Monterey, USA, 2005.
26. Damiano C.: Aeroacoustics research in Europe: The CEAS-ASC report on 2009 highlights", Journal of Sound and Vibration, Vol. 329, Issue 22, 25, pp. 4810–4828, 2010.
27. Yu-cun P., Huai-xin Z.: Numerical hydro-acoustic prediction of marine propeller noise, Journal of Shanghai Jiaotong University (Science), Vol. 15 No. 6, 707-712, DOI: 10.1007/s12204-010-1073-4
28. Ruchonnet N., Alligné S., Nicolet C., Avellan F.: Cavitation influence on hydroacoustic resonance in pipe, Journal of Fluids and Structures, 10.001, 2011.
29. Young-Zehr K., Jui-Hsiang K.: Underwater acoustic field and pressure fluctuation on ship hull due to unsteady propeller sheet cavitation, Journal of Marine Science and Technology, Vol. 16 No. 3, pp. 241-253, DOI: 10.1007/s00773-011-0131-4, 2011
30. Bogey C., Bailly C., Juv' e D., Computation of flow noise using source terms in linearized Euler's equations, AIAA Journal Vol. 40 No. 2, pp. 235–243, 2002.
31. Utzmann J., Schwartzkopff T., Dumbser M., Munz C.D.: Heterogeneous Domain Decomposition for CAA, Proceedings of 11th AIAA/CEAS Aeroacoustics Conference, Monterey, USA, 2005.
32. Zhao Y., J. Morris P., The Prediction of Fan Exhaust Noise Propagation, 11th AIAA Aeroacoustics Conference, No. 2005-2815, Monterey, USA, 2005.
33. Ewert R., Schröder W., Acoustic Perturbation Equations based on Flow decomposition via Source Filtering, Journal of Computational Physics Vol. 188, pp. 365–398, 2003.
34. Seo J., Moon Y., Linearized perturbed compressible equations for low Mach number aeroacoustics, Journal of Computational Physics Vol. 218 No. 2, pp 702–719, 2006.
35. Ffowcs-Williams J. E., Hawkings D.L.: Sound Generation by Turbulence and Surfaces in Arbitrary Motion, Proc. Roy. Soc. London, A264:321-342, 1969.
36. Proudman I.: The Generation of Noise by Isotropic Turbulence, Proc. Roy. Soc., A214:119, 1952.
37. Y. Pan, H. Zhang, „Numerical Hydro-Acoustic Prediction of Marine Propeller Noise", Journal of Shanghai Jiaotong Univ 15(6), pp. 707-712, 2010.
38. Seol H., Such J-C., Lee S., Development Of Hybrid Method for Prediction of Underwater Propeller Noise, Journal of Sound and Vibration.Vol..288, pp. 345-360, 2005.

## CONTACT WITH THE AUTORS

S. Kheradmand  
A. Rahrovi  
B. Mousavi

Department of Mechanical and Aerospace Engineering  
Malek-Ashtar University of Technology  
Shahin-shahr  
P.O. Box 83145/115  
Isfahan  
Iran

kheradmand@mut-es.ac.ir

# Computational simulation of motion of a rescue module during its launching from ship at rough sea

Czesław Dymarski, Prof.  
 Paweł Dymarski, Ph.D.  
 Gdańsk University of Technology, Poland

## ABSTRACT

*This paper is a continuation of the work titled : “A computational model for simulation of motion of rescue module during its launching from stern ramp of a ship at rough sea”. It presents results of computer simulations of motion of a rescue module with embarked persons during its launching on rollers along stern ramp of a ship at rough sea. The simulations were conducted for a selected ship fitted with a launching ramp , for a few selected scenarios of sea conditions. It was assumed that during this operation the ship drifts across direction of wave propagation.*

**Keywords:** lifeboat; rescue boat launch; innovation; launch ramp aft; computational model for simulation lifeboat; rescue boat launch; innovation; launch ramp aft; computational model for simulation

## INTRODUCTION

This paper is a continuation of the work titled : “A computational model for simulation of motion of rescue module during its launching from stern ramp of a ship at rough sea” [1]. A computer software based on the model was used for calculation of dynamic runs of position of contours of the ramp and rescue module moving along it as well as motion parameters of centre of gravity of the module during its launching from a ship at rough sea. This work was conducted within the frame of the European project SAFECRAFTS (Safe Abandoning of Ships - improvement of current Life Saving Appliances Systems), task: Establish escape craft dynamics, craft detached - novel systems.

## DATA FOR COMPUTATIONS

The calculations were conducted for a ship of the length  $L = 265$  m, breadth  $B = 32$  m and draught  $T = 7,8$  m, which drifts across direction of wave propagation. Fig. 1 shows , in a simplified way, contour of a stern ramp fitted with a floating pontoon, and contour of a rescue module with water surface marked on it. The elevation of the ramp fixing axle over water level ,  $H_{RF}$ , and the ramp slope angle  $\alpha_R$  are also shown there.

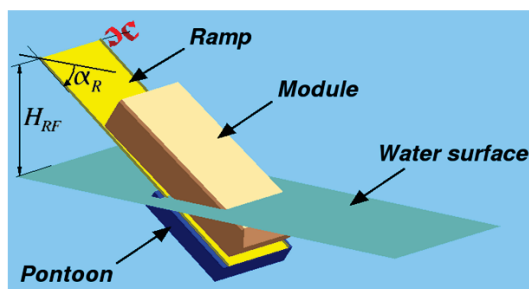


Fig. 1. The system consisted of a ramp, module, pontoon and water

## Pontoon:

Length	$L$	m	6.70
Breadth	$B$	m	6.50
Depth	$H$	m	1.20
Total volume	$V$	$m^3$	52.26
Mass	$M_P$	kg	8000
Moment of inertia around $x_0$ -axis	$I_{x_0}$	kg	29000
Moment of inertia around $y_0$ -axis	$I_{y_0}$	kg	31000
Moment of inertia around $z_0$ -axis	$I_{z_0}$	kg	58000

It was assumed that the pontoon centre of mass lies in its centre of geometry.

Moments of inertia  $I_{xx0}$ ,  $I_{yy0}$  and  $I_{zz0}$  were calculated with the use of the following formulas:

$$I_{xx0} = \frac{1}{12} M_P (B^2 + H^2) \quad (1)$$

$$I_{yy0} = \frac{1}{12} M_P (L^2 + H^2) \quad (2)$$

$$I_{zz0} = \frac{1}{12} M_P (L^2 + B^2) \quad (3)$$

## Ramp (without pontoon):

Length	$L$	m	18.30
Breadth	$B$	m	5.80
Mass	$M_R$	kg	22000
Moment of inertia around $x_0$ -axis	$I_{x_0}$	kg	62000
Moment of inertia around $y_0$ -axis	$I_{y_0}$	kg	614000
Moment of inertia around $z_0$ -axis	$I_{z_0}$	kg	676000
Maximum slope angle (in relation to horizontal position)		deg	36

Module:

Length	$L$	m	6.30
Breadth	$B$	m	5.65
Depth	$H$	m	2.50
Draught	$T$	m	0.60
Mass	$M_M$	kg	43626
Longitudinal coordinate of mass centre	$x_{G0}$	m	6.30
Vertical coordinate of mass centre	$z_{G0}$	m	1.09
Moment of inertia around $x_0$ -axis	$I_{xx0}$	kg	125000
Moment of inertia around $y_0$ -axis	$I_{yy0}$	kg	334000
Moment of inertia around $z_0$ -axis	$I_{zz0}$	kg	334000

where  $I_{xx0}$ ,  $I_{yy0}$ ,  $I_{zz0}$  was calculated by using the following formulas [7]:

$$I_{xx0} = (0.3B)^2 M_M \quad (4)$$

$$I_{yy0} = I_{zz0} = (0.225L)^2 M_M \quad (5)$$

## RESULTS OF COMPUTATIONS

### Scenario No. 1

The first set of calculation results graphically presented in Fig. 2, 3a and 3b, concerns favourable, but characteristic conditions: calm sea, ship a little trimmed by head so as to get maximum value of slope angle of the ramp. It means that the ramp rests on ship hull structure and the rescue module, when moving along the ramp, would not cause any change in its slope angle.

Elevation of ramp fixing axle	$H_{RF}$	m	9.0
Ramp slope angle at $t=0$	$\alpha_R$	deg	36.0
Wave height	$H_W$	m	0.0
Wave period	$T_W$	s	-
Wave phase shift	$t_{0W}$	s	-

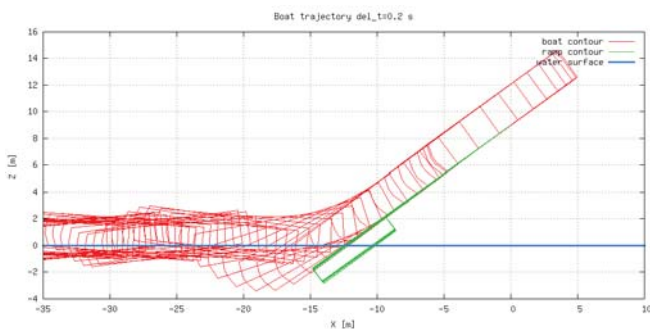


Fig. 2. Module and ramp contours in function of time,

A uniformly accelerated motion of the module along an emerging part of the practically motionless ramp may be clearly observed in the figure. The ramp slope angle, only a little increasing during the rolling down of the module, results from the fact that no flexibility of the ramp supports has been taken into account in the computational model. Maximum value of immersion of the fore part of the module is not very large in this case as it amounts to about 3,5 m only, and lasts for a short time. After that, motion of the module stabilizes very fast.

More information on the motion of the rescue module may be achieved from examining Fig. 3a and 3b which present runs of changes in acceleration and velocity of the module centre of gravity. Three characteristic phases of the motion may be distinguished, namely:

- 1st phase: the free rolling down of the module along the almost motionless ramp, during the period from the beginning of the motion up to the instance when the face side of the module reaches contact with water. Almost constant values of acceleration and angular velocity as well as constant rate of horizontal and vertical components of velocity of the module are characteristic for this phase of the motion.

- 2nd phase: the going into water of the module being still in contact with the ramp. This phase begins with a sudden change in sign of values of linear acceleration and velocity, at insignificant changes in values of angular acceleration and velocity, as a result of a high resistance to motion of the module in water, leading to its full braking at last.

The phase is ended with a noticeable disturbance of runs, especially of accelerations in the instance of loss of contact between the module and ramp.

- 3rd phase: The free going of the module off the ramp. In this phase changes in values of all motion parameters are distinctly lower and lower, that means the motion stabilizes as a result of damping action of water.

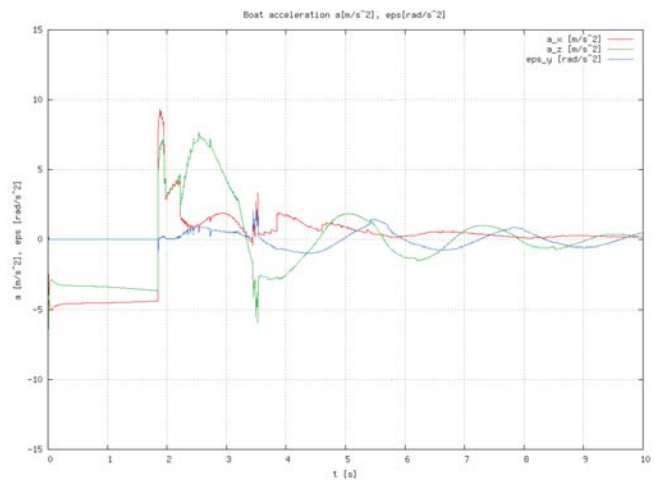


Fig. 3a. Module acceleration components: horizontal  $\alpha_x$ , vertical  $\alpha_z$  and angular  $\epsilon_z$

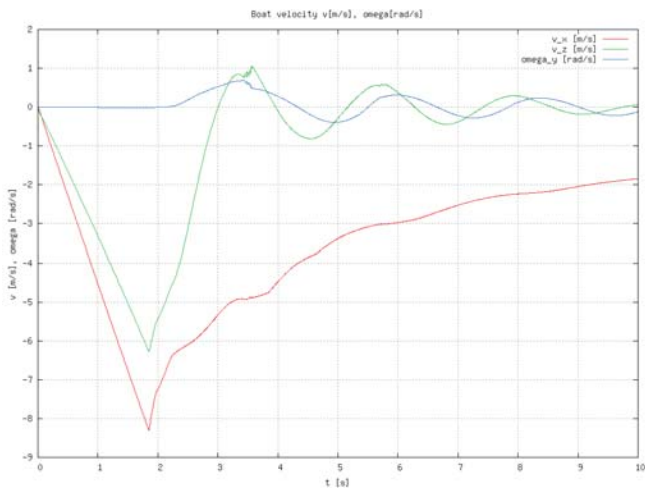


Fig. 3b. Module velocity components : horizontal  $v_x$ , vertical  $v_z$  and angular  $\omega_y$

Scenario No. 2

This scenario concerns the conditions which are close to normal, i.e. : rough sea, ship without trim, the elevation  $H_{RF}$  - lower than in the previous case; owing to this, the slope angle of the ramp is smaller than maximum one, that makes its changing during launching the module, possible. The conditions allow to better assess influence of application of the ramp - pontoon system and wave action on rescue module dynamics.

Ramp fixing axle elevation	$H_{RF}$	m	7.0
Ramp slope angle at t=0	$\alpha_R$	deg	26.0
Wave height	$H_W$	m	5.0
Wave period	$T_W$	s	12.0
Wave phase shift	$t_{0W}$	s	0.0

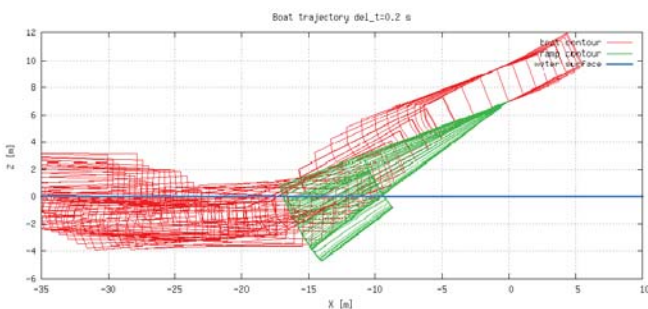


Fig. 4. Module and ramp contours in function of time,  $\Delta t = 0.2$  s

As results from Fig. 4 and 5 , the runs of contours of the ramp and module and values of motion parameters of module gravity centre during launching show much greater dynamic features in comparison to the first scenario. The maximum draught of the ramp reached almost 5 m. Similarly, the maximum draught of the module increased up to 4 m, and amplitude of its vertical displacements was also greater. Values of acceleration and velocity of motion of the module are changeable in all launching phases, though the acceleration and velocity damping process is close to that calculated for the previous case. The characteristic change in sign of the vertical velocity component in the final phase of motion of the module results from its heave on wave crest.

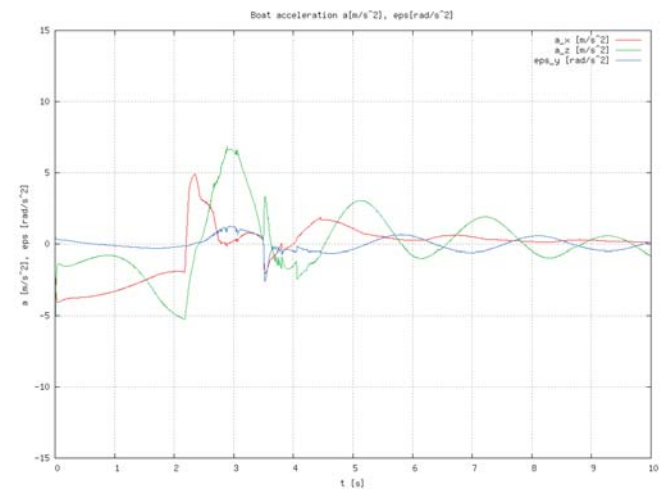


Fig. 5a. Module acceleration components: horizontal  $\alpha_x$ , vertical  $\alpha_z$  and angular  $\epsilon_z$

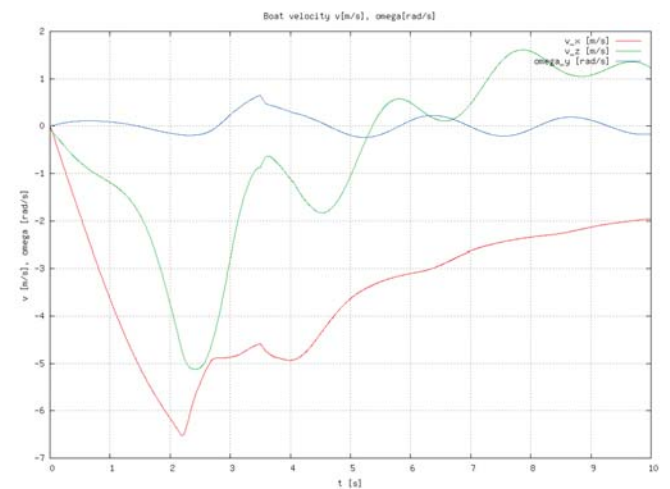


Fig. 5b. Module velocity components : horizontal  $v_x$ , vertical  $v_z$  and angular  $\omega_y$

Scenario No. 3

The research results presented below, were calculated for similar sea conditions as used in the previous case, but for the start of launching in the instance when the wave undergoes shift by a half of its length, in contrast to the previous case. It enables to assess influence of this parameter on module motion dynamics.

Ramp fixing axle elevation	$H_{RF}$	m	7.0
Ramp slope angle at t=0	$\alpha_R$	deg	26.0
Wave height	$H_W$	m	5.0
Wave period	$T_W$	s	12.0
Wave phase shift	$t_{0W}$	s	6.0

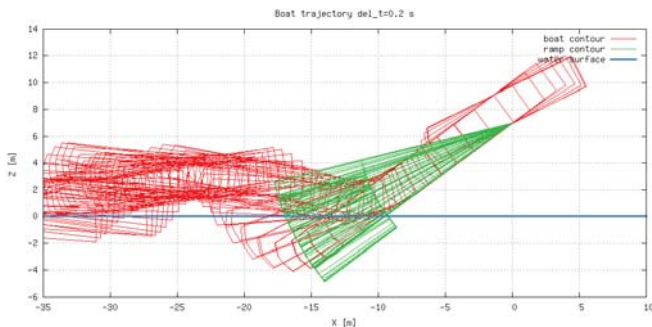


Fig. 6. Module and ramp contours in function of time,  $\Delta t = 0.2$  s

The shift of starting point of launching in relation to wave propagation phase has a significant influence on motion dynamics of the rescue module, which may be clearly observed in Fig. 7a, where for the time  $t \sim 9$  s, a violent disturbance in runs of the curves of all three acceleration components, is visible. The disturbance results from the instantaneous contact between the ramp (with the module on it) and its support when the ramp reaches its maximum slope. The event, though noticeable, did not greatly influence the runs of velocity of the module. It's worth mentioning, that the run of contours of the going-off module is distinctly convex (Fig. 6). It results from that wave crest crosses module motion trajectory just in this moment.

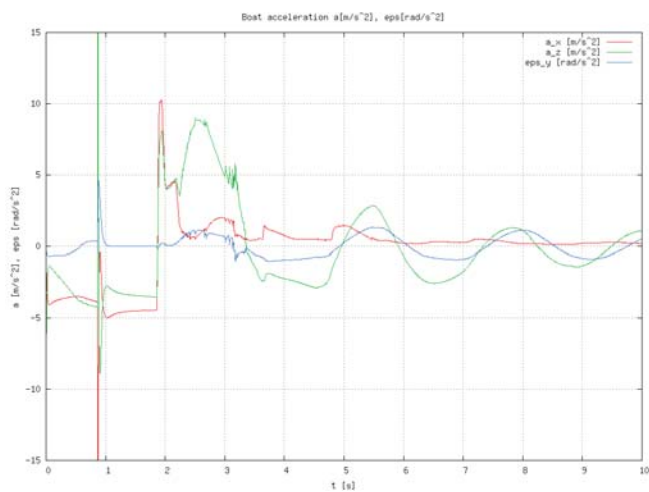


Fig. 7a. Module acceleration components: horizontal  $\alpha_x$ , vertical  $\alpha_z$  and angular  $\varepsilon_z$

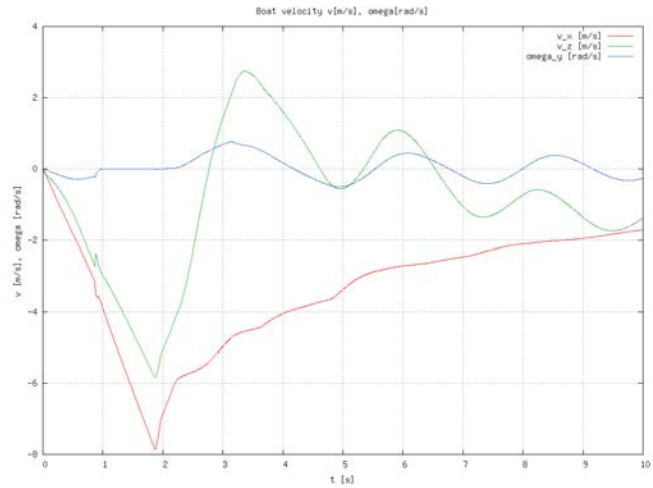


Fig. 7b. Module velocity components: horizontal  $v_x$ , vertical  $v_z$  and angular  $\omega_y$

#### Scenario No. 4

In this case the calculations were conducted for calm sea and the same initial values of ramp position parameters, but for the ship alist. Results of the calculations have been intended to show influence of ship's heel on motion of the launching rescue module.

Ramp fixing axle elevation	$H_{RF}$	m	7.0
Ramp slope angle at t=0		deg	26.0
Ship's heel angle	$\alpha_R$	deg	15.0
Wave height	$H_W$	m	0.0
Wave period	$T_W$	s	-
Wave phase shift	$t_{0W}$	s	-

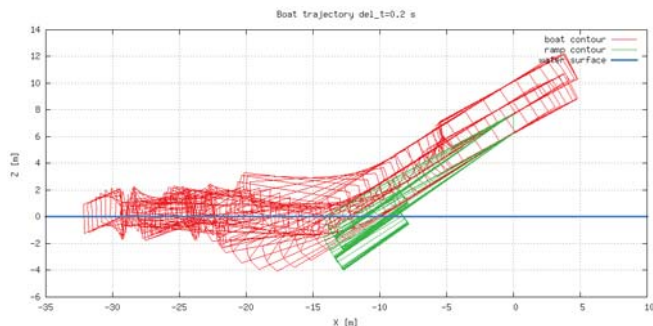


Fig. 8. Module and ramp contours in function of time,  $\Delta t = 0.2$  s

As results from Fig. 8, the runs of contours of the ramp and module in successive time intervals show that ship's heel greatly affects motion of the module, especially after its launching. It may be also observed that the distance covered by the module in the considered time interval is much shorter. It means that the motion of the module slows down due to increased module resistance to motion. The runs of accelerations and velocities

shown in Fig. 9 confirm the conclusion. The instantaneous disturbances observed in acceleration runs reveal the instances when side surfaces of the module and the rollers fixed in the heeled ramp over which the module rolls down into, enter into contact to each other. It seems that this unit of the escape craft (launching system) and its mathematical model may be so elaborated as to obtain a more stable mode in which lateral loads can be transferred by the unit. As results from analysis of the velocity runs, duration time of moving the module along the ramp is longer, therefore the motion is slowed down.

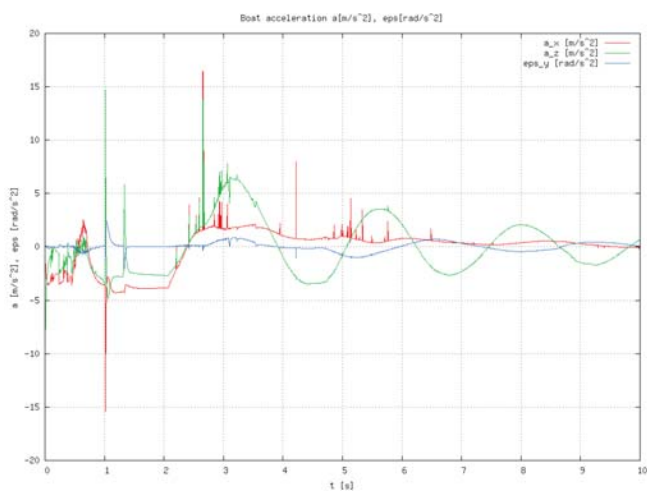


Fig. 9a. Module acceleration components: horizontal  $\alpha_x$ , vertical  $\alpha_z$  and angular  $\epsilon_z$

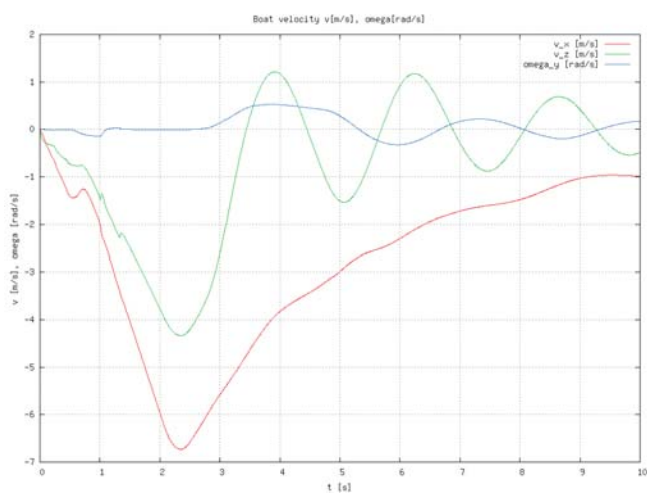
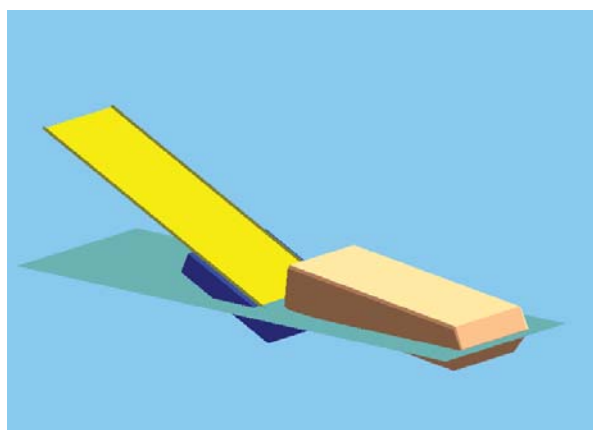
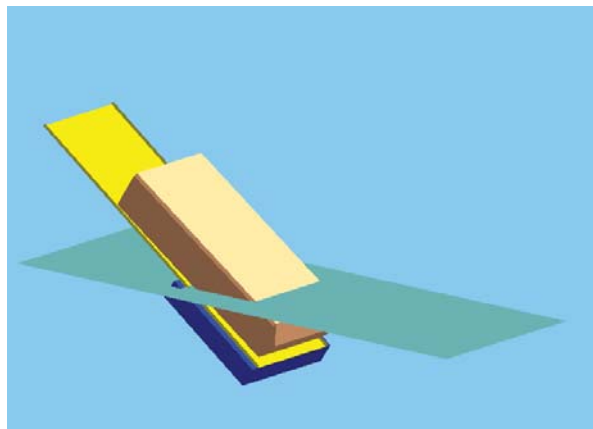
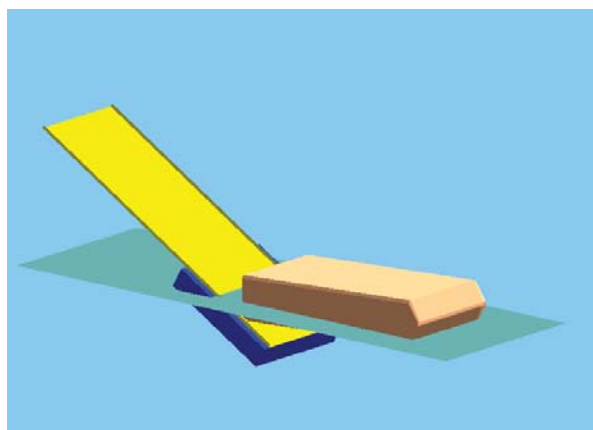
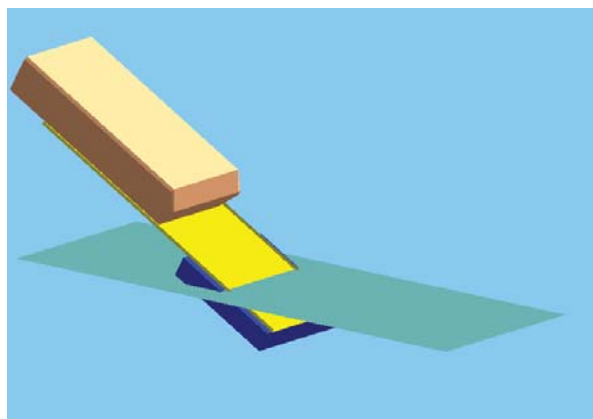


Fig. 9b. Module velocity components : horizontal  $v_x$ , vertical  $v_z$  and angular  $\omega_y$

### ANIMATION OF MODULE LAUNCHING

Fig. 10 and Fig. 11 show snapshots from animation of results of the computations conducted for scenario No. 1 and 6.



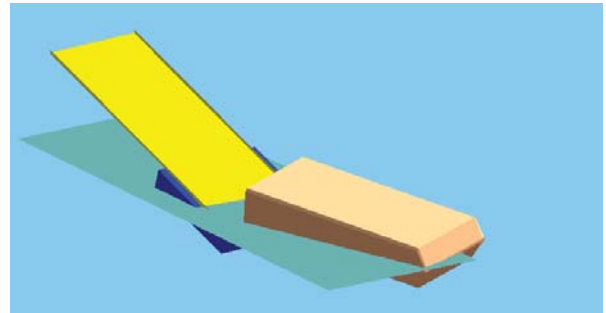
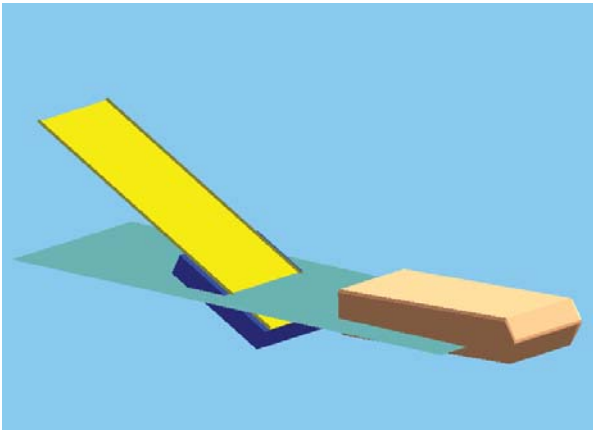
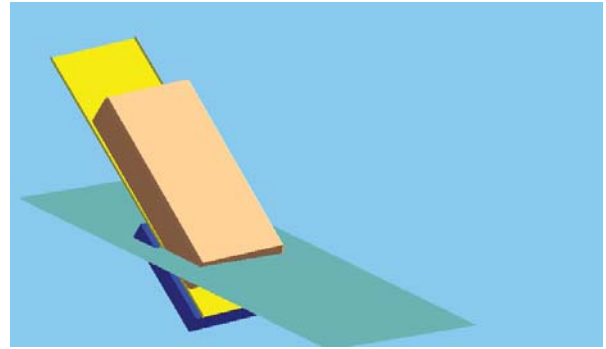
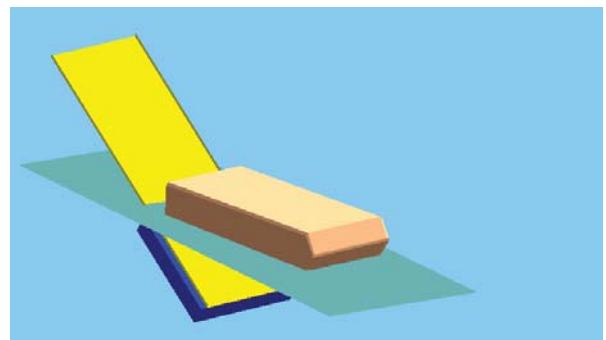
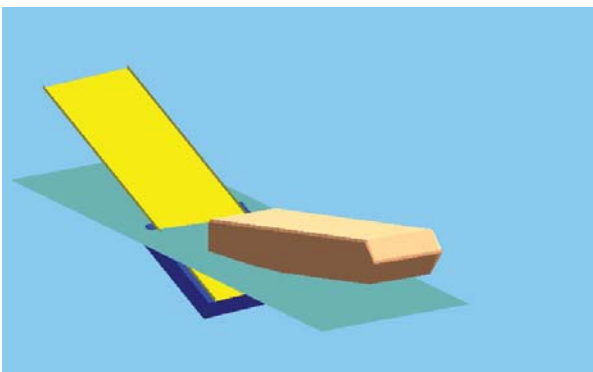
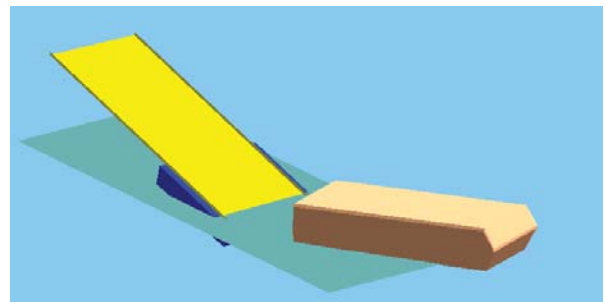
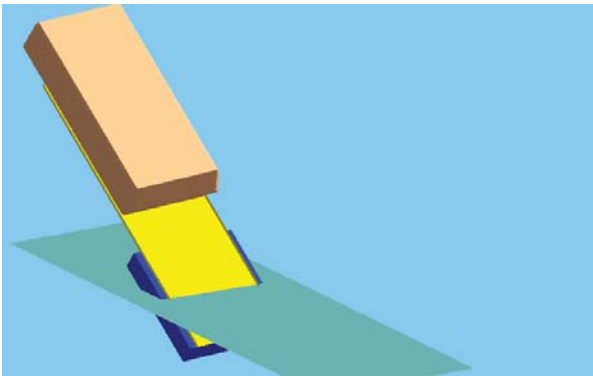


Fig. 10. Subsequent snapshots from simulation of rescue module launching into calm water,  $H_{RF} = 7$  m,  $a_R = 26$



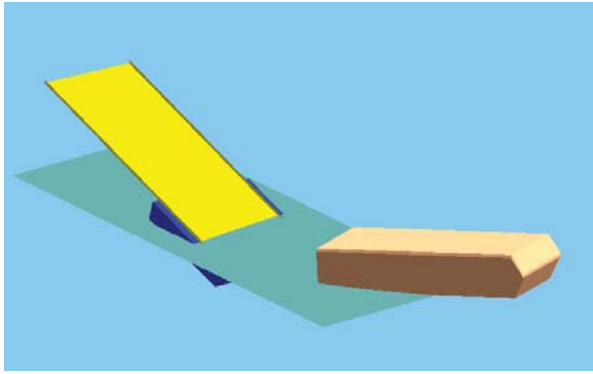


Fig. 11. Subsequent snapshots from simulation of rescue module launching into calm water,  $H_{RP} = 7$  m,  $a_R = 26^\circ$ , ship heel angle  $\theta = 15^\circ$

## CONCLUSIONS

The above presented results of computer simulations of performance of a rescue module during its launching dealt only with four selected scenarios, in view of a limited volume of this paper. The scenarios are relatively simple, but characteristic, and focused on correctness assessment of the developed method and computational software. However, it should be stressed that analysis of the presented runs enables to assess at least qualitatively the developed model. All the graphically presented results of calculations have been found in conformity with expectations and personal experience of these authors as far as the scientific field in question is concerned. Further research in this field is under way with hope of bringing results of simulations of escape craft motion in more complex and heavy weather conditions, with taking into account also ship motion in waves.

## BIBLIOGRAPHY

1. Dymarski P., Dymarski Cz.: „A numerical model to simulate the motion of a lifesaving module during its launching from the ship's stern ramp”. Polish Maritime Research. Vol. 21, No 2 (82), 2014.

## CONTACT WITH THE AUTOR

Czesław Dymarski, Prof.  
Paweł Dymarski, Ph. D.

Gdańsk University of Technology  
Faculty of Ocean Engineering  
and Ship Technology  
11/12 G. Narutowicza Street  
80-233 Gdańsk  
Poland

Telephone: +48 58 347 1608  
+48 58 347 2397

Email: cpdymars@pg.gda.pl  
pawdymar@pg.gda.pl

# The influence of wind, wave and loading condition on total resistance and speed of the vessel

Tadeusz Szelangiewicz<sup>1</sup>, Prof.

Bernard Wiśniewski<sup>2</sup>, Prof.

Katarzyna Żelazny<sup>3</sup>, Ph. D.

<sup>1,2</sup> Maritime University of Szczecin

<sup>3</sup> West Pomeranian University of Technology

## ABSTRACT

*Optimising the ship route is one of the most important tasks related to the operation of the vessel, its safety, and economic aspects of transport. Nevertheless, from a mathematical point of view, this problem has not been solved yet sufficiently precisely due to very high complexity of the model to be used to describe the motion of the ship along the shipping line, and time- and space-dependent average values of statistical weather parameters recorded during ship sailing. That is why various approximate methods are used, which, among other procedures, utilize ship speed characteristics, having the form of very simple relations between basic dimensions of the ship and the expected speed decrease at the assumed weather parameters. The paper presents a new method of calculating the speed decrease depending on technical and operating parameters of a given vessel. A computer code prepared based on this method is used for research on forecasting ship speed in real weather conditions.*

**Keywords:** optimization of route navigation of the vessel, vessel's speed calculation

## INTRODUCTION – REMARKS ON SHIP ROUTE OPTIMIZATION

Selecting the optimal route is one of most important tasks concerning the operation of a transport vessel. When choosing the optimal route, one or more criteria are taken into account including:

- minimum travel time,
- minimum fuel consumption for a given travel time,
- safety of the ship and cargo,
- passenger comfort during the trip.

The last criterion is generally used for cruise ships and does not apply to transport vessels.

The minimum travel time can be achieved by minimising the length of the route and/or maximising the speed of the ship.

The minimum fuel consumption can be achieved by minimising the length of the route and/or maintaining optimal operating parameters of the drive engine. In still water conditions (no wind and wave) these parameters define a point of engine operation which corresponds to constant speed of the vessel [9]. When the vessel floats on waves, searching for minimum fuel consumption (and the resultant optimum speed in given weather condition) may be associated with certain course changes resulting in a change of length of the route and extension of time [9]. The safety of the ship and cargo is associated with negative effects of the wind and waves acting on the ship (rocking, acceleration, slamming, flooding of the deck, propeller emergence). Reducing the impact of these phenomena

during the operation of the vessel is associated with speed reduction and/or course changes. Both of these manoeuvres will result in elongation of the route and time of shipping, which leads to the increased fuel consumption. Selecting the optimal shipping route is very complex and despite the use of different methods [8], there is no certainty that the chosen route will be optimal, due to the fact that statistical average wind and wave parameters are random variables in both time and space. This means that during the trip, the statistical average weather parameters can change. Therefore the shipping route selected as optimal for the weather parameters observed at the beginning of the trip does not have to turn out optimal when the ship reaches the destination port, because weather parameters can change during the trip.

## BASIC APPROACH TO THE ROUTE SELECTION

Finding the optimal route for ship navigation can be reduced to two steps:

1. developing a mathematical model to describe the movement of the vessel in the marine environment,
2. determining the optimal route for the vessel.

Determination of the optimal route consists in the application of an algorithm that makes use of a mathematical model of ship motion and one or more criteria for selecting the optimal route. This issue was discussed in a number of publications [8], [9], [10].

Mathematical description of ship motion can have a form of differential equations of motion, containing full ship dynamics (forces of inertia and damping), the model of the propulsion and steering system (propeller, drive engine, and rudder fin), and the model of excitation forces (wind, wave, surface sea currents). Depending on the adopted model of the excitation forces, wave motion for instance, the model of the ship can be more or less complicated, which affects the adopted solving method and the use of the model in the algorithm for searching the optimal navigation route. Difficulties in the use of a complex but, on the other hand, accurate model of ship motion for optimizing shipping routes, were a motivation for widespread use of vessel speed characteristics. These characteristics have the form of relatively simple relations of the speed of the vessel vs. basic parameters of the vessel and average statistical parameters of waves, wind, and surface currents. These relations are presented as nomograms or simple formulas prepared on the basis of measurements or calculations performed for many ships. In these relations, geometric parameters of the vessel are frequently replaced by one or two numerical coefficients which characterize the vessel. These speed characteristics make the basis for calculating vessel's speed in assumed statistical average weather conditions, or more precisely: the speed decrease resulting from additional resistance in relation to the speed in still water (no wind and waves).

On the wave, the above speed decrease is accompanied by other dangerous phenomena (rolling, acceleration, slamming, etc.), and when they are too intense they may endanger the safety of the vessel and cargo. To reduce these risks, we can deliberately reduce the speed of the vessel (the storm fall speed) and/or change the vessel course. These phenomena are also presented in the form of simple universal nomograms. Due to their simplicity, the speed characteristics formulas are not very accurate. The article presents a more accurate method of calculating the instantaneous speed of the vessel in given weather conditions.

### INSTANTANEOUS SPEED OF THE VESSEL IN GIVEN WEATHER CONDITIONS

During ship sailing on rough water, its standard still water resistance changes due to the action of other forces generated by wind, waves and surface sea currents. Beside contributing to drag increase, these forces give rise to the creation of the lateral force and the torque which rotates the vessel about the vertical axis. The lateral force provokes the drift of the ship, while the torque changes the vessel course. For the vessel course to be kept constant in a given water region at the presence of the active external torque, the passive rudder fin is to be inclined.

Assuming that local changes of vessel speed, resulting from swaying on waves for instance, are negligibly small, the instantaneous operating speed of the ship is reached when its total drag  $R_C$  is balanced by the pressure thrust  $T_S$  of the propeller:

$$R_C(P_P, P_G) = T_S(P_{GS}, P_P, P_{SN}) \cdot (1 - t)$$

where:

$P_P$  - weather parameters,

$P_G$  - geometric parameters of the hull of the vessel,

$P_{GS}$  - geometric parameters of the propeller,

$P_{SN}$  - parameters of the drive engine,

$t$  - suction factor which takes into account additional resistance of the hull induced by the ship propeller.

To determine the vessel speed available at a given propeller thrust  $T_S$ , the total resistance  $R_C$  which occurs when the vessel sails in real weather conditions should be known.

As can be seen from equation (1), weather parameters of ship sailing affect not only the total resistance but also the thrust of the propeller. Large wave swings and resultant relative motions of the vessel will lead to, among other effects, emerging of the propeller and trust decrease, which in turn will result in vessel speed decrease.

A mathematical model to calculate the total resistance of a ship in given weather conditions, and a model to calculate the thrust of the propeller (taking into account characteristics of the drive engine installed on the vessel) were presented in [6]. Substituting the equation (1) with three ship associated equations, separately for the X, Y, and Z axes in the rectangular coordinate system, and solving the system of equations created in this way enables to evaluate the speed of the vessel with the installed propulsion system in given weather conditions. The algorithm for solving the equation system and calculating the instantaneous operating speed is shown in [7]. If the still water speed is subtracted from the calculated speed, we get the ship speed decrease due to waves, wind and current.

### SHIP SPEED REDUCTION DUE TO DANGEROUS PHENOMENA CAUSED BY WAVES

When the ship sails on wavy water, a direct effect of waves is rolling of the ship and its derivatives: velocity oscillations and acceleration. Secondary phenomena which accompany the ship rolling are flooding of the deck, emergence of the propeller, wave hitting against the bottom and sides of the ship (slamming), worsened stability and manoeuvrability, and/or additional dynamic loads of the hull. Rolling of the ship and the accompanying phenomena depend on the parameters of the ship hull and the waves, as well as on the ship speed  $V$  and direction with respect to the wave (angle  $\beta_w$ ). These phenomena, especially when intensive, can be a direct cause of a disaster at sea. Reducing the scale of these phenomena, lateral rolling for instance, is possible by changing the direction of ship sailing in relation to waves (angle  $\beta_w$ ), the reduction of speed  $V$ , or simultaneous change in direction and speed.

When forecasting the average service speed, an accepted principle says that if:

$$\overline{U}_Z > \overline{U}_{Zdop}$$

where:

$\overline{U}_Z$  - average statistical value of the phenomenon  $Z$  caused by waves and considered hazardous to the ship

$\bar{U}_{Zdop}$  - acceptable value of the phenomenon Z caused by waves, at which the ship can still swim safely,

then the vessel speed is to be reduced and/or course changed in such a way that:

$$\bar{U}_Z \leq \bar{U}_{Zdop}$$

To assess the behaviour of the ship on waves and to make a decision whether the ship speed and/or course is to be reduced, the following aspects are to be taken into consideration:

- rolling
- pitching,
- vertical acceleration,
- transverse horizontal acceleration,
- flooding of the deck,
- slamming,
- emergence of the propeller.

These phenomena are usually considered, or recommended to be taken into account, in assessing sea keeping properties of the vessel, or when determining the cost efficiency of the vessel [1], [2], [3], [4], [5].

The algorithm for calculating wave induced phenomena which are dangerous for the ship was given in [4].

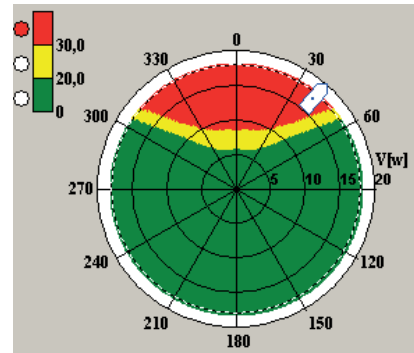
To test the condition (3), and possibly to correct the ship speed and/or course, we need to define certain criteria, which usually have the form of the permissible limits of wave induced phenomena at which the ship can still sail safely.

Years of observation and experience have made the basis for defining permissible limits for ship rolling and other accompanying phenomena, above which the safety of the ship and the crew or equipment working on the ship is endangered, which is equivalent to reducing the transport mission. The level of the permissible limits depends, among other factors, on the type and size of the ship. A sample set of criteria for the selected seagoing qualities is shown in table 1.

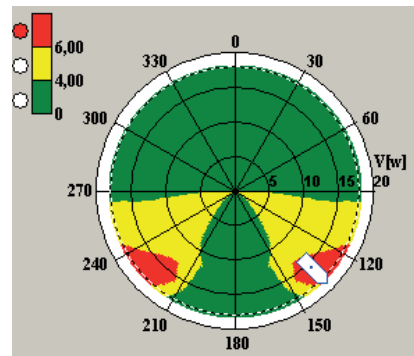
Table 1 Criteria for selected seagoing qualities [2]

	commercial vessels	warships	fast small units
Vertical accelerations at the bow (RMSD)	0,275 g small 0,1 g large	0,275 g	0,65 g
Accelerations in the wheelhouse (RMSD)	0,15 g	0,2 g	0,275 g
Horizontal lateral acceleration (RMSD)	0,12 g	0,1 g	0,1 g
Swaying (RMSD)	6,0°	4,0°	4,0°
Slamming (probability of occurrence for 100 waves)	0,03 small 0,01 large	0,03	0,03
Flooding the deck (probability of occurrence for 100 waves)	0,05	0,05	0,05

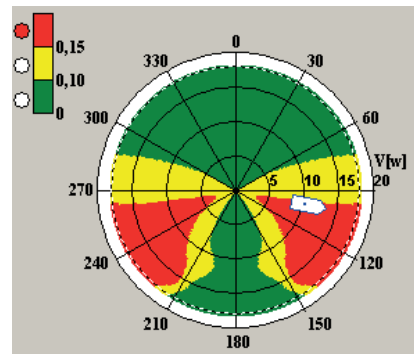
Figure 1 shows sample simulations of ship security threats caused by surge phenomena, calculated using the algorithm [4] and criteria from Table 1 for different vessel speeds and courses at selected weather parameters.



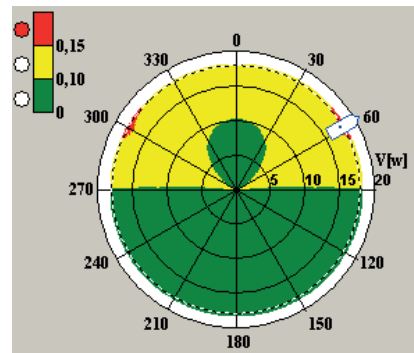
flooding the deck, V = 17 w, course = 40°



lateral rolling V = 15 w, course = 135°



horizontal lateral acceleration in the wheelhouse V = 10 w, course = 100°



vertical acceleration in the wheelhouse V = 17,5 w, course = 60°

-  - the ship sails securely
-  - warning about dangers (lower limit of the relevant criterion exceeded)
-  - threat to the safety of the ship (upper limit of the relevant criterion exceeded)

Fig. 1. Sample simulations of security threats for a container (Fig. 2) on the wave of parameters:

$$H_s = 8,5 \text{ m}; T_1 = 10,1 \text{ sec}; \mu = 0^0$$

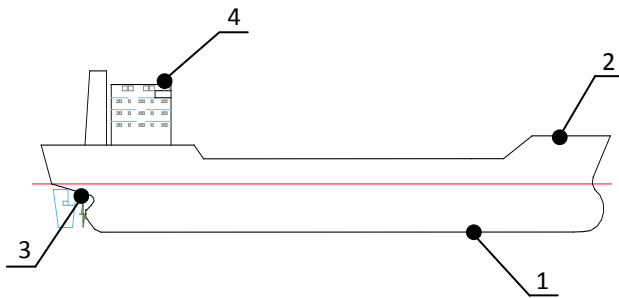


Fig. 2. Points for which the seakeeping characteristics shown in Figure 1 were calculated using the criteria from Table 1

- 1 - slamming, 2 - deck flooding and bow accelerations, 3 - propeller emergence, 4 - accelerations in the wheelhouse

## CALCULATING SHIP SPEED DECREASE IN SELECTED WEATHER CONDITIONS

### THE COMPUTER CODE PRESTAT

The mathematical model and the solution of the model algorithm presented in [6], [7] have made the basis for working out a computer code to calculate the ship speed in selected weather conditions. The code bearing the name of PRESTAT was written in Delphi and run in the Windows environment. This code is intended to be used for the investigating ship route optimization, and along with the ship speed it can calculate such parameters as: power and speed of the drive engine, propeller speed (on ships without gear: engine speed = propeller speed), marine environment generated forces acting on the ship, seagoing qualities. All these parameters are displayed on the computer screen (Fig. 3).

Data for the program

The data are entered to the program in two forms:

- as a batch file with all geometric dimensions of the vessel and necessary characteristics concerning: still water resistance coefficients, aerodynamic drag coefficients, wave drift force coefficients, and the characteristics of the propeller and the drive engine;
- as the data entered from the keyboard directly to the user's interface.

The data entered from the keyboard relate mainly to weather parameters, vessel traffic parameters, and selecting the mode of operation of the drive engine.

Specified weather parameters:

- waves
  - $H_s = \dots$  [m] - significant height  $0,0 \div 20,0 \text{ m}$
  - $T_1 = \dots$  [sec] - time period  $0,0 \div 30,0 \text{ sec}$
  - $\mu = \dots$  [deg] -  $\gamma$  geographical direction  $0 \div 360^0$
  - $\mu = 0^0$  - northern wave
  - $\mu = 90^0$  - eastern wave

- wind:
  - $V_A = \dots$  [m/sec] - average speed  $0,0 \div 50,0 \text{ m/sec}$
  - $\gamma_A = \dots$  [deg] - geographical direction  $0 \div 360^0$
  - $\gamma_A = 0^0$  north wind
  - $\gamma_A = 90^0$  east wind

- current surface:
  - $V_C = \dots$  [m/sec] - average speed  $0,0 \div 2,0 \text{ m/sec}$
  - $\gamma_C = \dots$  [deg] - geographical direction  $0 \div 360^0$
  - $\gamma_C = 0^0$  - current flows in the northerly direction
  - $\gamma_C = 90^0$  - current flows in the easterly direction

Operating state of the drive engine - the engine is running in the continuous operation mode, or is allowed to be overloaded or operated in the temporary operation mode.

Specified vessel course:

- $\psi = \dots$  [deg] ( $0 \div 360^0$ )
- $\psi = 00$  northern course
- $\psi = 90^0$  eastern course.

After entering and confirming the above data, the calculations are performed and the following results are displayed on the screen:

wave parameters :

- $H_s$  - significant height [m]
- $T_1$  - time period [sec]
- $\mu$  - geographical direction [deg]

wind parameters:

- $V_A$  - average speed [m/sec]
- $\gamma_A$  - geographical direction [deg]

sea current parameters:

- $V_C$  - average speed [m/sec]
- $\gamma_C$  - geographical direction [deg]

operating parameters of the vessel:

- $\psi$  - specified course of the vessel [deg]
- $V_E$  - calculated instantaneous operating speed [knots]
- $\delta_R$  - rudder angle [deg]
- $n_S$  - engine RPM [1/sec] (specified by the slider, or calculated)
- $N_S$  - engine power [kW]

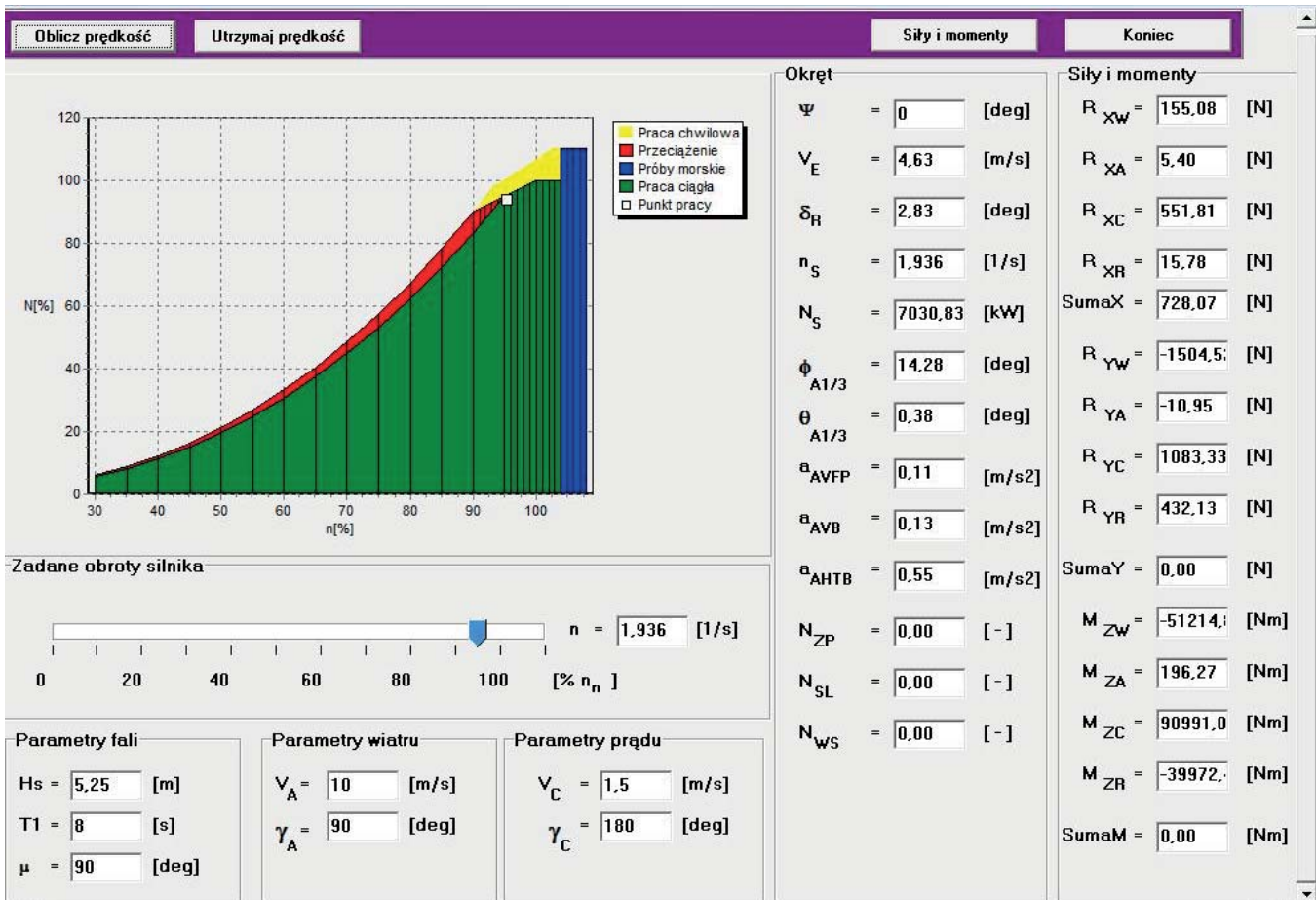


Fig. 3. Data entered from the keyboard, and the results of calculations displayed on the screen

Significant oscillation and acceleration amplitudes, and the frequencies of other phenomena for selected points of the ship to  $V_E, \psi, \mu, [m/s^2]$ :

$\phi_{A1/3}$  – significant amplitude of ship rolling for  $V_E, \psi, \mu, [deg]$

$\theta_{A1/3}$  – significant amplitude of ship pitching for  $V_E, \psi, \mu, [deg]$

$a_{AVFP}$  – component of vertical acceleration on the forward perpendicular,

$a_{AVB}$  – component of vertical acceleration in the wheelhouse,

$a_{AHTB}$  – component of transverse horizontal acceleration in the wheelhouse,

$N_{ZP}$  – flooding frequency (number of times per hour) for  $V_E, \psi, \mu, [-]$

$N_{SL}$  – frequency of slamming for  $V_E, \psi, \mu, [-]$

$N_{WS}$  – frequency of propeller emergence for  $V_E, \psi, \mu, [-]$

Note: Data on possible ship safety threats from waves can be displayed on a separate screen in the form shown in Figure 1.

External forces and moments generated by the marine environment:

$R_{XW}, R_{YW}, M_{ZW}$  – force and moment generated by the wave,

$R_{XA}, R_{YA}, M_{ZA}$  – power and moment generated by the wind,

$R_{XC}, R_{YC}, M_{ZC}$  – power and moment generated by the water (including the current when  $VC \neq 0$ )

$R_{XR}, R_{YR}, M_{ZR}$  – power and moment generated by the rudder

### INFLUENCE OF WEATHER PARAMETERS ON THE VESSEL SPEED DECREASE

The code PRESTAT calculates the instantaneous average operating speed  $V_E$  of the vessel in the selected conditions. By subtracting this speed from the speed  $V$  of the ship in still water we get the speed decrease which is used to forecast the optimal route of the ship.

By introducing different values of weather parameters we can investigate the influence of these parameters on the speed decrease at a given course (if the course is to be maintained), or look for the maximum speed  $V_E$  (or minimal speed decrease) when the course of the ship is changed.

The computer code was designed in such a way that the speed of vessel sailing in the selected weather conditions can be calculated assuming different working scenarios of the drive engine, such as maintaining constant RPM or engine power, constant specific fuel consumption, or constant ship speed in changing weather conditions.

The code also displays the calculated parameters of ship rolling and other hazardous phenomena (Fig. 2). The computer code does not automatically reduce the speed of the ship when the permissible limits of wave induced ship rolling are exceeded (Tab. 1), and it is only the navigator who can reduce deliberately the speed of the vessel.

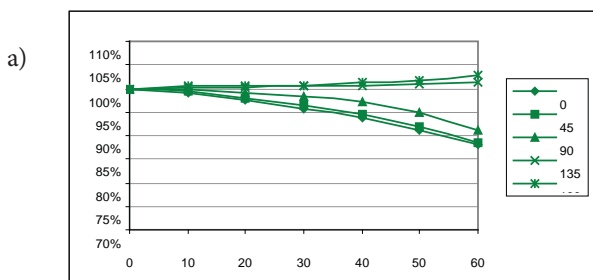
## VERIFICATION OF CALCULATIONS AND VESSEL SPEED DECREASE

The presented sample calculations were performed for a bulk carrier with parameters shown in Table 2, and compared with measurements made on a similar ship (Tab.2).

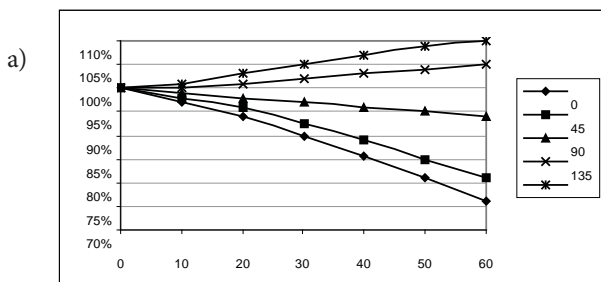
**Tab. 2.** Parameters of compared vessels

	$L_{PP}$ [m]	$B$ [m]	$T$ [m]	$\nabla$ [m <sup>3</sup> ]	$C_B$ [-]	$V$ [nodes] (m/sec)
Bulk carrier for which calculations were performed	185,0	25,3	10,6 4	0831 0	,820	14,6 (7,51)
Bulk carrier of "Diana" series, on which measurements were made	186,4/177,0	30,0	11,46/6,23	41260 0	,812/0,800	13,5/14,5 (6,9/7,5)

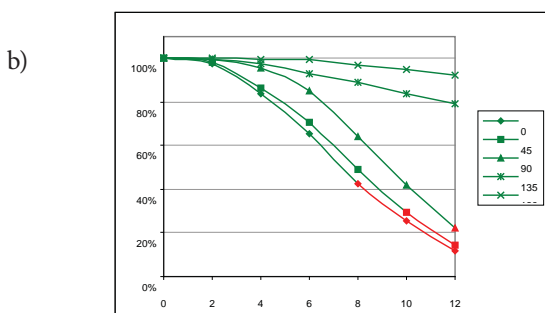
Figure 4 shows the speed decrease of the bulk carrier calculated for different parameters, and different wave and wind directions with respect to the vessel, while Fig. 5 presents rolling and other seagoing qualities, along with the selected criteria.



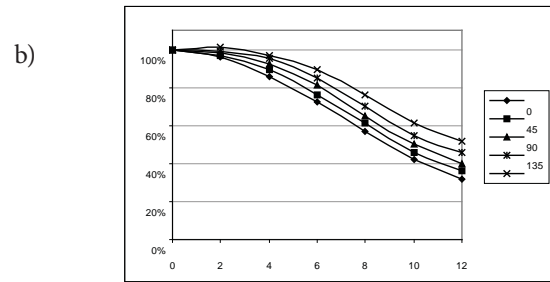
Bulk carrier LPP =185,0 m



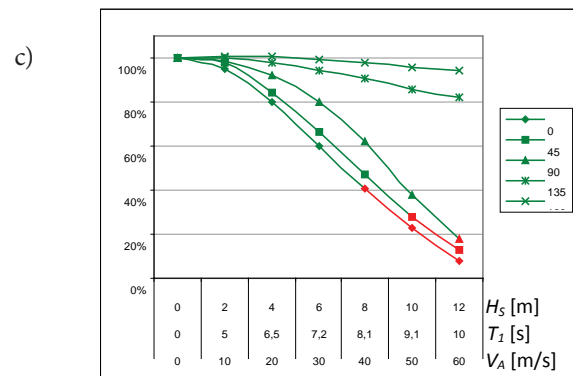
Bulk carrier of „Diana” series LPP =186,0/177,0 m



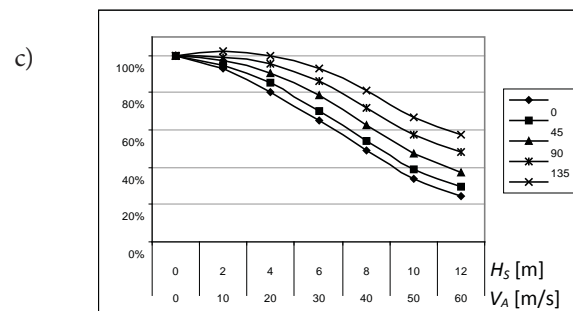
Bulk carrier LPP =185,0 m



Bulk carrier of „Diana” series LPP =186,0/177,0 m



Bulk carrier LPP =185,0 m

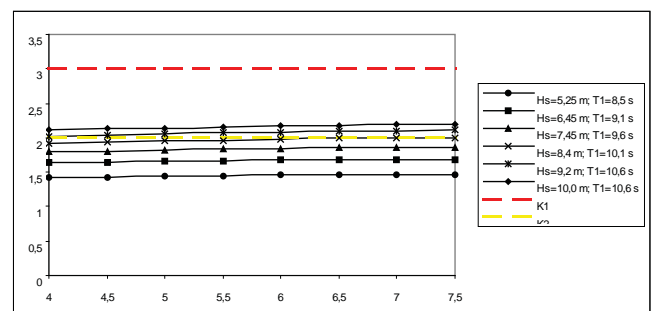


Bulk carrier of „Diana” series LPP =186,0/177,0 m

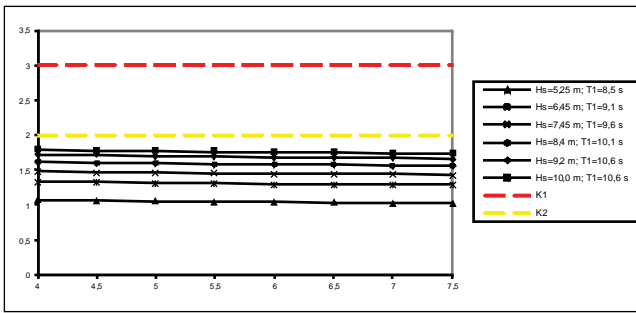
**Fig. 4.** Speed decrease for different parameters and wave and wind directions: the vessel course  $\psi = 0^\circ$  (green – continuous operation without overload, red – engine overload, Figure 3)

- a) impact of wind
- b) impact of waves
- c) combined impact of wind and waves

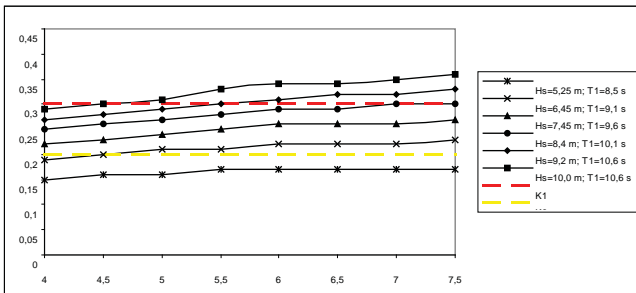
### Pitching ( $\beta$ w = 180<sup>0</sup>) - the average standard deviation



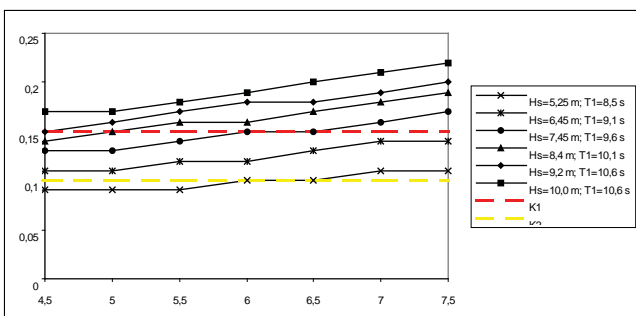
Pitching ( $\beta_w=0^0$ ) - the average standard deviation



Vertical acceleration at bow ( $\beta_w=180^0$ )



Vertical acceleration in the wheelhouse ( $\beta_w=180^0$ )



Slamming ( $\beta_w=180^0$ )

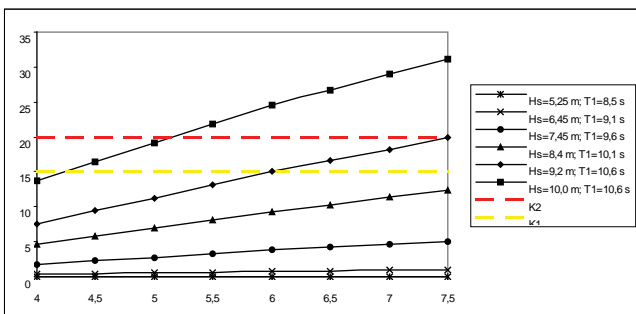


Fig. 5. Seagoing qualities of the vessel, with the marked selected criteria for bulk carrier LPP = 185.0 m (criterion K1 - warning of danger; criterion K2 - exceeding the permissible limit of seagoing qualities)

BIBLIOGRAPHY

1. Girtler J., Kitowski Z., Kuriata A.: Ship safety at sea (in Polish), Wydawnictwo Komunikacji i Łączności, Warszawa, 1995.
2. Karppinen T.: Criteria for Seakeeping Performance Predictions, Technical Research Centre of Finland, Ship Laboratory, ESPOO, Helsingfors, 1987.
3. Lloyd A.R.J.M.: Seakeeping: Ship Behaviour in Rough Weather, Ellis Horwood Series in Marine Technology, Chichester, England, 1989.
4. Szelangiewicz T.: Safety of the ship sailing in storming conditions (in Polish), Conference: Problemy eksploatacji statków morskich i śródlądowych oraz urządzeń portowych, EKSPLO-SHIP'99, Międzyzdroje 09-13 maja 1999, Tom 2, pp. 185 ÷ 192, 1999.
5. Szelangiewicz T.: Estimation of operational effectiveness of ship sails in waves, HYDRONAV'2001, 14th International Conference on Hydrodynamics in Ship Design, Szczecin-Międzyzdroje, Poland, September 27-29 2001, pp. 324 ÷ 334, 2001.
6. Szelangiewicz T., Żelazny K.: Calculation of the Mean Long-Term Service Speed of Transport Ship, Part I: Resistance of Ship Sailing on Regular Shipping Route in Real Weather Conditions, Polish Maritime Research, No. 4(50), Vol. 13, October 2006, pp. 23 ÷ 31, 2006.
7. Szelangiewicz T., Żelazny K.: Calculation of Mean Long-Term Service Speed of Transport Ship, Part II: Service Speed of Ship Sailing on Regular Shipping Route in Real Weather Conditions, Polish Maritime Research, No 1/2007, pp. 28 ÷ 32, 2007.
8. Wiśniewski B.: Ship route optimisation taking into account weather conditions (in Polish), Wyższa Szkoła Morska w Szczecinie, Szczecin 1986.
9. Wiśniewski B., Medyna P., Klein R., Jakubowski M.: The application of weather forecasts and average climate conditions in assessing routes for ships sailing with different operating speeds on the northern Atlantic (in Polish), EXPLO-SHIP 2002, Zeszyty Naukowe nr 65, Wyższa Szkoła Morska, 2002.
10. Wiśniewski B., Korwin-Piotrowski T., Wielgosz M.: Procedures of integrated oceanic ship route planning and programming with the assistance of the Ship Performance Optimisation System (in Polish), Wydawnictwo Naukowe Akademii Morskiej w Szczecinie, Szczecin 2012.

CONTACT WITH THE AUTOR

Tadeusz Szelangiewicz, Prof.  
Maritime University of Szczecin  
1-2 Wały Chrobrego Street  
70-500 Szczecin, POLAND

e-mail: t.szelangiewicz@am.szczecin.pl

# Fatigue analysis of deepwater hybrid mooring line under corrosion effect

Dongsheng Qiao<sup>a</sup>, Ph. D

Jun Yan<sup>b</sup>, M. Sc.

Jinping Ou<sup>a,b</sup>, Ph. D

a) Deepwater Engineering Research Center, Dalian University of Technology, Dalian, China

b) State Key Laboratory of Coastal and Offshore Engineering, Dalian University of Technology, Dalian, China

## ABSTRACT

*In the deepwater exploitation of oil and gas, replacing the polyester rope by a wire in the chain-wire-chain mooring line is proved to be fairly economic, but this may provoke some corresponding problems. The aim of this paper is to compare the fatigue damage of two mooring system types, taking into account corrosion effects. Using a semi-submersible platform as the research object, two types of mooring systems of the similar static restoring stiffness were employed. The mooring lines had the chain-wire-chain and chain-polyester-chain structure, respectively. Firstly, the numerical simulation model between the semi-submersible platform and its mooring system was built. The time series of mooring line tension generated by each short-term sea state of South China Sea S4 area were calculated. Secondly, the rain flow counting method was employed to obtain the fatigue load spectrum. Thirdly, the Miner linear cumulative law model was used to compare the fatigue damage of the two mooring system types in long-term sea state. Finally, the corrosion effects from zero to twenty years were considered, and the comparison between the fatigue damage of the two mooring system types was recalculated.*

**Keywords:** Mooring system; short-term sea state; fatigue damage; corrosion effect

## INTRODUCTION

Floating platforms and their mooring systems need to resist various ocean environmental conditions. Changes in wind, current, and wave loads provoke variable motion and stress in the mooring system. Gradual accumulation of the variable stress can lead to cumulative fatigue damage. In recent years, many fatigue damages of the mooring line in the practical projects have been recorded [1]. Therefore the investigation of fatigue damage is still necessary, and the problem is discussed by many scholars.

A traditional catenary mooring system is still widely used in practical projects nowadays [2-3]. It usually has the chain-wire-chain structure. With increasing water depth, the weight of the chain and the wire become very large, and the cost becomes uneconomic. Recently, the results of successful development of synthetic fibres have been applied to deepwater mooring system, for instance in the form of the polyester mooring system to FPSO-2 project conducted by Brazil Petroleum Company [4]. Some problems concerning the use of a new type of mooring system can be named, including the fatigue problem discussed in this paper.

At present, the commonly used calculation method of fatigue damage is the Miner linear cumulative law model which is based on the S-N curve, and this method is suggested by many criterions [5-7]. Another calculation method is the

fracture mechanics approach, which is not very mature and still needs to develop [8-9]. That is why the S-N curve was used to calculate the fatigue damage in this paper.

Mathisen et al. [10] applied the S-N curve to calculate the fatigue damage of the mooring system in the DEEPMOOR project, and indicated that the wave responses could provoke more fatigue damage than the drift responses. Omar et al. [11] applied the Dirlik method, the rain flow counting method, the narrowband spectra analysis method, and the broadband spectra revised method to count the mooring line tension, and used the S-N curve to calculate the fatigue damage. Gao and Moan [12] investigated a catenary mooring system for a semi-submersible platform, and calculated the fatigue damage under wave loads and drift loads. Han et al. [13] investigated the influences of different mooring layouts to the fatigue damage of a mooring line. Qiao and Ou [14] calculated the fatigue damage of the polyester mooring line based on the S-N curve. Huang et al. [15] used the Ariane software to calculate the fatigue damage of a taut mooring system in the South China Sea.

The influence of corrosion effects to the fatigue damage is a separate problem. Gao et al. [16] introduced the reliability calculation to the corrosion fatigue damage analysis. Lardier et al. [17] applied the S-N curve and the fracture mechanics method to calculate the fatigue reliability of catenary mooring lines under corrosion effect.

In those research activities, the scholars mainly applied the S-N curve to calculate the fatigue damage of a certain mooring system. This paper aims at comparing the fatigue damage between the chain-wire-chain and chain-polyester-chain mooring systems, taking into account the corrosion effects.

A semi-submersible platform was selected as the research object, along with two mooring system types of similar static restoring stiffness. The Miner linear cumulative law model was used to compare the fatigue damage, and the corrosion effects from zero to twenty years were considered in the calculation.

## FATIGUE ANALYSIS THE S-N CURVE

According to American Petroleum Institute (API) Recommended Practice 2SK [6], the S-N curve presents the number of cycles to failure for a specific mooring component as a function of a constant normalized tension range, based on the results of experiments. For mooring systems, the  $T - K$  approach which only considers the tension fatigue and ignores the bending fatigue is normally used. The formula (1) presents the  $T - K$  curve.

$$NR^M = K \quad (1)$$

where  $N$  is the number of cycles,  $R$  is the ratio of tension range to reference breaking strength, and  $M$  and  $K$  are material parameters in the  $T - K$  curve.

According to Miner's linear cumulative damage rule, the annual cumulative fatigue damage  $D$  can be summed up from the fatigue damage  $D_i$  arising in a set of short-term sea states.

$$D = \sum_{i=1}^n D_i \quad (2)$$

The fatigue damage  $D_i$  in the  $i$ -th short-term sea state:

$$D_i = \frac{n_i}{K} E[R_i^M] \quad (3)$$

where  $n_i$  is the number of tension cycles encountered in this short-term sea state,  $R_i$  is the ratio of the tension range to the referential breaking strength,  $E[R_i^M]$  is the expected value of the normalized tension range  $R_i$  raised to the power  $M$ .

In the calculations, the values of  $M = 9.0$  and  $K = 316$  for chain, and  $M = 5.05$  and  $K = 10^{(3.25 - 3.42 L_m)}$  for wire, were chosen from the  $T - N$  curve of wire recommended by API RECOMMENDED PRACTICE 2SK [6].  $L_m$  is the ratio of the mean load to the referential breaking strength for wire.  $M = 9.0$  and  $K = 7.5$  and were chosen from the curve of polyester recommended by API RECOMMENDED PRACTICE 2SM [18].

## CORROSION EFFECT

The corrosion effect has many influence parameters, such as salinity, humidity, current velocity, water depth, etc. Melchers et al. [19] investigated the corrosion on fully submerged chains, and indicated that the mean value of the corrosion rate is slightly smaller than that given in DNV OS-E301 [7]. So, the corrosion rate of the chain used in this paper was

assumed according to the DNV OS-E301. Besides, in practical applications a galvanized or plastic jacket is usually added to the wire or the polyester mooring component to protect against the corrosion effect [6], so only the corrosion effect of the chain was taken into account in this paper.

According to DNV OS-E301, the corrosion rate of a chain is divided into three parts. The corrosion rate in the splash zone is 0.8 mm/year, while the corrosion rates in the catenary and bottom zones are both 0.2 mm/year.

The influence of the corrosion effect to the fatigue damage is mainly represented in two ways. Firstly, the material parameters and in the curve are changed. Secondly, the stress in the mooring line is changed due to the reduction of the chain diameter provoked by the corrosion.

## SEMI-SUBMERSIBLE PLATFORM MODEL AND ENVIRONMENTAL CONDITIONS

### SEMI-SUBMERSIBLE PLATFORM

The main structure of the semi-submersible platform model consisted of two pontoons, four columns, a deck, and a derrick. The main characteristic parameters are listed in Table 1.

**Tab. 1.** Parameters of semi-submersible platform

Parameters	Value
Deck (m)	74.42×74.42×8.60
Column (m)	17.385×17.385×21.46
Pontoon (m)	114.07×20.12×8.54
Tonnage (kg)	48206800
Centre of gravity from water surface (m)	8.9
Roll gyration radius (m)	32.4
Pitch gyration radius (m)	32.1
Yaw gyration radius (m)	34.4
Initial air gap (m)	14
Diameter of brace (m)	1.8

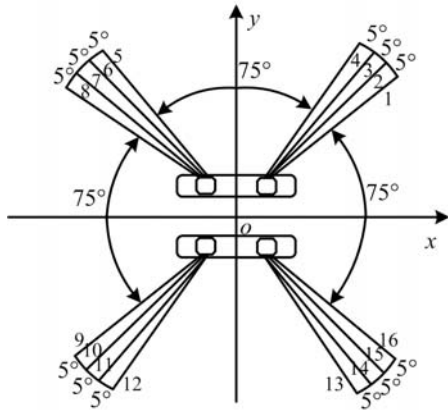


Fig. 1. Mooring system layout

### MOORING SYSTEM

The mooring system consisted of four (4x4) groups, as shown in Figure 1. Two mooring system types, which are chain-wire-chain and chain-polyester-chain, were used respectively during the calculation in combination with the semi-submersible platform. The mooring line properties are listed in Table 2. The static characteristics of the two mooring types are compared in Fig. 2 ÷ 3. A representative mooring line was chosen to compare the fatigue damage between the two mooring system types, shown as Fig. 4. According to Handbook of Offshore Engineering [20], the drift stiffness of polyester was used to calculate the fatigue damage.

Item		Steel mooring	Polyester mooring
Water depth (m)		1500	1500
Initial top pretension (KN)		2050	2150
Property of material	upper	K4 Studless Chain	K4 Studless Chain
	middle	Spiral Strand Wire	Polyester
	bottom	K4 Studless Chain	K4 Studless Chain
Line weight in water (N/m)	upper	1431.018	1431.018
	middle	268.036	40.082
	bottom	1431.018	1431.018
Line axial stiffness EA (MN)	upper	603.53	603.53
	middle	626.77	183.81/239.75
	bottom	603.53	603.53
Total line length (m)	upper	450	450
	middle	2000	2000
	bottom	1500	1500
Nominal diameter (mm)	upper	90.0	90.0
	middle	82.55	160.0
	bottom	90.0	90.0
Breaking strength (KN)	upper	8160	8160
	middle	5920	7840
	bottom	8160	8160

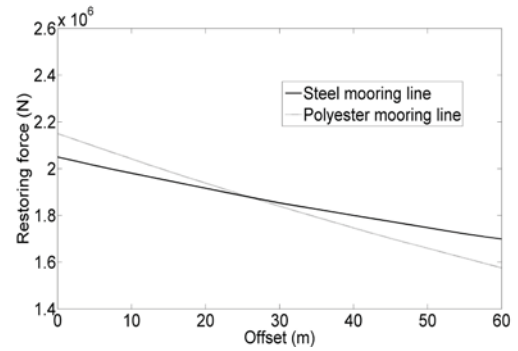


Fig. 2. Comparison of static stiffness of single hybrid mooring line

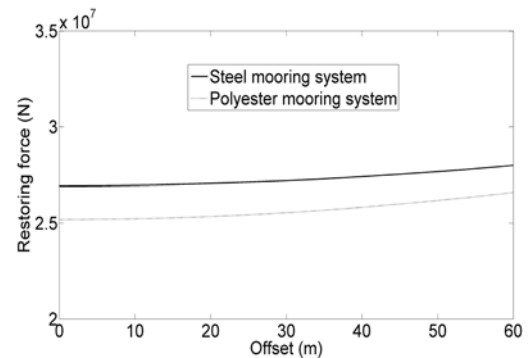


Fig. 3. Comparison of static stiffness of mooring system

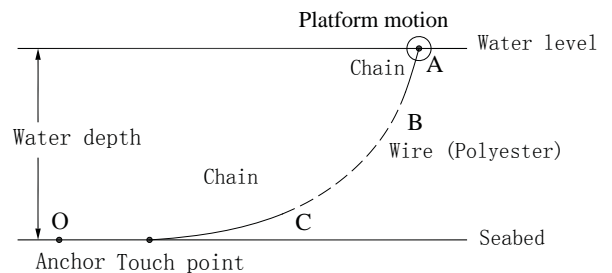


Fig. 4. Mooring line configuration

According to Fig. 2 ÷ 3, the static characteristics of the two mooring system types are similar. Then the two mooring system types were added to the semi-submersible platform.

### ENVIRONMENTAL CONDITIONS

Motion responses of the semi-submersible platform were calculated under the combination of wind, current, and wave loads. The sea state condition was selected from the South China Sea S4 area, along with the angle of incidence with respect to the X-axis. The long-term sea state usually consists of a number of short-term sea states. According to the wave scatter diagram of South China Sea S4 [15] in one year, the chosen sea states are listed in Table 3 and the JONSWAP spectra with the peak value  $\gamma = 2.0$  were used.  $H_s$  is the significant wave height,  $T_s$  is the zero up-crossing period.  $V_s$  is the wind speed. In the calculations the API wind spectrum was used.  $C$  is the mean current speed.  $P$  is the occurrence probability of each sea state.

Tab. 3. Parameter of short-term sea state

Sea state	(m)	(s)	(m/s)	(m/s)	(%)	Sea state	(m)	(s)	(m/s)	(m/s)	(%)
1	0.250	3.5	3.40	0.102	0.1	33	1.050	8	8.40	0.252	1.3
2	0.250	4	3.80	0.114	1.0	34	1.550	8	10.0	0.300	2.5
3	0.675	4	5.60	0.168	0.8	35	2.175	8	12.0	0.360	3.0
4	1.050	4	7.00	0.210	0.7	36	2.875	8	12.8	0.384	3.1
5	1.550	4	8.50	0.255	0.5	37	3.625	8	14.0	0.420	2.2
6	2.175	4	10.1	0.303	0.2	38	4.500	8	15.4	0.462	1.7
7	0.250	5	4.20	0.126	2.9	39	5.500	8	16.5	0.495	0.6
8	0.675	5	6.00	0.180	3.1	40	6.750	8	18.2	0.520	0.2
9	1.050	5	7.60	0.228	3.4	41	0.250	9	5.00	0.150	0.1
10	1.550	5	9.00	0.270	3.7	42	0.675	9	7.00	0.210	0.2
11	2.175	5	10.8	0.324	1.9	43	1.050	9	8.60	0.258	0.4
12	2.875	5	11.6	0.348	0.7	44	1.550	9	10.6	0.318	0.8
13	3.625	5	13.0	0.390	0.1	45	2.175	9	12.6	0.378	1.0
14	0.250	6	4.30	0.129	2.9	46	2.875	9	13.2	0.396	1.2
15	0.675	6	6.40	0.192	3.7	47	3.625	9	14.8	0.444	1.0
16	1.050	6	7.80	0.234	5.0	48	4.500	9	16.0	0.480	1.0
17	1.550	6	9.40	0.282	7.2	49	5.500	9	16.8	0.504	0.6
18	2.175	6	11.2	0.336	5.5	50	6.750	9	18.0	0.540	0.4
19	2.875	6	12.0	0.360	3.2	51	0.675	10	7.50	0.225	0.1
20	3.625	6	13.2	0.396	1.1	52	1.050	10	9.20	0.276	0.1
21	4.500	6	14.5	0.435	0.2	53	1.550	10	12.0	0.360	0.2
22	0.250	7	4.50	0.135	1.5	54	2.175	10	13.4	0.402	0.2
23	0.675	7	6.60	0.198	2.1	55	2.875	10	14.0	0.420	0.3
24	1.050	7	8.20	0.246	3.3	56	3.625	10	15.6	0.468	0.3
25	1.550	7	9.80	0.294	5.7	57	4.500	10	16.7	0.501	0.3
26	2.175	7	11.6	0.348	5.7	58	5.500	10	17.4	0.522	0.2
27	2.875	7	12.4	0.372	4.6	59	6.750	10	19.1	0.573	0.3
28	3.625	7	13.7	0.411	2.4	60	2.875	11	15.2	0.456	0.1
29	4.500	7	15.0	0.450	1.3	61	3.625	11	16.4	0.492	0.1
30	5.500	7	16.1	0.483	0.3	62	4.500	11	17.2	0.516	0.1
31	0.250	8	4.80	0.144	0.5	63	5.500	11	18.0	0.540	0.2
32	0.675	8	6.80	0.204	0.8	64	3.625	12	20.0	0.600	0.1

# NUMERICAL SIMULATION

## COUPLED MODEL BETWEEN THE SEMI-SUBMERSIBLE PLATFORM AND ITS MOORING SYSTEM

To calculate the coupled motion, the Cummins's method [21] was applied in this study. The wave forces on the semi-submersible platform were calculated using the boundary element method based on the diffraction theory and the commercially available program AQWA [22]. The panel model is shown in Figure 5. The model for the coupled analysis of the semi-submersible platform and its mooring lines is shown in Figure 6. A coupled model of the semi-submersible platform and its mooring system is known from the literature [23]. It was also established by the authors of this paper.

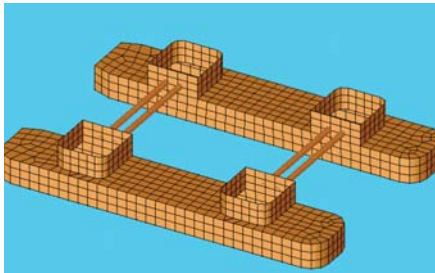


Fig. 5. Panel model

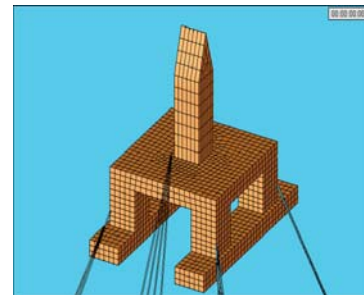
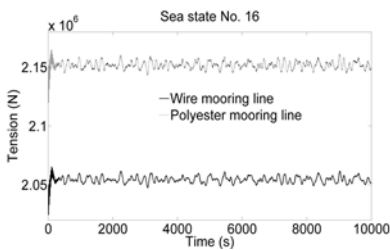


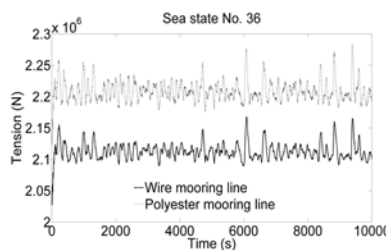
Fig. 6. Coupled analysis model

In the comparative analysis of fatigue damage, the fatigue load spectra of the mooring line need to be obtained firstly. In this study, the rain float counting method [24] was employed to count the mooring line tension. A histogram of the tension range can be obtained from this counting, in the form of fatigue load spectra of the mooring line.

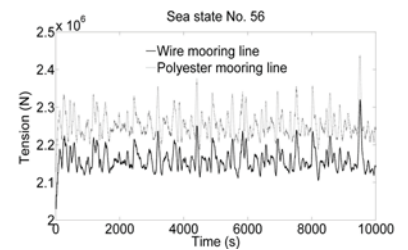
A time series of the mooring line tension at point A (shown in Fig. 4) between the two mooring system types under sea states No. 16, 36, 56 are plotted in Figure 7, and the corresponding fatigue load spectra are plotted in Figures 8 ÷ 9. The results under other sea states are omitted for brief.



7(a) sea state No. 16

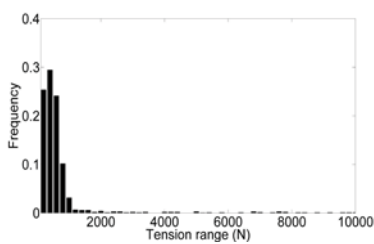


7(b) sea state No. 16

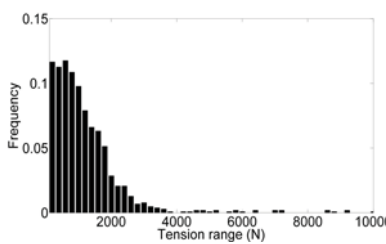


7(c) sea state No. 16

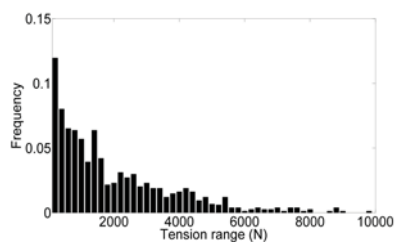
Fig. 7. Time series of mooring line tension at point A without corrosion



8(a) sea state No. 16

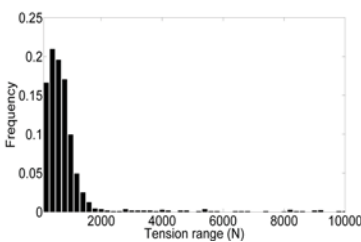


8(b) sea state No. 36

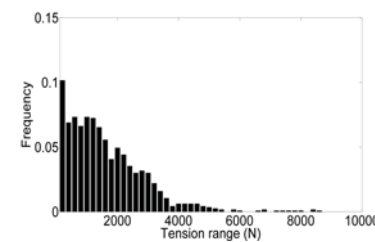


8(c) sea state No. 56

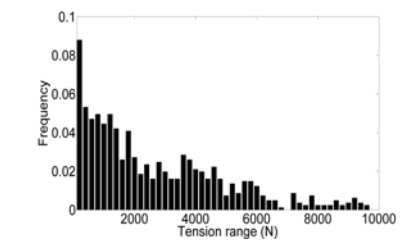
Fig. 8. Fatigue load spectra of point A in steel mooring line without corrosion



9(a) sea state No. 16



9(b) sea state No. 36



9(c) sea state No. 56

Fig. 9. Fatigue load spectra of point A in polyester mooring line without corrosion

The statistic analysis of the fatigue load spectra in all short-term sea states reveals that they don't satisfy the normal theory probability distribution. Therefore the histograms were employed to reflect the short-term distribution of tension range under all short-term sea states, and the rain flow counting results were used to calculate the fatigue damage directly in the later study.

## FATIGUE ANALYSIS

Based on the abovementioned fatigue damage calculation method, the fatigue damages of the two mooring system types were calculated. The fatigue damages of Point A, B, and C, which represent the upper end point of three segments in the mooring line (shown in Fig. 4), were compared without the corrosion effect. Then, the corrosion effect after 5 years, 10 years, 15 years, and 20 years was taken into account. The fatigue damages of Point A, B, and C under each short-term sea state were recalculated under the effect of the corrosion rate.

### FATIGUE DAMAGE WITHOUT CORROSION

The fatigue damages of the two mooring system types under each short-term sea state are plotted in Fig. 10 ÷ 11, and the comparisons of point A, B, and C are plotted in Fig. 12 ÷ 14. The vertical-axis is the logarithm of fatigue damage. According to Fig. 10 ÷ 11, in both cases of the two examined mooring system types the main fatigue damage occurred in the chain segment, independently of the fact whether the mooring line has the chain-wire-chain or the chain-polyester-chain structure. At the same time, the fatigue damage in the wire or polyester segment is relatively much smaller. In the chain-wire-chain mooring line, the fatigue damage in the upper chain is obvious larger than in the bottom chain, while for the chain-polyester-chain mooring line the fatigue damage in the upper chain is almost the same as in the bottom chain. This phenomenon should need additional attention in the practical project. When using the chain-polyester-chain mooring system, the most possible fatigue damage zone includes not only the upper chain in the splash zone, but also the bottom chain.

According to Fig. 12 ÷ 14, the fatigue damage of point B in the steel mooring line is larger than the one in the polyester mooring line, but the fatigue damages of point A and C in the steel mooring line are smaller than those in the polyester mooring line. In other words, replacement of the polyester rope for the wire in the chain-wire-chain mooring line resulted in a much smaller fatigue damage than that observed for the wire, but also provoked fatigue damages of the upper and bottom chains which are larger than those recorded for the chain-wire-chain mooring line. This interesting phenomenon still needs additional attention in the practical project. The replacement of the polyester rope for the wire in the chain-wire-chain mooring line means immolating the fatigue life of the chain to improve the fatigue life of middle segment.

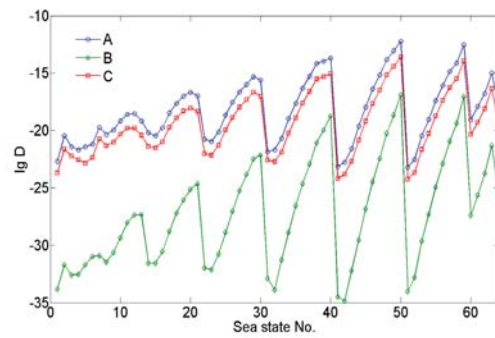


Fig. 10. Fatigue damage of steel mooring lines under short-term sea states without corrosion

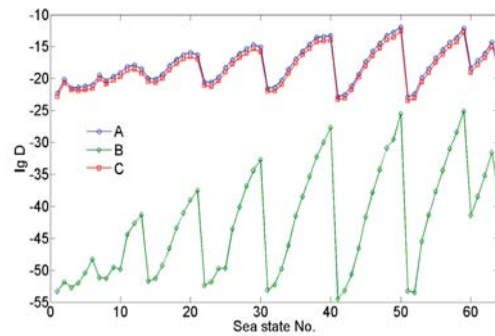


Fig. 11. Fatigue damage of polyester mooring lines under short-term sea states without corrosion

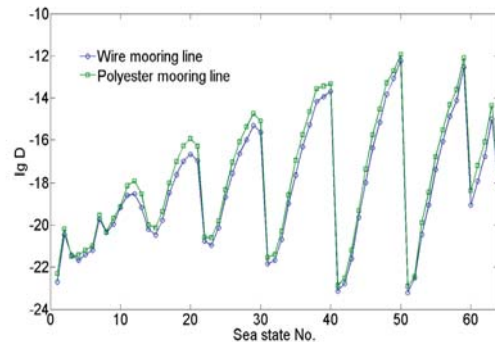


Fig. 12. Fatigue damage of point A under short-term sea states without corrosion

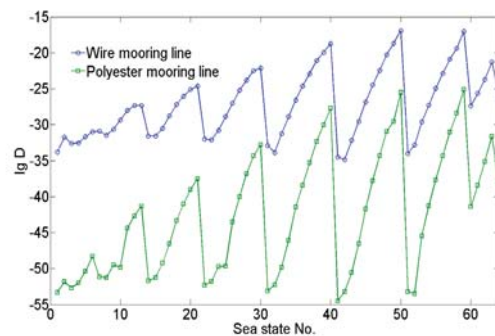


Fig. 13. Fatigue damage of point B under short-term sea states without corrosion

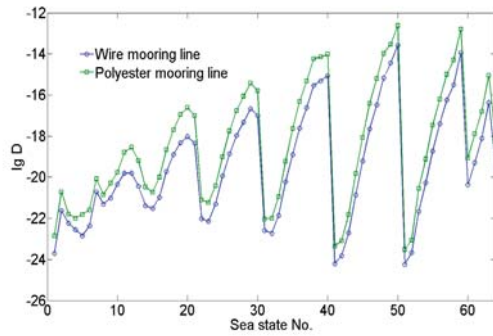


Fig. 14. Fatigue damage of point C under short-term sea states without corrosion

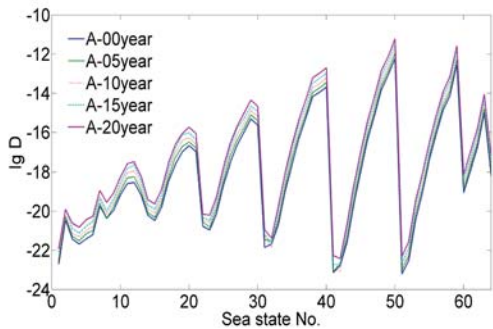


Fig. 15. Fatigue damage of point A in steel mooring lines under short-term sea states with corrosion

### FATIGUE DAMAGE WITH CORROSION IN DIFFERENT YEARS

Results of analysing the corrosion effect in different years are shown in Fig. 15 as the fatigue damages of point A in the steel mooring line under each short-term sea state, and in Fig. 16 ÷ 20 as the fatigue damages of two mooring system types under different years.

According to Fig. 15 ÷ 17, the nature of changes of fatigue damage under corrosion is similar to that without corrosion. With the increasing corrosion years, the fatigue damage increases under each short-term sea state. Meanwhile, the increase of the fatigue damage of point A under long-term sea state is much larger than the one of point B and C. This phenomenon indicates that the upper chain in the splash zone needs additional attention with respect corrosion effects.

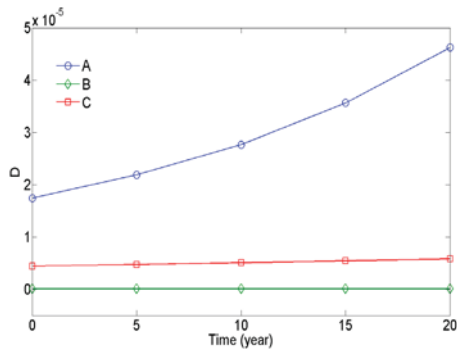


Fig. 16. Fatigue damage of steel mooring lines with corrosion

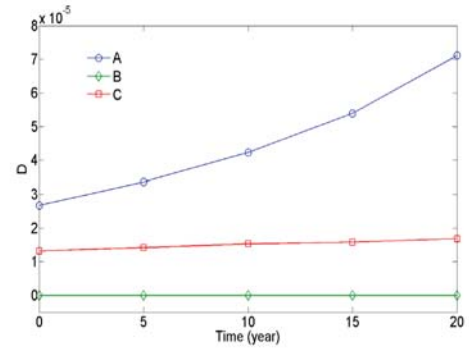


Fig. 17. Fatigue damage of polyester mooring lines with corrosion

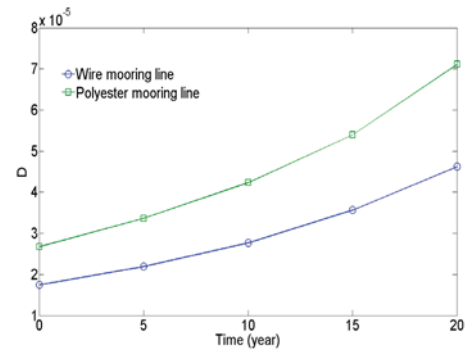


Fig. 18. Fatigue damage of point A with corrosion

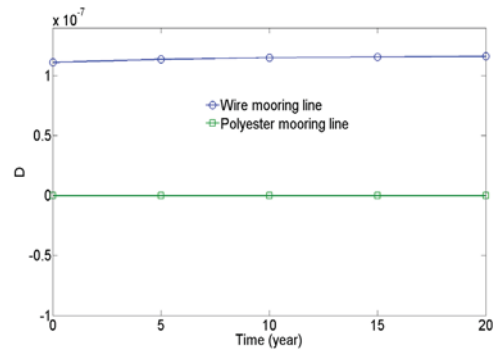


Fig. 19. Fatigue damage of point B with corrosion

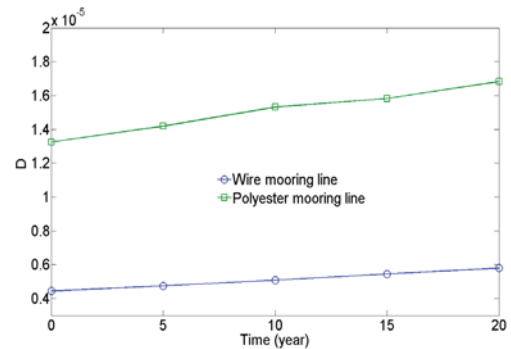


Fig. 20. Fatigue damage of point C with corrosion

According to Fig. 18 ÷ 20, the difference in the scale of the fatigue damage between the two mooring system types is getting bigger with the increasing corrosion years. Under the 20-year corrosion effect, the difference between the fatigue damage of the two mooring system types at point A, B, and C is much larger than the ones without corrosion. In other words, the corrosion effect increases the difference between the fatigue damages of the two mooring system types.

## CONCLUSIONS

The fatigue damages between the chain-wire-chain and chain-polyester-chain mooring systems applied for a semi-submersible platform were compared. The two types of mooring systems had a similar static restoring stiffness. The analysis took into account the corrosion effect. The following preliminary findings can be formulated:

- The fatigue load spectra of the mooring line don't satisfy the normal theory probability distribution and the rain flow counting results needs to be used directly in calculating the fatigue damage.
- The main fatigue damage occurred in the chain segment, and the fatigue damage in the wire or polyester segment is relative much small. In the chain-wire-chain mooring line, the fatigue damage in the upper chain is obvious larger than in the bottom chain, while in the chain-polyester-chain mooring line the fatigue damage in the upper chain is almost the same as in the bottom chain.
- The replacement of polyester rope for the wire in chain-wire-chain mooring line provokes the fatigue damage which is much smaller for the polyester than for the wire, but simultaneously the fatigue damages of the upper and bottom chains in the chain-polyester-chain mooring line are larger than those in the chain-wire-chain mooring line.
- The nature of fatigue damage changes under corrosion effect is similar to that without corrosion. With the increasing corrosion years, the fatigue damage under each short-term sea state also increases.
- Under the corrosion effect, the increase of the fatigue damage of point A under long-term sea state is much larger than the one of point B and C. The corrosion effect increases the difference between the fatigue damage of the two mooring system types.

## ACKNOWLEDGEMENTS

This paper is funded in part by National Basic Research Program of China (Grant NO. 2011CB013702; 2011CB013703), National Natural Science Foundation of China (Grant NO. 51209037; 51221961), and China Postdoctoral Science Foundation Funded Project (Grant NO. 2013T60287), and Fundamental Research Funds for the Central Universities (Grant NO. DUT14RC(4)30).

## BIBLIOGRAPHY

1. K. T. Ma, A. Duggal, P. Smedley, D. L'Hostis, and H. B. Shu, "A historical review on integrity issues of permanent mooring systems," in Offshore Technology Conference, Houston, TX, USA, 2013.
2. J. Mohanraj, S. Cawthorne, S. Alverley, S. L. Fletcher, and J. Verwaayen, "Development of a new generation of innovative synthetic wire mooring ropes," in Offshore Technology Conference Brazil, Rio de Janeiro, Brazil, 2011.
3. J. W. Beck and N. J. Vandenworm, "Mooring system design for a circular hull shape FPSO floater with spar like responses," in Offshore Technology Conference Brazil, Rio de Janeiro, Brazil, 2011.
4. P. Barusco, "Mooring and anchoring systems developed in Marlin Field," in Offshore Technology Conference, Houston, Texas, 1999.
5. ISO, Petroleum and Natural Gas Industries-Specific Requirements for Offshore Structures-Part 7: Station Keeping Systems for Floating Offshore Structures and Mobile Offshore Units, 2005.
6. American Petroleum Institute-API, Recommended Practice for Design and Analysis of Station Keeping Systems for Floating Structures-API RECOMMENDED PRACTICE 2SK, 2005.
7. Det Norske Veritas-DNV, Offshore Standard-Position Mooring-DNV OS-E301, 2004.
8. J. Mathisen and K. Larsen, "Risk-based inspection planning for mooring chain," *Journal of Offshore Mechanics and Arctic Engineering*, vol. 126, no. 3, pp. 250-257, 2004.
9. T. Lassen, J. L. Arana, L. Canada, J. Henriksen, and N. K. Holthe, "Crack growth in high strength chain steel subjected to fatigue loading in a corrosive environment," in Proceedings of the 24th International Conference on Offshore Mechanics and Arctic Engineering, Halkidiki, Greece, 2005.
10. J. Mathisen, T. Hørte, V. Moe, and W. Lian, DEEPMOOR-design methods for deep water mooring systems, calibration of a fatigue limit state-DNV Report, No. 98-3110, 1999.
11. V. A. Omar, E. G. Bruno, and S. L. V. Sudati, "Fatigue analysis and reliability of floating production systems mooring lines in deepwater," in Proceedings of the 17th International Conference on Ocean, Offshore and Arctic Engineering, Lisbon, Portugal, 1998.
12. Z. Gao and T. Moan, "Wave-induced fatigue damage of mooring chain under combined non-gaussian low and wave frequency loads," in Proceedings of 25th International Conference on Offshore Mechanics and Arctic Engineering, Hamburg, Germany, 2006.
13. J. S. Han, Y. H. Kim, Y. J. Son, and H. S. Choi, "A comparative study on the fatigue life of mooring systems with different composition," in 9th International Conference on Hydrodynamics, Shanghai, China, 2010.
14. D. S. Qiao and J. P. Ou, "Calculation on fatigue damage of deepwater catenary hybrid mooring line," *Journal of Ship Mechanics*, vol. 16, no. 4, pp. 422-432,

- 2012.
15. 15. W. Huang, H. X. Liu, G. M. Shan, and C. Hu, "Fatigue analysis of the taut-wire mooring system applied for deep waters," *China Ocean Engineering*, vol. 25, no. 3, pp. 413–426, 2011.
  16. 16. Z. Gao, T. Moan, and S. E. Heggelund, "Time variant reliability of mooring system considering corrosion deterioration," in *Proceedings of the 24th International Conference on Offshore Mechanics and Arctic Engineering*, Halkidiki, Greece, 2005.
  17. 17. J. Lardier, T. Moan, and Z. Gao, "Fatigue reliability of catenary mooring lines under corrosion effect," in *Proceedings of the 27th International Conference on Offshore Mechanics and Arctic Engineering*, Estoril, Portugal, 2008.
  18. 18. American Petroleum Institute–API, *Recommended Practice for Design, Manufacture, Installation, and Maintenance of Synthetic Fiber Ropes for Offshore Mooring Upstream Segment–API RECOMMENDED PRACTICE 2SM*, 2001.
  19. 19. R. E. Melchers, T. Moan, and Z. Gao, "Corrosion of working chains continuously immersed in seawater," *Journal of Marine Science and Technology*, vol. 12, no. 2, pp. 102–110, 2007.
  20. 20. S. K. Chakrabarti, *Handbook of Offshore Engineering*, Elsevier, the Boulevard, Langford Lane, Kidlington, Oxford OX5 1GB, UK, 2005.
  21. 21. W. E. Cummins, *The Impulse Response Function and Ship Motions*, Washington DC, DTMB, Report No. 1661, 1962.
  22. 22. AQWA User Manual, AQWA-LINE Manual, Horsham, Century Dynamics Limited, 2006.
  23. 23. D. S. Qiao and J. P. Ou, "Global responses analysis of a semi-submersible platform with different mooring models in South China Sea," *Ships and Offshore Structures*, vol. 8, no. 5, pp. 441–456, 2013.
  24. 24. N. E. Dowling, "Fatigue failure predictions for complicated stress-strain histories," *Journal of Materials*, vol. 7, no. 1, pp. 71–87, 1972.

## **CONTACT WITH THE AUTOR**

Dongsheng Qiao, Ph. D  
 Faculty of Infrastructure Engineering,  
 Building 4#, Room 306,  
 Dalian University of Technology,  
 Linggong Road No.2, Dalian, Liaoning,  
 116024, China

Telephone: 8641184706742

Fax: 8641184706652

Email: qds903@163.com

# Comments on linear summation hypothesis of fatigue failures

Grzegorz Szala, Assoc. Prof.  
 West Pomeranian University of Technology, Poland

## ABSTRACT

*This paper presents a comparative analysis of results of fatigue life calculations with the use of the linear summation hypothesis of fatigue failures (LHSUZ), confronted with experimental test results. The calculations and fatigue tests were performed for variable amplitude (VA), two-step and ten-step loading conditions, both in the low-cycle fatigue (LCF) and high-cycle fatigue (HCF) range, for the case of C45 steel as an example. Experimental verification of the hypothesis LHSUZ did not reveal any significant influence of load level and form of load spectrum on conformity of results of the calculation by using the LHSUZ, to results of fatigue tests on C45 steel. However, it enabled to assess magnitude of a correction factor which appears in the considered linear hypothesis.*

**Keywords:** fatigue life calculations, summation hypothesis of fatigue failures, variable load

## INTRODUCTION

Calculations of durability of structural elements, including fatigue life of ship structures [1], [2], [3], require: to know a load spectrum expressed in the form of sinusoidal cycles of variable amplitude parameters ( $S_a$  or  $\epsilon_{ac}$ ) and their mean values ( $S_m$  and  $\epsilon_{mc}$ ), cyclic properties of a material in the form of the fatigue characteristics  $N(S)$ ,  $N(S_a, S_m)$  or  $2Nf(\epsilon_{ac})$ ,  $2Nf(\epsilon_{ac}, \epsilon_{mc})$ , and to assume a failure summation hypothesis which constitutes a phenomenological description of fatigue process in structural materials. The problems are associated with some factors which affect conformity of results of fatigue life calculations to those resulting from experimental tests.

In this paper the issue of the LHSUZ hypothesis is analyzed under assumption that load spectra and material fatigue characteristics are constant elements.

The first LHSUZ hypothesis was published by A. Palmgren in 1924, who described - in a phenomenological way - the fatigue process of ball bearings. In the 1930s the hypothesis was described again by a few authors, a.o. B. F. Langren in 1937, and M. A. Miner who formulated anew the hypothesis by applying energy approach, in 1945. In the subject-matter literature the hypothesis is sometimes called Palmgren-Miner (PM) hypothesis. In its original form it was assumed that in the case of multi-step loading program, fatigue fracture will occur if the following condition is satisfied:

$$D_{N_c} = \sum_{i=1}^k \frac{n_i}{N_i} = 1,0 \quad (1)$$

or in the case of a load spectrum given in the form of amplitude distribution:

$$D_{N_c} = \int_{S_{f(-1)}}^{S_{a \max}} \frac{dn}{N(S_a)} = 1,0 \quad (2)$$

For this hypothesis the authors assumed that only these load cycles whose amplitude values exceed fatigue limit, take place in the summation process of fatigue failures:

$$S_{a_i} \geq S_{f(-1)} \quad (3)$$

Experimental verification of PM hypothesis showed that in many cases its conformity to experimental test results is rather low. In the 1950s and 1960s, many publications dealing with modification of PM hypothesis, come out. In the modifications the following condition was assumed firstly:

$$D_{N_c} = \sum_{i=1}^k \frac{n_i}{N_i} = a \quad (4)$$

and secondly - that also loads below fatigue limit have a significant effect on conformity of results of calculations to those of experimental tests. Therefore, the load cycles of the amplitudes:

$$S_{a_i} \geq k \cdot S_{f(-1)} \quad (5)$$

were summed up, where the coefficient  $k$  is comprised in the range from 0,4 to 0,6.

In 1963, S.V. Serensen published a formula for calculation of the correction factor  $a$  in Eq. (4), depending on a form of load spectrum characterized by the spectrum diagram factor  $\zeta$  and maximum load value appearing in the load spectrum:  $S_{a \max} = S_{a_i}$

The factor  $a$  can be calculated by using the formula:

$$a = \frac{S_{a \max} \cdot \zeta - k \cdot S_{f(-1)}}{S_{a \max} - k \cdot S_{f(-1)}} \quad (6)$$

and, the spectrum diagram factor  $\zeta$  is described as follows:

$$\zeta = \frac{1}{S_{a \max}} \sum_{i=1}^k S_{a_i} \frac{n_i}{n_c} \quad (7)$$

In spite of these modifications, PM hypothesis has been criticized for the reason of a weak physical background concerning recognition of phenomena which occur in structural materials during fatigue process, including the fact of not taking into account the factor  $\zeta$  in non-linearity of run of failure summation in fatigue process, sequence of cyclic loads and difficulties in assessing the value of the correction factor  $a$ .

According to G. Wallgren (1949), value of the factor  $a$  is comprised in the range from 0,5 to 3,0. Schütz and Zenner (1973) determined a distribution of  $a$  – values on the basis of results of 561 tests conducted on structural elements made of iron alloys, aluminium and titanium. As results from the above mention distribution,  $a$  – values are contained in the variability range from 0,1 to 10. J. Szala (1980) obtained similar results from verification of PM hypothesis on the basis of a review of 75 publications. In 1957 A. J. Bielanin made research on influence of load level ( $S_{max}/S_{f(-1)}$  and  $S_{min}/S_{f(-1)}$ ) as well as the form of load spectrum expressed by its diagram factor  $\zeta$ . He conducted fatigue tests on toothed wheels and concluded from the test results that the greater the factor  $\zeta$  and the higher the stresses kept in their relevant ranges:  $S_{min} = (0,4 \div 1,2) S_{f(-1)}$  and  $S_{max} = (1,4 \div 2,0) S_{f(-1)}$ , the higher conformity between results of experiments calculations. As results from the form of Serensen's formula (6), the factor is less than 1 ( $a < 1,0$ ) and is closer and closer to 1 as the factor  $\zeta$  increases (the factor  $a = 1,0$  for  $\zeta = 1,0$  which corresponds to a load of constant amplitude).

The uncertainty of PM hypothesis has resulted (since 1970) in intensive searching for more effective hypotheses on fatigue failure summation, based on new definitions of fatigue failure.

Publication [4] contains a collection of formulae describing fatigue failures, based on analysis of variation of: longitudinal elasticity modulus, propagation velocity of ultra-sound wave, plastic deformation under cyclic load of constant stress variability range, stresses under conditions of constant strain variability range, plastic deformation work, micro-hardness, mean size of dislocation cell, distance between slip bands, number of micro-cracks per area unit etc. The publication in question presents 15 different formulae for calculation of the fatigue failure parameter  $D$  which, as far as PM hypothesis is concerned, is the ratio of the total number of applied cycles  $n$  and the number of cycles to fatigue failure  $N$ :

$$D_n = \frac{n}{N} \quad (8)$$

On the basis of the new definitions of fatigue failure, more than 30 hypotheses on summation of failures, applicable to fatigue life calculation, were developed.

In publication [5] they were divided into the following groups:

- linear summation hypotheses of fatigue failures,
- non- linear summation hypotheses of fatigue failures,
- hypotheses based on a concept of lines of constant fatigue failures and line of residual fatigue life.

The hypotheses were also split, in relation to fatigue failure parameter, into the groups with regard to stress, strain and energy approach, respectively.

Application of the above mentioned hypotheses in practice requires to have a comprehensive specialty knowledge because their applicability ranges are strictly limited and number of publications on their experimental verification is rather low. For these reasons they have not found any wider implementation so far.

As results from comparative analysis of the linear hypothesis and the hypotheses based on the concepts of constant failure lines as well as residual fatigue life line, the linear hypothesis is a particular case of the two remaining hypotheses.

In the 1990s and the first years of this century a few procedures for fatigue life calculation of machinery structural elements, ship structures and other objects were developed.

FITNET procedures [6] and those dealing with sea-going ship fatigue calculations [1], [2] as well as relevant requirements of ship classification societies, exemplify this kind of procedures. In the procedures, PM hypothesis with some modifications has been implemented. This fact has drawn again interest of scientists and engineers to research on verification of the hypothesis with the aim of determining a range of its applicability and to assess an impact of various factors on its conformity to experimental data.

For the first period (till the 1980s) the verifications have been conducted in rather not precisely defined conditions concerning applied loads, as well as structural features of tested objects.

The above presented observation justifies the made decision on undertaking the research project aimed at experimental verification of the linear summation hypothesis of fatigue failures, to be conducted in a broad range of variable amplitude loads for C45 steel, as an example. Scope of the research covered two-step and ten-step load programs at the stress ratio  $R = -1,0$  (oscillatory load) and magnitude of load amplitudes both within low-cycle fatigue (LCF) and high-cycle fatigue (HCF) range, and for widely varying values of spectrum diagram factor. The test conditions was so selected as to make it possible to analyse influence of load values (both in LCF and HCF range) and a form of spectrum (the factor  $\zeta$ ) and to prevent against influence of any additional factors (e.g. cycle counting methods for random loads, used for preparation of load spectra, or methods for determination of local stresses and deformations in notched elements).

## FORMULATION OF THE PROBLEM

On the basis of results of the calculations performed with the use of Eq. (1) and (2) and results of the experimental tests carried out under the same conditions, the correction factor  $a$  in Eq. (4) may be calculated by means of the following formula:

$$a = \frac{N_{cex}}{N_{cobl}} \quad (9)$$

For the case  $N_{cex} > N_{cobl}$ ,  $a > 1,0$  should be taken for fatigue life calculations, for  $N_{cex} = N_{cobl}$  -  $a = 1,0$ , and for  $N_{cex} < N_{cobl}$  -  $a > 1,0$ . When the above specified values of the factor  $a$  are assumed, results of the calculations according to Eq. 4 comply with results of the experimental tests.

### STATIC AND CYCLIC PROPERTIES OF C45 STEEL

The static and cyclic properties of C45 steel were determined from fatigue tests conducted in the framework of the research project No. NN 503 2221 39, titled „A hybrid method for fatigue life calculation and its verification by using results of fatigue tests of Al-alloys and steel,“ (the project has been financed by Polish Ministry of High Education and Science).

The static properties of C45 steel are the following:  $R_m = 682$  MPa,  $R_c = 458$  MPa,  $E = 2,15 \cdot 10^5$  MPa. Its cyclic properties are described by the following formulae:

- Wöhler diagram:

$$\log S_a = -0,1020 \log N + 2,9611 \quad (10)$$

- fatigue limit for  $N_0 = 106$  cycles:  $S_{f(-1)} = 223,5$  MPa

- Manson-Coffin diagram:

$$\varepsilon_{ac} = \frac{1204}{2,15 \cdot 10^5} (2N_f)^{-0,1033} + 0,2179 (2N_f)^{-0,475} \quad (11)$$

- fatigue limit for  $2N_0 = 2 \cdot 10^6$  cycles:  $\varepsilon_{acf} = 1,472 \cdot 10^{-3}$

- Ramberg-Osgood diagram:

$$\varepsilon_{ac} = \frac{S_a}{2,15 \cdot 10^5} + \left( \frac{S_a}{1232} \right)^{5,06} \quad (12)$$

### VARIABLE LOADS

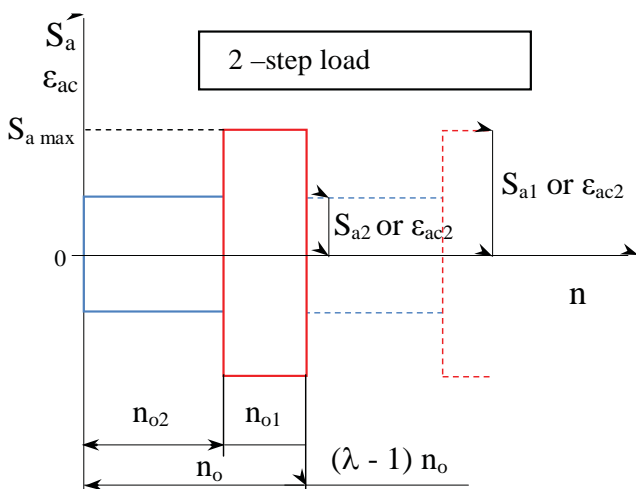


Fig. 1a. Schematic diagram of two-step load, with indicated relevant parameters which appear in fatigue life calculations and experimental tests.

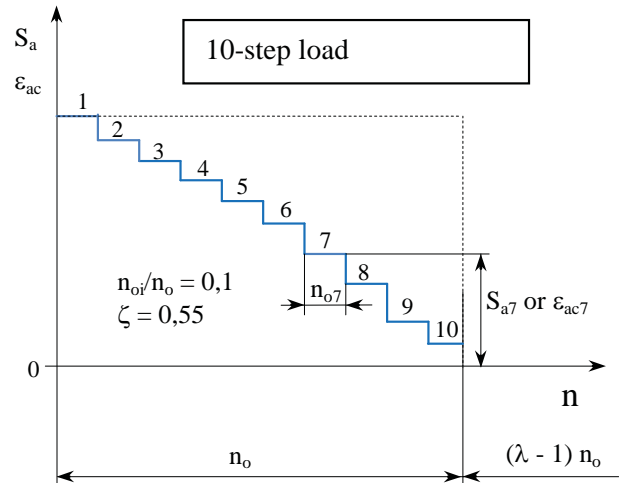


Fig. 1b. Schematic diagram of ten-step load, with indicated relevant parameters which appear in fatigue life calculations and experimental tests.

Fig. 1 shows schematic diagrams of two-step and ten-step loads where relevant parameters appearing in calculations and fatigue tests are also indicated. Form of two-step load spectrum is defined by the ratios:  $S_{a2}/S_{a1}$  or  $\varepsilon_{ac2}/\varepsilon_{ac1}$  and  $n_{o1}/n_o$  as well. On their basis, value of the spectrum diagram factor  $\zeta$  is calculated.

The calculations were conducted for  $S_{a2}/S_{a1} = 0,75; 0,5; 0,25$ , and  $n_{o1}/n_o = 0,75; 0,5; 0,25; 0,1$ . In the case of ten-step load spectra the same load increase per step, equal to  $0,1 S_{a1} (S_{a(i+1)} - S_{ai} = 0,1 S_{a1})$  and the same amount of cycles per step,  $n_{oi} = 0,1 n_o$ , were assumed for particular steps, which led to the value  $\zeta = 0,55$  calculated according to Eq. (7).

For both the cases the following levels of  $S_{a1}$  values (at stress approach): Level I -  $S_{a1} = 615$  MPa, Level II -  $520$  MPa, Level III -  $428$  MPa, and Level IV -  $325$  MPa, were assumed.

At strain approach, the following levels of  $\varepsilon_{ac1}$  values corresponding to the above given  $S_{a1}$  levels, were calculated by using Ramberg-Osgood formula (12): Level I -  $\varepsilon_{ac} = 4,24 \cdot 10^{-2}$ , Level II -  $2,22 \cdot 10^{-2}$ , Level III -  $8,93 \cdot 10^{-3}$ , Level IV -  $3,06 \cdot 10^{-3}$ .

The load levels were chosen under the assumption that in the extreme cases, i.e. Level I and  $S_{a2}/S_{a1} = 0,75$  or  $\varepsilon_{ac2}/\varepsilon_{ac1} = 0,75$ , the loads are entirely contained within LCF range, and for Level IV - within HCF range. The intermediate cases, i.e. load level II and III and lower values of  $S_{a2}/S_{a1}$  or  $\varepsilon_{ac2}/\varepsilon_{ac1}$ , contain only a part of steps within LCF range, and the remaining part of steps - within HCF range.

### METHOD OF CALCULATION AND METHOD OF EXPERIMENTAL TESTS

Detail calculation method based on PM hypothesis was described in the publication [7] where three calculation paths were assumed:

- 1<sup>st</sup> path - at stress approach - with the use of Wöhler diagram,
- 2<sup>nd</sup> path - at strain approach - with the use of Manson-Coffin diagram,

- 3<sup>rd</sup> path - hybrid calculation path covering strain - approach calculations of fatigue failures in LCF range, and stress- approach calculations of fatigue failure in HCF range.

Formulae, based on PM hypothesis, for calculation of fatigue failure resulting from one- step load program of the number of cycles  $n_0$ , are the following:

- for 1<sup>st</sup> path:

$$D_0 = \sum_{i=1}^k \frac{n_{0i}}{N_i} \quad (13)$$

- for 2<sup>nd</sup> path:

$$D_0 = \sum_{i=1}^k \frac{n_{0i}}{N_{fi}} \quad (14)$$

- for 3<sup>rd</sup> path:

$$D_0 = \sum_{i=1}^l \frac{n_{0i}}{N_{fi}} + \sum_{i=(l+1)}^k \frac{n_{0i}}{N_i} \quad (15)$$

Fatigue life expressed by a number of load program repetitions up to fatigue fracture,  $\lambda$ , is calculated from the formula:

$$\lambda = \frac{1,0}{D_0} \quad (16)$$

and the fatigue life expressed by a number of load cycles  $N_c$ , amounts to:

$$N_c = \lambda \cdot n_0 \quad (17)$$

The quantity 1,0 in the numerator of Eq. (16) shows that the calculations were conducted according to the original form of PM hypothesis described by Eq. (1). The yield point  $R_c$  was assumed to be a criterion for LCF and HCF ranges.

Experimental determination of fatigue life of specimens made of C45 steel was carried out by using the method of programmed fatigue tests consisting in multifold repetition

( $\lambda$  times) of program's period, in compliance with Fig. 1 [8], up to fatigue fracture of specimen.

## RESULTS OF CALCULATIONS AND TESTS

### TWO-STEP LOAD

Tab. 1 contains results of the fatigue life calculations and results of fatigue life tests conducted on specimens of C45 steel under two-step load conditions.

The specimens were prepared in accordance with PN-EN 10002-1;2004 standard for static tests and PN-84/H-04334 standard for fatigue tests, and then tested by using INSTRON 8501 testing machine in a laboratory having accreditation of Polish Centre of Accreditation (PCA) (Certificate No. AB 372).

On the basis of the results of the tests on 120 specimens, Gassner diagrams were prepared for particular load programs of different values of  $S_{a2}/S_{a1}$  and  $n_{01}/n_0$ . 12 diagrams of the kind were prepared altogether – they are described by the formulae shown in Tab. 2. Data contained in columns: 6, 10,

14 and 18 of Tab. 1, were calculated by means of respective formulae given in Tab. 2.

Values of  $N_c^S$ ,  $N_c^\varepsilon$ ,  $N_c^H$  given in Tab. 1 were calculated by using Eq. (13) through (17).

On the basis of the data contained in Tab. 1, values of the factor  $a$  were calculated with the use of Eq. (9). Results of the calculations are collected in Tab. 3, where the following notations are used, respectively:

- $a_s$  - the factor determined for fatigue life calculated according to 1<sup>st</sup> path ( stress approach)
- $a_\varepsilon$  - the factor determined for fatigue life calculated according to 2<sup>nd</sup> path ( strain approach)
- $a_H$  - the factor determined for fatigue life calculated according to 3<sup>rd</sup> path ( hybrid method).

### TEN - STEP LOAD

Programmed fatigue tests and fatigue life calculations for specimens made of C45 steel were conducted in a similar way as in the case of the above described calculations and tests for two-step load, and for the same values of  $S_{a1} = S_{amax}$  or  $\varepsilon_{acl} = \varepsilon_{acmax}$ .

On the basis of the tests on 15 specimens, a Gassner diagram described by the formula:

$$\log S_{amax} = -0,0983 \log N_c + 3,0124 \quad (18)$$

was prepared.

Tab. 2. Collection of formulae describing fatigue life diagrams (acc. Gassner) for specimens of C45 steel under two- step load.

$\frac{n_{01}}{n_0}$	$S_{a2}/S_{amax}$
	0,75
0,75	$\log S_{amax} = -0,0912 \log N_c + 2,9268$
0,5	$\log S_{amax} = -0,0995 \log N_c + 2,9747$
0,25	$\log S_{amax} = -0,1015 \log N_c + 2,9979$
0,1	$\log S_{amax} = -0,0906 \log N_c + 2,9826$
	0,50
0,75	$\log S_{amax} = -0,0977 \log N_c + 2,9443$
0,5	$\log S_{amax} = -0,1029 \log N_c + 2,9837$
0,25	$\log S_{amax} = -0,1013 \log N_c + 3,0133$
0,1	$\log S_{amax} = -0,0966 \log N_c + 3,0189$
	0,25
0,75	$\log S_{amax} = -0,1004 \log N_c + 2,9499$
0,5	$\log S_{amax} = -0,0981 \log N_c + 2,9684$
0,25	$\log S_{amax} = -0,0973 \log N_c + 3,0006$
0,1	$\log S_{amax} = -0,0876 \log N_c + 3,0060$

**Tab. 1.** Results of fatigue life calculations and results of fatigue life tests conducted on specimens of C45 steel under two-step load

No. of item	S <sub>a2</sub> /S <sub>a1</sub>	n <sub>01</sub> /n <sub>0</sub>															
		0,75				0,5				0,25				0,1			
		N <sub>c</sub> <sup>S</sup>	N <sub>c</sub> <sup>ε</sup>	N <sub>c</sub> <sup>H</sup>	N <sub>c</sub> <sup>Ex</sup>	N <sub>c</sub> <sup>S</sup>	N <sub>c</sub> <sup>ε</sup>	N <sub>c</sub> <sup>H</sup>	N <sub>c</sub> <sup>Ex</sup>	N <sub>c</sub> <sup>S</sup>	N <sub>c</sub> <sup>ε</sup>	N <sub>c</sub> <sup>H</sup>	N <sub>c</sub> <sup>Ex</sup>	N <sub>c</sub> <sup>S</sup>	N <sub>c</sub> <sup>ε</sup>	N <sub>c</sub> <sup>H</sup>	N <sub>c</sub> <sup>Ex</sup>
1	2	3	4	5	6	7	8	9	10	11	12	13	14	15	16	17	18
I	0,75	64	47	47	33	92	68	68	74	165	126	126	115	317	255	255	138
	0,5	65	47	47	39	97	71	71	78	194	142	142	164	482	354	352	241
	0,25	65	43	47	40	98	71	71	68	195	142	142	150	487	355	355	298
II	0,75	330	287	286	205	476	420	416	399	856	779	757	599	1642	1599	1492	878
	0,5	336	291	291	217	504	437	437	400	1006	873	872	860	2498	2178	2166	1367
	0,25	336	291	291	213	505	437	437	374	1009	874	874	839	2523	2185	2185	2017
III	0,75	2223	2480	2457	1739	3210	3630	3532	2823	5777	6771	6287	4081	11066	14082	11810	7538
	0,5	2267	2510	2510	1589	3398	3765	3761	2653	6780	7524	7504	5880	16837	18768	18622	10261
	0,25	2268	2511	2511	1482	3401	3766	3766	2718	6803	7531	7532	6197	17007	18824	18830	18549
IV	0,75	3301	5737	3301	3564	4766	8407	4766	4494	85682	15723	85682	6147	16432	32899	16432	15753
		5	7	5	0	4	3	4	7		0		1	2	4	2	2
	0,5	3365	5804	3365	2657	5045	8702	5045	3853	10067	17374	10067	8905	25001	43209	25001	17746
		9	8	9	6	1	1	1	9	6	0	6	5	2	8	2	1
	0,25	3367	5804	3367	2297	5050	8702	5050	4496	10101	17374	10101	1048	25253	43209	25253	31566
		1	9	1	9	7	1	7	4	4	0	4	07	3	8	3	6

S<sub>max</sub> : Level I – 615 MPa, Level II – 520 MPa, Level III – 428 MPa, Level IV – 325 MPa. ε<sub>ac1</sub> : Level I – 4,24·10<sup>-2</sup>, Level II – 2,22·10<sup>-2</sup>, Level III – 8,93·10<sup>-3</sup>, Level IV – 3,06·10<sup>-3</sup>.

N<sub>c</sub><sup>S</sup> - fatigue life calculated acc. 1<sup>st</sup> path, Eq. (13); N<sub>c</sub><sup>ε</sup> - fatigue life calculated acc. 2<sup>nd</sup> path, Eq. (14); N<sub>c</sub><sup>H</sup> - fatigue life calculated acc. hybrid method, Eq. (15); N<sub>c</sub><sup>Ex</sup> - fatigue life determined by means of programmed fatigue tests.

**Tab. 3.** Results of calculations of values of the correction factor a for C45 steel specimens under two-step load

No. of item	S <sub>a2</sub> /S <sub>a1</sub>	C45 steel															
		a = N <sub>c</sub> <sup>Ex</sup> /N <sub>obl</sub>															
		n <sub>01</sub> /n <sub>0</sub> = 0,75				n <sub>01</sub> /n <sub>0</sub> = 0,5				n <sub>01</sub> /n <sub>0</sub> = 0,25				n <sub>01</sub> /n <sub>0</sub> = 0,1			
1	2	3	4	5	6	7	8	9	10	11	12	13	14	15	16	17	18
I	0,75	0,9375	0,52	0,7	0,7	0,875	0,8	1,09	1,09	0,8125	0,7	0,91	0,91	0,775	0,44	0,54	0,54
	0,5	0,875	0,6	0,83	0,83	0,75	0,8	1,1	1,1	0,625	0,85	1,15	1,15	0,55	0,5	0,68	0,68
	0,25	0,8125	0,62	0,93	0,85	0,625	0,69	0,96	0,96	0,4375	0,77	1,06	1,06	0,325	0,61	0,84	0,84
II	0,75	0,9375	0,62	0,71	0,72	0,875	0,84	0,95	0,96	0,8125	0,7	0,77	0,79	0,775	0,53	0,55	0,59
	0,5	0,875	0,65	0,75	0,75	0,75	0,79	0,92	0,92	0,625	0,85	0,99	0,99	0,55	0,55	0,63	0,63
	0,25	0,8125	0,63	0,73	0,73	0,625	0,74	0,86	0,86	0,4375	0,83	0,96	0,96	0,325	0,8	0,92	0,92
III	0,75	0,9375	0,78	0,7	0,71	0,875	0,88	0,78	0,8	0,8125	0,7	0,6	0,65	0,775	0,68	0,54	0,54
	0,5	0,875	0,7	0,63	0,63	0,75	0,78	0,7	0,7	0,625	0,87	0,78	0,78	0,55	0,61	0,55	0,55
	0,25	0,8125	0,65	0,59	0,59	0,625	0,8	0,72	0,72	0,4375	0,91	0,82	0,82	0,325	1,09	0,99	0,99
IV	0,75	0,9375	1,08	0,62	1,08	0,875	0,94	0,53	0,94	0,8125	0,72	0,39	0,72	0,775	0,96	0,49	0,96
	0,5	0,875	0,79	0,46	0,79	0,75	0,76	0,44	0,76	0,625	0,88	0,51	0,88	0,55	0,71	0,41	0,71
	0,25	0,8125	0,68	0,4	0,68	0,625	0,89	0,52	0,89	0,4375	1,04	0,6	1,04	0,325	1,25	0,73	1,25

S<sub>max</sub> : Level I – 615 MPa, Level II – 520 MPa, Level III – 428 MPa, Level IV – 325 MPa. ε<sub>ac1</sub> : Level I – 4,24·10<sup>-2</sup>, Level II – 2,22·10<sup>-2</sup>, Level III – 8,93·10<sup>-3</sup>, Level IV – 3,06·10<sup>-3</sup>.

Tab 4 shows results of the calculations and tests for fatigue life of specimens under ten – step load . Values of the correction factor  $a$  for different methods of fatigue life calculations are given in columns : 7, 8 and 9 of this table; their notation is the same as that used in Tab. 3.

**Tab. 4.** Collected results of calculations and tests for fatigue life of specimens of C45 steel under ten – step load , and values of the correction factor  $a$  in PM hypothesis

$S_{a\max}$ MPa	$\epsilon_{ca\max}$	$N_c^S$	$N_c^e$	$N_c^H$	$N_c^{Ex}$	$a_s$	$a_e$	$a_H$
1	2	3	4	5	6	7	8	9
615	$4,24 \cdot 10^{-2}$	323	245	244	188	0,58	0,78	0,77
520	$2,22 \cdot 10^{-2}$	1675	1542	1515	1036	0,61	0,67	0,68
428	$8,93 \cdot 10^{-3}$	11288	13566	12129	7506	0,66	0,55	0,62
325	$3,06 \cdot 10^{-3}$	167612	325742	167612	123509	0,74	0,38	0,74

## ANALYSIS OF RESULTS OF CALCULATIONS AND TESTS

As results from the data in Tab. 3, values of the correction factor  $a$  are remarkably dispersed depending on a method used for fatigue life calculations ( acc. 1<sup>st</sup>, 2<sup>nd</sup> and 3<sup>rd</sup> path) and on load conditions. In the subject-matter literature, may be found only a few data concerning dependence of  $a$ -factor values on the spectrum diagram factor  $\zeta$  (variable load intensity) and load values contained in the spectrum. Eq. (6) formulated by Serensen may serve as an example of such attempt.

The further part of this analysis presents an attempt to investigate dependence of values of the factors  $a_s$ ,  $a_e$  and  $a_H$  on load levels (I, II, III and IV) and values of the spectrum diagram factor  $\zeta$ , and also to experimentally verify the formula (6).

### INFLUENCE OF LOAD LEVEL AND VALUE OF THE SPECTRUM DIAGRAM FACTOR $\zeta$

Exemplary data for the factor  $a_s$ , given in Tab. 3, are presented in the coordinate frame ( $\zeta$ ,  $a$ ), in Fig. 2.

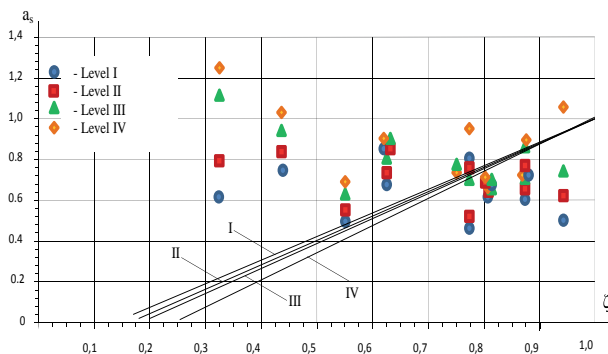


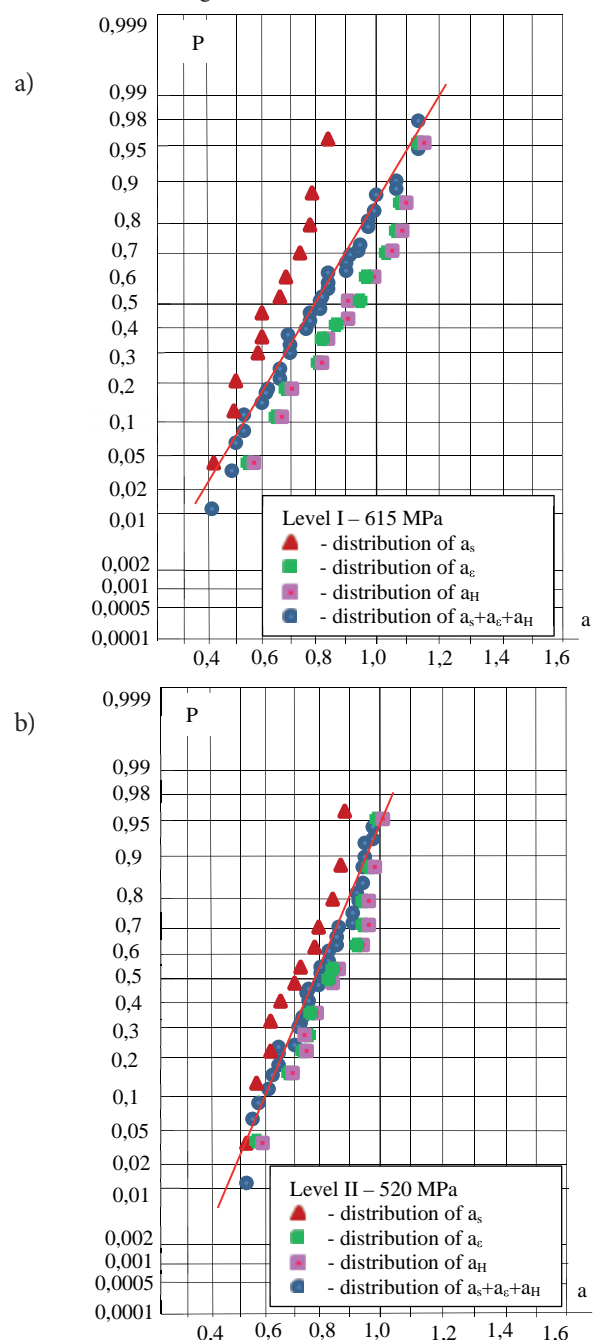
**Fig 2.** Diagrams of  $a$  – factor values calculated according to the formula (6)

As results from these data, values of the factor  $a$  are contained within the following ranges:

- from 0,44 to 1,15 for Level I ( $S_{a\max} = 615$  MPa;  $\epsilon_{ac\max} = 4,24 \cdot 10^{-2}$ ),
- from 0,53 to 0,99 for Level II ( $S_{a\max} = 520$  MPa;  $\epsilon_{ac\max} = 2,22 \cdot 10^{-2}$ ),
- from 0,54 to 1,09 for Level III ( $S_{a\max} = 428$  MPa;  $\epsilon_{ac\max} = 8,93 \cdot 10^{-3}$ ),
- from 0,4 to 1,25 for Level IV ( $S_{a\max} = 325$  MPa;  $\epsilon_{ac\max} = 3,06 \cdot 10^{-3}$ ).

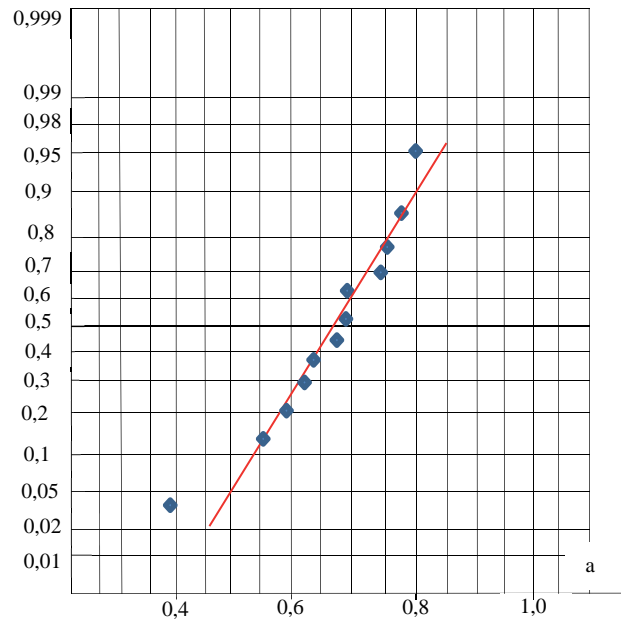
The  $a$ -factor values show no tendency to varying in function of the spectrum diagram factor  $\zeta$ .

Fig. 3 presents distributions of occurrence probability of  $a$ -factor values for particular load levels, depicted in normal distribution coordinate grid, whereas parameters of the distributions are given in Tab. 5.



**Tab. 5.** Parameters of probability distribution of a-factor values for particular load levels

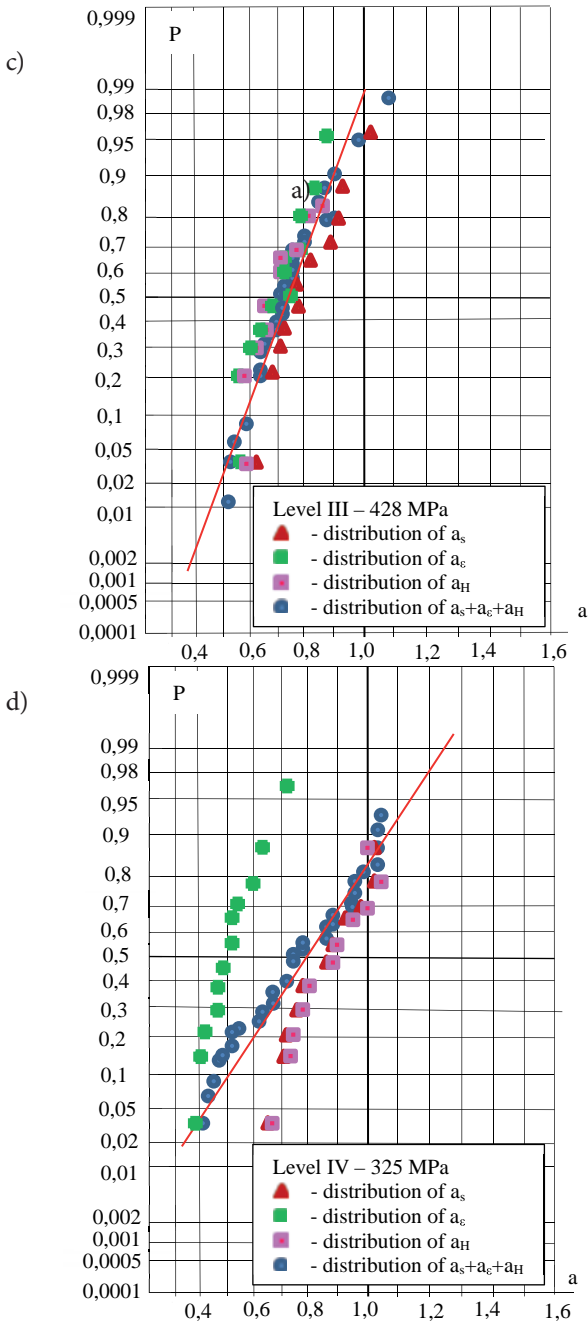
	Factor $a_i$	Mean value	Standard deviation	Skewness	Kurtosis
Level I	$a_s$	0,6583	0,1262	-0,1509	-1,1112
	$a_e$	0,8992	0,1815	-0,4812	-0,5981
	$a_H$	0,9267	0,2399	0,7908	1,5169
	$a = a_s + a_e + a_H$	0,8167	0,1997	0,0143	-0,9513
Level II	$a_s$	0,7108	0,1090	-0,2816	-1,3840
	$a_e$	0,8117	0,1362	-0,4382	-0,9255
	$a_H$	0,8183	0,1299	-0,3338	-1,2250
	$a = a_s + a_e + a_H$	0,7798	0,1343	-0,1429	-1,065
Level III	$a_s$	0,7875	0,1289	0,8982	0,9138
	$a_e$	0,7017	0,1249	0,7902	0,6932
	$a_H$	0,7067	0,1233	0,7514	0,7305
	$a = a_s + a_e + a_H$	0,7348	0,1283	0,7424	0,4617
Level IV	$a_s$	0,9283	0,2615	2,1647	5,7703
	$a_e$	0,5300	0,1556	2,3016	6,3149
	$a_H$	0,9283	0,2615	2,1647	5,7703
	$a = a_s + a_e + a_H$	0,7959	0,2987	1,2584	2,5523
Results of the tests under 10-step load conditions					
	$a = a_s + a_e + a_H$	0,6483	0,1077	-1,1501	1,8387



**Fig. 4.** Probability distribution of values of the factor  $a = a_s + a_e + a_H$  for ten-step load conditions

### EXPERIMENTAL VERIFICATION OF SERENSEN FORMULA

The Serensen's formula (6) takes into account influence of the spectrum diagram factor  $\zeta$  and load level on magnitude of the factor  $a$  in the modified PM hypothesis. As results from the form of the formula, value of the factor  $a$  increases along with the spectrum diagram factor  $\zeta$  and load level increasing. These relations have not found any confirmation in the test results analyzed in this work. The conclusion is illustrated in Fig. 2 where results of the tests and calculation of the factor  $a$  were used as an example.



**Pic. 3.** Distributions of occurrence probability of values of the factors:  $a_s$ ,  $a_e$  and  $a_H$  and the joint distribution of  $(a_s + a_e + a_H)$ : a) - for load level I, b) - for load level II, c) - for load level III, d) - for load level IV.

As results from the data in Tab. 5 and the diagrams in Fig. 3 and 4, mean value of the factor  $a$  decreases along with stress values increasing, in the range from 0,9283 to 0,658, value of the factor  $a_e$  increases along with strain values increasing, in the range from 0,53 to 0,8992. Variability of the factor  $a_H$  is the lowest and only a little dependent on load level, and comprised in the range from 0,7067 to 0,9286. It shows that the hybrid calculation method is useful in the case when the loading belongs both to LCF and HCF ranges.

As results from the data given in Tab. 5 and the diagrams in Fig. 3 and 4, the lower limit for values of the factors  $a_s$ ,  $a_e$  and  $a_H$  is equal to 0,5, that proves assumptions made for fatigue calculation procedures (e.g. FITNET procedures [6]) to be correct.

As results from Fig. 2, for low values of the factor  $\zeta$  ( which most often occur in service loads of structural elements) the calculation results for the factor  $a$  greatly differ from these experimental, likewise in the case of high values of the factor  $\zeta$ , where the calculation results of the factor  $a$  bring values much greater than experimental ones.

Another disadvantage of the discussed formula (6) is that negative values of the factor  $a$  ( $a < 0$ ) may arise in the case when value of the factor  $\zeta < k \frac{S_{f(-1)}}{S_{\sigma_{max}}}$ , which takes place at low values of  $S_{\sigma_{max}}$  (usually occurring in HCF range ).

### A CONCEPT OF DESCRIPTION OF MAGNITUDE OF THE CORRECTION FACTOR A

The below proposed concept of description of magnitude of the correction factor  $a$  in PM linear summation hypothesis of fatigue failures, consists in determining such variability ranges for the factor  $a$ , which would make it possible to delineate a domain for safe calculation results.

The empirical formula (19) which describes a lower limiting line for the set of experimental data, was developed on the basis of the test results given in Tab. 3. Values of the factor  $a$ , which lay below the limiting line, provide, as a result of calculations, a fatigue life which is lower than that experimentally obtained, therefore this result lies in the safe calculation domain.

The form of the above mentioned formula is as follows :

$$a_s = A \cdot S_{\sigma_{max}}^{-1} \cdot \zeta^d + a_0 \quad (19)$$

where the constants:  $A$  and  $d$  are experimentally determined, whereas value of  $a_0$  represents a lower limit for the results predicted on the basis of experimental data or literature sources.

Such data , for the case of tests and calculations according to stress approach, described in this paper , are the following :  $A = 1,3$ ;  $d = -4,3$  and  $a_0 = 0,5$ .

Fig. 5 shows a graphical illustration of the formula (19) for the data taken from the calculations and tests of the factor  $a_s$ . Similar analysis may be performed for values of the factors  $a_e$  and  $a_H$ . Tab. 6 contains comparison of results of the calculations for the factor  $a_s$  according to the formulae (6) and (19). As results from the comparison, values of the factor  $a_s$  significantly differ both in relation to  $S_{\sigma_{max}}$  and the factor  $\zeta$ .

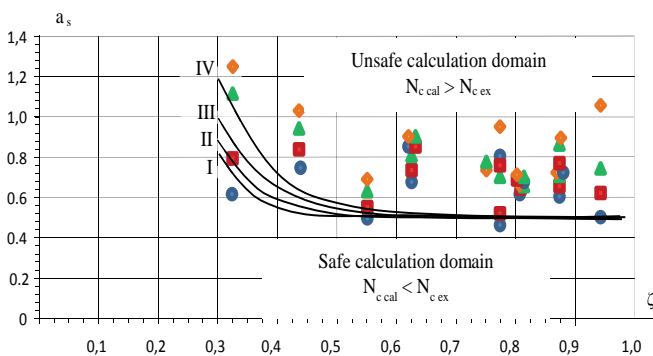


Fig. 5. Limiting lines for experimentally determined values of the factor  $a_s$

Tab. 6. Collected calculation results of the factor  $a_s$ , according to Eq. (6) and (19)

No.	$S_{\sigma_{max}}$	$\zeta$					Acc. Eq.
		0,3	0,4	0,5	0,7	0,9	
1.	615	0,18	0,29	0,41	0,64	0,88	(6)
2.		0,88	0,61	0,54	0,51	0,50	(19)
3.	520	0,15	0,27	0,40	0,64	0,88	(6)
4.		0,95	0,63	0,55	0,51	0,50	(19)
5.	428	0,12	0,24	0,37	0,62	0,87	(6)
6.		1,04	0,66	0,56	0,51	0,50	(19)
7.	325	0,03	0,17	0,31	0,59	0,86	(6)
8.		1,2	0,71	0,58	0,52	0,50	(19)

### CONCLUSIONS

1. No unambiguous recommendations concerning modification of LHSUZ hypothesis may be found in literature sources, including procedures for fatigue calculation of ship structures.

2. As results from experimental verification of the linear summation hypothesis of fatigue failures, the original form of the hypothesis (acc. Palmgren and Miner) provides, as a result of calculations, much higher fatigue life than that experimentally determined; such result lies in unsafe fatigue life domain.

3. Effectiveness of fatigue calculations may be improved by implementing the correction factor  $a$  in the linear summation hypothesis of fatigue failures. Lack of any method for assessing its magnitude makes its application difficult. The data searched from literature sources in which values of the factor  $a$  have been analyzed, are ambiguous, and in the extreme cases they show values from 0,1 to 10.

4. As results from the analysis presented in Subsection 4.2, the Serensen's formula (6), in case of C45 steel, does not comply with the experimental data over the whole variability range of the spectrum diagram factor  $\zeta$ , and in the extreme case of low  $\zeta$  - values, value of the factor  $a$  lies below zero, which is completely pointless.

5. The concept of delineation of a lower limiting line for the magnitude of the factor  $a$  (described in Subsection 4.3) makes it possible to conduct calculations in the safe fatigue life domain by choosing an appropriate value of the correction factor  $a$ .

6. Analysis of distributions of  $a$  - factor values indicates that the value  $a = 0,5$  which is assumed in the calculation procedures [6], corresponds to a low probability ( $P \leq 0,05$ ) of the exceeding, in calculations, of experimentally determined fatigue life.

7. On the basis of the analysis of the distributions of  $a$  - factor values achieved according to stress approach ( $a_s$ ), strain approach ( $a_e$ ) and hybrid one ( $a_H$ ), respectively, it may be concluded that results of the fatigue life calculations according to the hybrid method are the nearest to experimental test results. Moreover, the calculation results of the factor  $a_H$  show the smallest spread and are most close to 1,0 within the whole variability ranges of loads and the spectrum diagram factor  $\zeta$ .

## ACKNOWLEDGEMENTS

This work has been financed by Polish Ministry of Higher Education and Science in the frame of the research project No. 2221/B/T02/2010/39.

## BIBLIOGRAPHY

1. Fricke W., Petershagen H., Paetzold H.: Fatigue Strength of Ship Structures, Part I: Basic Principles, Germanischer Lloyd, Hamburg, pp. 34-36, 1997.
2. Fricke W., Petershagen H., Paetzold H.: Fatigue Strength of Ship Structures, Part II: Examples. Germanischer Lloyd, Hamburg, pp. 20-21, 1998.
3. Polish Register of Shipping (Polski Rejestr Statków): Fatigue strength analysis of ship steel hull ( in Polish), PRS Publ. No. 45/P, Gdańsk, pp. 35-43, 1998.
4. Szala J., Boroński D.: Assessment of state of material fatigue in diagnostics of machines and devices ( in Polish). Publ. Institute of Operation Technology – PIB, Bydgoszcz – Radom, 2008.
5. Szala J.: Hypotheses on summation of fatigue failures ( in Polish), ATR Publishers (Wydawnictwa Uczelniane ATR), Bydgoszcz, 1998.
6. Kocak M. ( Ed.), Webster S., Janosch J. J., Ainsworth R. A., Koers R.: FITNET Fitness-for-Service procedure-Final Drift. MK7, 2006.
7. Szala G., Ligaj B.: Comparative analysis of fatigue life calculation methods of C45 steel in conditions of variable amplitude loads in the low- and high-cycle fatigue ranges, Polish Maritime Research, No 4(76), Vol 19, 2012.
8. Ligaj B.: Influence of selected load programs generated from correlation table, on fatigue life of 18G2A steel (in Polish). Maintenance Problems, 3/2007, Radom, 2007.

## CONTACT WITH THE AUTOR

Grzegorz Szala, Assoc. Prof.  
West Pomeranian University of Technology  
Faculty of Mechanical Engineering and Mechatronics  
7 Kaliskiego Street  
85-789 Bydgoszcz  
Poland  
Email: gszala@utp.edu.pl

## NOMENCLATURE OF MAJOR NOTATIONS

$D_{Nc}$	- fatigue failure corresponding to fatigue fracture,
$D_0$	- fatigue failure resulting from $n_0$ load cycles,
$a$	- correction factor in the LHSUZ – general notation,
$a_s$	- correction factor in the LHSUZ – at stress approach,
$a_\varepsilon$	- correction factor in the LHSUZ – at strain approach,
$a_H$	- correction factor in the LHSUZ –at hybrid approach,
$k$	- number of load steps in a load program,
$l$	- number of load steps in a load program of LCF range,
$N$	- number of load cycles up to fatigue damage under sinusoidal load – general notation (fatigue life),
$N_c$	- fatigue life expressed by number of load cycles, determined in programmed load conditions,
$N_{fi}$	- number of load cycles up to fatigue fracture read from Manson-Coffin fatigue diagram for the total strain $\varepsilon_{aci}$ ,
$N_i$	- number of load cycles up to fatigue fracture read from Wöhler diagram for the stress amplitude $S_{ai}$ ,
$N_0$	- basic number of load cycles corresponding to fatigue limit,
$n_0$	- number of load cycles within the load program period,
$n_{01}$	- number of cycles in 1 <sup>st</sup> step of load program within its period,
$n_{0i}$	- number of cycles in $i$ th step of load program within its period,
$R = S_{min}/S_{max}$	- stress ratio,
$R_e$	- yield stress, MPa,
$R_m$	- tensile stress, MPa,
$S$	- stress – general notation, MPa,
$S_{max}$	- maximum stress in sinusoidal load cycle, MPa,
$S_{min}$	- minimum stress in sinusoidal load cycle, MPa,
$S_a = 0,5(S_{max} - S_{min})$	- stress amplitude in sinusoidal load cycle, MPa,
$S_m = 0,5(S_{max} + S_{min})$	- mean stress in sinusoidal load cycle, MPa,
$\varepsilon_{ac}$	- total strain,
$\varepsilon_{mc}$	- mean strain,
$\zeta$	- spectrum diagram factor,
$\lambda$	- number of program period repetitions up to fatigue fracture,
LCF	- low-cycle fatigue,
HCF	- high-cycle fatigue,
$S_{f(-1)}$	- fatigue limit determined under oscillatory sinusoidal load conditions ( $R = -1$ ),
$A, d, a$	- constants in Eq. (19).

# Application of alcohols to dual – fuel feeding the spark-ignition and self-ignition engines

Zdzisław Stelmasiak, Prof.  
Gdynia Maritime University

## ABSTRACT

*This paper concerns analysis of possible use of alcohols for the feeding of self-ignition and spark-ignition engines operating in a dual-fuel mode, i.e. simultaneously combusting alcohol and diesel oil or alcohol and petrol. Issues associated with the requirements for application of bio-fuels were presented with taking into account National Index Targets, bio-ethanol production methods and dynamics of its production worldwide and in Poland.*

*The considerations are illustrated by results of the tests on spark-ignition and self-ignition engines fed with two fuels: petrol and methanol or diesel oil and methanol, respectively. The tests were carried out on a 1100 MPI Fiat four-cylinder engine with multi-point injection and a prototype collector fitted with additional injectors in each cylinder. The other tested engine was a SW 680 six-cylinder direct-injection diesel engine. Influence of a methanol addition on basic operational parameters of the engines and exhaust gas toxicity were analyzed. The tests showed a favourable influence of methanol on combustion process of traditional fuels and on some operational parameters of engines. An addition of methanol resulted in a distinct rise of total efficiency of both types of engines at maintained output parameters (maximum power and torque). In the same time a radical drop in content of hydrocarbons and nitrogen oxides in exhaust gas was observed at high shares of methanol in feeding dose of ZI (petrol) engine, and 2-3 fold lower smokiness in case of ZS (diesel) engine. Among unfavourable phenomena, a rather insignificant rise of CO and NOx content for ZI engine, and THC and NOx – for ZS engine, should be numbered. It requires to carry out further research on optimum control parameters of the engines. Conclusions drawn from this work may be used for implementation of bio-fuels to feeding the combustion engines.*

**Keywords:** dual-fuel engine, alcohol, share of methanol, overall efficiency, toxicity

## Introduction

Necessity of using bio-fuels results from the requirements of National Index Targets (NCW) in which a gradual rise in share of reproducible fuels in overall amount of engine fuels, is assumed. According to a Polish Ministry Council's act concerning the NCW, dated 20.07.2013, share of bio-fuel energy should reach 8,5% in 2018, Fig. 1. It requires to introduce many changes in agricultural production industry, to rise investment expenditures for development of bio-fuel production works and to develop new fuel supply technologies for engines.

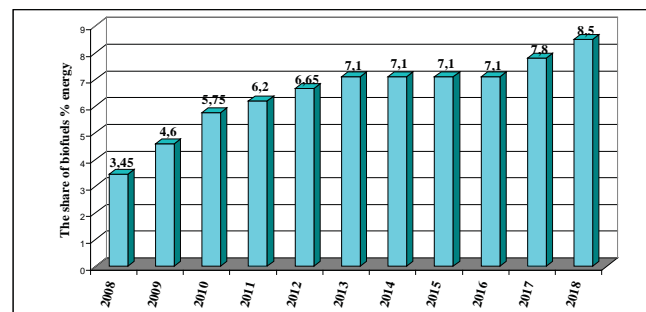
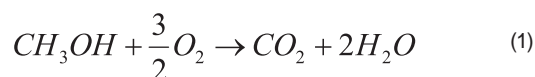


Fig. 1. Time rise in share of bio-fuels, acc. the NCW (National Index Targets)

Alcohols and esters of unsaturated fatty acids belong to the basic bio-fuels, the first group is applicable mainly to spark

ignition engines and the other – to diesel engines. Primary alcohols, i.e. methanol and ethanol can be produced from biomass which is a reproducible source of energy available in a very large quantity. In the nature bio-mass undergoes natural decomposition into carbon dioxide ( $\text{CO}_2$ ) and methane ( $\text{CH}_4$ ), both numbered among greenhouse-effect gases. However, due to the fact that bio-mass decay processes are natural, emission of  $\text{CO}_2$  and  $\text{CH}_4$  is not considered harmful. Exploitation of bio-mass and its conversion into alcohols and then combustion in engines results in  $\text{CO}_2$  emission to atmosphere, which is then consumed in photosynthesis process for production of biomass. In effect, use of bio-fuels may be considered a zero-emission process, in the aspect of  $\text{CO}_2$ , and that which additionally lowers natural emission of  $\text{CH}_4$  during decay processes.

Combustion of methanol and ethanol produces in effect carbon dioxide and water and the process runs according to the reaction as follows:



Mass share of carbon atoms in molecule of alcohols is lower in relation to traditional fuels and amounts to 0,375 for methyl alcohol and 0,520 for ethyl alcohol, whereas for petrol and diesel oil the ratio reaches 0,845 ÷ 0,850 approximately. However when differences in calorific values are taken into account, the gaining of the same energy amount from alcohols results in only a little lower  $\text{CO}_2$  emission (by about 2%) in comparison to petrol, Fig. 2. Alcohols, due to their perfect properties, first of all high octane number, high vapour heat, high combustion velocity, can be easily used both in spark ignition (ZI) engines (as only fuel or an addition to traditional fuels) and self-ignition (ZS) engines as an addition burned simultaneously with diesel oil.

This paper presents a proposal of feeding ZI and ZS engines by using a dual-fuel mode and shows some results of the tests conducted on the spark-ignition engine Fiat 1100 MPI and the self-ignition engine SW 680.

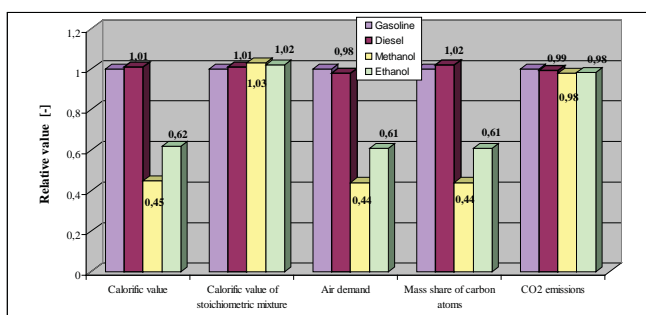


Fig. 2. Comparison of selected properties of liquid fuels in relation to petrol (gasoline) (for petrol the relative indices are equal to 1,0)

## Production of alcohols

Alcohols are chemical organic compounds which contain one or more OH hydroxyl groups connected with carbon atoms. The simplest alcohols known to people for thousands of years contain one OH group and are of a general formula:  $\text{C}_n\text{H}_{2n+1}\text{OH}$ . The following kinds belong to this group:

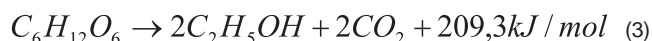
- methanol  $\text{CH}_3\text{OH}$  – methyl alcohol,
- ethanol  $\text{C}_2\text{H}_5\text{OH}$  – ethyl alcohol,
- propanol  $\text{C}_3\text{H}_7\text{OH}$  – propyl alcohol,
- butanol  $\text{C}_4\text{H}_9\text{OH}$  – butyl alcohol.

From the point of view of engine fuels, the two first, methanol and ethanol, especially the second which can be produced from biomass in large quantities by using technologies known for centuries, are most important. Anhydrous ethanol may be used as an only fuel E100 or as an addition to petrol of the kinds: E15, E20, E80. The remaining alcohols such as propanol and butanol are very rarely applied. Ethanol can be produced according to two technological methods schematically shown in Fig. 3:

- 1st generation method – in the conventional fermentation process of such raw plant materials as corn, potatoes, sugar reed, manioc, maize,
- 2nd generation method – with the use of cellulose, straw, maize cores, and other plant residuals.

Production of bioethanol based on 1st generation process is most often applied today, and research and development projects on 2nd generation biofuels are very intensively conducted worldwide. Full mastering of this technology is expected to be reached till 2030, and 2nd generation ethanol should be more widely used to this date as raw materials for it are commonly available [8].

Ethyl alcohol is obtained in fermentation process consisting in oxygen-free decomposition of sugars by yeasts and their enzymes. In general the alcohol fermentation equation has the following form:



Heat produced during the reaction (3) accelerates this process. As a result, many by-products such as vinegar acid, higher alcohols, esters, glycerine, are obtained. Their content and amount decide on taste merits of alcohol, however it is of no importance for application to fuels because their share is very low. The raw materials used for fermentation may be split into three groups:

- Containing sugar – mellase, sugar reed, fruits, juices,
- Containing starch – potatoes, rye, barley, wheat, maize,
- Containing cellulose – wood, straw, maize cores, plant waste, garbage.

Two first groups of raw materials are used for production of 1st generation bioethanol and edible ethanol; the third group – in production of 2nd generation bioethanol.

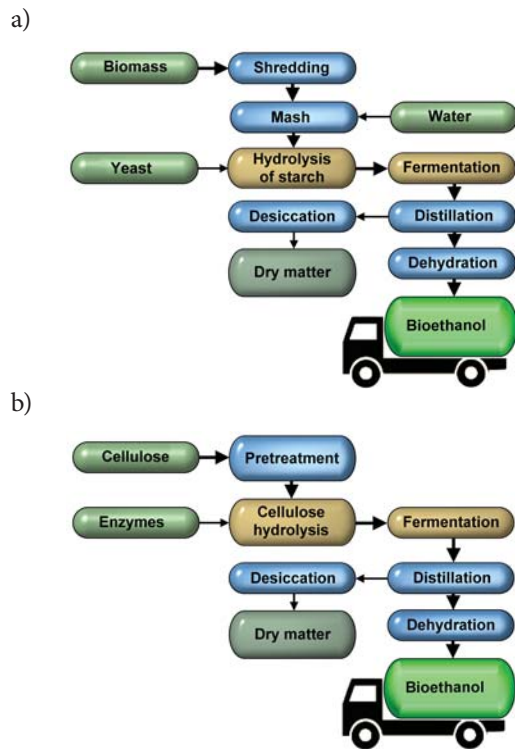


Fig. 3. Schematic diagrams of bioethanol production process: a) 1st generation bioethanol, b) 2nd generation bioethanol.

In fermentation process of 2nd generation ethanol, glucose obtained from enzymatic hydrolysis of cellulose contained in plant products, is used. They are composed of cellulose in about 60%, which, due to a large amount of biomass available worldwide, shows that significant supply of cellulose-based ethanol may be expected in the future. For this reason the 2nd generation production technologies are intensively developed in such countries as: Sweden, Norway, Finland, USA, Brazil and Canada. In present, production cost of cellulose ethanol is over twice higher than of that traditionally produced. However, development of 2nd generation bioethanol should lower the relations in a near future.

In present, USA and Brazil, leaders in alcohol production, deliver almost 65% of ethanol amount produced in the world, Fig. 4. European countries deliver about 15% of the ethanol produced in the world, but this share has significantly increased during last years. [7].

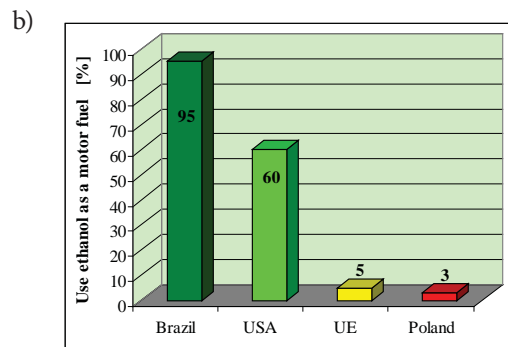
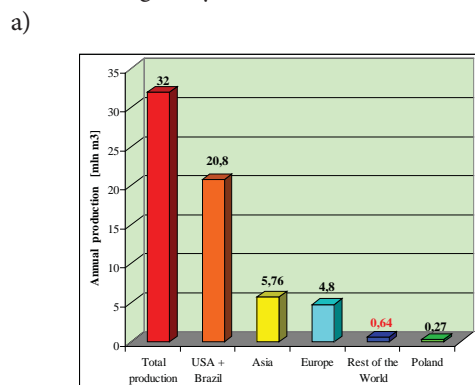


Fig. 4. Comparison of production and use of alcohols in selected countries worldwide: a) world production of ethanol in 2009 [9, 10, 11], b) use of ethanol as a fuel for engines [9, 12, 13]

In Brazil and USA a prevailing part of produced ethanol is intended for combustion as fuels (95% in Brazil and 60% in USA). For comparison, in European countries this part amounts to about 5%, and in Poland to 3% only, Fig. 4b.

Production of bioethanol in Poland does not satisfy demands of National Index Targets, and its participation in the whole quantity of used fuels is rather low, Fig. 5. Despite investments made in biofuel production industry within last ten years, rise in bioethanol production is rather low, and its level varies in particular years, Fig. 5a. It seems that without any radical change of regulations in this question and a decisive state intervention, Poland will gradually lag behind other EU countries where a big pressure is applied to production of bioethanol.

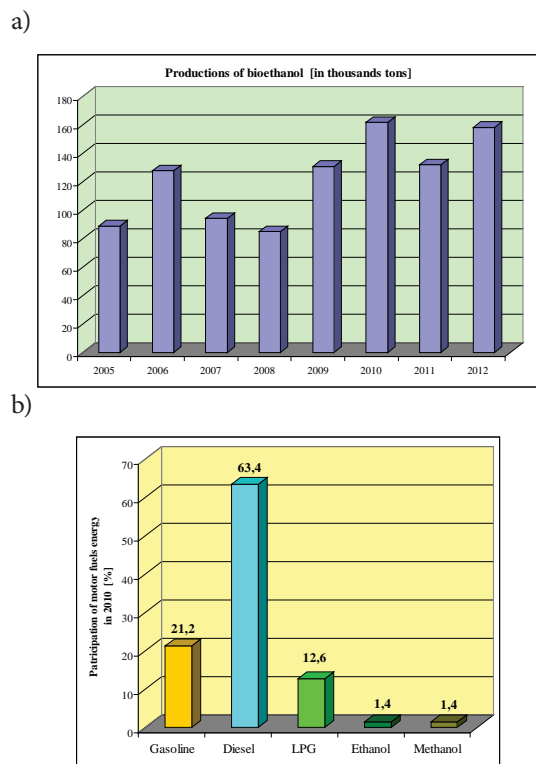
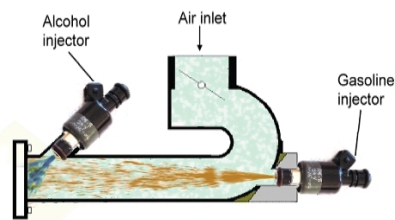


Fig. 5. Dynamic growth of bioethanol production and use of alcohols in Poland: a) production of bioethanol in Poland in the years 2005-2012 (acc. [7]), b) energy participation of engine fuels used in Poland in 2010 [14]

## Dual-fuel feeding the spark - ignition engines with the use of alcohol

In contemporary ZI engines multi-point injection of light fuels is used ( indirect injection to inlet collector and direct one to combustion chamber). This injection system was assumed to select a test engine and prepare it to dual-fuel feeding mode. The tests were carried out on a 1100 MPI Fiat, four-cylinder , spark- ignition engine with multi-point fuel injection system. In order to adjust the engine to dual-fuel feeding mode a prototype inlet collector with an additional injector in each cylinder, was applied, Fig. 6a. Methanol was injected close to inlet valve through original injectors of the engine. Petrol , during work of engine in dual-fuel mode , was injected by additional injectors placed in some distance from the inlet valve. Such injection method was aimed at improving methanol evaporation, especially during engine work under low load. The applied feeding system made it possible to operate with petrol only (during starting and heating the engine) , with methanol only during work under maximum load , and in dual – fuel mode at an arbitrary selected share of alcohol. The prototype feeding system was subjected to wide comparative and optimizing tests. In each work conditions the engine operated correctly and did not show any possible disturbance resulting from vibrations or indicator - controlled combustion process. Tab. 1 and Fig. 6b contain technical data of the engine.

a)



b)

Tab. 1. Technical data of 1100 MPI Fiat engine

Type of engine	Fiat 1100 MPI
Cylinder bore x stroke	70 x 72 mm
Stroke volume	1108 cm <sup>3</sup>
Compression ratio	9,6
Rated power/ rotational speed	40 kW/5000 rpm
Torque/ rotational speed	88 Nm/3000 rpm

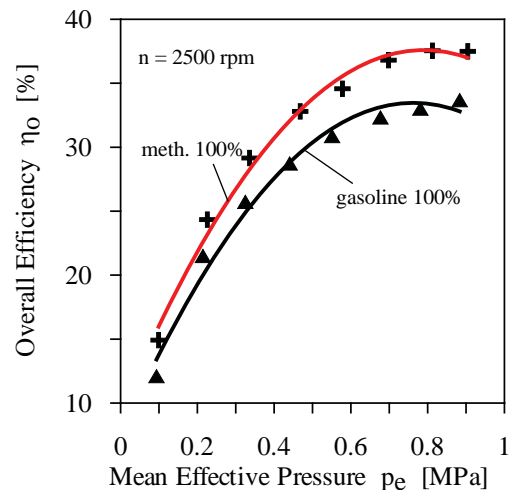
Fig. 6. Feeding system and technical data of 1100 MPI Fiat engine used for the tests: a) Scheme of the prototype inlet collector; b) Technical data of the tested engine

Comparison of overall efficiency of the engine shown in Fig. 7 indicates that efficiency of the engine fed with methanol only was high within the whole range of changes in loading and rotational speed. Differences in efficiency grow along with engine load rising, and in the range of medium and maximum load values the absolute differences amount to 3,5%, which results in a relative rise in efficiency ranging from

10 to 16%, deciding on operational consumption of energy. It is worth mentioning that the results were obtained without any optimization of ignition advance angle.

It seems that one of the causes of engine efficiency growth may be a greater combustion velocity of methanol, which leads to lower heat loss per cycle. The other cause is a higher evaporation heat of methanol which makes dose temperature lower during compression and at the beginning of combustion , that leads to lower mechanical losses during compression phase and in consequence to a higher efficiency. An additional reason may be a greater contraction factor of methanol in comparison to petrol (1,061 for methanol and 1,045 for petrol), which results in that from combustion of stoichiometric mixture of methanol a greater number of moles of exhaust gas is produced, which additionally rises cylinder pressure and leads to torque rising. Further increase of engine work parameters can be obtained by rising compression ratio and optimizing engine control.

a)



b)

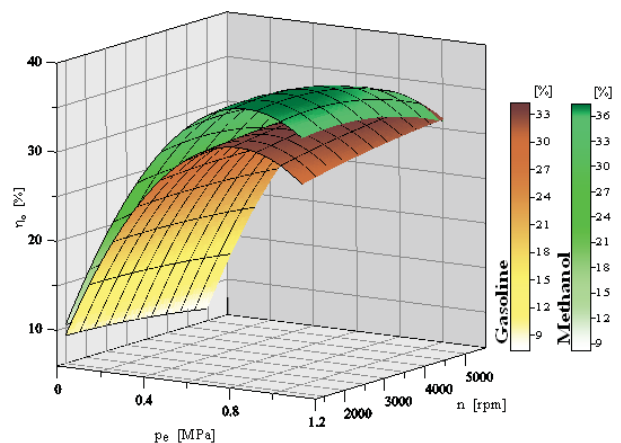


Fig. 7. Comparison of overall efficiency of 1100 MPI Fiat engine in case of feeding with petrol or methanol

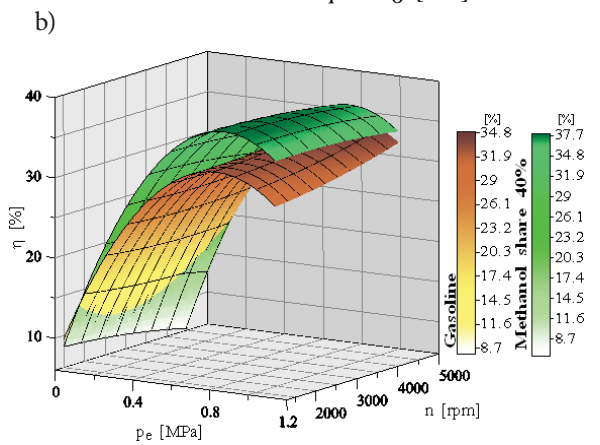
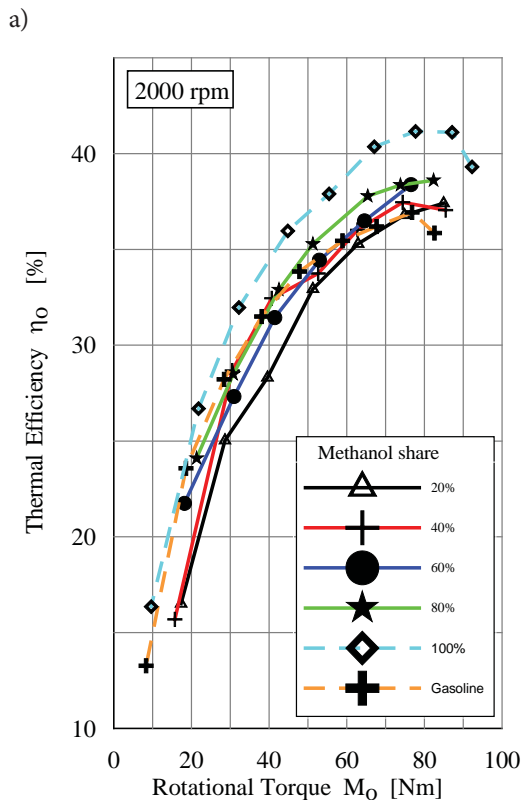


Fig. 8. Comparison of overall efficiency of 1100 MPI Fiat engine in case of feeding with petrol or two fuels at various shares of methanol

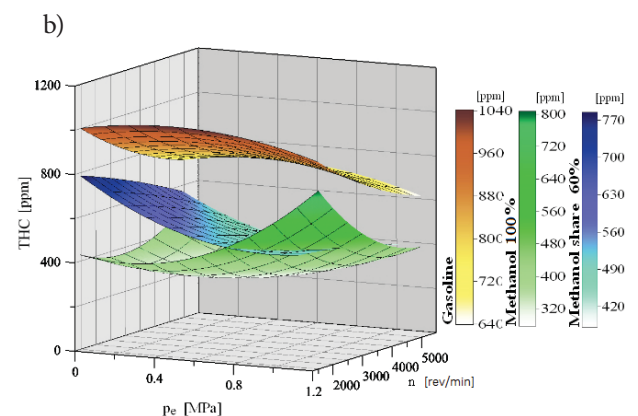
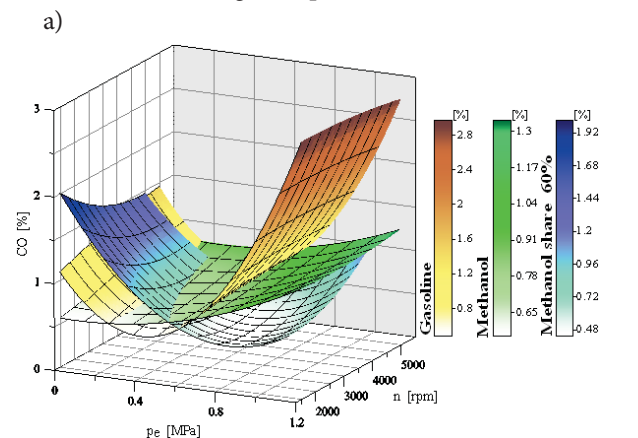
For small addition of methanol (20% share) and low engine load the overall efficiency of the dual-fuel fed engine was lower than in case of traditional feeding, Fig. 8. It seems that the fact of petrol injection through the additional injector placed in some distance from the inlet valve, affected the obtained results. As a result, conditions for producing petrol-air mixture were worsened (lower temperature, influence of fuel film formed on inlet channel walls). It may affect work steadiness in particular cylinders and increase fuel consumption and emission of noxious components of exhaust gas. In effect, the favourable influence of combustion of methanol, proportional to its dose share, did not compensate the loss in efficiency resulting from worsened conditions for evaporation of petrol and mixing it with air. It could be probably possible to improve efficiency of engine under low

load and at a low share of alcohol by applying a primary mixer of alcohol with petrol as well as by injecting the mixture through original injectors or by implementing a double injector used in dual-fuel, self-ignition engines.

At greater methanol shares efficiency of the engine was improved almost in the whole range of changes in its operational parameters, as shown in Fig. 8b. It suggests that even at unchanged compression ratio operational consumption of energy at dual-fuel feeding will be lower than that at feeding only with petrol.

Combustion of methanol, both as the only fuel and in mixture with petrol, affects content of toxic components in exhaust gas from ZI engine. The influence depends on alcohol share and engine load. At low methanol share values and low engine loads a greater content of CO was observed in comparison with that in case of feeding with petrol only, Fig. 9a. It was probably caused by decreased temperature due to presence of methanol, and worsened fuel evaporation resulting from some distance of the petrol injector. However at higher engine loads CO content, both in case of feeding with methanol only and in dual-fuel mode, was distinctly higher in comparison to that in case of petrol.

Combustion of methanol favourably affects emission of summary THC hydrocarbons, Fig. 9b. At dual-fuel feeding mode a distinct tendency to lowering THC emission may be observed and the lowering grows along with increasing share of methanol in combustion mixture. At feeding with methanol only, THC content was about 2,2,5 times greater than in case of feeding with petrol.



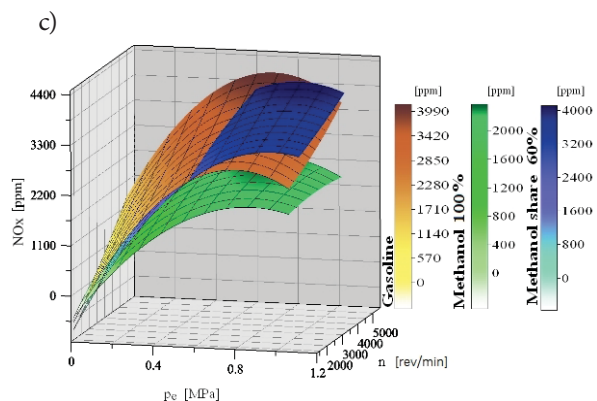


Fig. 9. Comparison of CO, THC and NOx content in exhaust gas from dual-fuel fed engine. Notation of the diagrams : for petrol – blue marked, for methyl alcohol (60% share) – bronze marked, for methyl alcohol only - green marked

Influence of methanol addition to fuel dose on changes in NOx content in exhaust gas is not unambiguous. During feeding with methanol only the lowering of NOx content was observed over entire working area of engine. However, during dual-fuel feeding changes in NOx content depended on engine load, Fig. 9c. In the range of low and medium load values the lowering of NOx content, but at higher loads – a rise of NOx content (by about 10÷15%) in relation to feeding with petrol, was observed. By controlling the air excess coefficient it was revealed that at dual-fuel feeding the engine was charged with somewhat poorer mixture in relation to its content in case of feeding with petrol and methanol only. It could cause an increase in NOx content at higher engine loads.

### Dual-fuel feeding the self- ignition engines with the use of alcohol

Alcohols have a high self-ignition temperature and low octane number, which makes it impossible to control their self- ignition in engine work conditions. For this reason combustible alcohol- air mixtures always require an external self-ignition source. In self-ignition engines the only possible feeding mode is a dual-fuel system for which a very good source of self-ignition is a dose of diesel oil. In this case, alcohol may serve as a basic energy source or as a small addition to improve diesel oil combustion. Alcohol for self-ignition engines may be delivered in three ways :

- in the form of alcohol vapour mixed with suck- in air (by evaporating alcohol in an evaporator using heat from cooling system or in the form of an aerosol comprising alcohol drops dispersed in air flux),
- by injecting liquid alcohol into inlet collector,
- by injecting alcohol directly to combustion chamber during final combustion phase.

Indirect delivery of alcohols to inlet collector, due to high evaporation heat of alcohols (2,5,3,3 times higher than that of diesel oil and petrol), results in lowering temperature of suck-in dose, which may unfavourably affect lag of ignition. However, while applying direct injection, high evaporation heat of alcohols, at their high shares, may be used for lowering

maximum temperature of a medium during its combustion. For this reason, this feeding mode is most advised, though it requires to apply an additional injector or dual-fuel injectors, which makes engine head construction a little more complex. Research projects on application of alcohols for dual-fuel ZS engines have been carried out by many centres worldwide, including Technical University in Radom, Poland, (see the publications of prof. Luft [1, 2] referring engine feeding with evaporated alcohol, and the publications of prof. Kowalewicz [3, 4, 5] referring application of methanol injection into inlet collector) as well as an external branch of Technical University of Łódź, Poland (see publication of this author [6] where a mixed feeding system for engines was discussed).

Selected results of the tests on a SW 680 self-ignition, slow-suction, six-cylinder engine fed with methanol and diesel oil, are presented below. Technical data of the engine are given in Tab. 2.

Tab. 2. Technical data of SW 680 engine

Parameter	Quantity
Cylinder bore	127 mm
Piston stroke	146 mm
Number of cylinders	6
Stroke volume	11,1 dm <sup>3</sup>
Compression ratio	15,8
Rated power	141–148 kW
Rotational speed at rated output	2200 rpm
Combustion chamber	toroidal in piston, direct symmetrical injection

Even a small addition of methanol favourably affects combustion of diesel oil, a main part of energy delivered to engine. In effect, overall efficiency of the engine under full load increases by about 3÷6% in relation to a traditionally fed engine, Fig. 10.

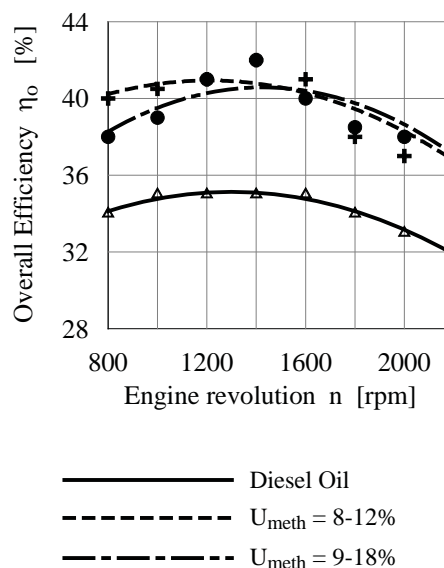


Fig. 10. Comparison of overall efficiency of traditionally-fed SW 680 engine and that dual-fuel fed by using diesel oil and methanol

Increases in overall efficiency of the engine at various shares of methanol are similar within the whole range of changes in rotational speed, while at a higher share, in the range of low rotational speeds, the efficiency increases are lower. It should be stressed that no optimization procedure of injection advance angle was conducted for the tested engine - the angle was constant and equal to 27° of single rotation before reaching upper return point, independently on rotational speed and load of the engine.

It seems that such increase in overall efficiency is associated with higher combustion rate of methanol as compared to that of diesel oil. It results in an increase of temperature of a medium in reaction zones and simultaneously in a greater number of diesel oil ignition spots. The last factor is especially important at maximum engine loads, when, at a complete biggest dose of diesel oil, initial combustion processes play significant role. The greatest changes in overall efficiency of the engine were then observed, Fig. 11.

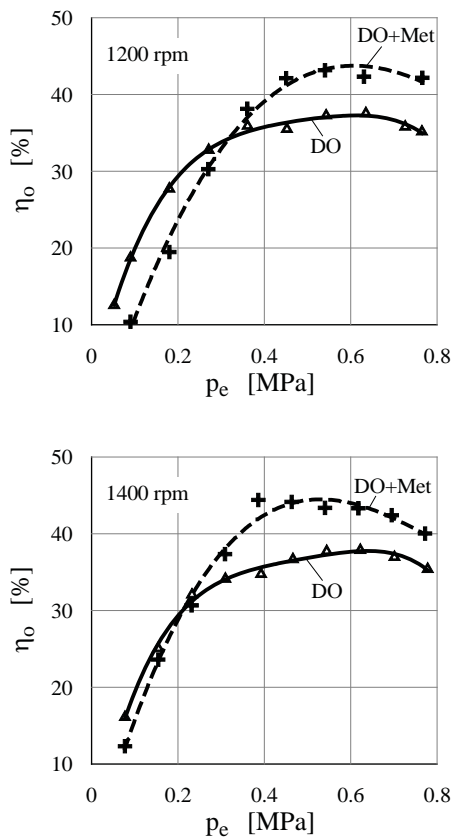


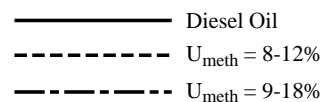
Fig. 11. Comparison of overall efficiency of traditionally-fed SW 680 engine and that dual-fuel fed by using diesel oil and methanol, presented in function of engine load.

In the presented tests a change in engine load was made by lowering diesel oil dose. At constant rotational speed, the selected control system caused methanol share increasing in total amount of energy along with engine load decreasing. In the range of low engine loads it could really affect charge temperature and decrease overall efficiency of the dual-fuel engine in relation to the traditionally fed engine. This is especially visible at the lower rotational speed of 1200 rpm (Fig.

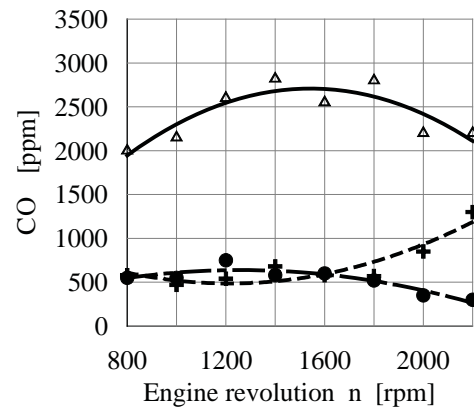
11). For higher rotational speeds the influence of methanol, because of a higher thermal load of engine, is smaller and the overall efficiencies are similar for both feeding modes in the range of low loads. It should be mentioned that at the lowest loads the share of methanol was significant, equal to 44÷50%, depending on rotational speed, in spite of that the methanol mixture was poor (the air excess coefficient  $\lambda_m > 3,8 \div 4,2$ ).

It seems that for combustion of poor methanol mixtures at low engine loads, interaction of liquid fuel jet plays crucial role. This observation is proved by results of the tests presented in Luft's publication [1] where the engine was fed with methanol vapour delivered from a special evaporator placed beyond inlet system (free from fuel evaporation cooling effect on to charge).

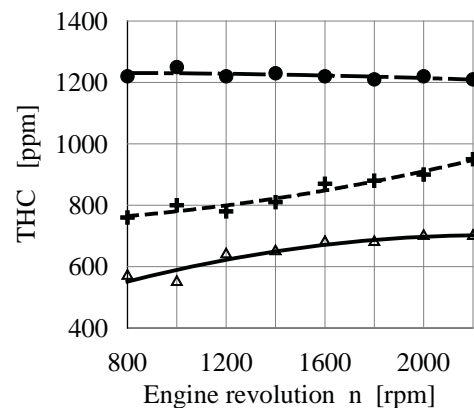
In more developed, turbo-charged engines changes in load are usually accompanied with the lowering of charging rate, which may also significantly influence methanol combustion process. It seems that it would be possible to make use from positive effect of methanol combustion also at lower engine loads by applying an appropriate control of charging rate. Additionally, it may be possible to change, if necessary, methanol share along with engine load changing, by applying methanol injection.



a)



b)



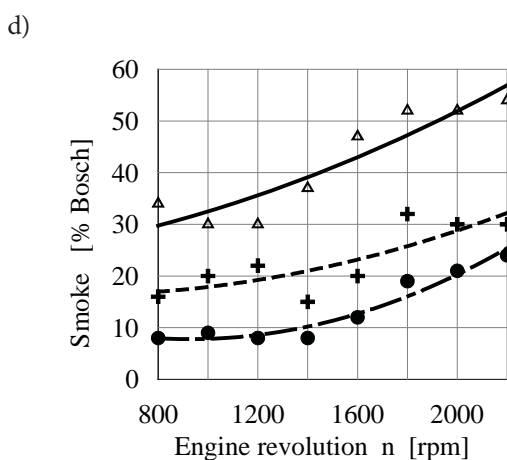
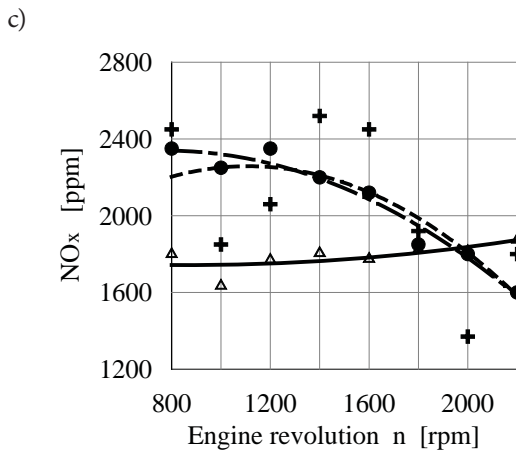


Fig. 12. Comparison of content of components of exhaust gas from SW680 engine fed respectively with diesel oil and two fuels : diesel oil and methanol [6]

Application of methanol addition to ZS slow-suction engines results in the significant lowering of exhaust gas smokiness and CO content at maximum engine loads, Fig. 12. However it may lead to a higher content of NOx and not fully burned hydrocarbons.

The lowering of smokiness is associated with the lowering of diesel oil dose and acceleration of its combustion by burning methanol vapour. The process depends on a methanol share in the whole energy dose delivered per cycle. For a lower share of methanol the lowering of smokiness is almost twofold in the whole range of changes in rotational speed. For a higher share of methanol the smokiness lowering was 2,6,3,0 -fold, which may be used for the lowering of emission of solid particles from engines installed in buses operating in towns with high road traffic. It is worth mentioning that such positive effect may be already reached by a small addition of methanol (or ethanol), while cost of adaptation of engine to dual-fuel feeding mode is rather low in the case in question.

The increased content of hydrocarbons in exhaust gas at mixed feeding mode may be associated with an escape of a part of charge as a result of sheltering the valves, which may be more intensive in charged engines. For this reason, in ZS engines alcohol injection should be applied, preferably

directly to cylinders. Research on this problem was carried out by prof. Kowalewicz of Technical University of Radom [3÷5]. It is also worth mentioning that methanol vapour is very toxic, which additionally makes injection systems preferable.

The increased content of NOx in exhaust gas at full engine load (Fig. 12c) is connected with an increased combustion rate of charge in dual-fuel, methanol-fed engine. The greatest differences in NOx content occur in the range of lower rotational speeds (increase by 30%), which decreases along with the speed increasing, while in the range of 2000, 2200 rpm the differences are even lower than in the case of traditional feeding.

## Conclusions

On the basis of the performed tests and analyses the following general conclusions may be offered:

- Dual-fuel feeding mode for self-ignition and spark-ignition engines with the use of alcohols is an interesting alternative which makes it possible to increase share of biofuels in total consumption of engine fuels.
- In the case of self-ignition engines alcohol may constitute a basic fuel or serve as an addition to improve combustion of diesel oil. Adaptation of engine to addition of alcohol does not require any wide changes in engine construction and may be introduced both in older engines and contemporary ones. However in both the cases injection of liquid alcohol to inlet collector or directly to cylinders, is preferable.
- Dual-fuel feeding mode in spark-ignition engines makes it possible to use an arbitrary share of alcohol (within the range of 0,100%) depending on load and thermal state of engine. Its compression ratio may be elevated this way by 1,5,2,5 units in relation to basic engine. Moreover, at high shares of alcohol, dual-fuel feeding mode does not require to use anhydrous alcohols as it is in the case of mixtures with petrol, as a result production cost of biofuels may be lower.
- Addition of methanol favourably affects combustion process of both petrol and diesel oil and results in the improving of operational parameters and overall efficiency of ZI and ZS engines. It is also possible to reach an increase in maximum effective power and torque at comparable loads (results of the tests are not presented in this paper). The rise in overall efficiency of ZI engine without any correction of compression ratio was equal to 3,5% at high shares of methanol, that is equivalent to the relative increase by 10,16%. In ZS engine the overall efficiency rise, at maximum loads, was obtained in the range of 3,6%, that is equivalent to the relative increase by 8,17%. The high relative increases in overall efficiency may contribute to a much lower consumption of energy by engines in operation. Addition of methanol leads to distinct changes in content of exhaust gas components emitted from dual-fuel engines. The following tendencies may be distinguished:
  - concerning ZI engines: the lowering of CO content at higher loads, the significant (2,2,5 - fold) lowering of

THC content, the lowering of NO<sub>x</sub> content at higher shares of methanol as well as its rise in some engine operation ranges.

- concerning ZS engines : the significant (2,3-fold) lowering of smokiness of exhaust gas, the lowering of CO content, the elevating of THC and NO<sub>x</sub> contents in some engine operation ranges.

It seems that certain unfavourable consequences of methanol combustion in ZI and ZS engines may be mitigated by optimizing control parameters of the engines.

### Bibliography

1. Luft S.: *Study on a self-ignition engine fed with methyl alcohol* ( in Polish). Professor degree dissertation. Publ. of Technical University of Radom, , Radom 1997.
2. Luft S.: *Analysis of influence of chocking suck-in air in dual-fuel ZS engine fed with methanol vapour on its operational parameters* ( in Polish). Journal of KONES Internal Scientific, Conference on Combustion Engines KONES'97, 1997.
3. Kowalewicz A., Pajączek Z.: *Dual-Fuel Engine Fuelled with Ethanol and Diesel Fuel*. Journal of KONES, International Combustion Engines, vol. 1-2, Warszawa 2003.
4. Kowalewicz A., Pajączek Z.: *Eco – Diesel engine with additional injection of ethanol*. Archive Combustions, vol. 23/2003 No. 3-4 , 2004.
5. Kowalewicz A.: *Emission Characteristics of Compression Ignition Engines Fuelled with RME/DF and Ethanol*. Journal of KONES, vol. 11/2004 No 1-2, 2004.
6. Stelmasiak Z.: *Dual-fuel self – ignition engines* ( in Polish). Institute of Operation Technology, Radom 2013, ISBN978-83-7789-200-8.
7. Borychowski M.: *Production and consumption of liquid biofuels in Poland and worldwide – prospects, hazards , arguable issues* ( in Polish). Roczniki Ekonomiczne Kujawsko–Pomorskiej Szkoły Wyższej w Bydgoszczy ( Annuals of Cuiavian – Pomeranian Higher School in Bydgoszcz ) No. 5 (2012), , pp. 39÷59.
8. Kupczyk A.: *Waste fats replace edible plants* ( in Polish). Agroenergetyka 2009, No. 4 (30).
9. Szewczyk K.: *Outline of possible applications of ethanol as a reproducible source of energy* ( in Polish). [www.mi.gov.pl](http://www.mi.gov.pl), 2008.
10. *Ethanol Internal Combustion Engines*. ETSAP Energy Technology Systems Analysis Programme, Technology Brief, June 2010.
11. Westcott P. C.: *Ethanol Expansion in the United States: How Will the Agricultural Sector Adjust?*. Economic Research Service, May 2007.
12. Gmyrek R.: *Bioethanol role in fulfilling NCW tasks in PKN Orlen Company* ( in Polish). *2nd Scientific Technical Conference „FUELS ZOOM - BIOETANOL ”, Cracow, 27÷28 April 2010.*
13. Szalkowska U.: *Bioethanol fuels: global prospects* ( in Polish). ). *2nd Scientific Technical Conference „FUELS ZOOM - BIOETANOL ”, Cracow, 27÷28 April 2010.*

14. Semikow J.: *Study on dual-fuel feeding system for spark ignition engine using petrol and alcohol* ( in Polish). Doctorate dissertation, ATH Bielsko-Biała, 2012.

### CONTACT WITH THE AUTHOR

Zdzisław Stelmasiak  
University of Bielsko -Biała  
2 Willowa Street  
43-309 Bielsko-Biala  
Poland  
email: [zstelmasiak@ath.bielsko.pl](mailto:zstelmasiak@ath.bielsko.pl)